COMPUTATIONAL MODELLING STUDIES OF MARTENSITIC TRANSFORMATION OF TiPd SHAPE MEMORY ALLOYS

By

RAMOGOHLO GIVEN DIALE

THESIS

Submitted in fulfillment of the requirements for the degree of

DOCTOR OF PHILOSOPHY

In

Physics

in the

FACULTY OF SCIENCES & AGRICULTURE

(School of Physical & Mineral Sciences)

at the

UNIVERSITY OF LIMPOPO

SUPERVISOR: PROF. H.R. CHAUKE

CO-SUPERVISOR: PROF. P.E. NGOEPE

: Dr. R. MODIBA

2021

DECLARATION

I declare that this thesis hereby submitted to the University of Limpopo, for the degree of Doctor of Philosophy in Physics has not previously been submitted by me for a degree at this or any other university; that it is my work in design and in execution, and that all material contained herein has been duly acknowledged.

Diale R.G. (Ms.)

31/05/2021
Date

DEDICATIONS

This work is dedicated to my husband Mighty Boshielo, my son Kutlwano, my parents Hellen and Alfred Diale, my sister Lucky and my brother Aubrey since they stood by me through all and gave me the reason to look into the future.

ACKNOWLEDGMENTS

First and foremost, I would like to express my sincere gratitude and appreciation to my supervisor, Prof. H.R. Chauke for leading me into the scientific research of computational materials science, for his great patience, professional guidance and continuous support during my studies, and for giving me strong confidence to do everything to the best of my ability.

I am also deeply indebted to my co-supervisors, Prof. P.E. Ngoepe and Dr. R. Modiba for leading me into an interesting and promising research world, for their continuous support and encouragements in my studies. The financial supports from the Council for Scientific and Industrial Research (CSIR), National Research Foundation (NRF) and Titanium Centre of Competence (TiCoC) are highly acknowledged.

Thanks to all the colleagues at the Material Modelling Centre for their helpful discussions and countless friendship.

Last but not least, I would like to express my deepest thanks to my dear parents, my brother and my sister for their endless support, encouragement and love.

I would like to give a special thanks to my husband Mighty Boshielo and my son Kutlwano. You have always been supportive and courageous.

ABSTRACT

Titanium-based shape memory alloys have attracted a lot of attention due to their important technological applications including actuator devices, electronics, and medical stents. This is due to their shape memory effects (SMEs) and superelasticity. $Ti_{50}Pd_{50}$ system is considered as one of the potential high temperature shape memory alloy (HTSMA) due to their high martensitic transformation temperature at 823 K. Previous studies revealed that this alloy is mechanically unstable displaying a negative C' ($C' < 0$) at 0 K. Furthermore, their strength collapses above 823 K, which results in low ductility, extremely poor shape memory and corrosion resistance. In the current study, multi-scale computational methods were used to investigate the stability and phase transformation of binary $Ti_{50}Pd_{50}$ and the ternary $Ti_{50}Pd_{50-x}M_x$ alloys. The ternary alloying of Ru, Pt, Ir, Co, Ni, Os, Al was carried out to enhance shape memory properties and the transformation temperature of the $Ti_{50}Pd_{50}$.

Firstly, density functional theory was used to investigate the stability of B2, $L1_0$, B19 and B19′ $Ti_{50}Pd_{50}$ shape memory alloys. A plane-wave pseudopotential method within the Perdew-Burke-Ernzerhof Generalized Gradient Approximation (PBE-GGA) was employed. The electronic properties, phonon dispersion curves and elastic constants were determined to check the stability of these alloys. It was found that the lattice parameters and heats of formation are well in agreement to within 5 % with the available experimental and theoretical data. More importantly, B19′ $Ti_{50}Pd_{50}$ was predicted to be the most stable structure (displaying the lowest heats of formation) as compared to B19, B2 and $L1_0$. This observation is consistent with the density of state stability trend. The elastic constants revealed mechanical instability of the B2 phase (C'>0) while $L1_0$, B19 and B19′ were found to be stable (C'<0). Furthermore, the B2

phase is vibrationally unstable due to the presence of soft mode emanating from the phonon dispersion curve.

Secondly, the supercell approach was used to investigate the effect of ternary alloying with Ru, Os, Pt, Ir, Co, Al and Ni on the B2 $Ti_{50}Pd_{50}$ structure. A 2x2x2 supercell was used to introduce the various dopants on the Pd sub-lattice. The heats of formation was found to decrease with an increase in Ru, Os, Pt and Ir concentrations (condition of stability), consistent with the density of states trend. This is in contrast to Co, Ni and Al addition which indicates that the thermodynamic stability is not enhanced (heats of formation increases). It was also found that an increase in Os, Ru and Co content stabilizes the $Ti_{50}Pd_{50}$ with a positive elastic shear modulus ($C' > 0$) above 18.25, 20 and 31 at. %, respectively. The results suggest that these dopants are likely to decrease the martensitic transformation temperature of the $Ti_{50}Pd_{50}$ alloy. Interestingly, partial substitution of Pd with Ir and Pt was found more effective in strengthening the compound and may enhance the martensitic transformation temperature of the $Ti_{50}Pd_{50}$ alloy further. The calculated moduli confirm that alloying with Ru, Os and Co effectively enhances the ductility in $Ti_{50}Pd_{50}$ systems. Anisotropy factor and Vickers hardness are studied and hardness is found to increase with an increase in Ru, Os and Co content.

Thirdly, the semi-empirical embedded atom interatomic potentials method incorporated in the LAMMPS code was employed to investigate the temperature dependence of the B19, B19′, B2, $L1_0$ binary $Ti_{50}Pd_{50}$ and ternary B19 $Ti_{50}Pd_{50-x}M_x$ (M= Co, Ni) structures. It was found that the B19 $Ti_{50}Pd_{50}$ gave a c/b ratio of 1.414 at approximately 1496 K which suggests that the B19 has transformed to a cubic B2 phase. Furthermore, the addition of Co and Ni lowers the transformation temperature from the B19 to the B2 phase.

The DFTB+ code was used to develop the sets of parameters for $Ti_{50}Pd_{50}$ and $Ti_{50}Pd_{50-x}Ru_x$ alloys employing the parameterization technique. As part of the validation, the developed set of parameters yielded results such as lattice parameters and bond distances that are in good agreement to within 5 % as compared to DMol^3 findings. Furthermore, temperature dependence calculations were performed to determine the transformation temperature of binary $Ti_{50}Pd_{50}$ and ternary $Ti_{50}Pd_{50-x}Ru_x$ alloys. It was observed that the addition of Ru reduces the transformation temperature of binary $Ti_{50}Pd_{50}$.

Finally, cluster expansion and Monte-Carlo simulations were employed to determine phase changes and high temperature properties of mixed $TiPd_{1-x}Ru_x$ and $Ti_{1-x}PdRu_x$ shape memory alloys. A total of 27 new structures for the B2 $TiPd_{1-x}Ru_x$ and 17 new structures for B2 $Ti_{1-x}PdRu_x$ were generated. The ground state line predicted 5 stable structures with negative formation energies for $Ti_{1-x}PdRu_x$ alloys, suggesting thermodynamic stability. It was found that $TiPd_2Ru$ (P4/mmm) is the most thermodynamic stable structure. All formation energies of $TiPd_{1-x}Ru_x$ alloys are positive, showing that there is a miscibility gap in the system and thermodynamic instability. The result showed that Ru prefers being substituted on the Ti-site than the Pd-site. It was found that Ti_2PdRu and $TiPd_2Ru$ mix at 1600 K and below 1400 K, respectively which were confirmed by the constructed phase diagram of $TiPd_{1-x}Ru_x$ and $Ti_{1-x}PdRu_x$.

Thus, multi-scale approaches were successfully used to understand the structural, electronic, elastic and vibrational stability, as well as the transformation behaviour of both binary and ternary alloys.

Contents

Lists of figures

List of Tables

Chapter 1

Introduction

This chapter provides some background information of shape memory alloys from previous theoretical and experimental studies. Firstly, the concept of shape memory alloys with regard to binary TiPd alloys are introduced; then the various other related binary and ternary alloys are discussed. The intentions of the study, aim, and objectives of the thesis are set out. Finally, the outline of the thesis is given.

1.1 Shape memory alloys

Shape memory alloys (SMAs) have the ability to remember their shape after being deformed and play an important role in many industries such as automotive, aerospace and medical [1, 2], this is due to their shape memory effects (SMEs) and superelasticity [1]. These alloys undergo a reversible martensitic phase transformation from the high symmetry austenite to the low symmetry martensite phase upon the influence of temperature or stress field [3, 4]. Note that the martensite phase transformation refers to a diffusionless solid-state phase transition occurring in alloys, where the parent phase changes into the product phase through coordinated lattice deformation. Amongst the SMAs, the Ti-Ni has been studied for a long period and is useful because of their unique sufficient ductility and shape memory properties [5]. However, these alloys have

a limited temperature around 373 K, so their applications are limited [6]. Copper-based SMAs such as Cu–Zn, Cu–Al, and their related alloys are also of commercial importance because of their low price, but they suffer instability of martensitic phase and brittleness [7].

Recently, SMAs are being developed to suit many applications in many fields, especially for engineering properties. There is an increasing demand for high temperature shape memory alloys (HTSMAs) for use in automobiles, pipe couplings and aircrafts engines and other applications. In order to design better SMAs, it requires that their working temperature and functional stability must be enhanced. The working temperature is critical for designing of HTSMAs, while the functional stability is important for improving their reliability of SMAs [8]. The working temperature and functional stability of SMAs can be adjusted by replacing their constituent elements with others, in particular precious metals such as Pt, Pd, Al, Ru, Ir, Os and Ni. For example, the working temperature of TiNi alloys can be increased to the range of 400–1200 K, when Ni is replaced with the same group elements, namely Pd or Pt [9, 10]. In recent studies, intermetallic compounds such as NiAl [11], TiPt [12, 13] and TiPd [14] have been given more attention for future HTSMAs development. This is due to their martensitic transformation temperature above 373 K.

1.2 TiPd SMAs

Titanium-based alloys in particular $Ti_{50}Pd_{50}$ are being developed for high temperature applications. $Ti_{50}Pd_{50}$ systems are considered as one of the potential

HTSMA's due to their high martensitic transformation temperature [15, 16]. The $Ti_{50}Pd_{50}$ has two stable phases - the high-temperature phase, called austenite and the low-temperature phase called martensite [17]. A high temperature phase of $Ti_{50}Pd_{50}$ has a simple cubic CsCl-type (cP2, B2) structure [18], while at ambient temperature the martensite phase has been reported as the orthorhombic AuCd-type (oP4, B19) structure [19, 20]. These alloys have excellent chemical and physical properties such as lightweight, oxidation resistance and ductility at 823 K [21, 22]. However, their strength collapses above 823 K, which results in low ductility, extremely poor shape memory and poor corrosion resistance [4, 14, 23, 21]. Consequently, the binary $Ti_{50}Pd_{50}$ alloy has no strength for use in actuators and aeronautic industry and ternary alloys will need to be established to improve their properties [24, 25]. The collapse is due to a possible phase transformation from body centered cubic (bcc) to other tetragonal and orthorhombic phases such as $L1_0$ and B19, similar to those reported in TiPt alloy [26]. Nonetheless, their transformation behaviour has not been ascertained explicitly. Furthermore, there is still a lack of knowledge to understand the equilibrium phase diagram especially in the near-equiatomic region that is the most important for practical applications as HTSMAs.

In order to enhance the transformation temperature and performance of the $Ti_{50}Pd_{50}$ SMA's which include hardening, forgeability, corrosion resistance and thermal stability, ternary alloying has been suggested. The elements such as Au, Ni, Ru, Rh, Ir, Pt, Zn, Rc, Tc, Os and Co were reported as the best site preference for both Ti and Pd substitution with less than 50 atomic percentage (at. %), while Ag and Cd prefer the Ti substitution site in B2 $Ti_{50}Pd_{50}$ structure [27]. The addition

of the third elements such as Ru, Ir, Pt, Co and Ni elements showed high work output and good workability [28]. The addition of such elements may enhance the transformation temperature of $Ti_{50}Pd_{50}$ to above 1000K [29]. Previously, the addition of Ni to $Ti_{50}Pd_{50}$ has shown improvement in shape memory characteristics for $Ti_{50}Pd_{30}Ni_{20}$ composition [21].

Cobalt and other PGMs elements have been in use for the production of various components such as vanes or combustion chambers in gas turbines for their exceptional heat-resistant properties [30]. Ru, in particular, is one of the most effective hardeners for platinum and palladium and is alloyed with these metals to increase resistance to heat and resistance to corrosion [31]. It can also be used to enhance the mechanical properties and corrosion resistance for titanium-based alloys and high-temperature single-crystal superalloys for application in jet engines [31, 32]. These alloys have a higher temperature capability and lower creep rate which will make the actuator more durable and increases aircraft efficiency [31]. Osmium is most often used as an alloying agent with other PGMs and found in electrical contacts, styluses and medical devices and in other applications that need great strength and stiffness [33]. The additions of Os, Ru, Ir, Pt, Co, Al and Ni may enhance the transformation temperature of $Ti_{50}Pd_{50}$ to above 1000 K.

In this thesis, the ternary alloying of $Ti_{50}Pd_{50}$ with Os, Ru, Ir, Pt, Co, Al and Ni have been performed using different approaches to investigate the thermodynamic, electronic, mechanical and thermal stability. Furthermore, the effect of Os, Ru, Ir, Pt, Co, Al and Ni on the ductility/brittleness has been deduced from the Poisson's ratio, Debye temperature and Cauchy pressure, which

confirms the strength of the systems. The calculated results will provide useful and practical guidance for further experimental and theoretical investigations on the future ternary shape memory alloys.

1.3 Structural properties

The TiPd system has various compositions, however, the focus on SMAs development at 50:50 composition where B2, B19, B19′ and $L1_0$ TiPd structures are observed. The B2 phase is a cubic high temperature structure with the space group Pm-3m while the B19 phase is an orthorhombic low temperature structure with the space group Pmma. The positions of B2 atoms are denoted by the Pearson symbol cP2 and the prototype is CsCl with all angles being 90°. The positions of B19 atoms are denoted by the Pearson symbol of oP4 and the prototype of AuCd with all angles being 90°. B2 experimental observed unit cell parameters are a=b=c=3.180 Å [23] while B19 experimental observed unit cell parameters are a=4.550 Å, b=2.780 Å and c=4.860 Å [20].

The B19′ structure is monoclinic with the space group $P2_1/m$ while the $L1_0$ structure is tetragonal having the space group P4/mmm. B19′ theoretical lattice parameters are a=2.744, b=4.797, c=4.460 [34], with prototype NiTi. Furthermore, $L1_0$ theoretical lattice parameters are a=b=2.855, c=3.907 [34] with the prototype of AuCu. This is detailed in Table 1-1 and the atomic arrangements of these structures are shown in Figure 1-1.

Table 1-1 Structural properties of B2, B19, B19′, L1$_0$ Ti$_{50}$Pd$_{50}$ from theoretical and experimental observations.

	B2 [20]	B19 [23]	B19′ [34]	L1$_0$ [34]
Lattice parameter (Å)	a=b=c=3.180	a=4.550	a=2.744	a=b=2.855
		b=2.780	b=4.797	c=3.907
		c=4.860	c=4.460	
Space group	Pm-3m	Pmma	P2$_1$/m	P4/mmm
Prototype	CsCl	AuCd	NiTi	AuCu
Pearson symbol	cP2	oP4	mP4	tP2
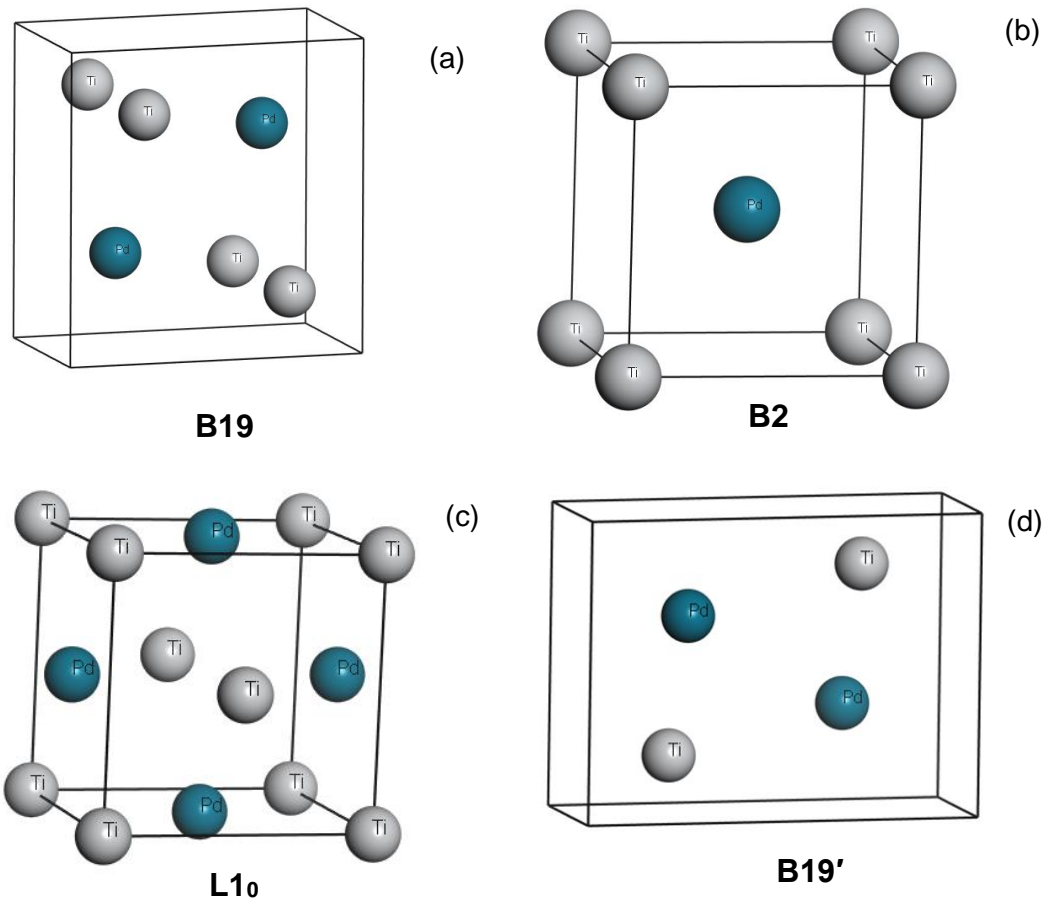
Figure 1-1 The Ti$_{50}$Pd$_{50}$ (a) B19 with 4 atoms per unit cell (b) B2 with 2 atoms per unit cell (c) L1$_0$ with 4 atoms per unit cell (d) B19′ with 4 atom per unit cell.

1.4 Intentions of the study

The study of $Ti_{50}Pd_{50}$ alloy is of interest mainly in automotive and aerospace applications for quite some time due to higher martensitic transformation at 823 K [21, 22]. This alloy continues to gain popularity due to many favourable shape memory properties such as high melting temperature, high yield strength at high temperatures, good resistance to oxidation and corrosion. Previous studies showed that B2 $Ti_{50}Pd_{50}$ is unstable displaying a negative elastic shear modulus (C') at 0 K [24, 35]. Furthermore, $Ti_{50}Pd_{50}$ displays poor shape memory behaviour during transformation, which results in poor corrosion resistance [4, 14, 21, 23, 36]. This then instigates a need to enhance their mechanical properties and understand the transformations behaviour in binary and ternary additions.

The intention of the study is to use computational modelling methods to determine the stability of binary $Ti_{50}Pd_{50}$ and ternary $Ti_{50}Pd_{50-x}M_x$ (M= Ru, Os, Pt, Ir, Al, Ni, Co). The equilibrium ground state properties will be determined using DFT based planewave pseudopotential [37] VASP code [38] employing the GGA-PBE [39]. Different equilibrium ground state properties such as lattice parameters and heats of formation of these alloys will be deduced. The elastic properties, thermal properties, electronic density of states and the phonon dispersions curves will be determined to check the stability of the ternaries. Effect of Ru, Os, Ir, Pt, Co, Ni and Al additions on $Ti_{50}Pd_{50}$ will be investigated using supercell approach to observe the stability at different compositions at 0 K. A 2x2x2 supercell will be constructed on the binary $Ti_{50}Pd_{50}$ and a substitutional search tool within the Medea software platform will be used to substitute Pd with Ru, Os, Ir, Pt, Co, Ni

and Al. A supercell approach will be performed mainly for up to five compositions 6.25, 18.75, 25, 31.25 and 43.75. Full geometry optimization will be performed to find the ground state properties for all the compositions. The electronic and mechanical properties will be determined from optimized structures. It will be established that Ru and Os substitutes are mostly favourable. This is in line with previous studies as Ru addition has shown to improve different properties such as Hardness in PtAl [40].

Furthermore, the temperature dependence of the lattice parameters, XRDs and the elastic constants for the $Ti_{50}Pd_{50-x}M_x$ (M= Co and Ni) will be studied using the LAMMPS code. The lattice parameters and XRDs will be used to determine the phase transformation as the temperature is increased. Mechanical properties will be determined to identify the strength of the structures at a higher temperature.

The DFTB+ technique will be used to derive interatomic potentials of both binary Ti-Pd and ternary Ti-Pd-Ru alloys. In order to obtain the set of parameters for Ti-Pd and Ti-Pd-Ru, the potential confinement radius for Ti, Pd, and Ru elements will be constantly adjusted until the suitable radii are obtained. Geometry optimization will be carried out to obtain the ground state properties. This will be considered converged if structural properties produced are in good agreement with available theoretical and experimental results. During geometry optimization, GGA-PBE and LDA-PWC exchange-correlation functionals will be used to check their suitability for describing the properties of the systems. The thermodynamic, electronic and elastic properties will be determined from optimized structures to deduce the possible stability and be compared with the results obtained using

standard DFT. The derived potential will be explored to determine the transformation occurrence and stability. A transformation temperature will be investigated to establish at what temperature does the system change, using the NPT ensemble within DFTB. The time step and simulation time will be determined before any temperature calculations would be done, which is critical for making a meaningful prediction.

Furthermore, the Cluster expansion and Monte Carlo simulations will be explored to generate new stable phases on B2 Ti-Pd-Ru. A flowchart will be used to generate ground-state structures which are compared with previous approach i.e. DFT, DFTB and LAMMPS. In order to assess the accuracy of the cluster expansion, the cross-validation score (CVS) will be considered. A cluster expansion with CVS< 5 meV/atom will be considered accurate. Monte Carlo simulations will be used to construct the ternary phase diagrams from the critical temperature of each concentration.

1.5 Aim

The aim of the study is to investigate the stability and phase transformation of binary $Ti_{50}Pd_{50}$ and the ternary $Ti_{50}Pd_{50-x}$ M (M= Ru, Pt, Ir, Co, Ni, Os, Al) shape memory alloys.

1.6 Objectives

In this study, we investigate the stability and phase transformation of binary $Ti_{50}Pd_{50}$ and the ternary $Ti_{50}Pd_{50-x}M$ alloys. Different codes such as VASP, LAMMPS, DFTB+ and Universal Cluster-Expansion (UNCLE) are used.

The objectives of the study are to:

i   determine the structural, thermodynamic and electronic stability of binary $Ti_{50}Pd_{50}$ and ternary $Ti_{50}Pd_{50-x}M_x$ (M= Ru, Pt, Ir, Co, Ni, Os, Al) SMAs,

ii   investigate the mechanical stability from the elastic properties and the phonon dispersion curves of the binary $Ti_{50}Pd_{50}$ and ternary $Ti_{50}Pd_{50-x}M_x$,

iii   determine the thermal stability by investigating the Debye temperature, heat capacity, thermal coefficient of linear expansion of the binary $Ti_{50}Pd_{50}$ and ternary $Ti_{50}Pd_{50-x}M_x$,

iv   investigate temperature dependence on the lattice parameters and XRDs to check the transformation temperature of binary $Ti_{50}Pd_{50}$ and B19 $Ti_{50}Pd_{50-x}M_x$ (Co, Ni) structures using LAMMPS code,

v   derive reliable interatomic potentials that can effectively describe stability and transformation temperature of the binary $Ti_{50}Pd_{50}$ and ternary $Ti_{50}Pd_{50-x}Ru_x$ systems using DFTB+ code,

vi   generate new stable phases of Ti-Pd and Ti-Pd-Ru system using UNCLE code,

vii   use Monte carlo simulation to predict the ternary Ti-Pd-Ru phase diagrams.

1.7 Hypothesis

If ternary alloying enhance the stability and martensitic transformation of $Ti_{50}Pd_{50}$ then possible alloys that can be used for high temperature application can be developed.

1.8 Research questions

The questions to be answered by this project are:

i. Which alloying elements would be more effective in enhancing the thermodynamic, electronic and mechanical stability of $Ti_{50}Pd_{50}$?

ii. Which alloying elements can be used to determine the thermal stability of $Ti_{50}Pd_{50}$ alloy?

iii. Which alloying elements can be utilised to enhance the transformation temperature of $Ti_{50}Pd_{50}$ alloy above 1400 K?

iv. Which interatomic potential are suitable to describe the stability and transformation temperature of binary Ti-Pd and ternary Ti-Pd-Ru alloys be determined?

v. What are the other possible binary and ternary structures that may exist in the new ground state line of both binary Ti-Pd and ternary Ti-Pd-Ru alloys?

vi. At what temperature and concentration range would Ti-Pd-Ru systems mix well using Monte Carlo simulation?

1.9 Outline

In chapter 1, we dealt with the background and introduction of the Ti-based shape memory alloys (SMAs).

In chapter 2, we give a brief summary of the literature review in terms importance and uses of the SMAs from previous experimental and computational approaches.

Chapter 3 give the detail of the methods that were used to perform the calculations in this study. We briefly introduce the density functional theory (DFT) and the approximation methods used such as the generalised gradient approximation (GGA) and the local density approximation (LDA). The plane-wave pseudopotential approach is outlined. We also introduce computational codes used such as VASP, PHONON, DMol^3, DFTB+, LAMMPS and UNCLE and their implementation in this study. Lastly, we give a brief theoretical background on the calculated properties, i.e. heats of formation, density of states, and elastic properties.

Chapter 4 present the results and discussion on the structural, thermodynamic, the density of states, phonon dispersion, phonon density and mechanical properties for $Ti_{50}Pd_{50}$ alloy and compare with the available experimental values.

In chapter 5, we discuss the temperature dependence of the $Ti_{50}Pd_{50}$ alloy. The temperature dependence of the lattice parameters and the XRD patterns of the

binaries are plotted and discussed. We also discuss the elastic properties of the $Ti_{50}Pd_{50}$ alloy.

Chapter 6 presents the structural, thermodynamic and electronic properties of $Ti_{50}Pd_{50-x}M_x$ alloys generated using the supercell approach. The equilibrium lattice parameters, heats of formation and densities of states are discussed in detail and compared with the available experimental results.

Chapter 7 focuses on the mechanical properties of the ternaries $Ti_{50}Pd_{50-x}M_x$. We discuss in detail the mechanical properties i.e. elastic constants, moduli (Bulk, Shear and Young's), Pugh (B/G) and Poisson's ratio as well as Cauchy pressure of the ternaries $Ti_{50}Pd_{50-x}M_x$. We also compare the trend of mechanical stability amongst the ternaries.

Chapter 8 presents the vibrational and thermal properties of $Ti_{50}Pd_{50-x}M_x$ alloys. In particular the phonon dispersion curves, Debye temperature, heat capacity and thermal coefficient of linear expansion.

In chapter 9, we present the temperature dependence of the $Ti_{50}Pd_{50-x}M_x$ (M = Co, Ni). The volume, density, lattice parameters and XRD patterns of the ternaries B19 $Ti_{50}Pd_{50-x}M_x$ are investigated and discussed. We also discuss the mechanical properties of the $Ti_{50}Pd_{50-x}M_x$ ternaries.

Chapter 10 focuses on the parameterization of the self-consistent-charge density functional tight-binding (SCC-DFTB) set of parameters for the binary $Ti_{50}Pd_{50}$ and ternary $Ti_{50}Pd_{50-x}Ru_x$. The validation of the developed set of parameters is given. We also present transformation temperature for both $Ti_{50}Pd_{50}$ and $Ti_{50}Pd_{50-x}Ru_x$ using the derived parameters.

In chapter 11, Cluster expansion and Monte carlo results on phase stability are discussed for binary Ti-Pd, ternary $TiPd_{1-x}Ru_x$ and $Ti_{1-x}PdRu_x$ alloys. We present generated new ground state structures for both binary Ti-Pd, ternary $TiPd_{1-x}Ru_x$ and $Ti_{1-x}PdRu_x$ systems. Furthermore, we discuss constructed phase diagrams of the $TiPd_{1-x}Ru_x$ and $Ti_{1-x}PdRu_x$ alloys.

Lastly, in chapter 12, we give the summary and conclusion of the study, recommendations and future work are also listed.

Chapter 2

Literature review

In this chapter, we give a review of previous studies on shape memory alloys (SMAs) and their applications. Furthermore, the transformation temperature of TiPd SMAs will be reviewed. Various binary and ternary SMAs that have been investigated previously using both experimental and computational studies are presented. Finally, a background on the ternary SMAs and the methods used to assess the properties of binary and ternary SMAs will be reviewed.

2.1   History of shape memory alloys

SMAs fall into the category of smart materials and are capable of recovering their shape, after being deformed at low temperatures, when the temperature is increased. The leading SMAs on the market are TiNi-based alloys which are used in the medical sector and, other applications where the application temperatures do not exceed 373 K [41]. Given the potential of SMAs at low temperatures, national aeronautics and space administration (NASA) and others have developed HTSMAs for use in higher temperature applications such as sensors and actuators in jet engines, including, core exhaust chevrons, flow control devices, and active clearance control devices, etc. The shape memory effect in these alloys is related to the reversibility of the martensitic transformation [42]. The SME was first observed on gold-cadmium alloys as a result of shape change enabling the ability to create macroscopic strains that lead to the production of a

15

large number of different alloys [43]. Furthermore, Chang and Read showed the reverse transformation of AuCd in terms of resistivity changes and metallurgical observation [44]. They also studied the effects of stress and temperature on diffusionless phase transformations which are responsible for shape memory effect and superelasticity [44]. It was also revealed that the nucleation in this diffusionless transformation is strongly influenced by the state of stress present in the specimen. Furthermore, it was found that the electrical resistivity of the tetragonal phase after transformation decreases slowly with time (finally reaching a stabilised value). A breakthrough in the medical application was made with regard to the treatment of bone fracture [45]. They managed to design and built bone holders using novel TiNi wires for 20 patients.

2.2 Application of shape memory alloys

The major applications of Ti-based alloys are in the medical sector, engineering and technical field and are used as stents, bone plates, eyeglasses, couplings and fasteners, actuators, thermal power plants, aircraft turbine engines, etc. This is mainly because these alloys are less expensive, easier to work with, have high fatigue strength and have a lot of shape-changing potential [46]. For example, TiNi alloys are used for noiseless operation in vehicles. Furthermore, nitinol was first used to create a reactive pipe coupler to join hydraulic lines on the F-14 aircraft with a low transition temperature below 153 K [47].

In the medical field, Nitinol is used in two ways: the development of stents [48] to treat narrow or weak arteries and secondly for implants in dentistry [49]. The first superelastic braces were developed three decades ago [49]. The coil spring in

cars was first outlined and developed in 1990 [1, 50]. In 2013, the first car to incorporate SMA actuators was developed and these actuators replace heavier motorised actuators in order to reduce the hatch vest from the trunk that releases air [51]. The recent applications of shape memory alloys are found in civil infrastructures including steel, concrete and timber structures [52]. It was revealed that SMA in civil infrastructures enhances the structural behaviour and energy dissipation of external excitation in seismic loads [52].

2.3 Transformation temperature in SMAs

Transformation temperature is the temperature at which there is a phase change in the structure [1]. The martensitic transformation occurs from austenite to martensite or vice versa by means of a lattice shearing mechanism [1]. An austenite phase has a high symmetry with a cubic lattice and occurs at high temperature while martensite is the lowest symmetry occurs in tetragonal or monoclinic at low temperature [1]. The sputter deposition of TiNi, TiNiPd and TiPd films was reported to display the two-way SME in sensors and actuators [53]. This behave is a common property of SMA, it is called Two Way SME. Two-way SME refers to the SMAs that are able to remember their shape above austenite final at high temperature and another shape below martensite finish (M_f) at low temperature on both heating and cooling. It was reported that TiPd transformation temperature is from austenite to martensitic as shown in Figure 2-1. The M_s represents the martensitic start temperature which implies that the initial phase change to martensite upon cooling occurs, while M_f represents the martensite finish temperature which means that the complete phase change to martensite

upon cooling. The A_s represents austenite start temperature which means that the initial phase change to martensite upon heating, while A_f represent the austenite finish temperature which means that is the complete phase change to austenite upon heating [1, 53].
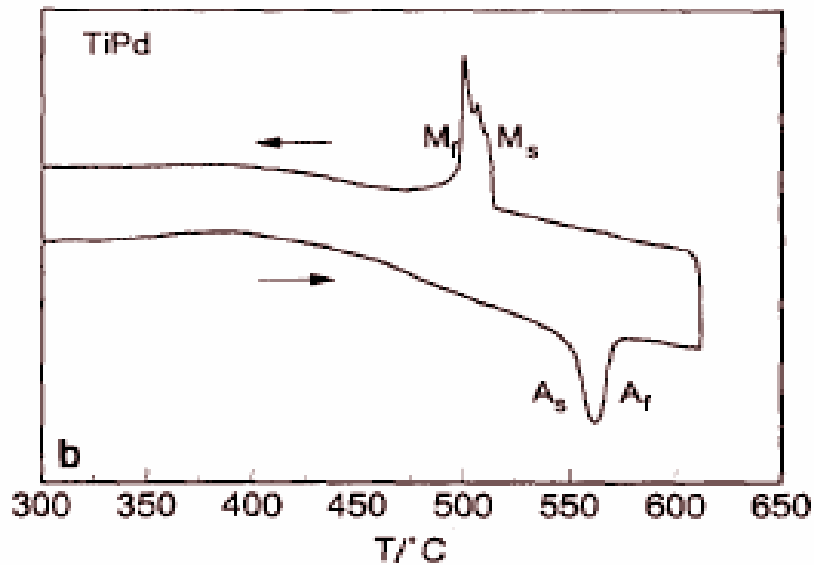
Figure 2-1 Show austenite to martensitic transformation temperature for TiPd [53].

2.4 Binary systems

In Table 2-1, we show various binary SMAs that exist or form. This Table is presented in order to indicate binary alloys which have been investigated previously either computationally or experimentally. The sign right (✓) indicate that the alloy has been investigated or its availability and cross (×) indicates unavailability or the alloy does not form.

18

Table 2-1 Various different binary SMAs.

	Ti	Zr	Hf	Mo	Fe	Ru	Co	Rh	Ir	Os
Ni	✓	✓	✓	✓	✓	✓	✓	✓	✓	✓
Pd	✓	✓	✓	✓	✓	✓	✓	✓	✓	✓
Pt	✓	✓	✓	✓	✓	✓	✓	✓	✓	✓
Cu	✓	✓	✓	✓	✓	✓	✓	✓	✓	✓
Ag	✓	✓	✓	✓	✓	✓	✓	✓	✓	✓
Au	✓	✓	✓	✓	✓	✓	✓	✓	✓	✓
Ti	✗	✓	✓	✓	✓	✓	✓	✓	✓	✓

2.4.1 Zr (Pd, Pt, Ni, Ag, Ti) alloy

The compounds ZrPd and ZrPt were reported to have the B2 or B33 (BCr-type) structures [54]. Furthermore, the ZrPd alloy was observed to transform to a monoclinic phase at 473 K before it undergoes a martensitic transformation from high temperature B2 to B33 at 875 K [55]. At room temperature, the martensitic phase in equiatomic ZrPd alloy is Cm [55]. It was previously reported that ZrNi and ZrPd amorphous alloys absorb an extensive amount of hydrogen [56]. The ZrPt alloy was reported to undergo a martensitic transformation from the B2-type structure to the B33-type phase near 1730 K [57]. Previously, the ZrPt system showed to have a B33 structure at low temperature [54] and have B2 structure at high temperature [54]. A recent study investigated the use of AgZr alloys as active brazers in composite materials suitable for applications requiring aggressive thermal and mechanical conditions [58, 59]. Furthermore, TiZr alloy has been

used for endosseous dental implant applications as tested in vitro, in animals and clinically [60].

2.4.2 Hf (Ni, Pd, Pt, Cu, Ti) alloy

Hf-based alloys, in particular, the equiatomic HfNi alloy was reported to exhibits a martensitic transformation from the B2-type structure to the B33-type structure near 1420 K [61]. Studies done by Stalick et al. [62] reported that the space group in equiatomic HfPd alloy at room temperature is identified as $P2_1/m$. This was done using the powder neutron diffraction data. Martensitic transformation in equiatomic HfPd alloy was found to be M_s=819 K, M_f=794 K, A_s= 928 K, A_f= 954 K, this was tested using differential scanning calorimetry measurement [63]. In the Hf‑Pt systems, their spin-orbit and the prototypes for TII and B33 were found to remain degenerate and the most stable. Furthermore, a considerable gap was preserved to the less stable B2 structure.

Previously, ab initio method was used to study the Cu-Hf systems employing the VASP code with Vanderbilt-type ultrasoft pseudo-potentials [64]. Furthermore, twenty-eight different structures have been studied, of which four, Cu_5Hf; Cu_8Hf_3; $Cu_{10}Hf_7$ and $CuHf_2$, were identified as stable. Previously, there was no experimental information about the structure of Cu_5Hf [65].

In the previous years, Ti and Hf have been proven to have good biocompatibility and osteoconductivity in both soft and hard tissues [66]. Furthermore, other studies focused on the effects of Hf content and heat treatment to understand the mechanical properties of Ti-Hf alloys [67]. It was found that the beta-quenched structures have higher strengths than the beta-furnace-cooled structures.

Another study conducted by Zhou [68] revealed that an increase in Hf content gently reduces the dynamic Young's modulus but strongly enhances the strength of Ti-Hf alloys. Furthermore, the $Ti_{60}Hf_{40}$ alloy was found to have the highest strength-to-modulus ratio among other structures [68].

2.4.3 Ti-based shape memory alloys

Previously, the Ti-Mo alloys were arc-melted and their compositions were analyzed by EDX, XRF and SEM from 4 to 20 at. % Mo [69]. It was found that their surfaces were without defects, while the Mo mapping showed a homogeneous distribution. Furthermore, significant retention of the β-phase was found for the alloy containing 10 at. % Mo, while at higher Mo concentrations (15 and 20 at. %), retention of β-phase was only verified. Lui et al. have studied the microstructures and mechanical properties of Ti-Mo alloys [70]. It was found that the addition of Mo can refine the microstructure of TiMo alloy greatly and raise sintering temperature which can effectively increase the alloy density without grain coarsening. On the other hand, Zhang et al. [71] studied the formation of stress-induced α martensite in a metastable TiMo-based alloy. This was done using X-ray diffraction and transmission electron microscopy. It was found that the growth of martensite laths from the resultant stacking faults occurs by the motion of interfacial disconnections. Davis et al. [72] reported that in Ti-Mo systems, the martensitic structure changes from hexagonal α' to orthorhombic α'' at Mo rates of approximately 6 %. More recently, Bania [73] reported that a minimum of 10 at. % Mo was required to completely stabilize the β phase at room temperature.

Previously, Niinomi et al. [74] conducted a study on the corrosion wear fracture of new β-type biomedical titanium alloys. It was indicated that β-titanium alloys composed of non-toxic elements such as Nb, Ta, Zr, Mo, and Sn showed lower elasticity modulus [74]. However, it was recommended that alloys with greater strength should be developed [74].

Mazhuga et al. reported thermodynamic calculation of phase equilibria in the Ti-Ru, Ti-Os, Ni-Ru binary systems [75]. It was reported that Ti-Os and Ti-Ru alloy phase diagrams could not be achieved using a sub regular solution model.

The studies showed that the Os-based structures particularly TiOs have considerably higher melting temperatures of 2433 K [54]. Furthermore, the B33 structure was found to be the least stable phase as it gave the highest heat of formation value [54]. Raman et al. on the other hand investigated the stability of Ti-Rh. It was reported that $L1_0$, B19 and B33 are stable at a lower temperature while the B2 phase was stable at high temperature [76]. Tan et al. [77] examined elastic properties and electronic structures of Ti-based binary and ternary shape memory alloys using first-principles study. It was found that both NiTi and TiCo are mechanically stable with positive C' ($C' > 0$) [77]. The melting point and phase transformation temperature of Ti-Au were reported to be ~ 100 K higher than that of Ti-Pd and Ti-Ni [78].

Equiatomic TiPt was reported to transform from B2 to B19 orthorhombic martensitic phase at 1300 K [9]. Furthermore, it was found to exhibit low strength (~450 MPa) in martensite and very low strength (~20 MPa) in the B2 phase region [9]. The martensitic start temperature was found as follows; TiNi have ($M_s \approx 350$ K), then TiAu ($M_s \approx 900$ K), also TiPt ($M_s \approx 1200$ K) and TiPd ($M_s \approx 800$ K) [79].

Table 2-2 shows the melting temperature and martensite start (M_s) temperature of TiNi, TiPd and TiPt alloys.

Table 2-2 Melting temperature and martensitic start temperature of TiNi, TiPd and TiPt [80].

B2 phase	Melting Temperature (K)	M_s (K)
TiNi	1583	333
TiPd	1673	783
TiPt	1830	1343

2.5   Recent research on Ti-Pd alloys

The Ti-Pd alloys have brought more attention due to their interesting mechanical properties and technological importance for engineering and medicine, particularly for the shape-memory effect [4, 19]. These alloys were observed to undergo a martensitic transformation temperature at about 800K, but transition temperature can be reduced to 410K with 8% substitution of Cr for Pd [22]. The TiPd had been reported to exist as a high temperature phase (austenite phase) which has a simple cubic B2 with a CsCl type-structure while at low temperature is known as the martensite phase with an orthorhombic B19 structure with AuCd prototype [22]. It has been reported that TiPd undergoes a B2-to-martensite phase transformation with Ms between 783 and 836 K [80].

Previous ab initio studies on TiPd SMAs system mainly focused on the structural properties, optical properties and the structural energies of (B2, B19, B19′ and L1$_0$) phase [34]. Ab initio approach was used to study the ground state, phase stabilities, enthalpies of formation, electronic and elastic properties [34]. The monoclinic B19′ TiPd was found to be the most stable structure with the lowest

value of heat of formation (-0.552 eV/atom). Furthermore, $TiPd_2$ orthorhombic $MoPt_2$-type structure was also reported to be stable but with slightly lower energy than the tetragonal $MoSi_2$-type structure above 1553 K [34].

Another study reported the enthalpies of formation of refractory intermetallic compounds TM and TM_3 formed between Group IV elements (T = Ti, Zr, Hf) and platinum group elements (M = Ru, Rh, Pd, Os, Ir, Pt) using first-principles calculation [54]. It was found that the trends of structural stabilities and the magnitudes of formation enthalpies were in good agreement with theoretical and experimental findings. For example, the formation energies of B19′ and B2 were found to be -0.552 (-0.552) [34] and -0.454 (-0.455) [34] eV/atom, respectively.

The accepted experimental binary Ti-Pd phase diagram was produced by Murray [81] and is shown in Figure 2-2. The phase diagram predicted four solutions (liquid, bbc, fcc, hcp) and eight intermetallic compounds ($TiPd_3$, $TiPd_2$, Ti_3Pd_5, Ti_2Pd_3, α-TiPd, β-TiPd, Ti_2Pd, and Ti_4Pd) [81]. At 50 at. % Pd two phases exist which are the α-TiPd with B19-type structure (lower phase) and β-TiPd with B2-type structure (higher phase). The α-TiPd phase was found to be stable up to 783 K while the β-TiPd phase was found stable up to 1673 K [81]. At the Pd-rich side, only four phases exist namely: Ti_3Pd with two space groups $P6_3$/mmc and Pm-3m, Ti_3Pd_5 with space group P4/mmm and lastly Ti_2Pd_3 with Space group Cmcm. The study showed that Ti_3Pd exists being from 23 to 28 at. % Pd and forms peritectoidally at a temperature between 723 and 823 K [81]. At the Ti-rich site, only one phase exists Ti_2Pd with space group I4/mmm.
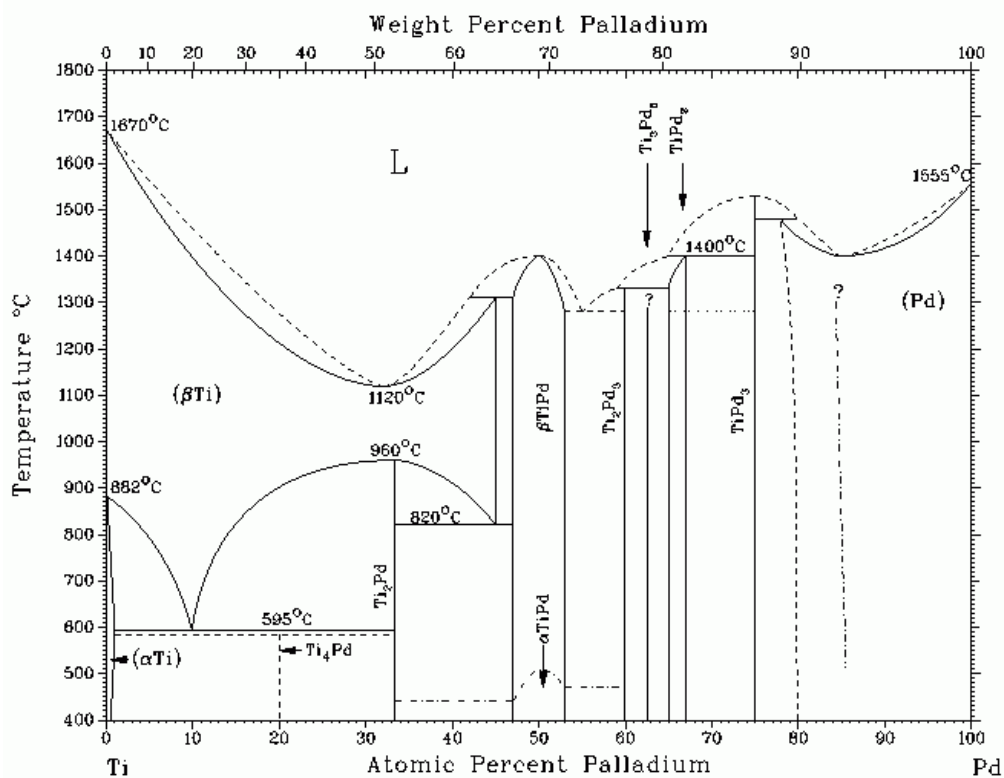
Figure 2-2 The binary Ti-Pd phase diagram [81].

On the other hand, Jankowski [82] the formation of thin films of vapour phases in Pd-Ti alloys containing 20, 25 and 30 at. % Pd using magnetron sputter deposition. It was revealed that $PdTi_3$ exists within a range from 23 to 28 at. % Pd and forms peritectoidally at a temperature between 723 and 823 K.

Yamamuro et al. [83] used differential scanning calorimetry (DSC), transmission electron microscopy (TEM), and scanning electron microscopy (SEM) to reconfirm the Pd-Ti phase diagram in the Ti-rich side. A peritectoid reaction at 963 K was confirmed to form the PdTi3 structure [83].

2.6 Ternary shape memory alloys

In Table 2-3, we give a summary of ternary SMAs. The alloy systems are categorized as available and non-existent and are indicated by right (✓) and cross (×), respectively. Four major Ti-based binary SMAs are listed, that is TiAu, TiNi, TiPd and TiPt. These alloys are checked if they can form ternary alloys with eight alloying elements (Cr, Co, Hf, Ir, Ni, Pt, Pd, Zr). The alloying elements have been suggested to have the potential to improve the transformation temperature. Those are the most common elements used in the development of SMAs.

It can be clearly seen that only five ternary alloys are either not possible or have not been studied or have no shape memory properties that is TiAu-Hf and TiAu-Ir, while TiNi-Ni, TiPd-Pd and TiPt-Pt can only for binary alloy. Thus the majority of the alloying elements are likely to form SMAs for a variety of industrial applications.

Table 2-3 Summary of ternary SMAs.

	Cr	Co	Hf	Ir	Ni	Pt	Pd	Zr
TiAu	✓	✓	×	×	✓	✓	✓	✓
TiNi	✓	✓	✓	✓	×	✓	✓	✓
TiPd	✓	✓	✓	✓	✓	✓	×	✓
TiPt	✓	✓	✓	✓	✓	×	✓	✓

2.6.1 Ti-Ni-M (M=Pt, Pd, Cu, Zr, Hf) SMAs

Previously, ternary TiNi-based alloys have been investigated [84]. Amongst these, TiNiPd, TiNiPt and TiNiAu alloys are known to exhibit SME at high temperatures along with a small hysteresis. Their transformation temperature ranges were found between 373 and 1073 K depending on the amount of ternary alloying elements [84]. It was reported that the TiNiHf and TiNiZr alloys are less costly and also exhibit high transformation temperatures [85, 86]. As a result, they are unsuitable for actuator applications due to their large thermal hysteresis (~45 K). Moreover, it was found that the addition of Hf or Zr causes drastic deterioration in the ductility, which makes them difficult to process [85, 86].

Other studies reported that Pd is considered a better choice as a third alloying element in TiNi-based ternary HTSMAs because it offers an attractive combination of high transformation temperatures, small hysteresis, adequate workability and a relatively lower cost compared with Au and Pt [21, 10].

Another study examined the mechanical and physical properties of TiNiPt and TiNiPd HTSMAs to find which materials have the best mechanical and physical properties for high temperature applications, especially in the actuation industry [87]. Furthermore, TiNiPt and TiNiPd alloys showed viability and value in terms of capability and performance in actuator application up to 573K [87]. Davis revealed that the addition of Cu has the ability to improve fatigue and the low cost material for TiNiCu alloys, which enable the material to be used for different engineering applications [71]. The studies show that TiNiZr and TiNiHf have brought much attention to high temperature material industries because of the low cost of buying the material [79]. Currently, the findings show that TiNiHf and

TiNiZr were found to have nanoscale form precipitates which result in an increase of strength and having superelasticity at around 523 K [79]. Many researches have been done on martensite transformation temperature by the addition of Pt, Pd, Au, Hf, and Zr to TiNi [88]. Recent development in shape memory alloys found that NiTi has shown to have fragile phases which depend on the composition during the addition of Zr or Hf while the addition of Pd does not have a fragile phase [27].

2.6.2 Ti-Pt-M (M= Co, Ru, Hf, Ir Ni, Zr) SMAs

Wadood et al. [9] investigated the TiPt-Co and TiPt-Ru high temperature shape memory alloys. It was found that the partial substitution of Pt with Co and Ru enhances the high temperature strength and also SMA properties in $Ti_{50}Pt_{50}$ alloy [9]. Furthermore, $Ti_{50}Pt_{45}Co_5$ and $Ti_{50}Pt_{45}Ru_5$ were found as the most stable structures which can be used for high temperature shape memory materials applications [9]. They also [89] studied the effect of partial substitution of Zr and Ru in $Ti_{50}Pt_{50}$ on strength and shape memory properties above 1073 K. It was revealed that partial substitution of Ti with Zr, Hf and Ir improve the high-temperature strength and properties. Furthermore, $Ti_{45}Zr_5Pt_{50}$, $Ti_{45}Hf_5Pt_{50}$ and $Ti_{50}Pt_{25}Ir_{25}$ were found to be the most stable structures [89]. In another study, Wadood et al. [90] also investigated the mechanical properties of TiPt-Zr and TiPt-Ru alloys with temperature. It was found that partial substitution of Ti and Pt with Zr and Ru improves the strength of the martensitic phase as well as B2 phase, respectively. Yamabe-Mitarai et al. studied the Ti (Pt, Pd, Au) based high temperature shape memory alloys. They found that the yield stress of TiPt-Zr was almost triple compared to the TiPt yield stress [91].

Modiba et al. [92] investigated the stability of $Ti_{50}Pt_{50-x}M_X$ (M=Co, Ni, Pd, Ir) ternary using both solid solution and supercell approaches. It was found that $Ti_{50}Pt_{40}Co_{10}$ is the most electronic stable structure using a solid solution approach. Furthermore, $Ti_{50}Pt_{25}Pd_{25}$, $Ti_{50}Pt_{25}Ni_{25}$, and $Ti_{50}Pt_{43.75}Co_6$ systems were found to be the most stable structures in terms of elastic and electronic properties when using the supercell approach [92].

2.6.3 Ti-Pd-M (M= V, Fe, Zr, W, Cr, Hf, Ni) SMAs

There are few studies conducted computationally and experimentally to evaluate the mechanical stability and martensitic transformation of $Ti_{50}Pd_{50}$ alloy, especially the B2 phase. This was done through ternary alloying with V, Fe, Zr, W, Cr, Hf, Ni, etc. For example, Yamabe-Mitarai et al. studied compositions with 5 at.% of transition elements such as V, Cr, Zr, Nb, Mo, Hf, Ta, W, Co, Ru, and Ir when added to $Ti_{50}Pd_{50}$ [93]. It was found that martensitic transformation temperatures (MTTs) decreased when adding the elements, resulting in ranges between 673 and 873 K, except for Cr and Mo. Furthermore, the MTTs of Cr and Mo were found to decrease drastically to the range 533–673 K. It was also found that Zr and Hf are the most effective alloying element in improving shape recovery [93]. In the case of 5 at. % Ru addition, the transformation temperature was found to be 708 K for M_s, 665 K for M_f, 713 K for A_s and 754 K for A_f [93].

Arockiakumar et al. investigated the microstructure, mechanical and shape memory properties of Ti-55Pd-5x (at. %) (x=Zr, Hf, V, Nb) alloys to identify potential alloy systems for functional applications in the temperature range of 673–873 K [94]. It was revealed that the yield strength of martensite and austenitic phases is improved as compared to binary TiPd alloy.

The studies of $Ti_{50}Pd_{30}Ni_{20}$ have received much attention for some engineering applications. This was due to their higher martensitic transformation temperature found above 473 K [95]. It was found that the B19′ phase exhibits a much higher elastic modulus than B19.

In another study, Nakayama et al. [96] investigated the characteristics of $Ti_{50}Pd_{50-x}W_x$ HTSMA. It was reported that the composition of the TiPd matrix was almost the same in the $Ti_{50}Pd_{47}W_3$ and $Ti_{50}Pd_{45}W_5$ samples, and the transformation temperatures were also almost the same. Furthermore, the transformation temperatures in $Ti_{50}Pd_{47}W_3$ alloys are M_s= 767 K, M_f= 748 K, A_s= 792 K and A_f= 812 K which was the same as $Ti_{50}Pd_{45}W_5$ alloys [96].

Another study has been conducted experimentally to improve the mechanical stability and transformation temperature of TiPd by adding alloying elements such as Hf, Zr, V, Nb, Ta, Cr, Mo, W, Ir and Co [4]. Interestingly, the transformation temperature decreased with perfect shape recovery being obtained. As found by Yamabe-Mitarai et.al, the transformation temperature of the alloys decreased minimally with W, Co and Ta addition. Furthermore, it was found that the transformation temperature of $Ti_{50}Pd_{50-x}Ir_x$ (x=2, 4, 8) decreases with an increase in compositions. For example, the transformation temperature values of $Ti_{50}Pd_{48}Ir_2$ were found to be 781 K for M_s, 773 K for M_f, 829 K for A_s and 854 K for A_f. Recently, there has been work reported on the transformation temperature of $Ti_{50}Pd_{50-x}Co_x$ (x=2, 4, 8) experimentally [4]. The transformation temperature values of $Ti_{50}Pd_{50-x}Co_x$ were found to be 860 K, 766 K and 671 K for x=2, 4 and 8, respectively, which is much lower than the pure $Ti_{50}Pd_{50}$ system. Another study has been done on the effect of martensite aging in TiPd and TiPdNi high

temperature shape memory alloys using DSC measurements and TEM observations [97]. As found by Cai et al., the magnitude of the aging effect in the $Ti_{50}Pd_{40}Ni_{10}$ alloy was much greater than that of $Ti_{50}Pd_{50}$ alloy with a decrease in transformation temperature. The transformation temperature was found to be 668.8 K for M_s, 645.1 K for M_f, 678.8 K for A_s and 692.8 K for A_f [97].

Based on the literature review above, it is clear that not much has been done on the stability and phase transformation of binary $Ti_{50}Pd_{50}$ and the ternary $Ti_{50}Pd_{50-x}M_x$ shape memory alloys. This then initiated the need to study various properties in particular structural, thermodynamic, electronic and mechanical properties, as well as the martensitic transformation of both binary and ternary alloys. The other reason is that $Ti_{50}Pd_{50}$ alloy display poor shape memory behaviour during transformation, which resulted in poor corrosion resistance [4, 14, 23, 21, 36]. Thus the development of ternary shape memory alloys with better shape memory effect for application in actuators has been considered in this study. In particular, focusing on the addition of precious metals Pt, Ru, Ir, Ni, Os and other elements with better melting temperature such as the Co and Al. The findings will add to the current knowledge of $Ti_{50}Pd_{50}$ as a potential high temperature shape memory alloy for industrial applications like automotive space.

Chapter 3

Methodology

In this chapter, we give a brief review of density functional theory (DFT) [98, 99], density functional based tight-binding method (DFTB) [100] and Molecular dynamics (MD) [101, 102] approaches that have been used to investigate properties of $Ti_{50}Pd_{50}$ and $Ti_{50}Pd_{50-x}M_x$ shape memory alloys. DFT has become the most widely used tool to study the electronic structure of atoms, molecules and solids and can predict the ground-state energy of many-body systems. The DFTB approach is capable of investigating the electronic structure of large systems over long timescales which cannot be exploited with the standard DFT methods. In this study, DFTB is used to determine the interatomic potentials of binary $Ti_{50}Pd_{50}$ and ternary $Ti_{50}Pd_{50-x}M_x$ alloys. The code is also capable to simulate temperature dependences.

Furthermore, the LAMMPS code [103] was used employing the embedded atom method (EAM) [104]. The embedded atom method is computationally efficient for large scale simulations in describing structural, and mechanical properties of metallic systems and is used to investigate the temperature dependence on the structures.

The cluster expansion method [105] is used to generate stable multi-component crystal structures and ranks metastable structures by the formation energy. This method maintains the accuracy of density functional theory. Monte Carlo simulations [105] will be used to construct phase diagrams of ternary Ti-Pd-Ru from critical temperature at each concentration.

Thus a multi-scale multi-model approach has been used to understand the shape memory behaviour, phase transformation, martensitic transformation temperature and alloy compositions. These techniques have been described in detail in the next sections.

3.1 Density functional theory

Density functional theory (DFT) is a quantum-mechanical method used for calculating ground state properties of condensed matter systems without dealing directly with many electron states. DFT was first formulated by Hohenberg and Kohn in 1964 [98] then secondly developed by Kohn and Sham in 1965 [99]. Using DFT, independent particle methods have been developed that take into account particle correlations and interactions. The first theorem of Hohenberg-Kohn showed that the ground state properties of a many-electron system are determined by an electron density that is dependent only on three spatial coordinates,

$$E = E[\rho(\vec{r})],$$
(3-1)

where E is the total energy and ρ is the density.

Kohn and Sham derived different set of differential equations which enable the calculation of ground state density $\rho_0(\vec{r})$ to be found. The ground state energy of the electronic structure is calculated from the four equations as follows:

$$E[\rho(\vec{r})] = T_s[\rho(\vec{r})] + \frac{1}{2}\int\int\frac{\rho(\vec{r})\rho(\vec{r}')}{|\vec{r}-\vec{r}'|}d\vec{r}d\vec{r}' + E_{XC}[\rho(\vec{r})] + \int\rho(\vec{r})V_{ext}(\vec{r})d\vec{r}.$$
(3-2)

The kinetic energy of non-interacting electron gas with density $\rho(\vec{r})$ is represented by $T_s\left[\rho(\vec{r})\right]$ as follows:

$$T_s\left[\rho(\vec{r})\right] = -\frac{1}{2}\sum_{i=1}^{N}\int \psi_i^*(\vec{r})\nabla^2\psi_i(\vec{r})d\vec{r},$$

(3-3)

The kinetic energy is not for real system and equation (3-2) is defined as exchange-correlation energy functional $E_{XC}\left[\rho\right]$. Introducing a normalization constraint on the electron density, $\int \rho(\vec{r})d\vec{r} = N$, we get:

$$\frac{\delta}{\delta\rho(\vec{r})}\left[E[\rho(\vec{r})] - \mu\int \rho(\vec{r})d\vec{r}\right] = 0 ,$$

(3-4)

$$\Rightarrow \frac{\delta E[\rho(\vec{r})]}{\delta\rho(\vec{r})} = \mu .$$

(3-5)

The above equation can be rewritten in terms of an effective potential, $V_{eff}(\vec{r})$:

$$\frac{\delta T_s[\rho(\vec{r})]}{\delta\rho(\vec{r})} + V_{eff}(\vec{r}) = \mu ,$$

(3-6)

where $V_{eff}(\vec{r}) = V_{ext}(\vec{r}) + \int \frac{\rho(\vec{r}')}{|\vec{r}-\vec{r}'|}d\vec{r}' + V_{XC}(\vec{r})$ and $V_{XC}(\vec{r}) = \frac{\delta E_{XC}[\rho(\vec{r})]}{\delta\rho(\vec{r})}$. (3-7)

The ground state energy, E_0 and the ground state density, ρ_0 the one electron Schrödinger equation is written as follows:

$$\left(-\frac{1}{2}\nabla_i^2 + V_{eff}(\vec{r}) - \in_i\right)\psi_i(\vec{r}) = 0 .$$

(3-8)

So, solving $\rho(\vec{r})$ we get:

$$\rho(\vec{r}) = \sum_{i=1}^{N} |\psi_i(\vec{r})|^2,$$ (3-9)

The self-consistent solution is required due to the dependence of $V_{\text{eff}}(\vec{r})$ on $\rho(\vec{r})$. Calculations of electronic structures E_{XC} are generally approximated through local density approximations or generalized gradient approximations [106].

3.2 The exchange-correlation functionals

The two main types of exchange-correlation functionals used in DFT are the local density approximation (LDA) [107] and the generalized gradient approximation (GGA) [108], which will be discussed in sections 3.2.1 and 3.2.2.

3.2.1 Local density approximation

The local density approximation (LDA) is an approximation in which the exchange-correlation (XC) energy functional in density functional theory (DFT) depends upon the value of the electronic density at each point in space [107]. It was first discovered by Kohn and Sham in the context of DFT which can be expressed as:

$$E_{XC}[\rho(r)] \cong \int dr \rho(r) \varepsilon_{XC}(\rho(r)),$$ (3-10)

where $\varepsilon_{XC}(\rho)$ is the exchange-correlation energy per electron in a uniform electron gas of density n [107]. In the uniform electron gas, electrons are distributed in interacting systems with an arbitrary spatial density ρ which acts as a parameter. Local density approximation quantities can be calculated accurately using Monte carlo techniques at a wide range of densities at the limit of high density. It has been demonstrated that LDA delivers accurate results even if the electron density in the system is not gradually varied. The function $\varepsilon_{XC}(\rho)$ is a combination of exchange and correlation contributions of $\varepsilon_{XC}(\rho) = \varepsilon_X(\rho) + \varepsilon_C(\rho)$. It is possible to calculate the exchange energy per particle of a uniform electron gas as follows:

$$\varepsilon_{XC}(\rho) = c_x \rho^{1/3}, \tag{3-11}$$

where $c_x = -(3/4)(3/\pi)^{1/3}$. $\tag{3-12}$

3.2.2 Generalized gradient approximation

The GGA is known to be semi-local approximations which means that the functional does not use the local density $\rho(r)$ value but its gradient $\nabla\rho(r)$. Perdew and Wang [108] developed generalized gradient approximation (GGA) which improves the total energies, atomization energies, energy barriers and also the difference in structural energies. GGA takes the form:

$$E_{XC}^{GGA}[\rho] = \int (\rho(r), \nabla\rho(r)) dr, \tag{3-13}$$

The spin-independent form is considered in GGA but practically functional is more generally formulated in terms of spin densities $(\rho\uparrow, \rho\downarrow)$ and their correspondence gradients of $(\nabla\rho\uparrow, \nabla\rho\downarrow)$.

There are several GGA based functionals that is the PBE [39], PBEsol [109], RPBE [110], BLYP [111] and AM05 [112]. PBEsol functional is a simple modification of PBE which differs only with two parameters. It is designed to improve the equilibrium properties of bulk solids and their surfaces of PBE in physics and surface science communities. The revised version of the PBE, such as the RPBE functional is widely used in catalysis to improve the performance of PBE. In the case of AM05, it gives the best performance for applications of catalysis. The GGA-BLYP functional is widely used in the chemistry environment.

Other known GGA-based functionals are meta-GGA [113], hyper-GGA and generalized random phase approximation. An extension of the GGA, the meta-GGA uses the kinetic energy density and its gradient as inputs to the function and gradient along with the functional density. Hyper-GGA offers an accurate treatment of correlation that goes beyond the level of LDA or GGA when using exact exchange (EXX) to deal with exchange-correlation. The generalized random phase approximation use EXX and exact partial correlation.

In this work, the GGA-PBE [39] functional will be used to optimize the $Ti_{50}Pd_{50}$ and $Ti_{50}Pd_{50-x}M_x$ systems as it provides accurate parameters for this material.

3.3 Plane-wave pseudopotential method

The plane-wave pseudopotential method [114] is a powerful and reliable tool to study the properties of a wide class of materials such as metals, semiconductors, insulators, minerals, metal alloys, etc. The method is capable of simulating the total energy and related properties as well as structural studies based on a quantum-mechanical treatment of electronic systems. This method was developed to simplify the DFT problems by considering only valence electrons. Specifically, core electrons are excluded since they are not affected by changes in the chemical environment [114].

3.3.1 Plane-wave basis sets

An infinite plane-wave basis set is employed to expand the electronic wave functions [115]. The method is described by using Bloch's theorem which states that the electronic wave functions at each k-point can be expanded in terms of a discrete plane-wave basis set [115]. This theorem defines the crystal momentum k as a good quantum number and φ_k as a single particle wave function which gives the boundary condition and can be written as:

$$\varphi_k\left(r + R_L\right) = e^{ik.R_L}\varphi_k\left(r\right),$$

(3-14)

which is equivalent to all eigen functions φ_{ki} of a single-particle Schrödinger equation with periodic potential can be written as a periodic function u_{ki} modulated by a plane-wave vector k [116] and R_L is a direct lattice vector.

$$\varphi_{kj}\left(r\right) = e^{ikr}u_{kj}\left(r\right),$$

(3-15)

u_{ki} can be expanded due to its periodicity as a set of plane-wave basis as follow:

$$u_{kj}(r) = \sum_G C_{j,G} e^{iG.r} \, ,$$ (3-16)

where G represents reciprocal lattice vectors and u_{ki} can be expanded in a set of plane waves as it is periodic. Thus, the electronic wavefunction with the exponential predator can be written as:

$$\varphi_{kj}(r) = \sum_G C_{j,k+G} e^{i(K+G)r} \, ,$$ (3-17)

where $C_{j,k+G}$ represent the coefficient of the periodic plane waves. The number of wave functions used is determined by the largest wave vector in the expansion with an infinite number of basis functions which is required to accurately reproduce the real wavefunction. This is the same as imposing a cut-off on the kinetic energy as the kinetic energy of an electron with wave vector k as follow:

$$E_k = \frac{\eta^2 |k+G|^2}{2m} \, ,$$ (3-18)

which obey only plane-wave in the following:

$$E_k = \frac{\eta^2 |k+G|^2}{2m} < E_{cut} \, ,$$ (3-19)

and are included in the basis. The energy must be increased until the calculated energy has converged to avoid errors in the computed total energy. It is highly recommended to use much denser k points to reduce errors and ensure convergence when calculating the total energy. We write the Kohn-Sham equation of DFT before making use of the plane-wave expansion of the wavefunction in the following way [115]:

$$\sum \left[\frac{\eta^2}{2m} |k + G|^2 \delta_{GG} + V_{eff}(r) \right] C_{j,k+G} = \varepsilon_j C_{j,k+G},$$ (3-20)

where

$$V_{eff}(r) = V_{ext}(r) + V_H[n(r)] + V_{XC}[n(r)],$$ (3-21)

$V_{ext}(r)$, $V_H[n(r)]$, and $V_{XC}[n(r)]$ are Fourier transforms of the external potential of the nuclei, Hartree and exchange-correlation potentials, respectively.

3.3.2 Pseudopotential approximation

The pseudopotential approximation [117] is used to describe the complicated effects of the motion of the core such that the core electrons and the strong attractive Coulomb potential inside the ionic core are replaced by a weaker pseudopotential. Weaker pseudopotentials describe the silent effects occurring to a valence electron as it moves through a crystal, as well as relativistic effects [37, 118]. Therefore, the pseudo-ion cores and pseudo valence electron now replaces the original solid. Inside the core region, the two pseudo electrons have a much weaker potential than the original electrons, but outside the core region, they have a similar potential to the original electrons. Figure 3-1 illustrates the ionic potential (Z/r), the valence wave function φ_v, the corresponding pseudopotential V_{pseudo}, and pseudo-wave function (φ_{pseudo}), respectively [115].

The pseudopotential approximation has the advantage that fewer plane-wave basis states are required to expand the electronic wave function, thus saving a large amount of computational time [115].

The pseudopotential takes the form:

$$V_{NL} = \sum_{lm} |lm\rangle V_l \langle lm|,$$
(3-22)

where $\langle lm|$ is the spherical harmonics and V_l is the pseudopotential for angular momentum l. Pseudopotentials that utilize the same potential for all angular momentum components are known as local pseudopotentials. Local pseudopotentials depend only on their distance dependence.
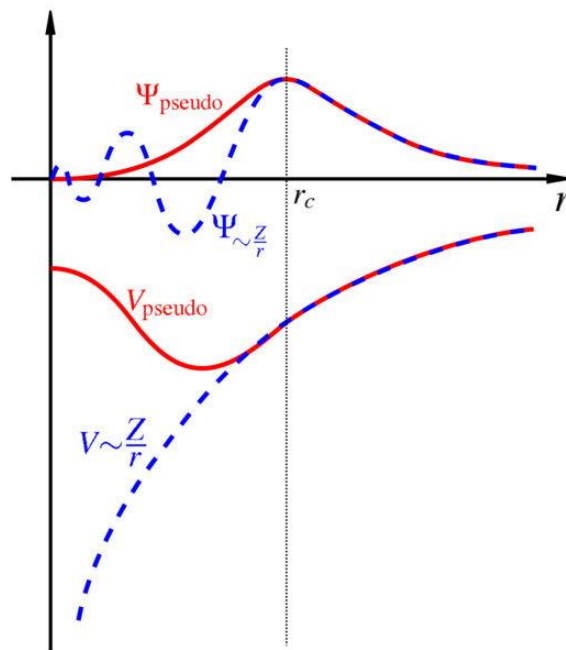
Figure 3-1 Comparison between Coulomb potential of the nucleus (blue) to the one in the pseudopotential (red) of a wavefunction. The real and the pseudo wavefunctions and potentials are the same above a certain cutoff radius r_c [115].

There are two types of pseudopotentials which are norm-conserving pseudopotential (NCP) and ultrasoft pseudopotential (USP). In the NCP [119], different potentials are used for each component of the angular momentum in the wave function, while the USP relaxes the norm-conserving constraint to reduce the basis-set size [117]. In the USP scheme, the pseudo wave function can be

as soft as possible within the core region. Currently, the USP [117] has been implemented in planewave calculations.

In this study, ultrasoft pseudopotential by Vanderbilt [117] in VASP code for total energy calculations were used since they give an accurate result for the systems under investigation.

3.4 *k*-point sampling

The *k*-point sampling technique is well suited to the plane wave's method, which makes the calculations to be simple and accurate. The total energy is calculated using a denser set of *k*-points, which reduces errors in the calculation. In the case of very close *k*-points, the wavefunction is almost the same for all. The electronic states are calculated at a finite number of *k*-points in order to define the Fermi surface precisely and hence the electronic potential and the total energy for solids. The computational cost increases linearly when performing a very dense sampling of *k* space with the number of *k*-point in the Brillouin zone (BZ). Monkhorst and Pack [120] developed the *k*-points method that uses symmetry properties when forming the special *k*-points set.

3.5 Projector augmented wave

The projector augmented wave (PAW) is a technique used in ab initio electronic structure calculations which allows DFT calculations to be performed with greater computational efficiency. It was developed by Blöchl [121] within which an

accurate, all-electron, illustration of the electronic system is placed in matched correspondence with a pseudopotential-like treatment of the valence electrons. PAW methodology relies on the transformation between the all electron Kohn-Sham wave functions, and the smooth pseudo-wave-functions with frozen core states of the atoms. This methodology is a significant upgrade over earlier norm-conserving (NC) and ultra-soft (US) pseudopotential methods because it is derived directly from an all-electron formalism. The PAW formalism is well-founded theoretically and computationally efficient, though it's additionally advanced to implement than an NC or US one.

Implementing this methodology allows DFT to calculate the electronic structure of periodic solids, as well as the forces and stresses associated with them. The essential transformation of this methodology happens once all-electron wave functions ψ_{nk}, with the *n* index resembling a summation over the bands and *k* indexing the k-points, are obtained ranging from pseudo ones $\left(\tilde{\psi}_{nk}\right)$ by using linear transformation:

$$\left|\psi_{nk}\right\rangle = \left|\tilde{\psi}_{nk}\right\rangle + \sum_{i}\left(\left|\Phi_i\right\rangle - \left|\tilde{\Phi}_i\right\rangle\right)\left\langle\tilde{p}_i\left|\tilde{\psi}_{nk}\right\rangle\right. . \tag{3-23}$$

The index i represents the atomic position, the angular momentum (l, m) and an additional index n to label differential partial waves for the same site and angular momentum. Throughout transformation, the all-electron Φ_i and pseudopotential $\tilde{\Phi}_i$ partial waves are equal outside the PAW sphere. Therefore, as within the norm-conserving and ultra-soft pseudopotential scheme, $\psi_n = \tilde{\psi}_n$ outside a core

radius $\left(r_c^l\right)$. So, the projector functions $\left(\tilde{p}_i\right)$ are equal to the pseudopotential partial waves as follows:

$$\left\langle \tilde{p}_i \middle| \tilde{\Phi}_j \right\rangle = \delta_{ij} , \tag{3-24}$$

This methodology uses two grids, a radial one inside the PAW sphere and a regular one in the whole simulation cell. In correspondence, partial waves and projector functions are grouped according to angular and radial parts as follows:

$$\Phi_i\left(\vec{r}\right) = \frac{\Phi_{n_i l_i}(r)}{r} S_{l_i m_i}\left(\hat{r}\right); \quad \tilde{\Phi}_i\left(\vec{r}\right) = \frac{\tilde{\Phi}_{n_i l_i}(r)}{r} S_{l_i m_i}\left(\hat{r}\right), \tag{3-25}$$

$$\tilde{p}_i\left(\vec{r}\right) = \frac{\tilde{p}_{n_i l_i}(r)}{r} S_{l_i m_i}\left(\hat{r}\right), \tag{3-26}$$

with $S_{lm}\left(\hat{r}\right)$ representing the real spherical harmonics. On the other hand, plane-wave basis sets are used to expand the pseudowave functions as follow:

$$\tilde{\psi}_{nk}\left(\vec{r}\right) = \sqrt{\frac{1}{\Omega}} \sum_{\vec{G}} c_{nk}\left(\vec{G}\right) e^{i\left(\vec{K}+\vec{G}\right).\vec{R}} , \tag{3-27}$$

With Ω representing the volume of the unit cell.

In this study, the PAW method has been employed as implemented within the VASP code [38].

3.6 Molecular Dynamics

Molecular dynamics (MD) is a computer simulation that is used to study the physical movements of atoms and molecules. The atoms and molecules are allowed to interact at a given period, providing a view of the motion of the atoms and molecules. This is done numerically by solving Newton's equations of motion for a system of interacting particles, based on molecular mechanics force fields,

which define forces between different particles and potential energy. In MD, laws of classical mechanics are considered, and most especially Newton's law:

$$\vec{F}_i = m_i a_i,$$

(3-28)

where m_i represents atom mass, F_i represents force acting upon it, due to the interactions with other atoms and a_i represent the acceleration of the atom given by:

$$a_i = \frac{d^2 r_i}{dt^2}.$$

(3-29)

After the acceleration has been determined, the equation of motion has to be Integrating using the Verlet algorithm [122] to describe the dynamic behaviour. The Verlet algorithm is derived from the simplest second-order difference equation in terms of atomic positions and velocities. Integrating Newton's equation (3-28) using the Verlet algorithm in the form of atomic positions and velocity is given by:

$$r(t + \Delta t) = r(t) + \Delta t \upsilon(t) + \frac{1}{2} \Delta t^2 a(t),$$

(3-30)

$$\upsilon(t + \Delta t) = \upsilon(t) + \frac{1}{2} \Delta t [a(t) + a(t + \Delta t)],$$

(3-31)

This algorithm needs storage of $r(t)$, $\upsilon(t)$ and $a(t)$. More importantly, the errors in calculated positions $r(t)$ are of the order of Δt^4 while those in calculated velocities $\upsilon(t)$ are of the order of Δt^2. The algorithm is exactly reversible in time and easy to program.

Therefore, MD has been used to study the temperature dependence and time evolution of the alloy systems and other materials of interest. This is possible when an initial set of positions and velocities are known [101]. During the MD run, a measurement of a physical quantity is calculated as an arithmetic average of the

values assumed by that quantity.

By using MD simulations, one can determine a material's thermodynamic properties and phase diagram. Beyond the known use, MD is used to study non-equilibrium processes. In the past, molecular dynamics methods have been studied using canonical ensembles [123, 124].

The various quantities that are necessary to describe the properties of a system within MD simulation are explained in the next sections.

3.6.1 Energy

The internal energy is easily achieved as the ensemble average of the energies during the simulation as follow:

$$U = \langle E \rangle = \frac{1}{M} \sum_{i=1}^{M} E_i \, .$$
(3-32)

The average potential energy V is achieved through an average of its instantaneous value, which is obtained at the same time as the force computation is made. Thus, potential energy is defined as:

$$V(t) = \sum_i \sum_{j \geq 1} \Phi(| r_i(t) - r_j(t) |),$$
(3-33)

The kinetic energy is given by:

$$K(t) = \frac{1}{2} \sum_i m_i [\overline{v}_i(t)]^2,$$
(3-34)

where m_i is the mass of atom i and $\overline{v}_i$ is the velocity of atom i. For given velocities, positions, and kinetic energies, the system's total energy can be calculated as follows:

$$E_{tot} = K(t) + V(t) \, .$$
(3-35)

3.6.2 Temperature

The temperature of a system depends on the kind of ensemble used for that simulation. For example, in a canonical ensemble, the total temperature remains constant, but in a microcanonical ensemble, the temperature varies. The kinetic energy of a system is related to temperature in the following way:

$$K = \sum_i^N \frac{\left|\dot{P_i}\right|}{2m_i} = \frac{K_B T}{2}(3N - N_c) \text{ ,} \tag{3-36}$$

Where P_i is the total of particle i, m_i is its mass and N_c is the number of constraints on the system. According to the principle of equipartition of energy, each degree of freedom contributes $k_B T/2$. If there are N particles, each with three degrees of freedom, then the kinetic energy is equal to $3Nk_BT/2$. It is very common in molecular dynamics simulations to constrain the system 's total linear momentum to zero, which results in the elimination of three degrees of freedom and Nc equals to 3.

3.6.3 Pressure

In computer simulations, pressure is calculated based on the Clausius-virial theorem. Virials are calculated from the sum of the products of the coordinates of the particles and their forces. Usually, this is written as:

$$W = \sum x_i \, \dot{p}_{x_i} \text{ ,} \tag{3-37}$$

where x_i is a coordinate and $\dot{p}_{xi}$ is the first derivative of the momentum along that coordinate ($\dot{p}_i$ is the force, according to Newton's second law). According to the virial theorem, the virial is equal to $-3Nk_BT$. The only forces in an ideal gas are those arising from the interaction between the gas and container, therefore a virial

of -3*PV* is present. This result can be obtained directly from the following equation:

$$PV = Nk_BT \,.$$

(3-38)

The force between the particles in the actual gas or liquid affects the viral force and therefore the pressure. The total virile of the real system is equal to the sum of the ideal gas fraction (-3*PV*), which is attributed to the interaction between the particles. The result obtained is:

$$W = -3PV + \sum_{i=1}^{N}\sum_{j=i+1}^{N} r_{ij}\frac{dv(r_{ij})}{dr_{ij}} = -3Nk_bT \,.$$

(3-39)

If $d(r_{ij})/dr_{ij}$ is written as f_{ij} the force acting between *i* and *j* then pressure can be written as follows:

$$P = \frac{1}{V}\left[Nk_BT - \frac{1}{3k_BT}\sum_{j=i+1}^{N} r_{ij}f_{ij} \right] \,.$$

(3-40)

It takes very little extra effort to calculate the virial and thus the pressure since these forces are calculated as part of the molecular dynamics simulation. In the NPT setting, the total system pressure is constant, while in the NVT setting, the pressure fluctuates throughout the simulation process.

3.6.4 Ensembles

Integrating Newton's equations of motion allows you to explore the constant energy surface of a system. There are three most common ensembles that are often used in MD simulations known as NVT, NVE and NPT ensembles.

3.6.4.1 Constant temperature molecular dynamics

In a molecular dynamic simulation, we often encounter limitations and inconsistencies which arise from the use of the micro-canonical ensemble corresponding to simulations at constant energy. Many molecular dynamics

simulations are performed at constant energy and volume, while in ordinary laboratory experiments, they are performed at constant temperature and pressure. So, the temperature T can be related to the average kinetic energy:

$$\frac{\sum_{1}^{n} p_i^2}{2m_i} = \frac{3}{2} NkT .$$

(3-41)

Using constant-energy molecular dynamics, the temperature can only be determined after calculating and calculating the average kinetic energy. To solve this problem, constant temperature and constant volume (NVT) simulation methods have been developed.

3.6.4.2 Microcanonical ensemble

The microcanonical ensemble is the thermodynamic state known by a fixed number of atoms, fixed volume, and a fixed energy E. Microcanonical ensemble corresponds to an isolated system with constant energy. The degeneracy of the system is the total number of microscopic states corresponding to this value of the system's energy as indicated by:

$$\Omega = \Omega(E, N, V).$$

(3-42)

So, the temperature of the system is calculated by

$$\sum_{i=1}^{N} \frac{p_i^2}{2m_i} = \frac{3}{2} Nk_B T ,$$

(3-43)

Where T is the temperature, N is the number of particles and k_B is the Boltzmann constant. Each energy in a microcanonical ensemble corresponds to

a different temperature, so to calculate the dynamics of the system at a given temperature, the energy must be determined correctly.

3.6.4.3 Isothermal-isobaric ensemble

NPT ensemble is also called an isothermal-isobaric ensemble. In the NPT ensemble, pressure and temperature are kept constant. In most cases, the NPT ensemble is used to compare MD simulations with experiments. Langevin method in NPT ensemble is used to control temperature. The partition function can be written as the weighted sum of the partition function of canonical ensemble, Z (N, V, T) as follows:

$$\rho(N,P,T) = \int Z(N,V,T)e^{(-\beta p V)C dV} ,$$ (3-44)

where

$$\beta = \frac{1}{k_B T} ,$$ (3-45)

k_B is the Boltzmann constant and V is the volume of the system.

3.7 Cluster expansion formalism

Cluster expansion is a technique used to construct an efficient Hamiltonian to predict the energy of a precisely defined system that takes into account its multiple degrees of freedom. In this technique, there can be different types of excitation, such as vibrations, electrons, etc. This technique verifies the properties of the system based on its composition and atomic disorder. Crystalline solids, crystal lattices, crystallographic positions, and interstitial positions must be well defined. In the case of solids, due to the relaxation of the

ions, the atoms do not occupy exact lattice positions. We are studying configurational disorder in order to understand how the arrangement of species in the system affects the total amount of energy in the system. For example, in a crystal with m sites and two species potentially occupying those sites, there would be a total of 2^m possible arrangements. For each cluster, we can write a cluster function as the product of the occupation variables at the cluster sites:

$$\phi_\alpha(\vec{\sigma}) = \prod_{i \in \alpha} \alpha i .$$

(3-46)

Equation 3-44 defines specifically for the paired cluster. If we wanted to evaluate ϕ_α the configuration, it would be

$$\phi_\alpha = \delta_{\alpha 1} \times \delta_{\alpha 2} = (-1)(+1) = -1 .$$

(3-47)

Sanchez et al. [125] have indicated that these cluster functions form a complete orthonormal basis in configuration space. Then, the expression for the energy of a given configuration known as the effective Hamiltonian or Cluster Expansion (CLEX) can be written as:

$$E(\vec{\delta}) = V_0 + \sum_\alpha V_\alpha \phi_\alpha(\vec{\phi}),$$

(3-48)

where V_0 and V_α represent the constant expansion coefficients, much like in a Fourier series are referred to as Effective Cluster Interactions (ECI). Otherwise, we can write:

$$E(\vec{\delta}) = V_0 + \sum_i V_i \delta_i + \sum_{i,j} V_{ij} \delta_i \delta_j + \sum_{i,j,k} V_{ijk} \delta_i \delta_j \delta_k ,$$

(3-49)

where i; j; k; represent the individual cluster sites. Note that equations (3-48) and (3-49) are the generalized Ising Hamiltonian that contains all multi-body interactions in the entire infinite crystal.

3.7.1 Determination of effective cluster interaction coefficients

In order to calculate the energy of a definite structure, the cluster expansion equation (3-49) needs two inputs. Equation (3-50) is just the result of a complete crystal basis, and the cluster expansion can be condensed to include no more than four or five terms. Calculating the ECI requires fitting a set of formation energies calculated using DFT with the least squares. In order to assess the quality of the parameterization, two metrics are used: root mean square (RMS) error, which measures reproducability of formation energies, and cross validation score (CVS), which determines how closely the fit follows a given model [126]. The CVS is calculated as follows:

$$CV^2 = \frac{1}{N}\sum_{i=1}^{N}\left(E(\vec{\delta_i}) - E'(\vec{\delta_i})^2\right)$$

(3-50)

where $E(\vec{\delta_i})$ represent energy of the configuration i calculated using first principle (DFT), $E'(\vec{\delta_i})$ is the predicted value of $E(\vec{\delta_i})$ obtained by performing a least-squares fit to the data from the other *N*-1 configurations and then evaluating the resulting expansion at $\vec{\delta_i}$. The optimal set of crystal basis functions to describe the system will minimize the CVS. By using RMS values and CVS values in expansion, some configurations could be predicted as stable, even when they are classified by first principles methods as unstable or metastable.

3.8 Monte carlo simulations

Monte carlo (MC) simulation is an approach that is used to determine phase transition properties because the integration process in calculating the equations of motion will overshoot a transition point due to the discontinuity in energy during a first order phase transition. In this work, the MC technique is used without lattice vibrations. Since the phase points chosen are spread over the whole phase space, this procedure does not produce a very efficient result for tasks such as finding a global minimum. It can be used to describe a thermodynamical system at finite temperatures since the configurational entropy can be calculated. In the MC calculation, there are two possible ensembles namely; grand-canonical and canonical ensemble. Calculations are being performed on atoms in a box with a given extension and bounds: the box is a unit cell. Grand-canonical and canonical calculations are different in this implementation and are discussed in the next detail in sections 3.8.1 and 3.8.2.

3.8.1 Grand canonical ensemble

The grand canonical ensemble is utilized which simulates the system at constant chemical potential, μ, temperature, T and volume, V. Both the number and energy of particles fluctuate in the grand canonical ensemble. This study employs the Metropolis algorithm, which is a relatively fast method for reading successive states of a Markov chain starting with an arbitrary configuration [127]. The

following rule gives the probability of transition from the current configuration A to the next configuration B:

$$P(A-B) = \begin{cases} 1 & \Omega_B < \Omega_A \\ e^{-\Delta\Omega/k_BT} & \Omega_B \geq \Omega_A \end{cases},$$
(3-51)

where $\Delta\Omega = \Omega_B - \Omega_A$ is the difference in energy between the two states, k_B is the Boltzmann constant, and T is the temperature. The grand canonical energy is defined as follows:

$$\Omega = E(\vec{\delta}) - \mu N,$$
(3-52)

where $E(\vec{\delta})$ represents the average energy, μ is the chemical potential, and N is the number of atoms.

3.8.2 Canonical ensemble

In canonical MC, the number of particles and volume is fixed, specified as inputs to the simulation. Averaging over a large number of simulation runs, we can then calculate the pressure using the virial relation. The pressure and density (i.e. the volume of a simulation box based on a fixed number of particles) need to be specified. A task of this type naturally leads to the isothermal-isobaric ensemble. When the composition changes its state, its energy changes, resulting in the following transition rate:

$$P_{\delta\delta'}^* = \begin{cases} 1 & if \ \in < e^{-\left(E(\delta')-E(\delta)\right)/kT} \\ 0 & if \ \in > e^{-\left(E(\delta')-E(\delta)\right)/kT} \end{cases}.$$
(3-53)

The random walkthrough phases are carried out until either a chosen number of steps has been taken or a given limit in energy has been reached.

3.9 Computational codes and implementation

This study uses the plane-wave VASP [38] and PHONON [128] codes to investigate the properties of $Ti_{50}Pd_{50}$ and $Ti_{50}Pd_{50-x}M_x$ alloys. A detailed explanation of these two codes is explained in sections 3.9.1 and 3.9.2. DFTB+ and LAMMPS codes were used to deduce the transformation temperature of alloys and these codes are explained in detail in sections 3.9.5 and 3.9.7. The DMol^3 code is used to optimize structures before parameterization and is discussed in section 3.9.4. Furthermore, UNCLE code is used to generate ground state structures and phase diagrams of precious metals alloys and the theory is given in section 3.9.8.

3.9.1 VASP code

The Vienna Ab initio Simulation Package (VASP) [38] is a computer program for atomic scale materials modelling which deals with electronic structure calculations and quantum-mechanical molecular dynamics using first principles. VASP can compute an approximate solution by solving the Kohn-Sham equations within DFT. In VASP central quantities such as one electron orbitals, electron change density and local potential are expressed in the form of plane-wave basis sets. The ultra-soft pseudopotentials (US-PP) [129] or by the projector-augmented-wave (PAW) method [121] is used to describe the interactions between the electrons and an ion in VASP. The US-PP method (and the PAW method) are effective in reducing the number of plane waves per atom in transition metals and first row elements. The code consists of two main loops namely: the outer and inner loop, where the outer loop optimizes the charge

density while the inner loop optimizes the wavefunction. VASP code uses a wide range of exchange-correlation functionals such as LDA and GGA as well as Meta- and hyper-GGA and hybrid functionals. All functionals found in VASP have spin-degenerate and also spin-polarized versions.

In this study, the VASP code [38] was used to calculate structural, thermodynamic, electronic and mechanical properties of binary B2, L1$_0$, B19, B19′ Ti$_{50}$Pd$_{50}$ and ternary Ti$_{50}$Pd$_{50-x}$M$_x$ (M=Ru, Pt, Ir, Co, Ni, Al, and Os) alloys. A convergence test was done as shown in section 4.1 before calculating any properties. A precision was set at "accurate" to make errors of the calculation into a reasonable scale. Before the calculations of elastic constants, electronic structure, and phonon dispersion curves, the structures were fully relaxed with respect to the volume, shape, and internal atomic positions until the atomic forces were less than 0.01 eV/Å for the unit cell. This was done in order to prepare the structures to be at their ground state energy before determining any property. The effects of exchange-correlation interaction are treated with the generalized gradient approximation (GGA) [99] of Perdew–Burke–Eruzerhof (PBE) [39] and the local density approximation (LDA) [107] were used with the PAW potential [121]. After geometry optimization, the density of states and mechanical properties of B2, L1$_0$, B19, and B19′ Ti$_{50}$Pd$_{50}$ were determined. The strain value of 0.005 was chosen for the deformation of the lattice when calculating elastic properties.

In the case of ternary Ti$_{50}$Pd$_{50-x}$M$_x$, the calculations were carried out using a 2x2x2 supercell with 16 atoms. The ternary Ti$_{50}$Pd$_{50-x}$M$_x$ alloys were constructed using a substitutional search tool within the Medea software platform which provided

the most stable composition at the desired symmetry. A convergence test was also done and a plane-wave cutoff energy of 500 eV and a 12X12X12 k-point were found to converge the total energy of $Ti_{50}Pd_{50-x}M_x$. Full geometry optimization was performed to find the ground state at different compositions. Then, the density of states and elastic properties were determined from optimized structures. The implementation of the VASP code is summarised in Figure 3-2.

3.9.2 PHONON code

The PHONON code is a software used to calculate phonon dispersion curves and phonon density spectra of crystals, mainly those crystals with defects, surfaces, adsorbed atoms on surfaces, etc [128] from either a set of force constants or from a set of Hellmann-Feynman forces calculated within an *ab initio* calculations. By using this code, a supercell can be optimized and the Hellmann-Feynman forces can be calculated, either using VASP, Wien2k, Medea, or another ab initio code. Note that Phonon builds a crystal structure using one of the 230 crystallographic space groups, finds the force constant and calculates the phonon dispersion relations and intensities, using the Hellmann-Feynman forces. In the Phonon, the total and partial phonon density of states are calculated based on the polarization vectors, as well as the irreducible representations of phonon modes (the Gamma points). It plots the internal energy, free energy, entropy, heat capacity and tensor of mean-square displacements (Debye-Waller factor).

PHONON code [128] as implemented in Materials Design within the MedeA software platform was used to evaluate the phonon dispersion curves. Using the

same code, we calculated thermal properties such as Debye temperature, heat capacity, and thermal coefficient of linear expansion.

3.9.3 VASP and PHONON code flowchart

In this section, we use a flowchart to summarise how VASP and PHONON codes were used in this study (the details are described in sections 3.9.1 and 3.9.2).

1. The flowchart begins with the determination of functional using VASP code- a GGA-PBE was selected.

2. A convergence test was conducted to determine the suitable cut-off energy and k-point mesh parameter for systems.

3. A full geometry optimization was performed to determine the ground state parameters for the binary systems.

4. Determine the structural, thermodynamic, electronic and elastic properties of binary systems.

5. A 2X2X2 supercell was built on B2 $Ti_{50}Pd_{50}$ alloy.

6. Use the substitutional search tool to generate ternary alloys, i.e. substitution of Pd with Ru, Os, Ir, Al, Co, Pt and Ni.

7. A full geometry optimization was performed on ternary systems.

8. Evaluate the properties of interest, such as thermodynamic- heats of formation, electronic density of states, elastic constants and moduli.

9. Use the PHONON code to determine the phonon dispersion curves, thermal-Debye temperature, heat capacity and thermal coefficient of linear expansion.
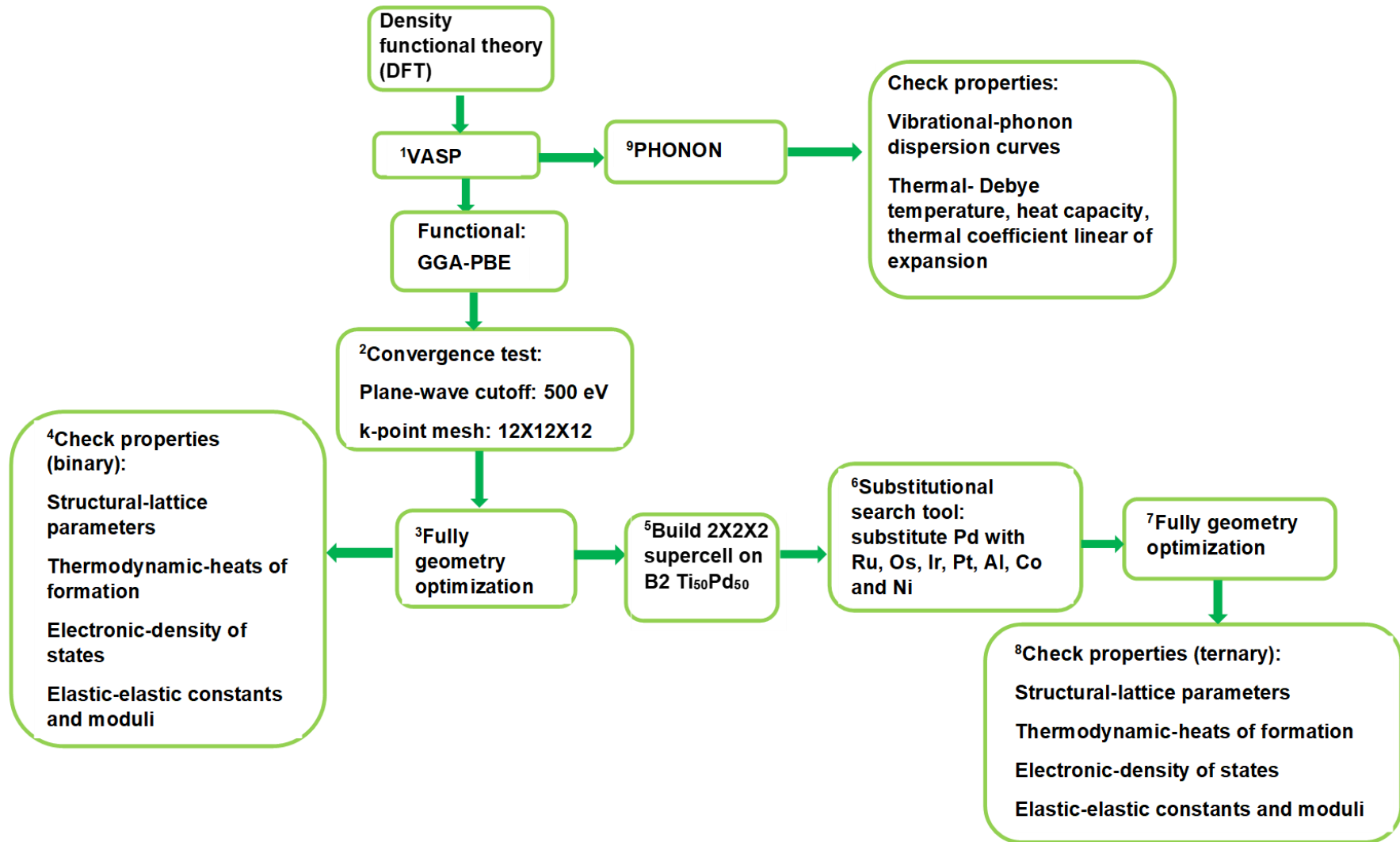
Figure 3-2 Flowchart on implementation of VASP and PHONON codes.

3.9.4 DMol^3

DMol^3 is a commercial software package that uses DFT to predict various properties such as structural and electronic [130, 131]. The study of DMol^3 is broad which includes organic and inorganic molecules, molecular crystals, metallic solids, covalent solids, and the surfaces of material which enable the prediction of structure, reaction energies, reaction barriers, thermodynamic properties, optics and vibrational spectra. The DMol^3 method has long been used for solving quantum mechanical equations since it offers a unique way to deal with these equations. This code can handle larger systems that contain over 500 atoms. The code can be used to study both molecular and solid-state problems, offering a way to study the widest range of problems in one package. DMol^3 can perform both All Electron and pseudo-potential calculations.

In this study, DMol^3 was used for geometry optimization of binary $Ti_{50}Pd_{50}$ and $Ti_{50}Pd_{50-x}Ru_x$ structures before deriving the interatomic potentials. This was done in order to prepare the structures to be at their ground state energy before being used for the self-consistent-charge density functional tight-binding (SCC-DFTB) parameterization process. Both the GGA-PBE and LDA-PWC exchange-correlation functionals were used. The implementation of the DMol^3 code is summarized in Figure 3-3.

3.9.5 Density functional based tight-binding method

Density functional based tight-binding (DFTB+) is a useful software package that can carry out atomistic quantum mechanical calculations fast and can also perform calculations for larger systems that contain up 10 000 atoms. The density-functional tight-binding (DFTB) was developed by Seifert and Co-workers [132]. DFTB and SCC-DFTB can be used to calculate electronic properties, binding energies, and relative energies of several kinds of systems, and their geometries can be determined using these procedures [133].

In DFTB, a series of models are derived using Taylor series expansion of Kohn-Sham density functional total energy around a properly selected reference density $\rho(r)$. Instead of finding the electron density that minimizes the energy a reference density ρ^0 is assumed which is perturbed by some density fluctuation [100] and $\rho(r)$ is represented as follow:

$$\rho(r) = \rho^0(r) + \delta\rho(r).$$
(3-54)

The standard DFTB approach is suitable when the electron density of a structure with many atoms may be represented as a sum of atomic-like densities [134]. According to this method, the Kohn-Sham total energy is expanded with the second order with respect to the fluctuations in charge density [134, 135, 136] as follow:

$$E_{tot} = E_{BS} + E_{rep} + E_2(\rho, \Delta\rho),$$
(3-55)

where E_{tot} represent the total energy which includes the electrostatic-interaction term $E_2(\rho, \Delta\rho)$ to the standard tight-binding E_{BS}, which is the sum over the occupied electronic eigenstates of the tight-binding Hamiltonian and the short range repulsive two-particle interaction E_{rep} terms. When the electrostatic-interaction fluctuate it can be written as:

$$E_2(\rho, \Delta\rho) = \frac{1}{2} \sum_{x,y}^{M} \gamma_{xy} \Delta q_x \Delta q_y. \tag{3-56}$$

This term is represented by the Mulliken charges-based atomic charge fluctuation Δq_x and Δq_y together with the analytical interpolating function γ_{xy}.

Parameterization is the process of developing Slater-Koster files which contain electronic parameters, short range potentials and Hubbard terms, selected for a set of element pairs for a particular system. It involves the fitting of the repulsive potentials in the repulsive term E_{rep} and expressed as:

$$E_{rep} = \sum_{i<j} V_{rep}^{ij}(R_{ij}), \tag{3-57}$$

where *ij* represents pair of atoms and $V_{rep}^{ij}(R)$ are the pair-wise repulsive functions depending only on the atomic numbers [137]. The selected cutoff radius is then used in the fitting of the $V_{rep}^{'}(R)$ and the repulsion is then expressed as:

$$V_{rep}(R) = -\int_{R}^{R_{cut}} {'}V_{rep}^{'}(r) dr. \tag{3-58}$$

Self-consistent-charge density functional tight-binding parameterization and geometry optimization were carried out with a DFTB+ program [134]. In the

DFTB+ code, atomic parameters for the interaction between atoms were considered before performing various calculations such as geometry optimization and molecular dynamics. The SCC parameters were developed for both binary $Ti_{50}Pd_{50}$ and ternary $Ti_{50}Pd_{50-x}Ru_x$. The set of parameters for Ti-Pd and Ti-Pd-Ru were obtained by constantly adjusting the potential confinement radius for Ti, Pd, and Ru elements until the suitable radii were obtained. During geometry optimization, thermal smearing was varied from 0.003 to 0.008 Ha. The successful SCC-DFTB parameterization implies that the structural properties produced are in good agreement with available theoretical and experimental results. Both the GGA-PBE and LDA-PWC exchange-correlation functionals were used. The electronic and elastic properties were calculated from optimized structures and analysed.

Lastly, the temperature dependence of binary and ternary was also determined from the SCC parameters using the NPT ensemble. Before any temperature calculations were done, the time step and simulation time were determined and 10 fs and 30 ps were found to be sufficient enough for the binary and ternary systems.

3.9.6 DMol^3 and DFTB+ code flowchart

In this section, we give a summary of how DMol^3 and DFTB+ code were used and is given in the form of a flowchart as shown in Figure 3-3. Implementation details are explained in sections 3.9.4 and 3.9.5. Figure 3-3 shows a schematic diagram indicating step by step calculations done using both codes as follows:

1. The flowchart starts with the computational code (DMol^3) which was used to determine ground state properties.

2. A suitable functional GGA-PBE was found appropriate to predict the structural parameters.

3. A convergence test was carried out to determine the suitable cut-off energy and k-point mesh parameter for the systems.

4. A full geometry optimization was performed for binary $Ti_{50}Pd_{50}$ and $Ti_{50}Pd_{50-x}Ru_x$ structures.

5. Determine the structural properties (lattice parameters and bond distances) of systems.

6. Use the DFTB+ code to carry out the parameterization process.

7. Parameterization was performed to find a suitable set of parameters by varying the potential confinement radius.

8. A full geometry optimization was again performed using a suitable set of parameters for both binary and ternary systems.

9. Determine properties such as structural-lattice parameters, electronic-density of states and elastic-elastic constants and moduli.

10. Temperature dependence calculation was carried out.

11. Determine suitable time step and simulation time-10 time steps and 30 simulation times were selected.

12. Evaluate the transformation temperature from lattice parameters of binary and ternary systems.
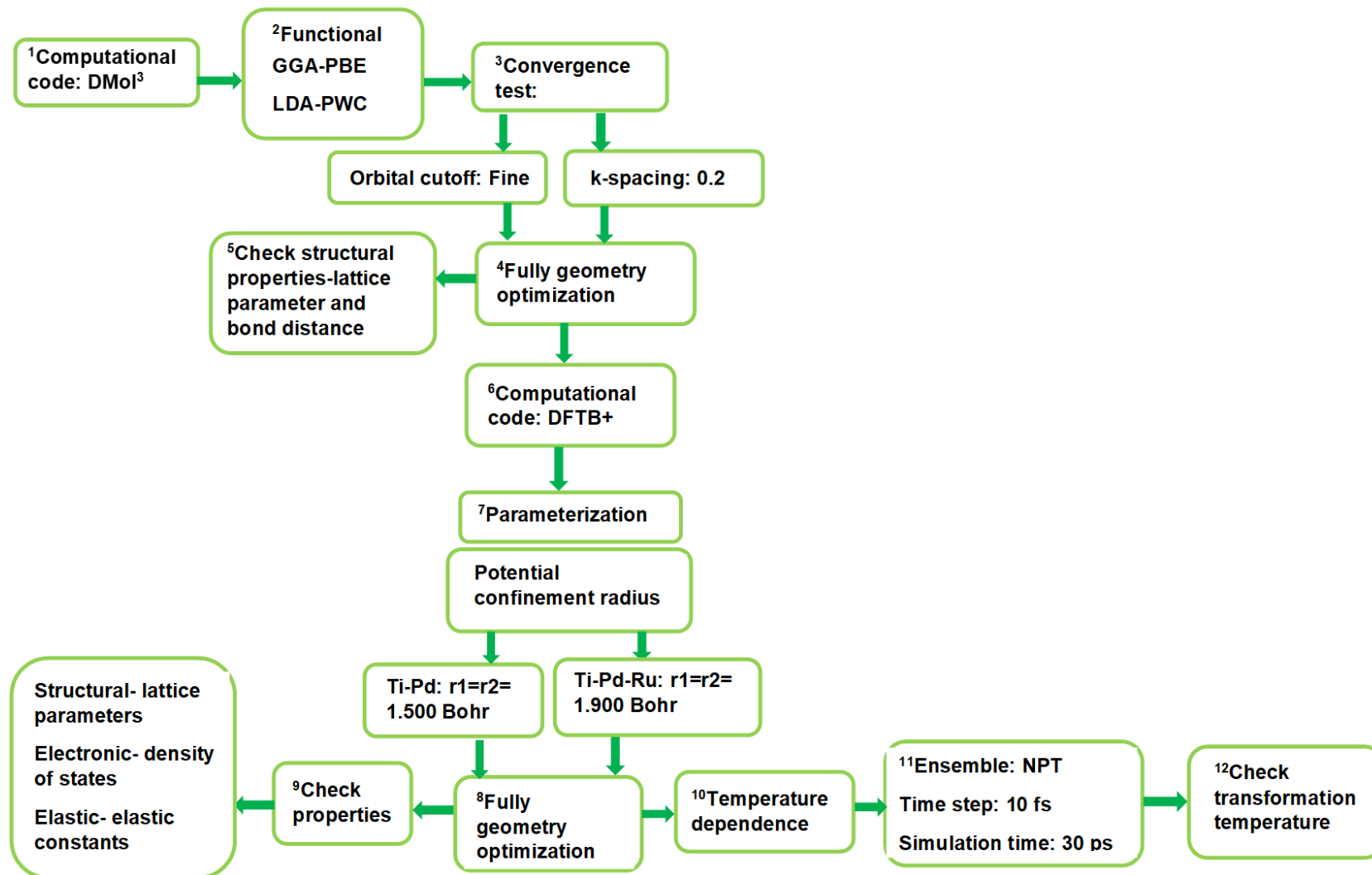
Figure 3-3 Flowchart on implementation of DMol[3] and DFTB+ codes.

3.9.7 LAMMPS code

Large-scale Atomic/Molecular Massively Parallel Simulator (LAMMPS) is a classical molecular dynamics code that can model solid-state materials (metals, semiconductors) and soft matter (biomolecules, polymers) and coarse-grained from Sandia National Laboratories [103]. It works on a single processor and also on multiple processors using message-passing techniques and also a spatial-decomposition of the simulation domain into small 3d subdomains. Many models have versions that provide accelerated performance on CPU's, and Intel Xeon Phis. It combines spatial-decomposition of the simulation domain over the nodes and thread-based parallelization within each node to achieve both high parallel efficiency and single-node performance.

The LAMMPS model has new capabilities, such as force fields, types of atoms, boundary conditions, or diagnostics which can be modified or extended as needed. In LAMMPS, Newton's equations of motion are integrated with atoms, molecules, or macroscopic particles interacting with either short- or long-range forces and a variety of initial and boundary conditions. LAMMPS uses neighbour lists to keep track of nearby particles to maximize computational efficiency. In LAMMPS, the particles that are repulsive at short distances are so that the local density of particles becomes suitable for the calculation. LAMMPS also has many built-in quantities, like translational and rotational kinetic energy, helpful for evaluating the system [103].

The LAMMPS uses the powerful flowchart interface which enables the easy setting up of the complex calculations by connecting the stages. A stage can be

a computation, e.g. energy minimization, NVT and NPT dynamics, as well as an operation such as setting the density to that computed by the previous stage or building a larger simulation box. It is possible to chain together any number of stages to perform detailed calculations that are reproducible. LAMMPS is capable of automatically analysing the results, including graphs, fitting to appropriate forms, and statistical analysis. The summary of this method is described using a flowchart as depicted in Figure 3-4. It is worth noting that the flowchart has eight (08) significant steps which are duly indicated in the Figure.

In this study, the temperature dependence calculations of binary B2, L1$_0$, B19, B19′ Ti$_{50}$Pd$_{50}$ and Ti$_{50}$Pd$_{50-x}$M$_x$ (M= Co, Ni) alloys were achieved by utilizing the Large-scale Atomic/Molecular Massively Parallel Simulator (LAMMPS), an Embedded Atom Method (EAM) module. For this simulation, large supercells of 8X8X8 were constructed for both binary and ternary alloys. This code uses a flowchart which is highlighted in Figure 3-4. NPT ensemble and Nose Hoover thermostat and barostat were employed for 100 ps with a time step of 2 fs. The temperature is varied from 73 to 1800 K.
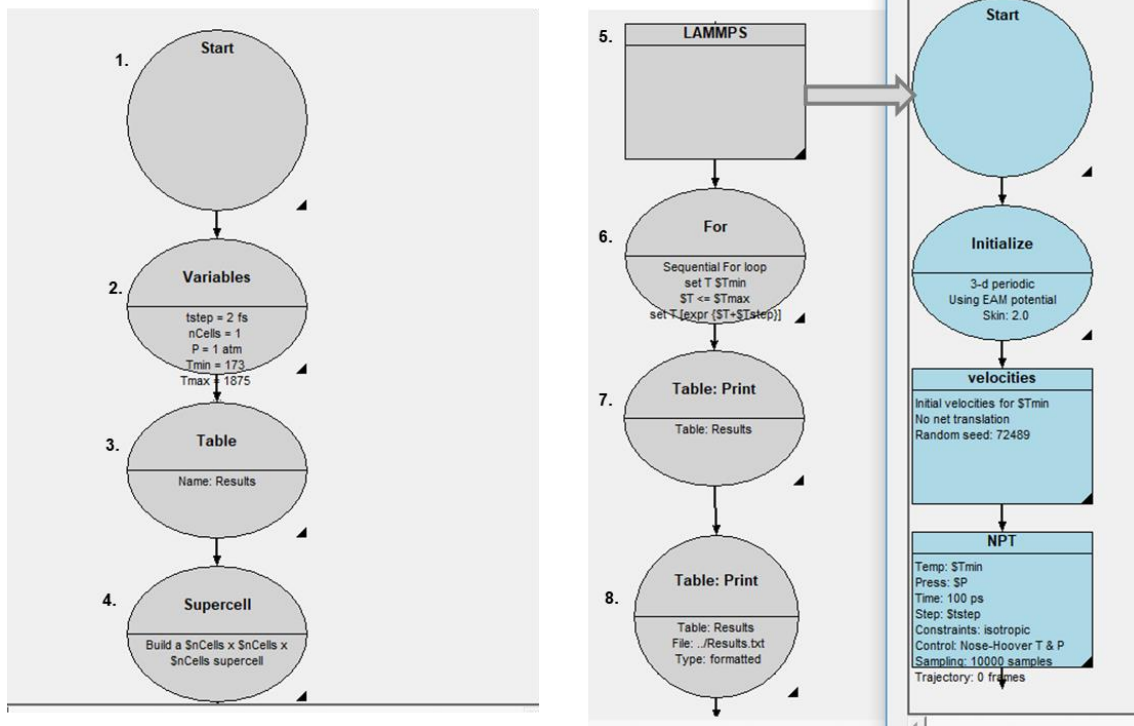
Figure 3-4 Flowchart of simulation procedures in LAMMPS code.

3.9.7.1 Embedded atom method

The embedded atom method (EAM) [104] is a semi-empirical method which provide a computationally efficient description of structural, mechanical, and thermal properties of metallic systems. Daw and Baskes developed the EAM for scheming the full energy of an absolute arrangement of atoms in metal [104, 138]. EAM forcefield is able to predict structural, thermal and mechanical properties of varied metallic structures. Regardless of atom size, EAM can evaluate energy associated forces even faster than first-principles calculations that are linearly proportional to the number of atoms.

An EAM describes how an atom behaves when positioned in an electron density that is exceedingly outlined. In the following equation, the total energy is shown

as two additive terms representing the pairwise sum of the electron densities of the atoms and an electron density by the atomic site:

$$u_{metallic} = \sum_{i=1}^{N-1} \sum_{j=i+1}^{N} V(r_{ij}) + \sum_{i=1}^{N} F(\rho_i),$$

(3-59)

$$\rho_i = \sum_{j=1}^{N} \psi_j(r_{ij}).$$

(3-60)

$u_{metallic}$ is the total energy of the system, i and j indicate the unique pair of atoms within the N atoms of the system, r_{ij} is their interatomic separation (r_{ij}) is a pairwise potential, and $F(\rho_i)$ is the embedding function for atom I which depends on the electron density, ρ_{ij} experienced by that atom. One must calculate the electron density at the position of an atom *i* in order to assess its embedding function. In equation (3-60), atomic densities are superimposed and their densities are in turn described by a density function, $\psi_j(r)$. When electron density increases, embedding energies become more negative until a minimum is reached beyond which increasing electron density results in less favorable system energies. These massive scale simulations will be readily undertaken by EAM, which is a computationally economical method.

For the purpose of this study, Zhou [139] interatomic forcefields were applied.

3.9.8 Universal cluster expansion code

All the CE calculations of the present work were done by making use of the program package Universal Cluster-Expansion (UNCLE) which was developed by the group of S. Muller, now at the Technical University of Harburg-Hamburg. With this code, a complete CE fit can be performed using a genetic algorithm, and the ground state of systems containing up to three elements can be predicted. Configurational entropies are thus taken into consideration. Currently, the UNCLE code's format for structural information has been designed to match that of the VASP code and adopted. Figure 3-5 illustrates a working scheme of cluster expansion.
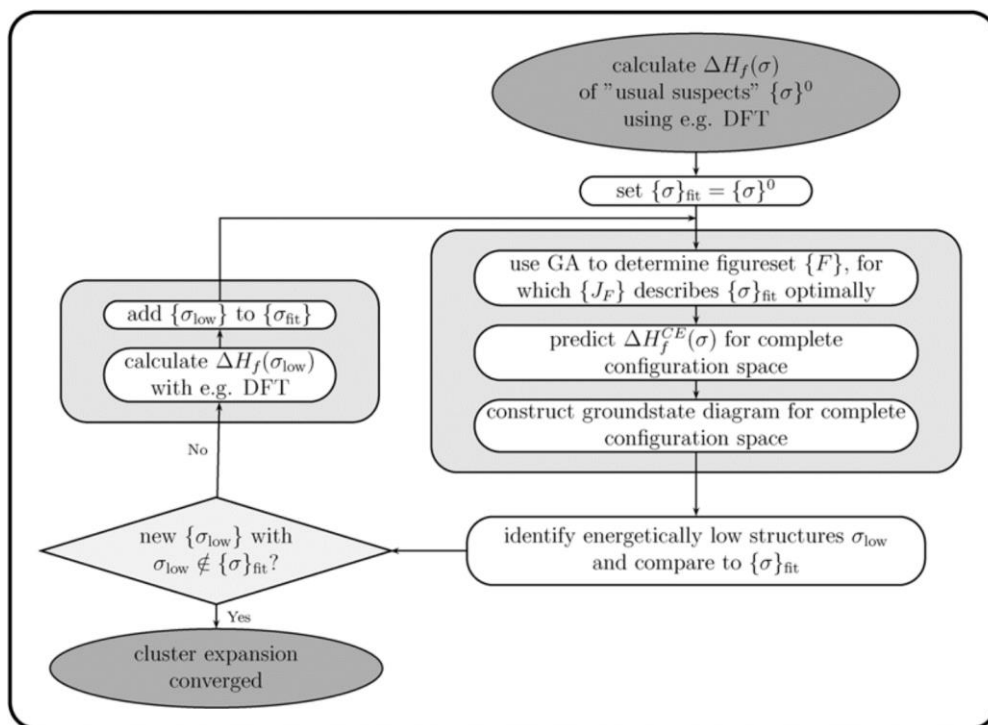
Figure 3-5 Self-consistent working plan as used by UNCLE for the cluster expansion for finding new input structures [105].

The ground-state structure of binary Ti-Pd, ternary $TiPd_{1-x}Ru_x$ and $Ti_{1-x}PdRu_x$ alloys were performed using the UNCLE code. This code is used as a script interface to VASP which defines a parameter that automatically sets up the k-point mesh for similar systems which we used 0.2 k-spacing. A flowchart is used to determine ground-state structures and is illustrated in Figure 3-6. To assess the accurate fit of the cluster expansion, the cross-validation score (CVS) is considered. A cluster expansion is considered accurate if the CVS is <5 meV/atom. The code employ step by step flowchart which consists of 4 steps as shown in Figure 3-6.
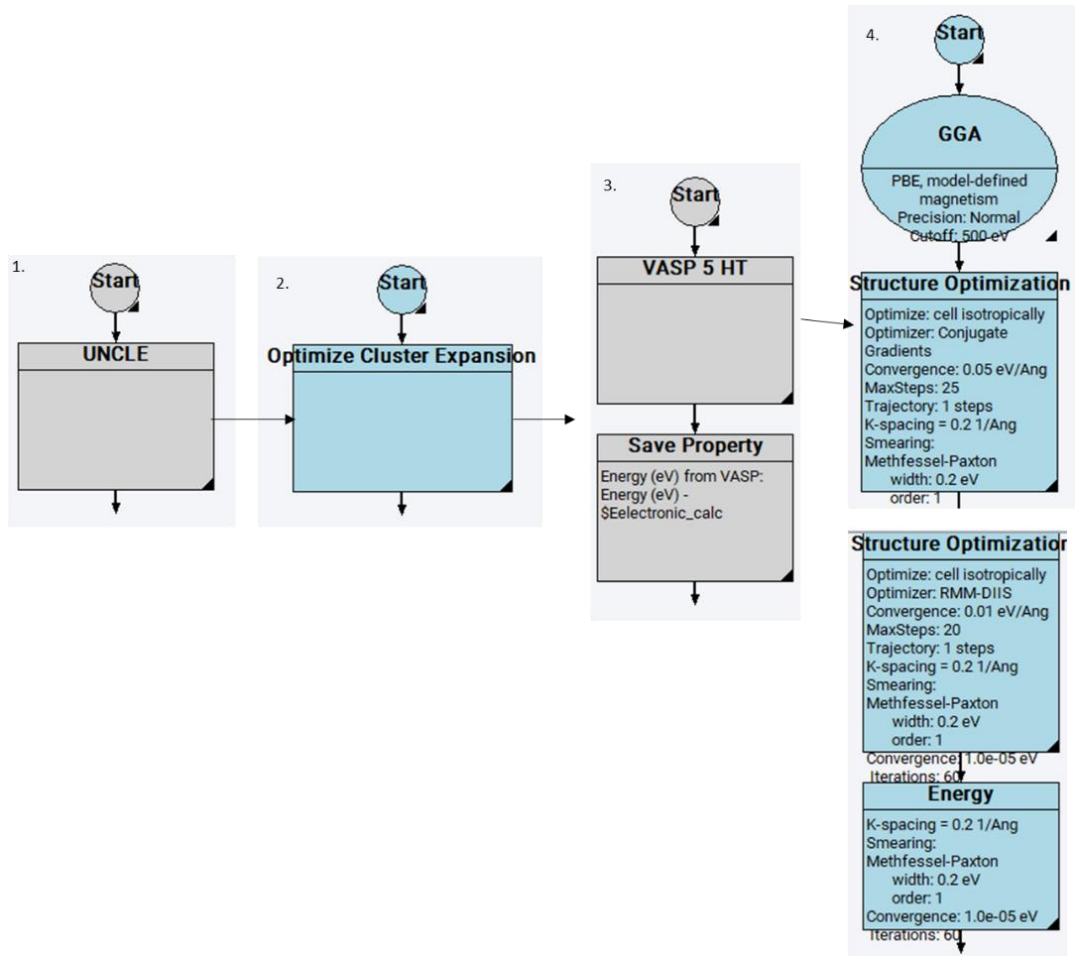
Figure 3-6 Flowchart of simulation procedures using UNCLE code.

3.10 Theoretical background on calculated properties

3.10.1 Heats of formation

The heat of formation (ΔH_f) is the enthalpy change when one mole of a compound is formed from the elements in their stable states is essential in determining the structural stabilities of the different crystal structures. The heat of formation is estimated by the following expression:

$$\Delta H_f = E_C - \sum_i x_i E_i \ ,$$
(3-61)

where E_c is the calculated total energy of the compound and E_i is the calculated total energy of the element in the compound. In order for a structure to be stable, the heat of formation must have the lowest negative value ($\Delta H_f < 0$). The heat of formation will be used to determine the stability trend of $Ti_{50}Pd_{50}$ for B2, B19, B19′ and $L1_0$ structures as well as ternary $Ti_{50}Pd_{50-x}M_x$ alloys (M= Ru, Pt, Ir, Co, Ni, Os, Al).

3.10.2. Density of states

The term density of states (DOS) refers to the occupancy and density of the electronic states in a crystalline solid. It is described by a function, g (E), as the number of electrons per unit volume and energy with electron energies near E. At a specific energy level, a high DOS means many states are open for occupation. In the case of states with DOS of zero, there is no state that can be occupied. In general, a DOS is an average over all the spaces and times that the system occupies. The local density of states (LDOS) is a measure of variation due to distortion of the original system. LDOS can locally be non-zero if the DOS of an undisturbed system is zero due to the presence of local potential.

In that case, the DOS are the total number of states that are available in the system within the plane-wave framework of DFT. It is possible to calculate each orbital's contribution (partial DOS) to determine which orbitals are occupied or involved in bonding. The electrical behaviour of a material is determined by the location of E_f within the DOS. Metal alloys stability can be predicted using the density of states (DOS). Any material's electronic density of states can be viewed as a qualitative measure of its electronic structure.

It is especially useful from the perspective of the partial density of states (PDOS). In PDOS, states are attributed to the basic functions and then to the atoms constituting the unit cell. DOS is then calculated as the sum of atomic contributions. The DOS is calculated by using the following expression:

$$n(\varepsilon) = 2\sum_{n,k} \delta(\varepsilon - \varepsilon_n^k) = \frac{2}{V_{BZ}} \sum_n \int \delta(\varepsilon - \varepsilon_n^k) dk \ , \qquad (3\text{-}62)$$

where δ is the Dirac delta function and the k is integral extends over the BZ. The number of the electron in the unit cell is given by, $\int_{-\infty}^{\varepsilon f} n(\varepsilon) d\varepsilon.$

3.10.3 Elastic properties

3.10.3.1   Theory of elasticity

The elastic constants (C_{ij}) contain some of the more important information that can be obtained from ground-state total-energy calculations. For a structure to exist in a stable phase, certain relationships must be observed between the elastic constants. The C_{ij} also determines how a crystal will respond to external forces, such as Bulk modulus, Shear modulus, Young's modulus, and Poisson's ratio, which are all factors of strength [140]. A compound's mechanical stability can also be verified using elastic constants. The existence and properties of new materials can therefore be predicted using first principle calculations.

3.10.3.2   Elastic stability criteria

There is various criterion established to deduce elastic stability of crystals for different lattice crystals. Accurately determining the elasticity of a compound is

vital in understanding its mechanical stability and elastic properties. The elastic constants depend on the type of lattice *i.e.* for the cubic, tetragonal, orthorhombic and monoclinic crystals, there are three (c_{11}, c_{12}, c_{44}), six (c_{11}, c_{12}, c_{13}, c_{33}, c_{44}, c_{66}), nine (c_{11}, c_{22}, c_{33}, c_{12}, c_{13}, c_{23}, c_{44}, c_{55}, c_{66}) and thirteen (c_{11}, c_{22}, c_{33}, c_{12}, c_{13}, c_{23}, c_{44}, c_{55}, c_{66}, c_{15}, c_{25}, c_{35}, c_{46}) independent elastic constants, respectively [26, 141]. As an example, applying two types of strains (ε_1 and ε_4) to the cubic system gives stresses relating to three elastic coefficients, this is a useful method for obtaining elastic constants. The mechanical stability condition for the cubic system as outlined [141] is given as follows:

$$c_{44} > 0; \ c_{11} > c_{12} \text{ and } c_{11} + 2c_{12} > 0, \tag{3-63}$$

As for tetragonal crystal stability condition is as follows:

$$c_{44} > 0, c_{66} > 0, c_{11} > |c_{12}| \text{ and } c_{11} + c_{12} - \frac{2c_{13}^2}{c_{33}} > 0, \tag{3-64}$$

For orthorhombic stability condition as outlined [142] is as follows:

$$\left(c_{11} + c_{22} + 2c_{12}\right) > 0, \ \left(c_{11} + c_{33} - 2c_{13}\right) > 0, \ \left(c_{22} + c_{33} - 2c_{23}\right) > 0, \ c_{11}$$
$$> 0, \ c_{22} > 0, \ c_{33} > 0, \ c_{44} > 0, \ c_{55} > 0, \ c_{66} > 0,$$
$$\left(c_{11} + c_{22} + c_{33} + 2c_{12} + 2c_{13} + 2c_{23}\right) > 0, \tag{3-65}$$

Lastly monoclinic crystal stability condition outlined [143] is as follows:

$$\left[c_{11} + c_{22} + c_{33} + 2\left(c_{12} + c_{13} + c_{23}\right)\right] > 0, \left(c_{33}c_{55} - c_{35}^2\right) > 0, \left(c_{44}c_{66} - c_{46}^2\right) > 0,$$
$$\left(c_{22} + c_{33} - 2c_{23}\right) > 0, \left[c_{22}\left(c_{33}c_{55} - c_{35}^2\right) + 2c_{23}c_{25}c_{35} - c_{23}^2c_{55} - c_{25}^2c_{33}\right] > 0,$$
$$\left\{2\left[c_{15}c_{25}\left(c_{33}c_{12} - c_{13}c_{23}\right) + c_{15}c_{35}\left(c_{22}c_{13} - c_{12}c_{23}\right) + c_{25}c_{35}\left(c_{11}c_{23} - c_{12}c_{13}\right)\right] - \left[c_{15}^2\left(c_{22}c_{33} - c_{23}^2c_{11}\right) + c_{25}^2\left(c_{11}c_{22} - c_{12}^2\right)\right] + c_{55}g\right\} > 0$$
$$\left(g = c_{11}c_{22}c_{33} - c_{11}c_{23}^2 - c_{22}c_{13}^2 - c_{33}c_{12}^2 + 2c_{12}c_{13}c_{23}\right) \tag{3-66}$$

3.10.4 Phonon calculation

3.10.4.1   Phonon Dispersion and Polarization Vectors

Based on the diagonalization of the supercell dynamical matrix, the frequencies $\omega^2(k, j)$ of phonon modes j are calculated along the identified Brillouin zone path, which creates phonon dispersion curves,

$$D(k)e(k, j)\omega^2(k, j)e(k, j).$$ (3-67)

At the Γ (0, 0, 0) point, it is possible to determine all the phonon modes, as well as the Raman and infrared activity for the modes. Orthonormality is satisfied by the vectors of complex polarization:

$$\sum_{j} e_i^*(k, j; \mu)e_l(k, j; \nu) = \delta_{il}\delta_{\mu,\nu},$$ (3-68)

$$\sum_{i}\sum_{\mu} e_i^*(k, j; \mu)e_i(k, j; \mu) = \delta_{i,j}.$$ (3-69)

In reciprocal space, the polarization vectors $e(k, j; \mu)$ associated with the wave vector k centered at the origin differ from those associated with the wave vector k_τ pointing from the center of a Brillouin zone labelled by the reciprocal vector τ. Because of $k = \tau + k\tau$ the relation between these differently defined polarization vectors is:

$$e(k, j; \mu) = e(k, j; \mu)\exp\left[-2\pi\tau.r_\mu\right].$$ (3-70)

By calculating the polarization vectors of phonons, we can determine their displacement and intensity. Considering the amplitude Qk and phase $0 \leq \varphi_k \leq 1$

of the displacement wave, the displacements U (n, μ) of atoms (n, μ) for a given

wave vector *k* and phonon branch j can be calculated from the equation:

$$U(n,\mu) = \frac{Q_k}{2\sqrt{M_\mu}}\{\text{Re}\,e(k,j;\mu)\cos[2\pi(k.R(n,\mu)-\phi_k)] - \text{Im}\,e(k,j;\mu)\sin[2\pi(k.R(n,\mu)-\phi_k)]\}.$$

(3-71)

The intensity of phonon modes is found from the form factors. On the wave

vector, the form factor is well defined as follows:

$$F^{(p)}(k,j) = \frac{1}{k^2}\left|\sum_\mu \frac{k.e(k,j;\mu)}{\sqrt{M_\mu}}\right|^2.$$

(3-72)

However, the simple form factors can provide insight into the intensity of phonon

modes:

$$F^{(s)}(k,j) = \frac{1}{k^2}\left|\sum_\mu \frac{e(k,j;\mu)}{\sqrt{M_\mu}}\right|^2,$$

(3-73)

which may be applied to eliminate unnecessary phonon branches originating

from back folding, or to estimate relative intensities of all modes in varying

Brillouin zones. Using the MedeA-Phonon code [128], you can work directly on

the lattice dynamics of systems without relying on any particular code to construct

forces and total energies. However, together with VASP, MedeA provides a highly

automatic and parallel procedure.

Chapter 4

Structural, electronic and mechanical properties for the binary Ti$_{50}$Pd$_{50}$

In this chapter, firstly we discuss the convergence test with respect to the cutoff energy and k-points for the binary Ti$_{50}$Pd$_{50}$ alloys. We also discuss the equilibrium properties such as the lattice constants and heats of formation and where possible the results are compared with the available experimental data. Secondly, the elastic constants, Bulk moduli, Young moduli, Shear moduli, anisotropy ratio, Cauchy pressure, Bulk to Shear modulus ratio (B/G), Poisson 's ratio (σ) and Vickers Hardness (H$_V$) of the binary B19′, B19, L1$_0$ and B2 Ti$_{50}$Pd$_{50}$ alloys are discussed. Lastly, the phonon dispersion curves are presented to evaluate the vibrational stability of Ti$_{50}$Pd$_{50}$ structures. The phonon density of states are also presented to indicate the orbital contribution of individual atoms, in particular which atom is responsible for soft modes.

4.1 Cutoff energy and k-point convergence

4.1.1 Cutoff energy

In order to determine the appropriate cutoff energy of Ti$_{50}$Pd$_{50}$ structures, single point energy calculations were performed for different kinetic energy cutoffs at the default number of k-points for each system. The cutoff energy is necessary for determining the accurate ground state of the system. This was then calculated for B2, B19, B19′ and L1$_0$ Ti$_{50}$Pd$_{50}$ structures (see Figure 1-1) using the plane-

wave pseudo potential within the GGA-PBE functional. The energy cutoff was varied from 200 eV up to 700 eV at fixed *k*-point for B2, B19, B19′, and $L1_0$ structures. For example, the energies gave a constant slope at certain points and energy change with a difference of less than 1 meV/atom was found from 400 eV, the cutoff energy of 500 eV was chosen in all structures for the purpose of this study. Figure 4-1 shows the curve of total energy per atom against cutoff energy for B2, B19, B19′, and $L1_0$ structures. It is clear that all curves show a similar trend with a zero slope from 400 eV, thus a choice of 500 eV cutoff energy will be used for the binary as well as ternary systems.
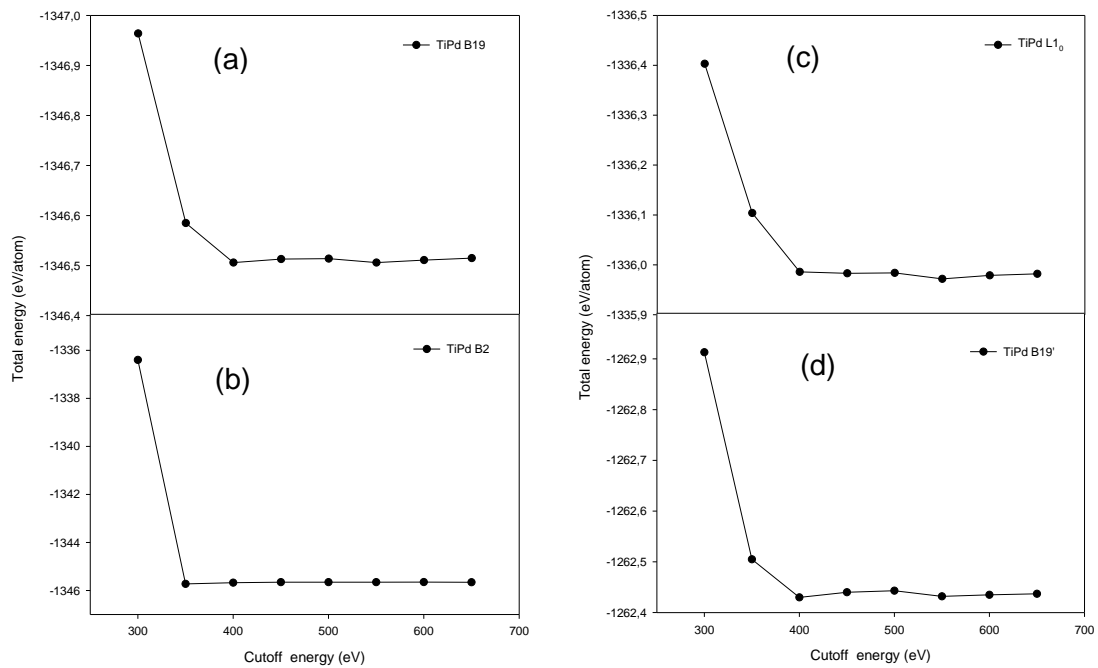
Figure 4-1 The graph of total energy against energy cutoff for (a) B19, (b) B2, (c) $L1_0$ and (d) B19'.

4.1.2 *k*-point

In this section, we show the convergence of the total energies with respect to the *k*-point sampling set size, as illustrated in Figure 4-2. We have carried out a total energy calculation at fixed cutoff energy of 500 eV for each structure (as determined in Figure 4-1) while the number of *k*-points was varied. The total energy with respect to the number of *k*-points was considered converged when the energy change per atom (between two consecutive points) was within 1meV per atom. The separations were varied to find a suitable number of *k*-points of $Ti_{50}Pd_{50}$ for B2, B19, B19′ and $L1_0$. The *k*-points chosen were 12×12×12 for B2 (cubic), 12×12×9 for $L1_0$ (tetragonal), 9×15×9 for B19 (orthorhombic), 12×7×6 for B19′ (monoclinic) as shown in Figure 4-2.
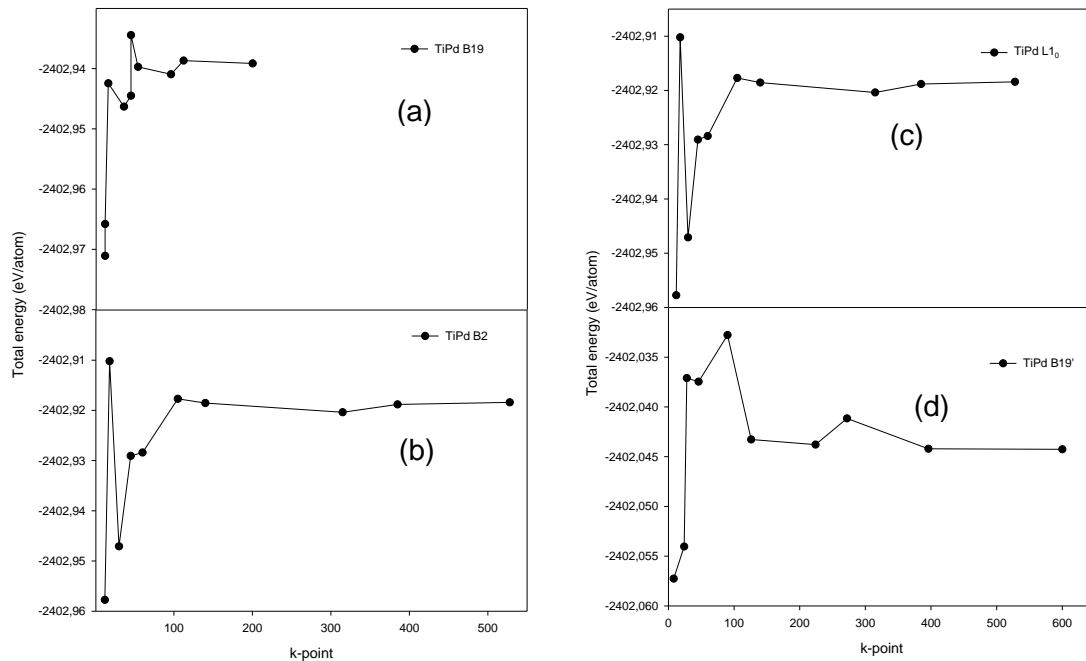
Figure 4-2 The total energy against *k*-points for (a) B19, (b) B2, (c) $L1_0$, and (d) B19'.

4.2 Equilibrium thermodynamic properties for Ti-Pd alloys

In order to determine the equilibrium properties, we performed full geometry optimization calculations within the GGA using the energy cutoff of 500 eV and chosen *k*-points as indicated in section 4.1 above. The equilibrium lattice parameters were determined from relaxed structures, where the volume and unit cell were allowed to change. This was done for all the Ti-Pd structures found in the binary phase diagram.

Table 4-1 shows the results of the equilibrium lattice parameters and the heats of formation. The results of equilibrium lattice parameters were in agreement with available experimental values to within 5% agreement. For example, the B2 gave a lattice parameter of 3.170 Å while compares with 3.180 Å.

Now, the thermodynamic stability of these systems is deduced from the heats of formation (ΔH_f) calculations. In order for a structure to be stable, the heat of formation value must have the lowest negative value otherwise a positive value implies instability. The heats of formation (ΔH_f) *is* estimated by the following expression:

$$\Delta H_f = E_C - \sum_i x_i E_i \tag{4-1}$$

where E_C is the calculated total energy of the compound and E_i is the calculated total energy of the element in the compound. The results of the heats of formation are plotted in Figure 4-3 for Ti-Pd alloys. The Ti$_3$Pd phase was found to be the least stable than the other phases with the heat of formation of -0.350 eV/atom. However, P6$_3$/mmc TiPd$_3$ was found to be the most stable phase with the heat of

formation of -0.620 eV/atom and their results accord well with the previous experimental and theoretical data. The trend of Ti-Pd alloys is compared on the graph of heats of formation against atomic percentage in Figure 4-3.

At 50 at. % Pd, the most stable structure is found to be monoclinic B19′ $Ti_{50}Pd_{50}$ phase with the heat of formation of -0.533 eV/atom. The calculated ΔH_f results agree well with those found theoretically to within 5 %. The least stable structure was found to be cubic B2 $Ti_{50}Pd_{50}$ with a heat of formation of -0.454 eV/atom (since the structure has the highest negative value). The calculated ΔH_f results of the B2 phase agree well with the theoretical value to within 1%. The predicted ΔH_f for tetragonal phase $L1_0$ agrees well with the findings from the theoretical view within 1%. The results show that at low temperature B19′ and B19 phases are more stable than B2. The calculated heats of formation were also in agreement with available theoretical values within 5% agreement.

Now, the predicted order of stability of TiPd at 50 at. % Pd: B19′>B19>$L1_0$>B2 which coincide with theoretical values as highlighted in section 2.5.

Table 4-1 Lattice parameters and heats of formation for Ti-Pd alloys. The experimental and theoretical values are given in parenthesis.

Structure	Prototype	Space group	a (Å)	b (Å)	c (Å)	ΔH_f (eV/atom)
Ti_3Pd	Cr_3Si	Pm3-n	5.045 (5.055) [144]	5.045 (5.055) [144]	5.045 (5.055) [144]	-0.350 (-0.375) [145]
Ti_2Pd	Si_2Mo	I4/mmm	3.100 (3.090) [82]	3.100 (3.090) [82]	9.897 (10.054) [82]	-0.433 (-0.466) [34]
TiPd B2	CsCl	Pm-3m	3.170 (3.180) [23]	3.170 (3.180) [23]	3.170 (3.180) [23]	-0.454 (-0.455) [54]
$L1_0$	AuCu	P4/mmm	2.826 (2.855) [34]	2.826 (2.855) [34]	3.891 (3.907) [34]	-0.523 (-0.522) [54]
B19	AuCd	Pmma	4.587 (4.550) [20]	2.789 (2.780) [20]	4.897 (4.860) [20]	-0.531 (-0.542) [54]
B19′	NiTi	$P2_1/m$	2.792 (2.744) [34]	4.912 (4.797) [34]	4.582 (4.460) [34]	-0.533 (-0.552) [54]
Ti_2Pd_3	Ti_2Pd_3	Cmcm	14.338 (14.330) [144]	4.615 (4.610) [144]	4.689 (4.640) [144]	-0.598 (-0.600) [34]
$TiPd_3$	$TiNi_3$	$P6_3/mmc$	5.554 (5.489) [144]	5.554 (5.489) [144]	9.001 (8.964) [144]	-0.620 (-0.650) [34]
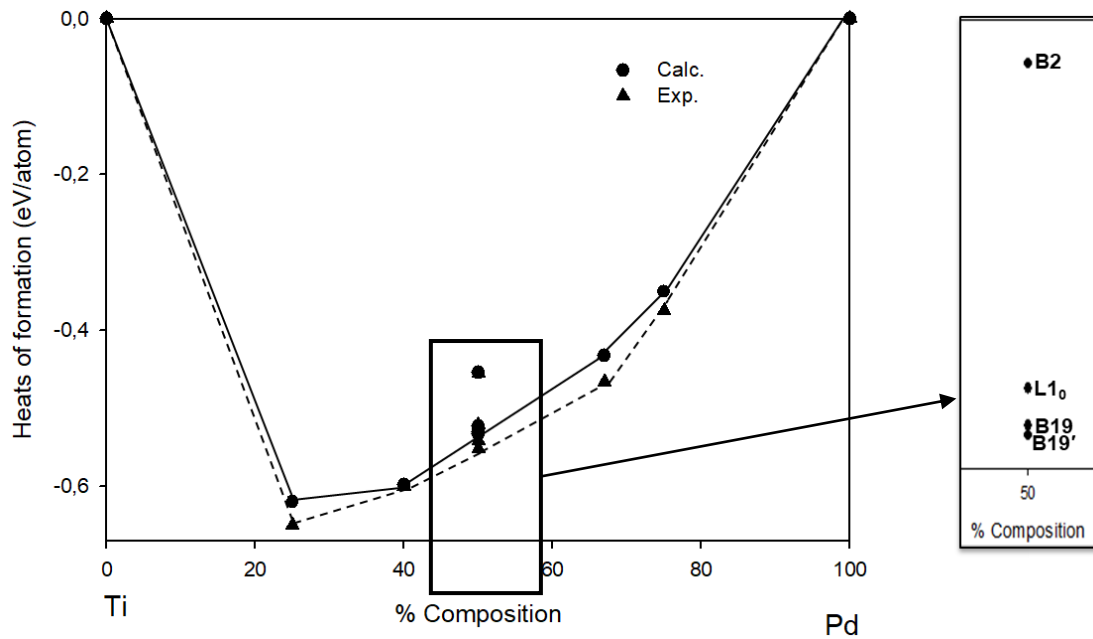
Figure 4-3 Graph of the heats of formation (eV/atom) against the atomic % composition for Ti-Pd. The insert shows the contribution at 50 at. % Pd.

4.3 Elastic properties

Table 4-2 lists the results on elastic constants, bulk, Shear, Young moduli, Pugh and anisotropic ratios of TiPd structures at 50 at. % Pd. In order to describe the mechanical stability of the binary $Ti_{50}Pd_{50}$ systems, we follow the stability criteria as set for each lattice, and this was outlined in chapter 3 (section 3.10.3). However, cubic B2 appears to have the highest value of c_{12} which is greater than c_{11}, and this leads to C' being negative which indicates the instability of the B2. This can be observed from the results of our calculations shown in Table 4-2. So, the negative shear modulus of the B2 phase is due to its instability at low temperatures.

The $L1_0$ phase is stable with the positive c_{44}, c_{66} and shear modulus which satisfies the tetragonal stability criteria. However, the B19 phase has a positive

shear modulus (condition of stability) and also meets the orthorhombic stability criteria which agree well with the heat of formation. The monoclinic B19′ appears to have the highest value of c_{11} compared to B19, $L1_0$ and B2 phases. Thus, from the results, we see that the monoclinic B19′ appears to be the most stable phase since the structure has the highest positive value of $C′$ compared to other phases and also meets the stability criteria as described in section 3.10.3.2. suggesting mechanical stability of monoclinic systems.

Now, we consider the anisotropy behaviour of the structures. The elastic anisotropy of crystals is highly correlated with the possibility to induce microcracks in the materials [146]. For a completely isotropic material, the A factor takes the value of 1, while values smaller or greater than unity measure the degree of elastic anisotropy [147].

Elastic anisotropy for cubic phase is indicated by *A* while for non-cubic is indicated by *A*1, *A*2 and *A*3. The calculated *A* of the B2 phase shows anisotropic behaviour. The calculated *A*2 of $L1_0$ and *A*1 for the B19 phase show isotropic behaviour. Furthermore, the calculated *A*1 of the B19′ phase (*A*≈1) shows isotropic behaviour. There is a good agreement with the heats of formation and elastic properties as they predict the same stability trend.

Table 4-2 Elastic constants and anisotropic ratios for B2, L1$_0$, B19, B19'.

Elastic constants (GPa)	B2	L1$_0$	B19	B19'
c_{11}	149.10	228.83	240.82	300.88
c_{12}	159.83	105.48	125.19	80.10
c_{13}		128.31	124.42	85.18
c_{15}				-0.05
c_{22}			262.65	265.43
c_{23}			90.00	136.46
c_{25}				-0.06
c_{33}		251.16	250.62	244.70
c_{35}				-0.06
c_{44}	43.74	91.81	30.52	41.57
c_{46}				32.33
c_{55}			39.17	53.82
c_{66}		17.42	48.52	112.04
C'	-5.37	61.91	57.82	110.39
$A=2c_{44}/(c_{11}-c_{12})$	-8.15			
$A_1=2c_{66}/(c_{11}-c_{12})$		0.282	0.840	1.015
$A_2=2c_{44}/(c_{11}+c_{33}-2c_{13})$		0.822	0.252	0.222
$A_3=c_{44}/c_{66}$		5.270	0.629	0.371

Table 4-3, shows the calculated Bulk, Shear, Young, Pugh and Poisson (σ) ratio and Vickers Hardness (Hv) for Ti$_{50}$Pd$_{50}$ alloy. The Bulk modulus (B) can be used to measure hardness while the Shear modulus (G) provides a measure of the ability to resist shape change caused by shear stress and the Young modulus (E) can be used to estimate the stiffness of a material. The orthorhombic B19 structure appears to be the hardest since it has the highest bulk moduli of elasticity and is followed by tetragonal L1$_0$. Furthermore, the B19' structure has the highest Young 's and Shear moduli as compared to orthorhombic B19, while

the cubic B2 appears to have the lowest Young 's modulus which indicates its weakness stiffness. The cubic B2 structure appears to be easily compressible (soft) as the results have the lowest shear modulus values which imply that the structure is not stable at low temperature. The calculated Cauchy pressure (c_{12}-c_{44}), Pugh (B/G) 's ratio and Poisson 's ratio are used to assess the ductility/brittleness of the materials. For the deduced Cauchy pressure, a positive value reveals their ionic character and ductile behaviour whereas a negative value indicates weak covalent bond character and exhibits brittle behaviour [148]. As shown in Table 4-3, the calculated Cauchy pressure is positive for all phases which reveals their ionic character and ductile behaviour.

Furthermore, we calculated the ratio of Bulk to Shear modulus (B/G) to investigate the extent of fracture range in these structures. Pugh [149] proposed that material is predicted to be ductile behaviour if the value of Pugh 's criterion B/G> 1.75. It is clear that all structures satisfy the ductile conditions since B/G values are greater than 1.75. Poisson 's ratio can be used to estimate the ductility and brittleness of the compound [140]. The results showed that all four phases satisfy the stability criteria as Poisson 's ratio is greater than 0.26. Furthermore, Poisson's ratio is also used to analyse the bonding of $Ti_{50}Pd_{50}$ alloy. For covalently bonded structure have a small value of ~ 0.10, for the ionic bonded structure have a value of 0.25 while for metallic materials is above 0.33 [150]. The values of σ are all greater than 0.33 which suggests that the structures are metallic. The Vickers hardness (H_V) of $Ti_{50}Pd_{50}$ alloys are also calculated and shown in Table 4-3. The calculated hardness of B19′ is 5.40, which indicates that B19′ is expected to be the hardest among other phases (L1$_0$, B19 and B2).

**Table 4-3 The calculated Bulk modulus B (GPa), Shear modulus G (GPa), Young
's modulus E (GPa), Cauchy pressure (c_{12}-c_{44}) in GPa, Bulk to Shear modulus
ratio (B/G), Poisson 's ratio (σ), and Vickers Hardness (H_V) (GPa) of $Ti_{50}Pd_{50}$ alloy.**

Phase	B	G	E	c_{12}-c_{44}	B/G	σ	Hv
B2	156.25	3.83	8.81	116.09	47.16	0.49	0.03
$L1_0$	159.80	57.86	154.80	61.65	2.762	0.34	5.13
B19	159.11	47.62	132.13	94.67	3.26	0.36	3.70
B19′	157.10	58.82	174.29	38.53	2.66	0.33	5.40

4.4 Thermal properties

The heat capacity at constant volume (C_V) plays an important role to reflect the
thermal properties of $Ti_{50}Pd_{50}$ alloy. The heat capacity at constant volume C_V is
expressed as [151]:

$$C_v = 3nk\left[4D\left(\Theta/T\right) - \frac{3\Theta/T}{e^{\Theta/T}-1}\right] \tag{4-2}$$

where $4D\left(\Theta/T\right)$ represents the Debye integral and n is the number of atoms per
formula unit and k is Boltzmann's constant.

Figure 4-4 illustrates the C_V for B19', B19, B2 and $L1_0$ $Ti_{50}Pd_{50}$ alloy. It is observed
that C_V rises sharply as the temperatures range of 0-1000 K and reaches a zero
slope above this temperature. A weaker bond state is reached due to bigger
thermal vibrations of atoms above 1000 K as shown in Figure 4-4. The present
results suggest that the electron excitation occurs at a very low temperature
below 1000 K for all phases (B19', B19, B2 and $L1_0$). A stronger C_V is observed
for B2 $Ti_{50}Pd_{50}$ while the weakest heat capacity was observed for B19' $Ti_{50}Pd_{50}$
alloy. The values of C_V for temperature range from 0-1000 K the sequence or
trend is as follows: B2> $L1_0$> B19 > B19´.
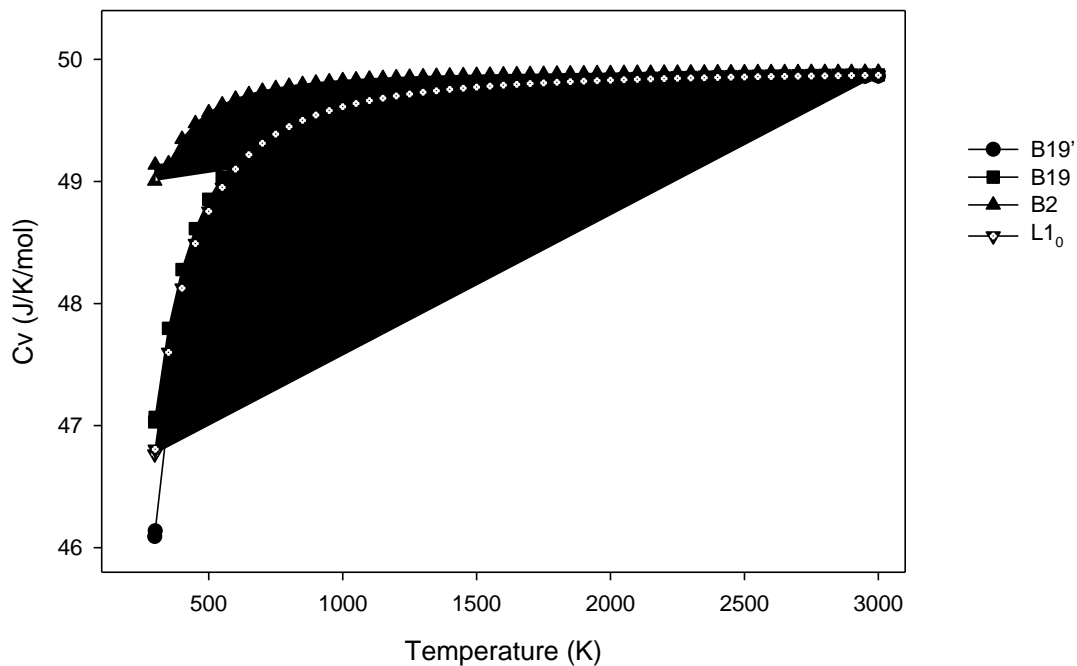
Figure 4-4 The heat capacity at the constant volume C_V of B19′, B19, B2 and L1$_0$ Ti$_{50}$Pd$_{50}$ alloy.

A thermal coefficient of linear expansion (α) for B19', B19, B2 and L1$_0$ is shown in Figure 4-5. It is also observed that the thermal expansion increases at a lower temperature (<500 K) and approaches similar values above. The thermal coefficient of linear expansion for the B2 Ti$_{50}$Pd$_{50}$ alloy is higher than that of B19' and other compositions (L1$_0$ and B19) at low temperatures below 500 K. The result indicate that the material expands more at a low content of B2 expand more compared to other phases (L1$_0$, B19 and B19').

The α show the following stability sequence from 0-500 K: B2> L1$_0$> B19 > B19' while for temperature range from 500-3000 K, show the following stability trend: B19'> L1$_0$> B19> B2.
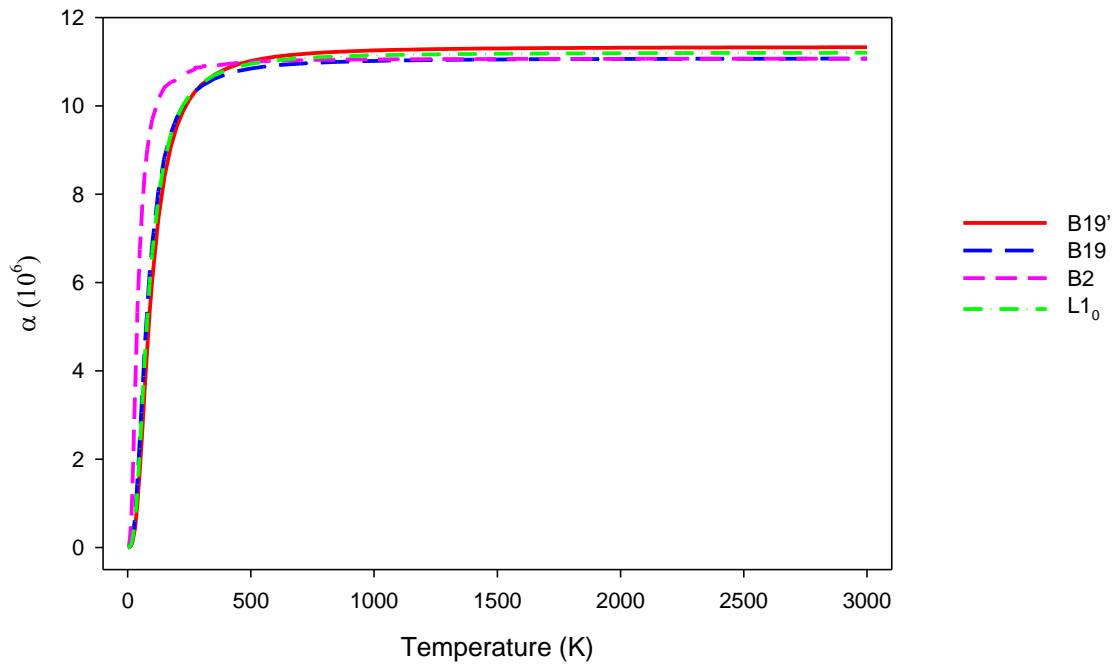
Figure 4-5 The linear thermal expansion coefficient of B19', B19, B2 and $L1_0$ $Ti_{50}Pd_{50}$ alloy.

4.5 Phonon dispersion and phonon density

4.5.1 Phonon dispersion

Phonon dispersion curves for B19, B19′, B2 and $L1_0$ were calculated and are shown in Figure 4-6. The dispersion curves exhibit two types of phonons namely the optical and acoustic modes corresponding to the upper and lower sets of curves in the diagram, respectively. As has been seen in the heats of formation and elastic properties, our phonon dispersion calculations (Figure 4-6) confirm that B2 structure is unstable since there are soft modes observed in the phonon calculations. The soft modes are observed along M and R directions. The negative slope of the acoustic Γ-M branch corresponds to a pure elastic instability ($C'=1/2$ (c_{11}-c_{12})<0). There is a gap between acoustic and optical phonon

branches of 1.74 THz which indicates the instability of the B2 phase. The highest value of frequency is 7.4 THz along the X branch. The soft modes observed on the B2 phase along gamma point (0, 0, 0) could be attributed to the negative shear moduli as observed in the elastic properties calculations. This can also be observed from the anisotropy ratio being negative for the B2 phase.

Furthermore, orthorhombic B19 structure display imaginary soft mode (negative frequency) along Z in the phonon dispersion curve which corresponds to less stable structure behaviour as shown by the heats of formation and the elastic constants. However, in the $L1_0$ and B19′ phonon dispersion spectra, no soft modes are observed which means that the structures are vibrationally stable. This also confirms the predicted order of stability as B19′> $L1_0$ > B19> B2, in agreement with the elastic constants and heats of formation.
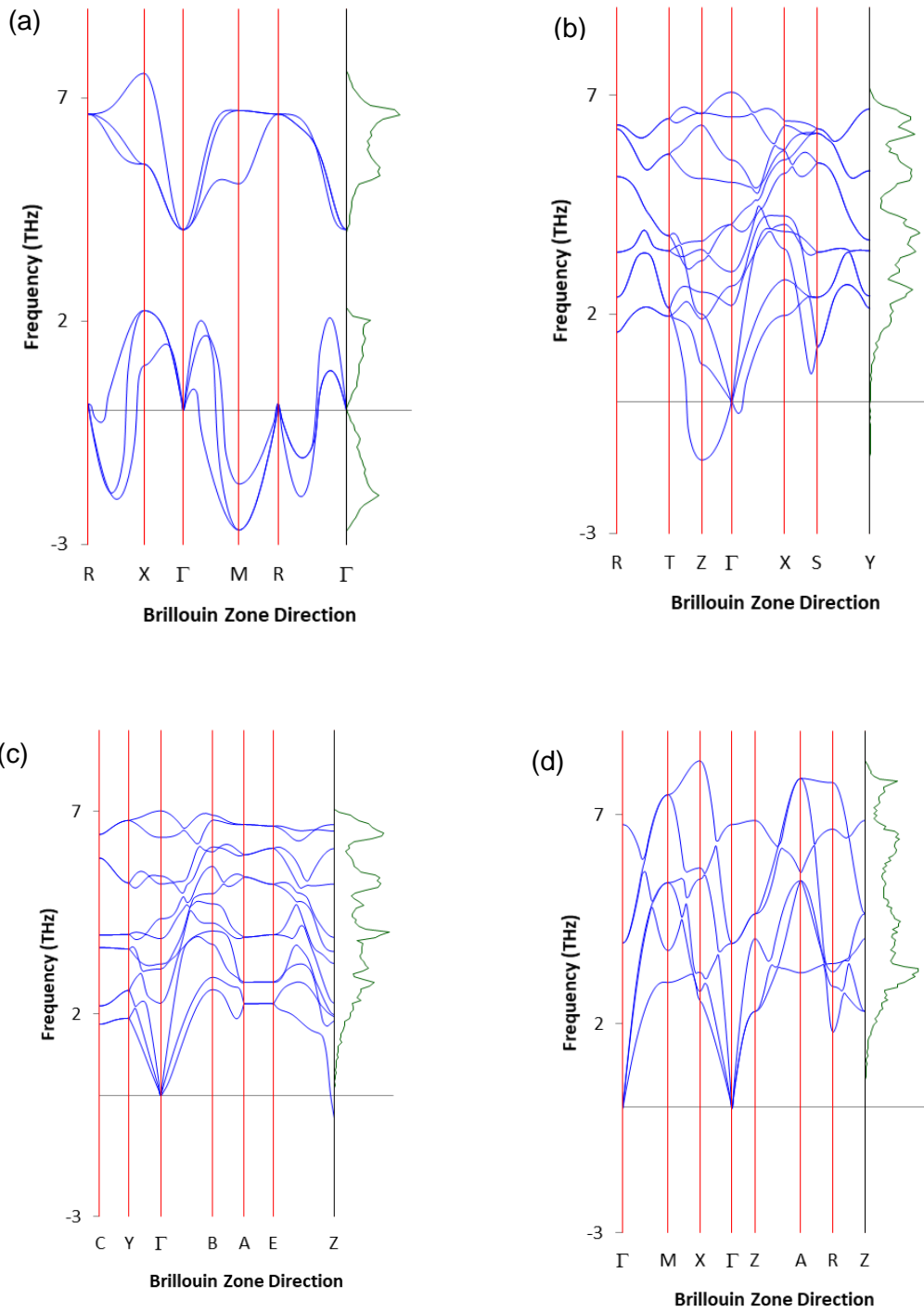
Figure 4-6 Phonon dispersion curves for (a) B2, (b) B19, (c) B19' and (d) L1$_0$.

4.5.2 Phonon density of states

The phonon density of states for B19, B19′, B2 and $L1_0$ were calculated and are shown in Figures 4-7. Recall that there were no negative vibrations observed for B19, B19′ and $L1_0$ (condition of stability). Thus, it is clear that the phonon DOS of the B19, B19′ and $L1_0$ structures have shifted to the higher frequency above zero indicating that the phases are stable.

In the case of B19, there is a small sharp peak along 2.5 THz which indicates the contribution of Pd while the contribution of Ti is ascribed to the DOS peak around 5 THz. This behaviour is similar to that of B19′. There is a slight shift for the $L1_0$, the sharp peak observed at about 3 THz corresponds to the contribution of Pd while the contribution of Ti is observed at around 6 THz.

Now, considering the B2 phonon DOS. The vibrational sharp peak at -2 THz and 2 THz are contribution of Pd with a very minimal contribution of Ti. It is noted that the negative frequency (vibrations) is a contribution of Pd. This suggests that Pd vibrations are responsible for the instability of the B2 $Ti_{50}Pd_{50}$ structure.
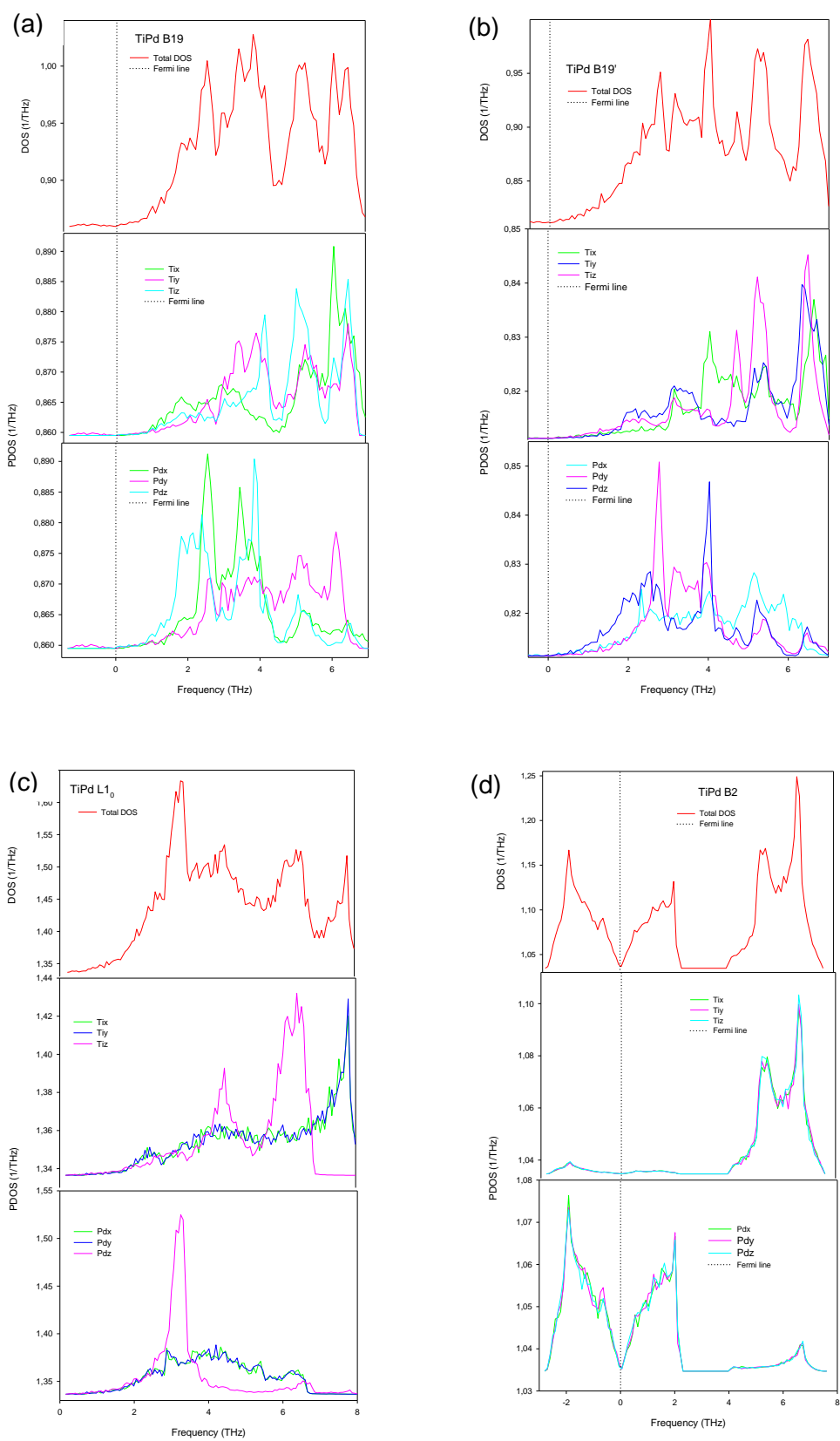
Figure 4-7 Phonon densities of states for (a) B19, (b) B19', (c) L1$_0$ and (d) B2 structures.

4.6 Total and partial density of state

4.6.1 Total density of states

The total density of states (tDOS) is shown in Figure 4-8 for B2, B19, B19′ and L1$_0$. The tDOS are used to predict the electronic stability by observing the behaviour of states near the Fermi level (E-E$_f$=0) with respect to the pseudogap. This analysis has been adopted from previous work [26]. The structure with the highest and lowest density of states at E$_f$ is considered the least and most stable, respectively [26]. The calculation of density of states was performed using VASP code and the graphs of B2, B19, B19′ and L1$_0$ Ti$_{50}$Pd$_{50}$ are compared in Figure 4-8. In the case of the orthorhombic B19 structure, the total DOS shows that the pseudogap shifted to the right Fermi level and similarly for B19′. The total DOS of the B19′ structure has the lowest states at E$_f$ which suggests that it is the most stable as compared to B19, L1$_0$ and B2.

The L1$_0$ structure hits the top of the total DOS peak indicating instability of the structure. It is clear that the B2 phase has the highest number of density of states at E$_f$ as compared to the other structures which confirm that it is the least stable. The B2 structure hits the total DOS in the middle of the peak near the Fermi level indicating instability of the structures at low temperature. The results suggest that B2 is less stable compared to other structures and this is consistent with the prediction of heats of formation.
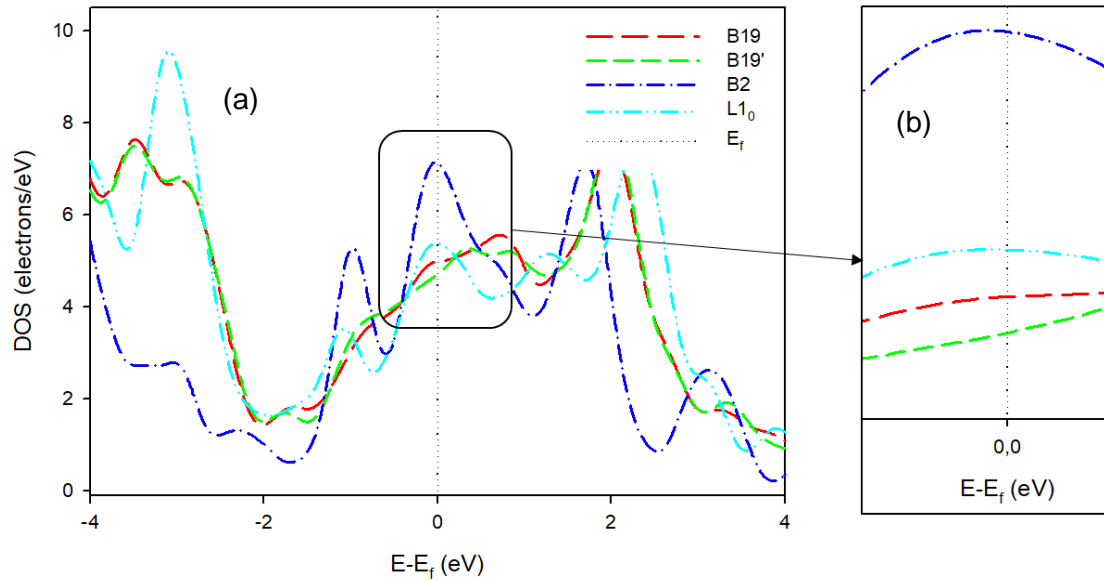
Figure 4-8 (a) Total density of states for B19, L1$_0$, B2 and B19' against total energy. (b) Is the enlargement of the DOS graph near the Fermi energies.

4.6.2 Partial density of states

The calculation of partial density of states was performed to indicate the contribution of Ti and Pd atomic orbitals. The graphs of B2, B19, B19′ and L1$_0$ Ti$_{50}$Pd$_{50}$ are plotted in Figure 4-9. We note that the lower energy side is occupied by the sets of peaks coming mainly from d-states of Pd and the higher energy peaks are due to the d-states of Ti. The peaks at the E$_f$ are mainly from both Pd d and Ti d-orbital. In B19′ and B19 phases, the E$_f$ hits the DOS at the shoulder of the dropping peak contributed mainly by the Ti d-states, as can be clearly seen in the Ti PDOS. The s and p orbital contributions are negligible since they play a little role in donating some electrons to the Ti d-states. It is clear that the Ti d-states rise gradually below the E$_f$ which results in the cubic B2 being unstable. In L1$_0$, the lower energy peaks are mainly due to the Pd d-states.
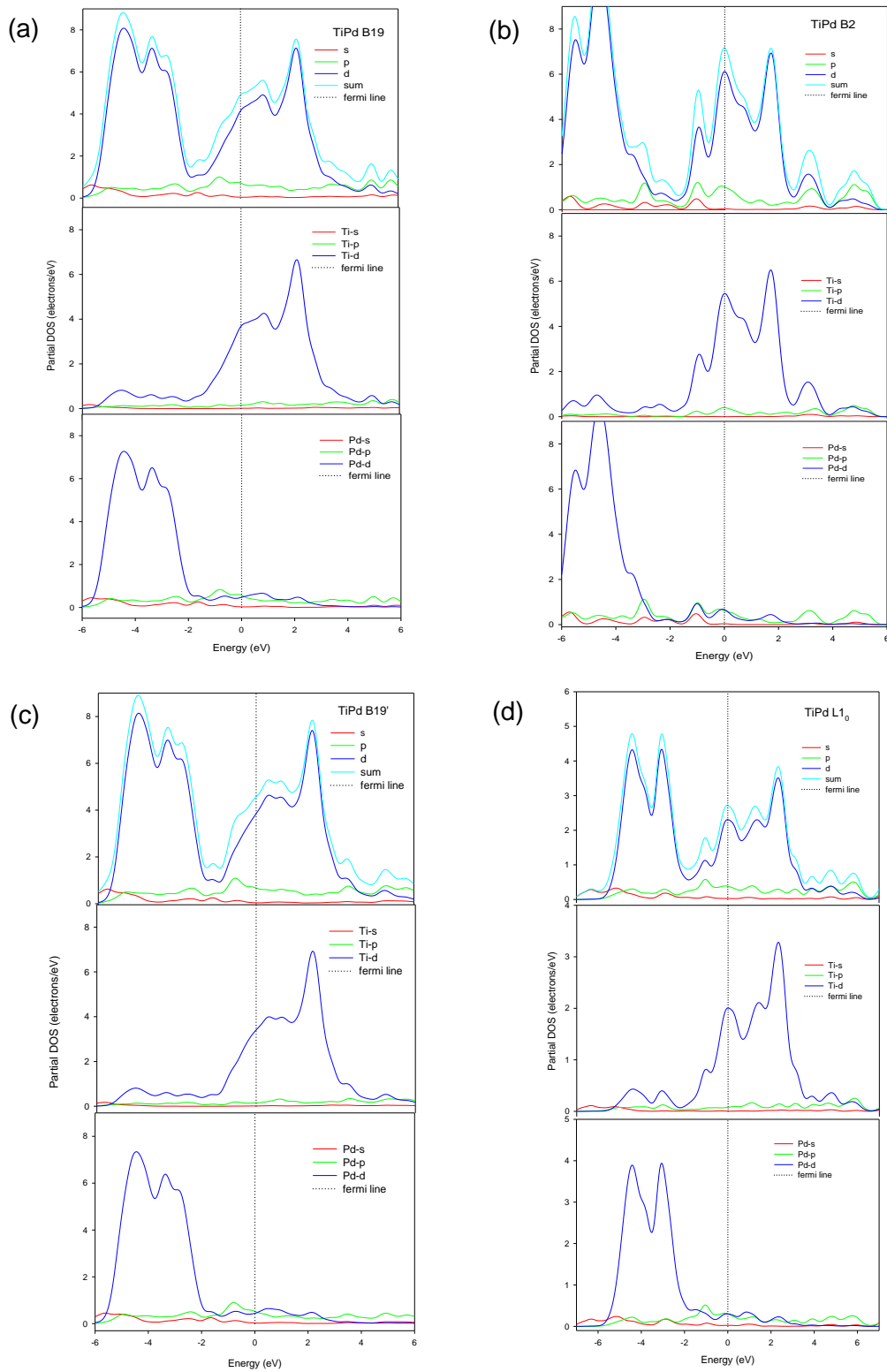
Figure 4-9 Partial densities of state against total energy for (a) B19, (b) B2, (c) B19', and (d) L1$_0$.

Chapter 5

Temperature dependence of the binary Ti$_{50}$Pd$_{50}$

In this chapter, the volume, density, lattice expansion, x-ray diffraction and elastic properties for the binary B19, B19′, L1$_0$ and B2 Ti$_{50}$Pd$_{50}$ alloys are investigated at varied temperatures. The LAMMPS code which employs the embedded atom method (EAM) [104] was used to investigate the temperature dependence of these alloys. The calculations were performed at a varied temperature range from 100 to 1800 K to check the possible transformation from martensitic to the austenite phase. So, the findings in this chapter will provide a better understanding of the transformation that occurs between the orthorhombic B19 (known as martensite phase) and the cubic B2 phase (known as the austenite phase).

5.1   Temperature dependence of the volume and density

The graphs of volume and density against temperature are shown in Figures 5-1 and 5-2, respectively. Firstly, from the graph of volume against temperature (Figure 5-1), we note that the volume increases with an increase in temperature. The volume of the four phases increases with the same trend and reaches a transformation temperature at 1600 K (B19 and L1$_0$) while B2 and B19′ are slightly at a higher temperature of about 1700 K. This behaviour may suggest structural deformation at these temperatures.
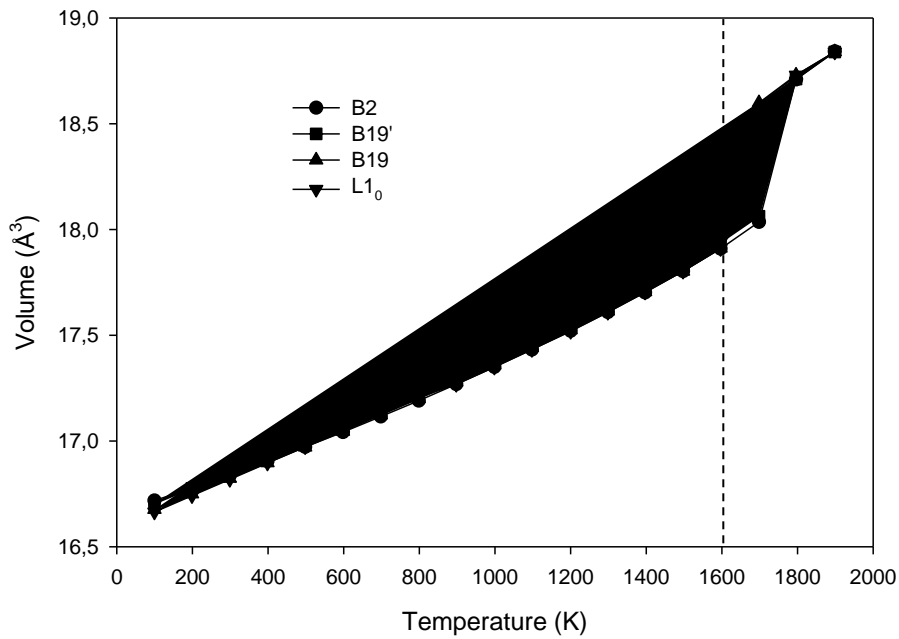
Figure 5-1 Volume against temperature for B2, B19', B19 and $L1_0$.

Secondly, in Figure 5-2 the graph of density against temperature shows that the density decrease with an increase in temperature as expected. The density of the four phases decreases with the same trend until the melting temperature at about 1600 K, and the structures become less dense.

Table 5-1 Shows the effect of temperature on the (B2, B19', B19 and $L1_0$) structures at different temperatures (1000-1800 K). At temperatures below 1600 K, structures are ordered or show a uniform pattern, however, these patterns change at high temperature above 1600 K. In the case of B2, we observed that the atoms are well arranged in patterns below 1600 K. However, as the temperature is increased from 1700-1800 K, the atoms become randomly distributed indicating that the bond between atoms are broken which suggest that the melting temperature have been reached.
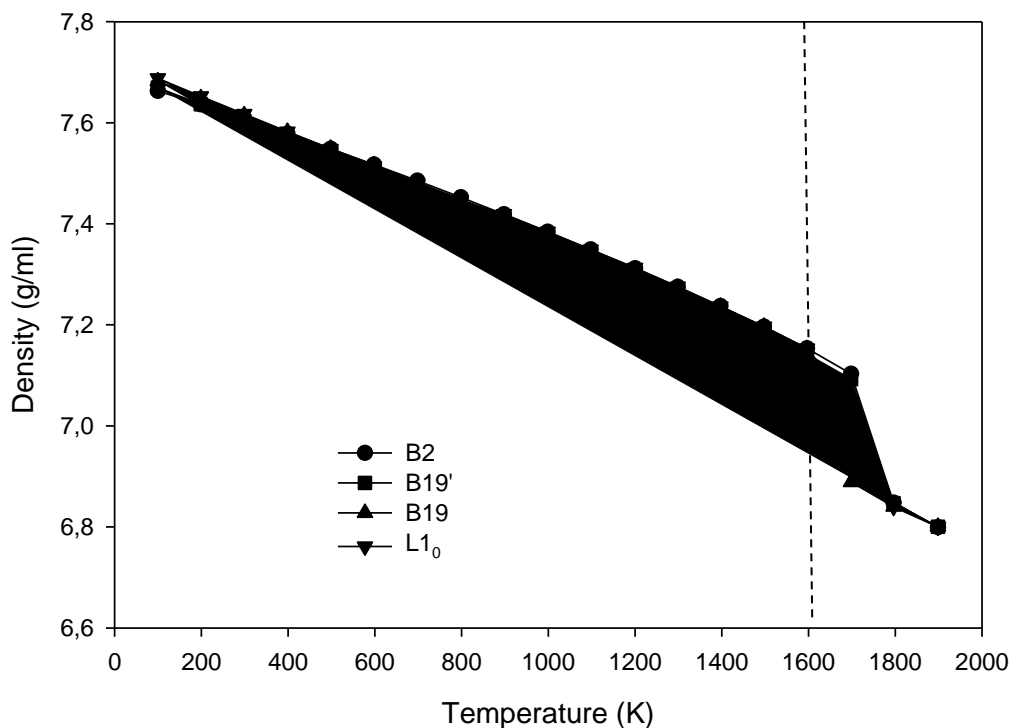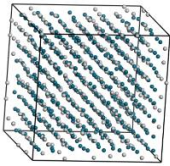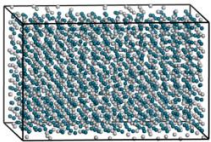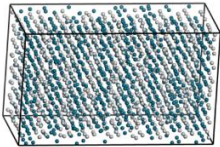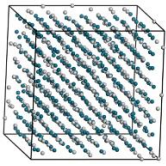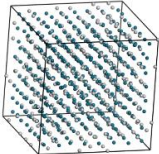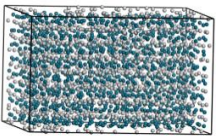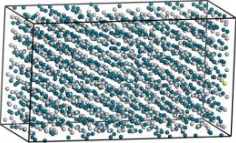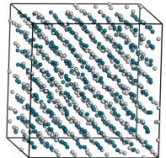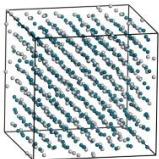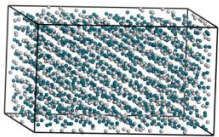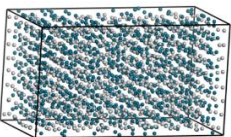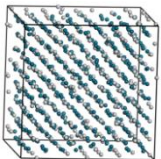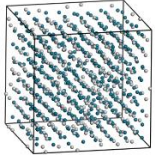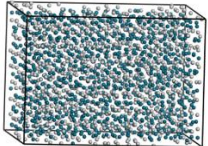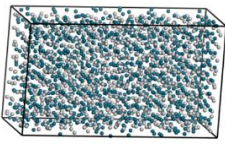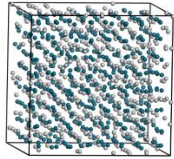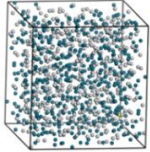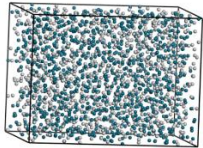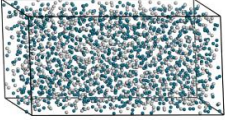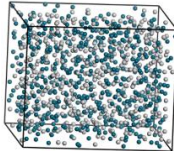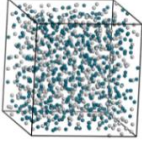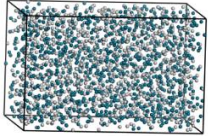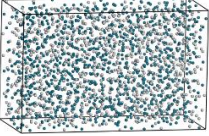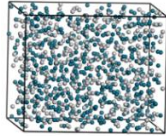
Figure 5-2 Density against temperature for B2, B19', B19 and L1$_0$.

We observed similar behaviour for B19 and B19' as the temperature is increased from 1600-1800 K. This behaviour is due to B19 and B19' attempting to adapt to a high temperature phase since the maximum operating temperature of B19 was found to be 773 K [152]. Moreover, the B19 and B19' structures start to lose their shape and patterns above 1600 K (melting temperature is reached). We also observe a change in the L1$_0$ structure at 1600 K since atoms start to move randomly and display a similar trend as observed above 1700 K.

Table 5-1 The structures of B2, B19, B19' and $L1_0$ with 1024 atoms at a temperature from 1600- 1800 K.

Temperature (K)	B2	B19	B19'	$L1_0$
1000				
1200				
1400				
1600				
1700				
1800				

5.1.1 B19 $Ti_{50}Pd_{50}$

The effect of temperature on the lattice parameters of the B19 phase was investigated and is shown in Figure 5-3. This is to show the extent of lattice expansion and transformation behaviour at different temperatures. The size of the supercell was 1024 atoms since it gives results close to the experimental

findings. From the results, we note that the a and c lattice parameters increase minimally with an increase in temperature up to 1400 K. However, the lattice parameters collapses drastically above 1400 K (1496 K) for both a and c (give a similar value of 4.66 Å) which suggest a possible transformation from B19 to B2 phase. The b lattice parameter also shows an increase with an increase in temperature. The a/b and c/b ratios decrease with an increase in temperature and there is an extreme decrease in the ratio at approximately 1496 K.

In order for transformation to occur from orthorhombic B19 to cubic B2, the ratios of a/b and c/b must be close to 1.414 [13]. The decrease of a/b and c/b with increasing temperature in orthorhombic B19 is reasonable and is significant to describe the structural change from B19 to cubic B2 above 1496 K. It is clearly seen that the a/b and c/*b* ratios are above 1.41, indicating that the phase is still orthorhombic B19 up to 1397 K. The ratio c/b of the B19 $Ti_{50}Pd_{50}$ is 1.414 at approximately 1496 K which suggests that B19 phase has transformed to the cubic B2 phase.

5.1.2 B19′ $Ti_{50}Pd_{50}$

In Figure 5-4, we show the lattice parameter against temperature for the B19′ $Ti_{50}Pd_{50}$ structure. We note that the a and c lattice parameters increase with an increase in temperature similar to the b lattice. Furthermore, we note that the a and c lattice parameters collapse at 1798 K while b increases monotonically at this temperature. This resulted in the a/b and c/b ratios to give a decreasing trend with an increase in temperature. This behaviour predicted the ratio of c/b and a/b

as 0.931 and 0.537, respectively. At above 1798 K, no transformation was observed.
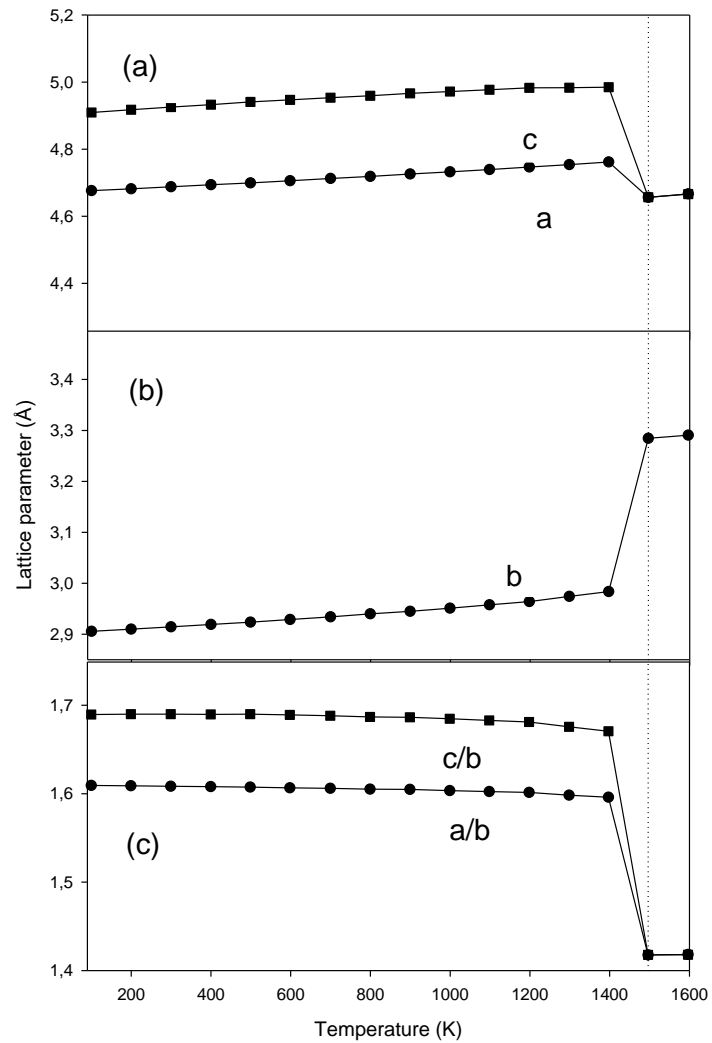
Figure 5-3 The effect of temperature on the (a) a and c (b) b (c) a/b and c/b lattice parameters of the B19 Ti$_{50}$Pd$_{50}$.
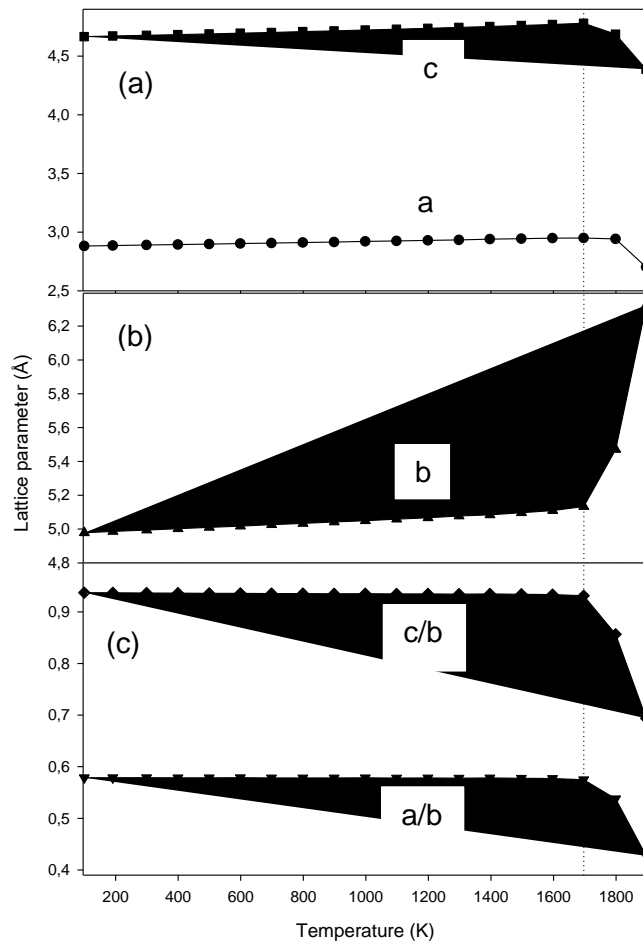
Figure 5-4 Lattice expansions (a) a and c (b) b (c) a/b and c/b against temperature for B19'.

5.1.3 L1$_0$ Ti$_{50}$Pd$_{50}$

The dependence of the lattice parameters of the L1$_0$ on temperature is plotted in Figure 5-5. Similar to the B19 and B19', the a lattice parameter increase with an increase in temperature as shown in Figure 5-5 (a). In the case of the c lattice parameter, we observe a slight increase in temperature. The b lattice parameter increases linearly with an increase in temperature. A drastic increase in the b lattice parameter is observed between 700 to 900 K as shown in Figure 5-5 (b). Furthermore, the a/b and c/b ratios are also shown in Figures 5-5 (c). In order for

transformation to occur from tetragonal $L1_0$ to cubic B2, the ratios a/b and c/b should be closer to 1.00 since a=b=c. In the c/b ratio, there is an extreme decrease observed at 897 K which suggests that the $L1_0$ phase has transformed to the B2 phase. The plots of c/b and a/b ratios collapse to a ratio of 1.00 and remain the same with an increase in temperature. It can be clearly seen that the $L1_0$ to B2 transformation has occurred at 897 K, and hence for the B2 phase is observed on a temperature range of 897- 1696 K. The structure then reached the melting temperature above 1696 K. The temperature at which the transformation occurs for $L1_0$ ($L1_0$-B2) is lower (897 K) as compared to B19 phase (B19-B2) at 1497 K.
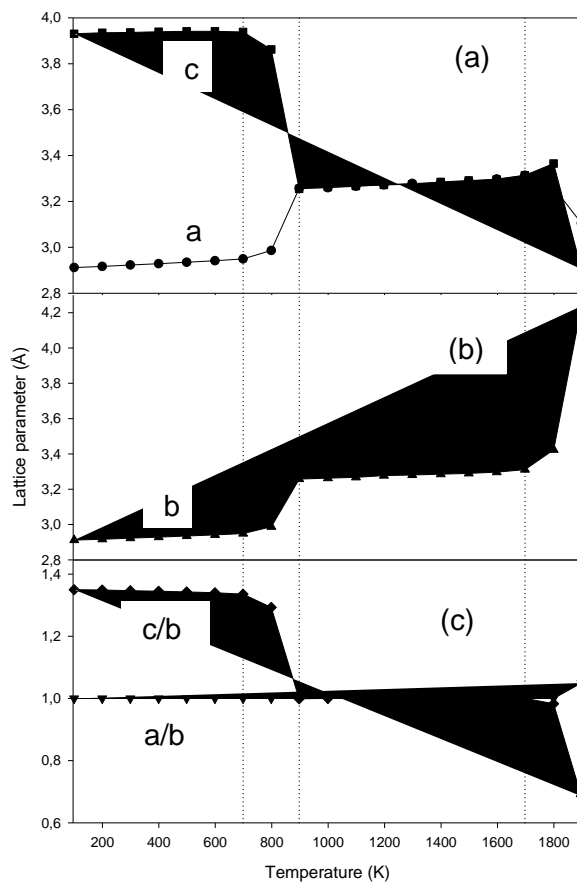
Figure 5-5 Lattice parameters (a) a and c (b) b (c) a/b and c/b against temperature for $L1_0$.

5.1.4 B2 Ti$_{50}$Pd$_{50}$

Figure 5-6 show the effect of temperature on the lattice parameters for the B2 phase. It is observed that the a, b and c parameters increase slightly as the temperature is increased (below 800 K). The results suggest that the transformation is suppressed and remains B2 below 800 K. The B2 structure transforms to B19 between 800-1300 K since a≠b≠c as shown in Figure 5-6 (a). Interestingly, as the temperature is increased to 1490 K, the structure transforms back to the B2 phase (a=b=c). This suggests a possible transformation from the B19 martensite phase into the B2 phase.

The ratios of c/b and a/b collapse to a ratio of 1.00 and remain the same with an increase in temperature above 1490 K. Similar behaviour was observed when the B19 phase transforms to the B2 phase at 1490 K (as discussed in Figure 5-3). It is noted that the structure remains stable up to 1698 K and beyond this point, a possible deformation occurs, as shown in Table 5-2. The predicted melting temperature for the B2 (1695 K) and is in good agreement with the experimental finding of 1673 K [80], this has been shown in chapter 2 (see Table 2-2).

The lattice parameter ratios at a temperature from 1598-1898 K and predicted phases are summarised in Table 5-2. The c/b, a/b and c/a ratios are close to 1, indicating the phase is still B2 phase below 1698 K. Furthermore, we observe that c/b=1.260, a/b=0.923 and c/a=1.265 with increasing temperature in cubic which suggest that the melting temperature have been reached.
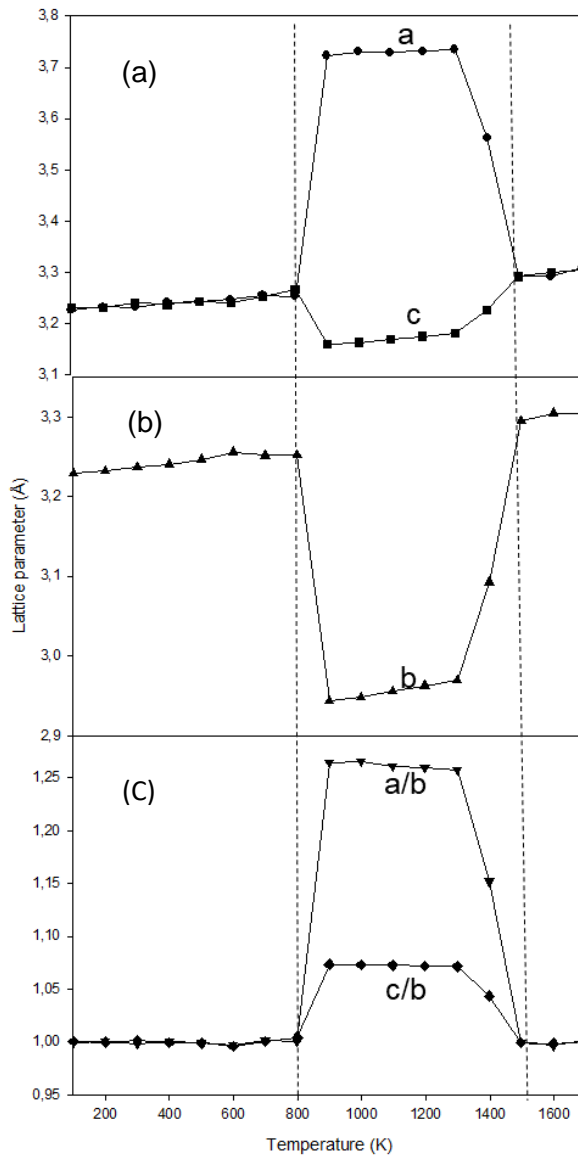
Figure 5-6 Lattice expansions (a) a, b and c (b) a/b and c/b against temperature for B2.

Table 5-2 Lattice parameters and predicted phases at a temperature from 1598-1898 K.

Lattice parameter (Å)	1598	1698	1798	1898
c/b	0.998	0.999	1.260	1.401
a/b	0.998	0.999	0.923	1.085
c/a	1.000	1.000	1.265	1.302
Predicted phase	B2	B2	deformed	deformed

5.2 X-Ray diffraction patterns

X-ray diffraction (XRD) is a rapid analytical technique primarily used for phase identification of a crystalline material and can provide information on unit cell dimensions [153]. In this section, we analyse the XRD for B19, L1$_0$, B19′ and B2 Ti$_{50}$Pd$_{50}$ from ambient to high temperatures. The temperature was increased from 100- 1800 K at a difference of 100 K steps. However, for the purpose of discussion, we selected only a significant plot showing the transformation or changes in the XRD patterns for the four phases (B19, L1$_0$, B19′ and B2).

5.2.1 B19 X-ray diffraction patterns

A simulation of the temperature dependence of the XRD patterns was conducted on the pure B19 Ti$_{50}$Pd$_{50}$, with 1024 atoms, as shown in Figure 5-7. The B19 X-ray indices, 001, 101, 010, 011 and 002 are observed at different temperatures. The structure remains B19 phase from 100 to 1298 K with the same set of peaks observed. As the temperature is increased, there is an increase in intensity and number of peaks (< 40 2θ) at 1368 K which suggests a possible transformation from B19 to B19′. The transformation from B19 to B19′ structure, characterized by XRD indices 001, 101, 010, 011 and 002 at elevated temperatures with an increase in intensity at 101 peak (1368 K).

Interestingly, the number of peaks reduces at 1447 K and assumes the patterns of the B2 phase. At this temperature, the peaks (001 and 101) are close to each other and shift to the left of the 2θ to 26° and 30°. This observation suggests a possible transformation from the B19′ to the B2 phase. The transformation from

B19-B19′ and B19′-B2 suggest that the B19′ phase exists in a narrow or temperature (1368-1447 K).

A transformation is observed where there is the disappearance of the 101 peak close to 30° at a temperature of about 1496 -1596 K, the disappearance of the peak suggests possible transformation from B19′ to B2. At a temperature of 1696 K and above, the peaks are broad and suggesting that the structure melted at this temperature and thus the structure is lost. It is interesting that the transformation temperature of the B19 phase correlates well with the a/b and c/b ratios change, which is at approximately 1496 K (section 4.1.2). A similar observation is true for B19′.
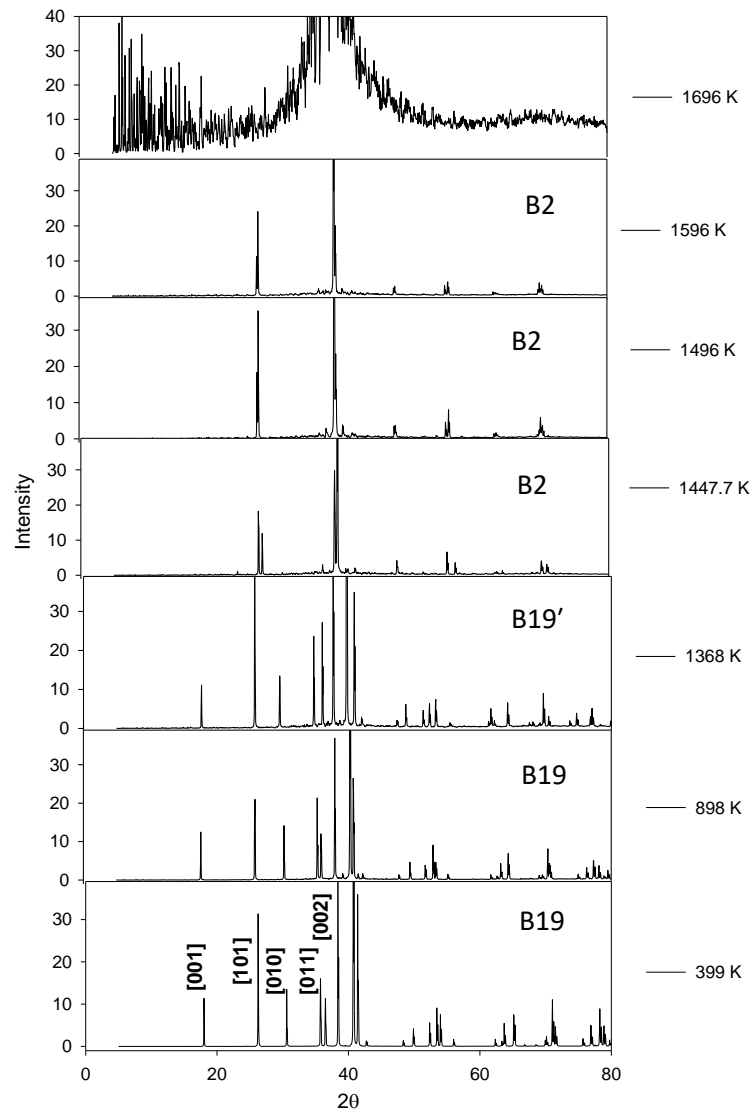
Figure 5-7 Diffraction patterns at a various temperatures from 399-1696 K for B19.

5.2.2 L1₀ X-ray diffraction patterns

In Figures 5-8, the simulated XRD patterns of $L1_0$ are shown from 399-1697 K. The $L1_0$ X-ray indices, 001, 100 and 011 are observed below 30° at different temperatures. It can be clearly seen that the structure remains $L1_0$ phase from 399 to 778 K with the same set of peaks observed. At a temperature above 897 K, the number of peaks reduces and the B2 phase patterns are observed.

Furthermore, when the temperature is increased above 897 K, the disappearance of the 100 peak close to 30° is observed. At this temperature possible transformation has occurred from the $L1_0$ phase to the B2 phase since the peaks are assumed to be the patterns of the B2 phase. This agrees reasonably well with the ratio of a/b and c/b where the transformation is occurring at approximately 897 K (Figure 5-5). The melting temperature of B2 $Ti_{50}Pd_{50}$ from the phase diagram was found to be 1673 K [80]. From the XRD patterns, the structure above 1597 K is lost which means that the structure has reached the melting temperature at 1697 K.

5.2.3 B19′ X-ray diffraction patterns

The temperature variations of XRD patterns for the B19′ are shown in Figure 5-9. The observed B19′ X-ray indices are 010, 011,100 and 110 are found below 40° from 399-1697 K. At approximately 898 K, the intensity of the peak [011] becomes smaller at 25°. The result suggests that no transformation takes place; rather the structure remains unchanged below 1000 K. Furthermore, above 1696 K the peaks are broad and the structure is lost suggesting that the structure melted. This observation is similar to the results of the lattice expansion discussion above.
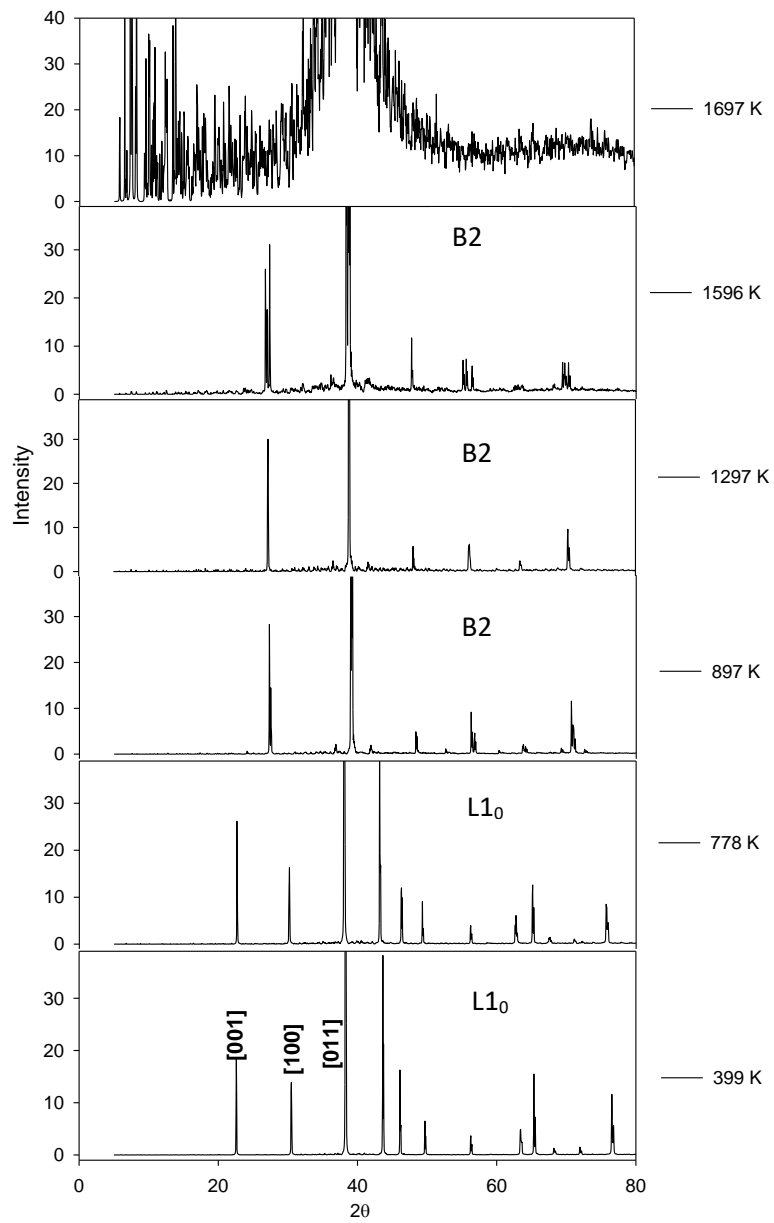
Figure 5-8 Diffraction patterns at various temperature from 399 K-1697 K for L1$_0$.
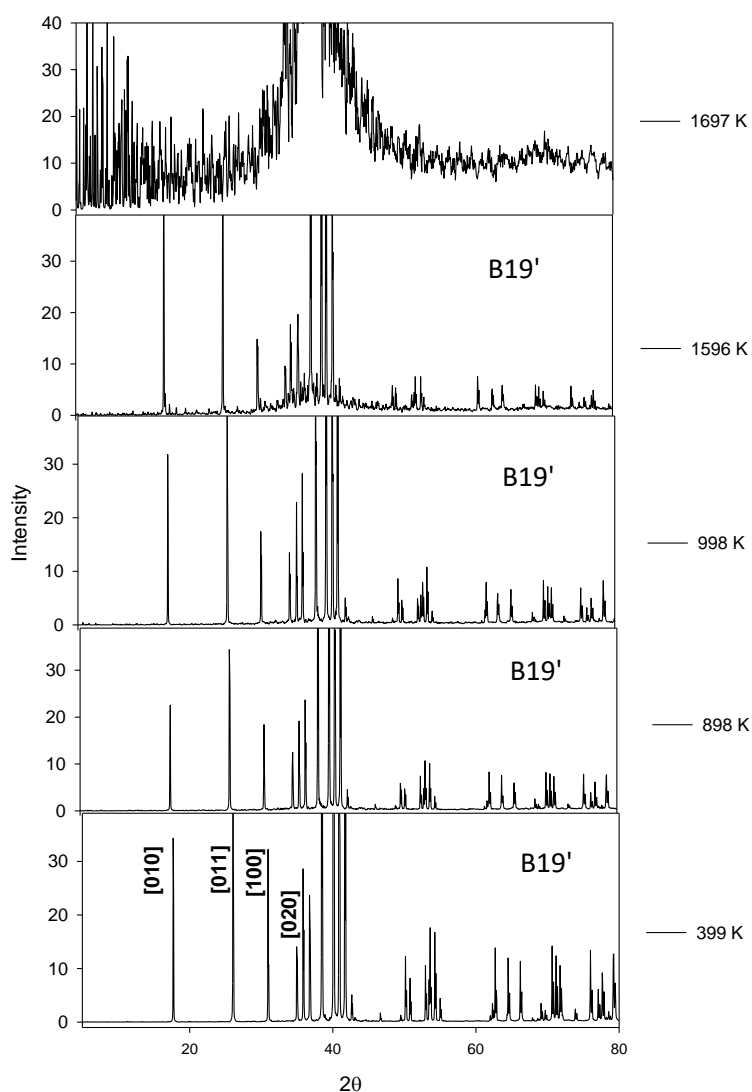
Figure 5-9 Diffraction patterns at various temperatures from 399-1697 K for B19'.

5.2.4 B2 X-ray diffraction

The XRD plots of the B2 $Ti_{50}Pd_{50}$ at various temperatures are shown in Figure 5-10. The 001 and 011 peaks are observed in the XRDs below 40 2θ. It is well known that B2 $Ti_{50}Pd_{50}$ is a high temperature phase which is unstable at room temperature hence it will be more interesting to see the effect of low temperature on the system. It is observed that the number of peaks in the XRD pattern increase as the temperature is increased to 898 K. The patterns are assumed to

be of the B19 phase. As the temperature is increased to 1497 K, the patterns decreases which suggests a transformation of B19 to B2 phase as shown in Figure 5-10. The structure remains B2 phase from 1497 to 1596 K with the same set of peaks observed. There are two transformations observed from B2 to B19 martensite phase as well as from B19 to B2 Austine phase and this agrees very well with the ratio of a/b and c/b until melting is reached.
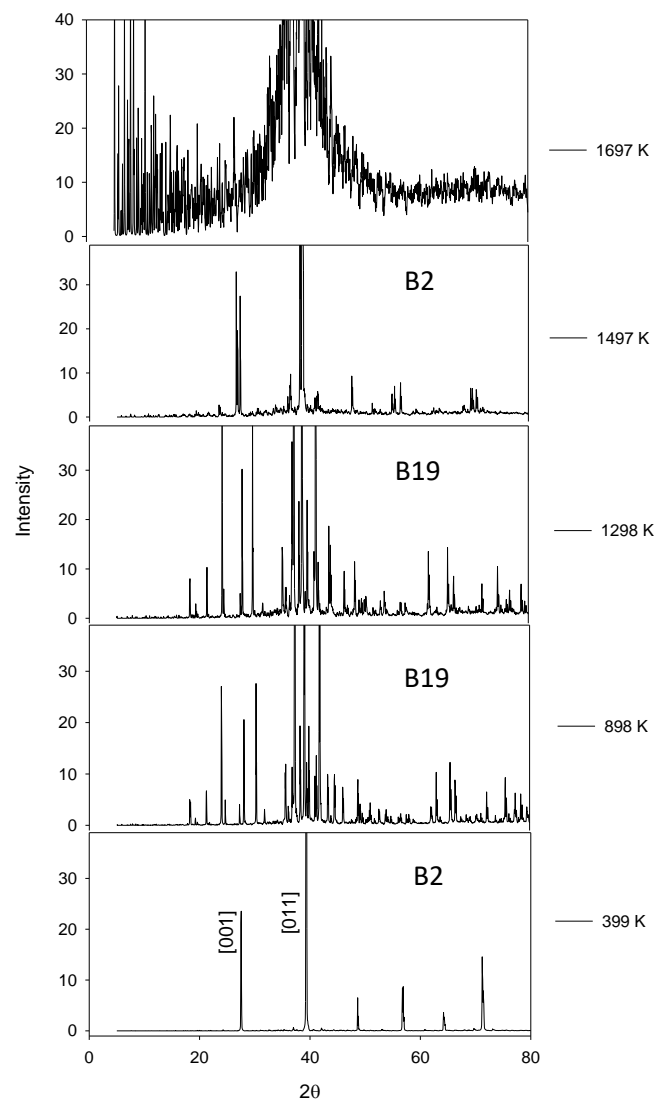
Figure 5-10 Diffraction patterns at various temperatures from 399-1696 K for B2.

5.3 Temperature dependence of the elastic properties

In order to understand the mechanical stability of B19, B19′, B2 and $L1_0$ $Ti_{50}Pd_{50}$ at various temperatures, related elastic constants and shear moduli were calculated using forcefield based LAMMPS code.

5.3.1 B2 $Ti_{50}Pd_{50}$

Temperature variation of elastic constants of B2 structure was calculated and shown in Figure 5-11. In the first region of the plot, the elastic constants (c_{11}, c_{12}) decrease minimally with an increase in temperature and tend to converge above 1695 K. This behaviour can be attributed to the initially B2 specified structure attempting to reach melting temperature. The second region, elastic constant (c_{44}) decrease linearly with an increase in temperature and converge above 1695 K. It is observed that as the temperature is increased, from ambient values, the predicted shear modulus $C' = (c_{11} - c_{12})/2$ of the B2 phase is initially positive, and approaches zero above 1695 K. The shear modulus (C') decreases with increasing temperature, suggesting less stability of the B2 phase. So, above 1695 K the structure is mainly characterised by C' becoming less positive, as the magnitude of $c_{11} = c_{12}$, hence suggesting mechanical stability of the B2 phase at high temperature, consistent with the experimental of 1673 K.
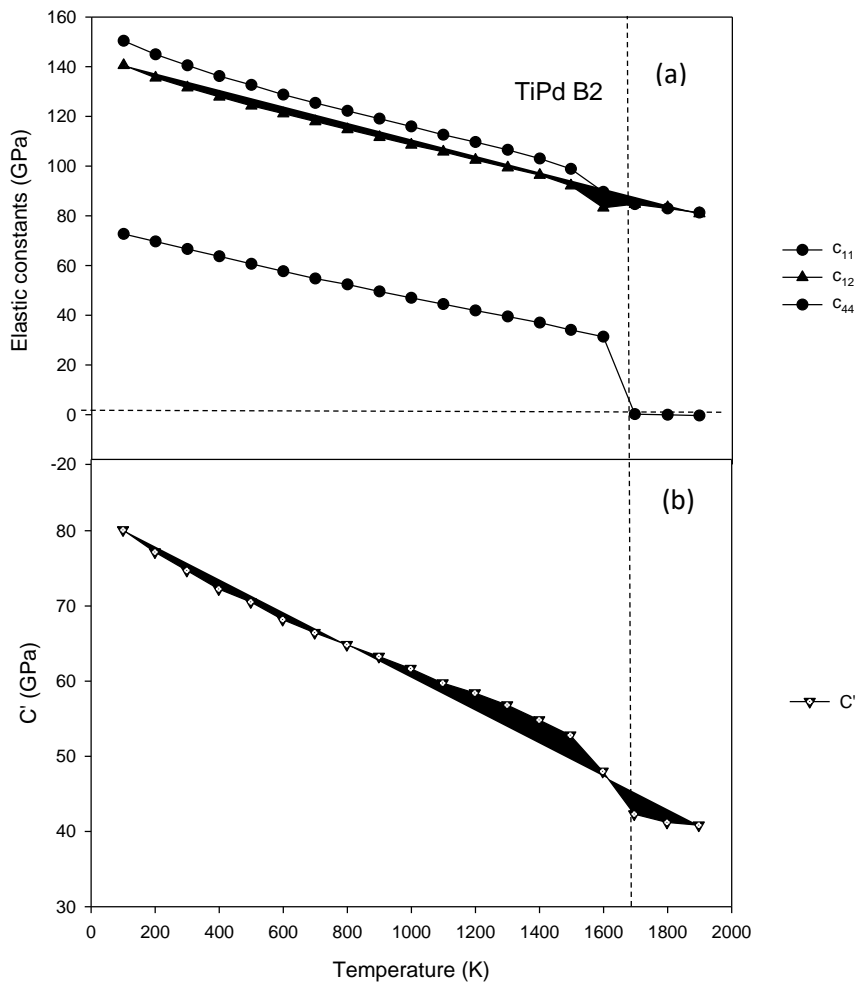
Figure 5-11 (a) elastic constants and (b) C' against temperature for B2. The dotted line is used to guide an eye with respect to stability and possible transition temperature.

5.3.2 B19′ Ti$_{50}$Pd$_{50}$

Figure 5-12, shows the effect of temperature on elastic constants and shear moduli for the monoclinic B19′ phase. In the case of B19′, the first group of elastic constants c_{11}, c_{22} and c_{33} decrease linearly with temperature below 1798 K and tend to converge to a common value above 1798 K. Furthermore, the second group of elastic constants c_{12}, c_{13} and c_{23} reduces slightly with an increase in temperature, and a possible convergence with elastic constants above 1798 K

was observed. Such convergence suggest melting temperature is reached, where $c_{11} = c_{22} = c_{33}$ and $c_{12} = c_{13} = c_{23}$. Furthermore, elastic moduli c_{44}, c_{55}, c_{66}, c_{25}, and c_{35} constitute the third group and decrease minimally with an increase in temperature. However, they all tend to converge at the highest calculated temperatures above 1798 K.

The shear moduli $(c_{11} + c_{22} + c_{33} + 2(c_{12} + c_{13} + c_{23}))$, $(c_{33}c_{55} - c^2_{35})$, $(c_{44}c_{66} - c^2_{46})$ and $(c_{22} + c_{33} - 2c_{23})$ are positive at lower temperature, and negative at high temperature, which does not satisfying the requirements for mechanical stability of monoclinic systems as discussed in section 3.10.3. The shear moduli $c_{33}c_{55} - c^2_{35}$ decrease linearly up to the highest calculated temperature and tend to converge around 1798 K. It is clear that the shear moduli $c_{44}c_{66} - c^2_{46}$ and $c_{22} + c_{33} - 2c_{23}$ decrease minimally and become negative below 1300 K which indicates the instability of structure at high temperature.
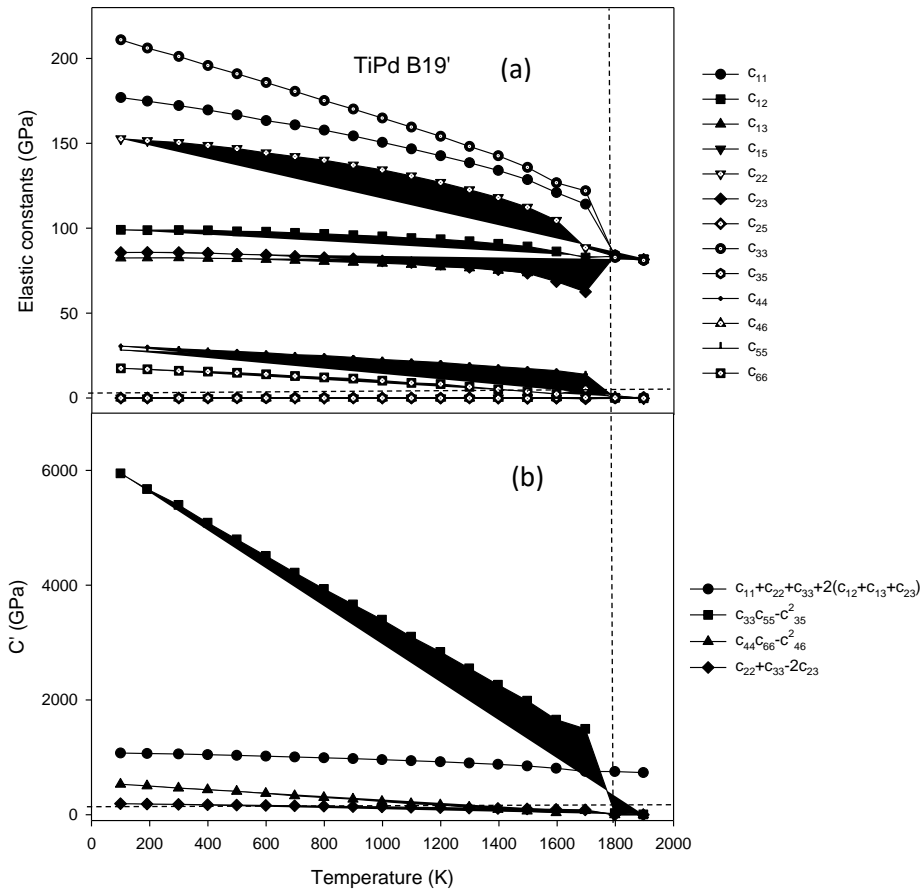
Figure 5-12 (a) elastic constants and (b) C' against temperature for B19'. The dotted lines are used as a guide to an eye with respect to stability criteria.

5.3.3 L1$_0$ Ti$_{50}$Pd$_{50}$

Figure 5-13 shows the effect of temperature on the elastic constants and shear moduli for tetragonal L1$_0$ phase from 100-1896 K. In the case of L1$_0$, the first group of elastic constants c_{11}, c_{12}, c_{13} and c_{33} decrease linearly whereas the second group, c_{44} and c_{66}, reduce slightly with an increase in temperature. However, all elastic constants tend to converge at the highest calculated temperature above 1798 K, which proposes melting temperature being reached. This behaviour, suggests that $c_{11}= c_{12} =c_{13}= c_{33}$ equals $c_{44}= c_{66}$ at that temperature, which could be an equivalent of $c_{11}= c_{12}$ in the cubic B2 austenite

phase. The shear moduli $(c_{11} + c_{22})$, $(c_{11} + c_{33} - 2c_{13})$ and $(2c_{11} + c_{33} + 2c_{12} + 4c_{13})$ have positive shear moduli throughout the temperature which shows the stability of $L1_0$. Furthermore, the results satisfying the requirements for mechanical stability of tetragonal alloys as discussed in section 3.10.3.
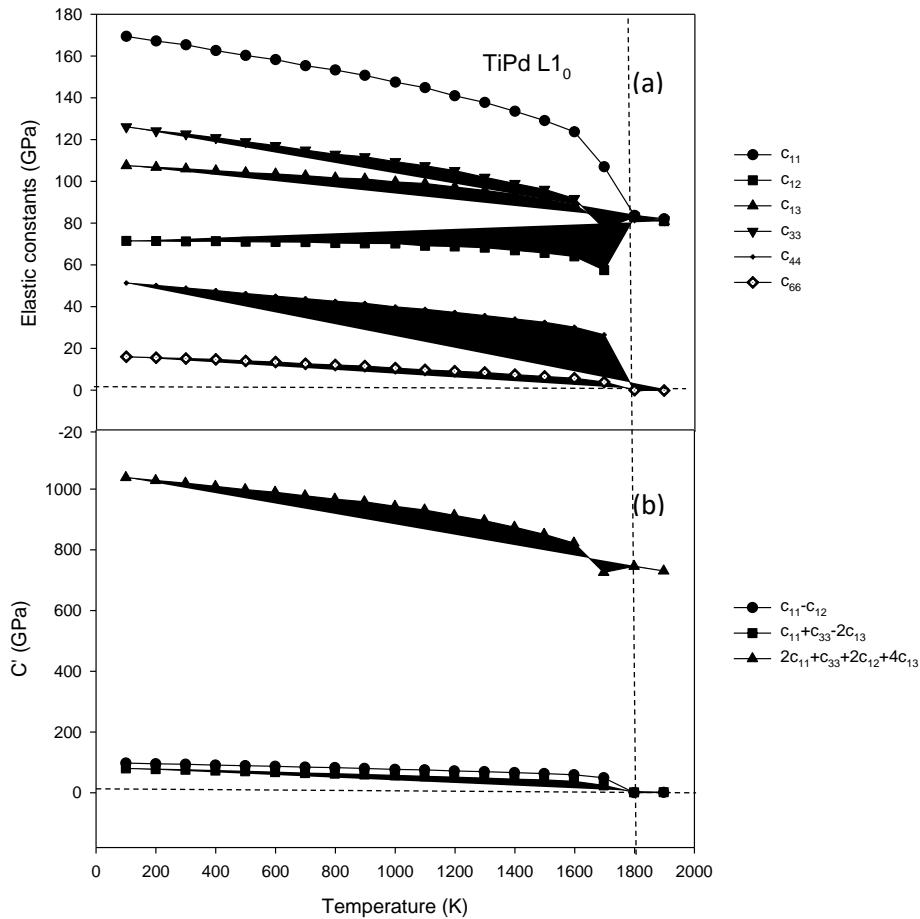
Figure 5-13 (a) elastic constants and (b) C' against temperature for $L1_0$. The dotted lines are used as a guide with respect to stability.

5.3.4 B19 $Ti_{50}Pd_{50}$

The elastic constants and shear moduli are calculated and shown in Figure 5-14 at different temperatures (100-1895 K) for the orthorhombic B19. The first group of elastic constants c_{11}, c_{22} and c_{33} decrease significantly and linearly with temperature and all tend to converge to a common value at 1696 K. Similarly, the

same trend was observed with the second group of elastic constants c_{12}, c_{13} and c_{23}. The last group of elastic moduli c_{44}, c_{55} and c_{66} decrease minimally with an increase in temperature below 1696 K. The c_{55} moduli become negative at temperature 1696 K which shows the instability of the structure at high temperature. Furthermore, three shear moduli (c_{11} + c_{22} -2c_{12}), (c_{11} + c_{33} -2c_{13}) and (c_{22} + c_{33} -2c_{23}) are positive at lower temperatures and reduce as the temperature is increased.

The shear moduli become smaller with the increase in temperature and converge to a common value at 1696 K which shows the instability of B19 at high temperatures. Furthermore, we note sudden collapse from the three shear moduli from 1598 -1696 K which is due to the melting temperature being reached at 1680 K. It can be suggested that from the elastic properties, the B19 structure tends to be mechanically unstable at a temperature higher than 1696 K as it undergoes melting temperature. Furthermore, the calculated elastic constants and moduli of the B19 phase satisfy conditions of the mechanical stability of the orthorhombic symmetry at low temperatures below 1696 K as stated in section 3.10.3. In an enlarged insert, the instability of B19 is clearly indicated.
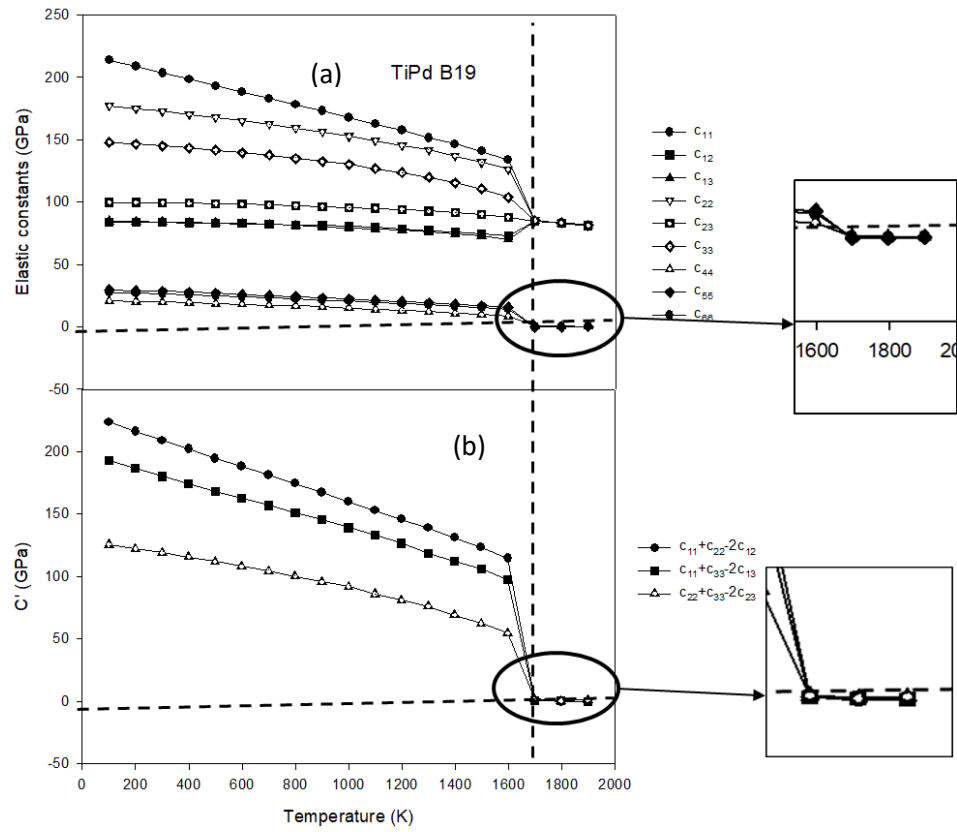
Figure 5-14 (a) elastic constants and (b) C' against temperature for B19. The dotted line is used to guide the eye with respect to stability.

Chapter 6

Structural, thermodynamic and electronic properties for B2 $Ti_{50}Pd_{50-x}M_x$

In this chapter, we present DFT results on the B2 $Ti_{50}Pd_{50-x}M_x$ alloys, where M represent the alloying elements i.e. Ru, Pt, Ir, Co, Ni, Al and Os. A supercell approach was used to generate their various compositions. These structures were constructed from B2 $Ti_{50}Pd_{50}$ using a 2x2x2 supercell with 16 atoms (as shown in Figure 6-1). The substitutional search tool embedded in VASP was used to substitute Pd with Ru, Pt, Ir, Co, Ni, Al, and Os atoms which provided the most stable compositions at the desired symmetry. There are five possible compositions that will be considered in these calculations namely; 6.25, 18.75, 25, 31.25, and 43.75 at. % M.

The calculations were performed using VASP code. The structures were subjected to full geometry optimization (by allowing both lattice parameter and volume to vary) in order to achieve ground state properties with precision. Structural and thermodynamic properties, such as equilibrium lattice parameters and heats of formation were investigated. Furthermore, the electronic properties in particular the total and partial density of states will also be analysed and discussed to show stability by monitoring the trend of the Fermi level with respect to the possible pseudogap [154].
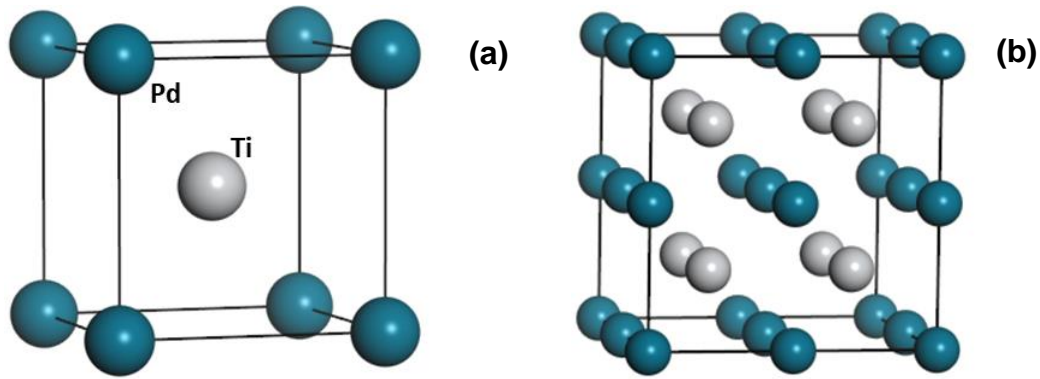
Figure 6-1 (a) The B2 Ti$_{50}$Pd$_{50}$ structure with 2 atoms per unit cell and (b) a 2X2X2 supercell with 16 atoms per unit cell structures.

6.1 Structural and thermodynamic properties of B2 Ti$_{50}$Pd$_{50-x}$M$_x$.

In Figure 6-2, the calculated equilibrium lattice parameters for the B2 Ti$_{50}$Pd$_{50-x}$M$_x$ (M=Ru, Pt, Ir, Co, Ni, Al, and Os) systems are shown. It is observed that the partial substitution of Pd with Ru reduces the lattice parameters of the Ti$_{50}$Pd$_{50-x}$Ru$_x$ minimally (Figure 6-2). The lattice parameters or volume decreases with the addition of Ru content and this may be attributed to the small atomic radius of Ru as compared to that of Pd.

Furthermore, the lattice parameters of the Ti$_{50}$Pd$_{50-x}$M$_x$ system decrease as the Ni, Ir, Co, and Os content is increased. This can be understood since the atomic radius of Pd is larger in size than Ni, Ir, Co, and Os. Recall that the lattice parameter of binary Ti$_{50}$Pd$_{50}$ was predicted to be 3.170 Å which is larger than those calculated for the Ti$_{50}$Pd$_{50-x}$M$_x$ systems. The lattice parameters of the Ti$_{50}$Pd$_{50-x}$Co$_x$ behave similarly to that of Ti$_{50}$Pd$_{50-x}$Ni$_x$ and this is due to their comparable atomic numbers and masses, both Co and Ni are transition elements on the same period.

The heats of formation for the B2 $Ti_{50}Pd_{50-x}M_x$ systems are shown in Figure 6-3. As discussed in chapter 4, the heats of formation are calculated to check the thermodynamic stability of the system. We observe that the ΔH_f decreases as Ru is increased this implies that the structure becomes stable at high Ru concentration (thermodynamically stable). Similar behaviour was observed for Ir, Pt, and Os as their values decrease with an increase in concentration indicating thermodynamic stability. Furthermore, the addition of Al, Ni and Co concentrations becomes less stable since the values of heats of formation increase as the content is increased. It is seen that Al, Ni and Co substitution show less stability, while the addition of Os, Ru, Ir and Pt enhances the stability of the $Ti_{50}Pd_{50}$ system at high concentration ($0 \le x \le 50$). More importantly, Ir addition is the most favourable (most stable) below 40 at. % Ir.
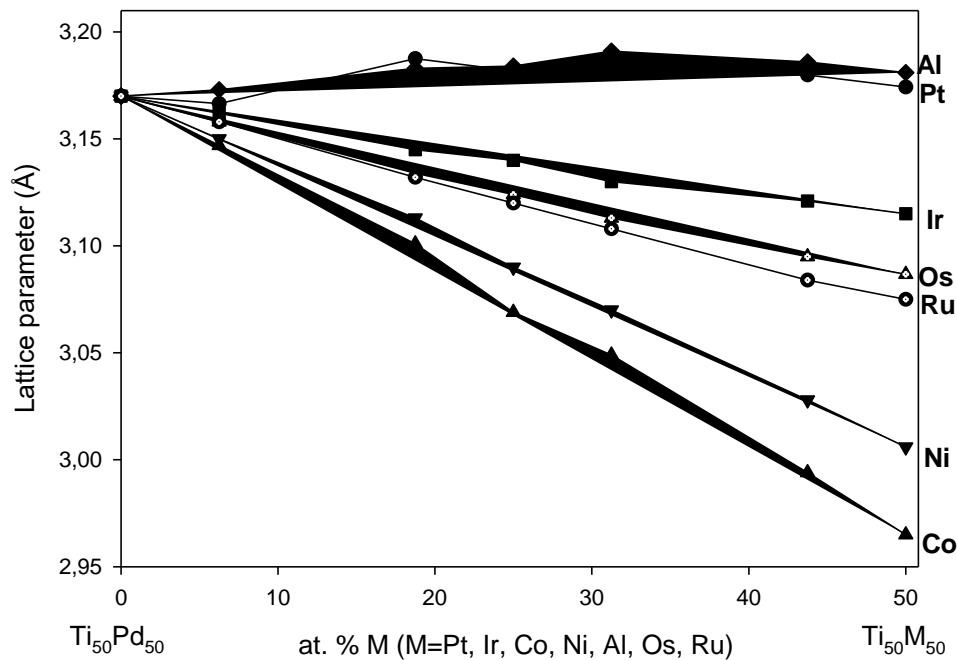
Figure 6-2 Equilibrium lattice parameter against atomic percent (at. % M) for $0 \le x \le 50$ composition range.
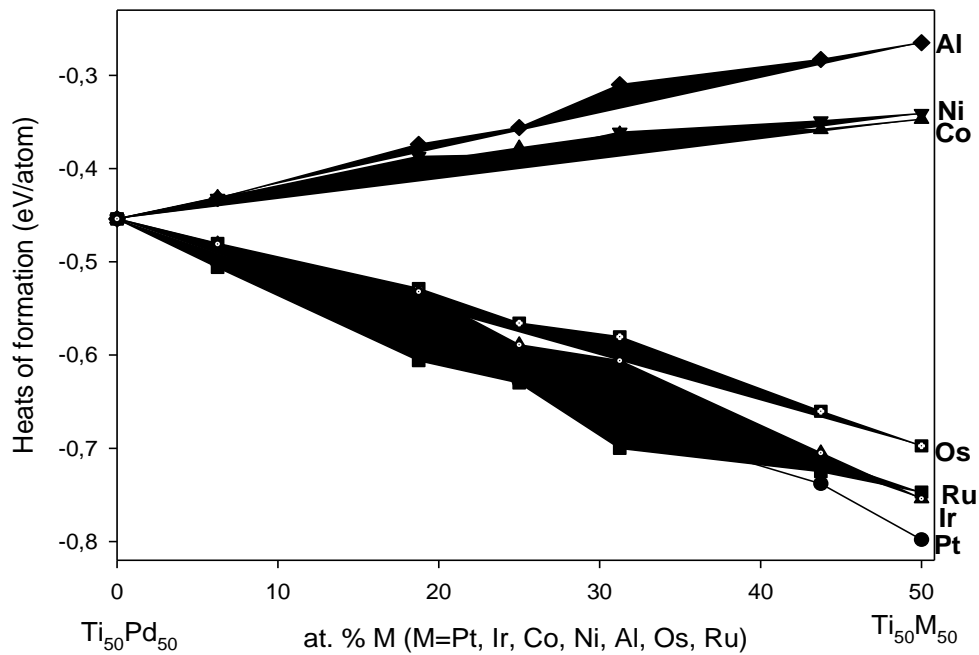
Figure 6-3 Heats of formation against atomic percent (at. % M) for 0 ≤ x ≤ 50 composition range.

6.2 The comparison of heats of formation between the B2 and B19 phases

Figure 6-4 shows the comparison of heats of formation between B2 and B19 $Ti_{50}Pd_{50-x}M_x$ (M= Ru, Pt, Ir, Co, Ni, Al, Os) alloys at 0 K. We see that as the amount of Pt is added to B2 $Ti_{50}Pd_{50}$ alloy, it is observed that the heats of formation decrease linearly. A similar trend is observed for the B19 phase. The results suggest that Pt enhances the thermodynamic stability of the B19 $Ti_{50}Pd_{50}$ more compared to the B19 phase as shown in Figure 6-4 (a). In Figure 6-4 (b), it is noted that the heats of formation decrease with an increase in Ir content for both B2 and B19 $Ti_{50}Pd_{50-x}Ir_x$ alloys (condition of stability). The heats of formation for the B2 phase were higher (less stable) than that of the B19 phase (more stable) which implies that Ir addition prefers the B19 phase at 0 K.

125

Furthermore, as the amount of Os is added to the system, the values of heats of formation decrease for both B2 and B19 phases. It is noted that at concentrations below 20 at. % Os the heats of formation for B2 is greater than that of the B19 phase as shown in Figure 6-4 (c). Interestingly, we observed that at 25 at. % Os the B19 is favourable than the B2 $Ti_{50}Pd_{50-x}Os_x$ system. Furthermore, it is observed that above 25 at. % Os the values of heats of formation are identical for both B2 and B19 $Ti_{50}Pd_{50-x}Os_x$ systems. This behaviour suggests that Os can be used to improve the thermodynamic stability of both B2 and B19 phases above 20 at. % Os. Similar behaviour was observed when Ru was added to the system as the values of heats of formation decreases with an increase in Ru content for both B2 and B19 systems (Figure 6-4 (d)). Thus the addition of Os and Ru enhances the stability of $Ti_{50}Pd_{50}$ for both the B2 and B19 in a more similar manner. This may be attributed to their similar atomic radius.

In contrast to the above, we see that the calculated heat of formation increases as the concentrations of Ni is increased. This suggests that the structures are becoming thermodynamically less stable which indicates weak chemical interactions between Pd and Ni. The results showed that heats of formation increase with an increase in Ni content implying the B2 and B19 $Ti_{50}Pd_{50}$ are less preferable compared to the B2 and B19 $Ti_{50}Ni_{50}$ alloys (Figure 6-4 (e)). To note that the addition of Ni has been shown to improve the thermodynamic stability of the B19 phase better compared to the B2 phase ($B19_{\Delta H_f} > B2_{\Delta H_f}$).

Similar behaviour was observed with Co, and Al additions as shown in Figure 6-4 (f) and Figure 6-4 (g), respectively. The findings suggest that Ni, Co and Al are not favourable for improving the thermodynamic stability of both B2 and B19

$Ti_{50}Pd_{50}$ alloys. Based on the comparison between B2 and B19 $Ti_{50}Pd_{50-x}M_x$, it can be concluded that the addition of Pt, Ir, Os, and Ru enhances the thermodynamic stability of both B2 and B19 phases while Ni, Co, and Al display less stability as the concentration is increased.
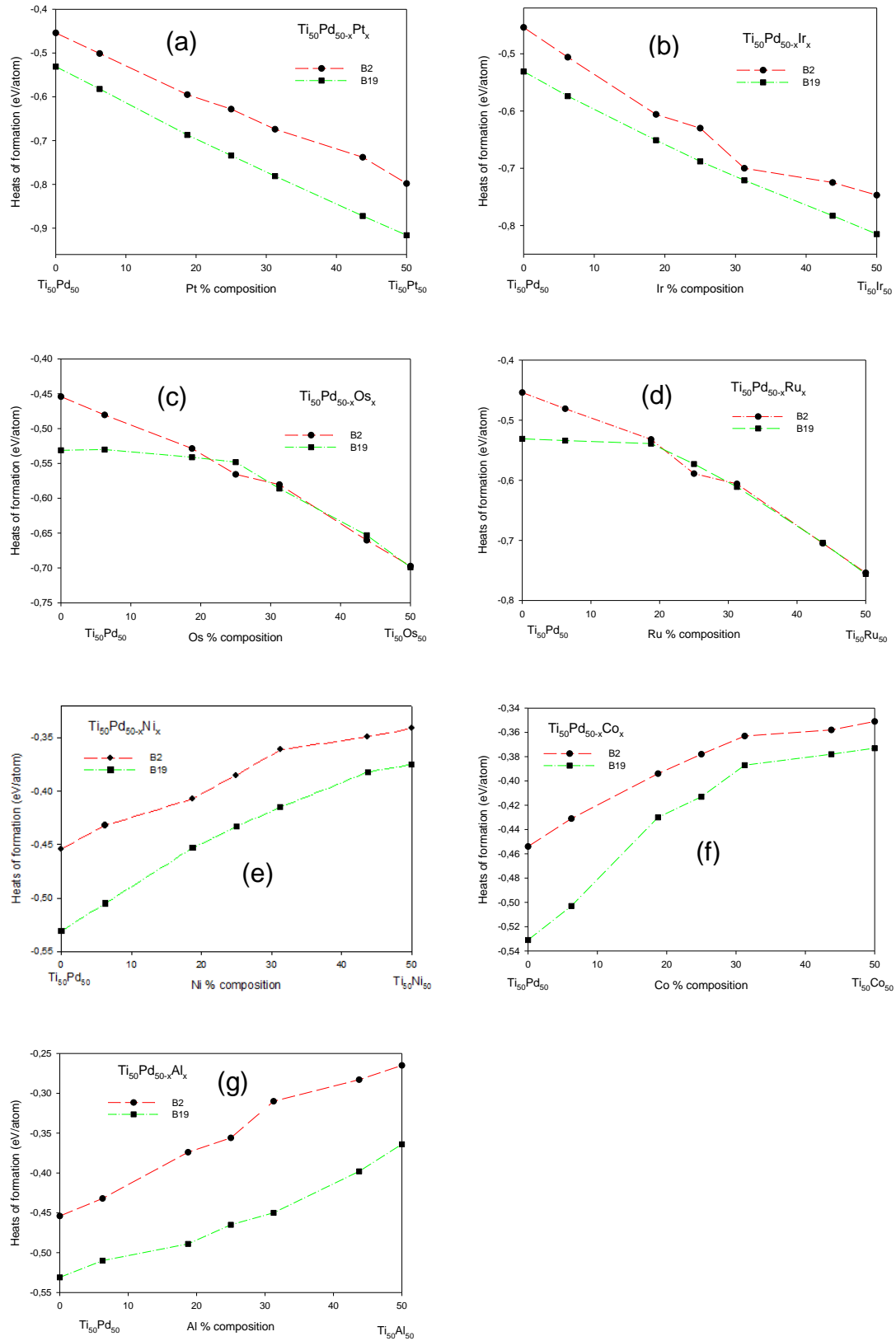
Figure 6-4 Trend of heats of formation against composition between B2 and B19 Ti$_{50}$Pd$_{50-x}$M$_x$ (M=Ru, Pt, Ir, Co, Ni, Al, and Os) ternary alloys (a) Pt, (b) Ir (c) Os (d) Ru (e) Ni (f) Co and (g) Al are substitute.

6.3 Total density of states (tDOS) of B2 $Ti_{50}Pd_{50-x}M_x$

Electronic structure calculations have been performed to investigate the stability of $Ti_{50}Pd_{50-x}M_x$ alloys by observing the trend of the total density of states (tDOS) near the Fermi level (E_f) with respect to the pseudogap. Similar approaches have been used to describe the electronic stability trend for structures of the same composition [26, 155, 156]. The structure with the highest and lowest density of state at E_f is considered the least and most stable, respectively. The DOS is expressed as the number of states per atom per energy interval.

6.3.1 B2 $Ti_{50}Pd_{50-x}M_x$ alloys: (M= Ru, Os)

The total DOS for $Ti_{50}Pd_{50-x}Ru_x$ is shown in Figure 6-5. We observe that the DOS shift towards the conduction band (CB) when Ru is added to the system. It is clearly seen that at 50 at. % Ru ($Ti_{50}Ru_{50}$) the Fermi level coincides with the pseudogap displaying the lowest states at E_f. This confirms the stability of the system in agreement with the predicted heats of formation (Figure 6-3). Contrary to the $Ti_{50}Ru_{50}$ structure, the Fermi level hits the top of the total DOS peak indicating instability of the $Ti_{50}Pd_{50}$ structure. As the composition of Ru is added, the pseudogap moves toward the Fermi level showing that the $Ti_{50}Pd_{50-x}Ru_x$ became electronically stable, in particular for composition above 20 at. % Ru. This observation suggests that $Ti_{50}Pd_{50-x}Ru_x$ is electronically stable at the high content of Ru. It is noted that there is a good agreement between the heats of formation (Figure 6-3) and the density of state stability trend. Figure 6-5 has been published in an accredited journal [35].

In Figure 6-5, we plot the total DOS for B2 $Ti_{50}Pd_{50-x}Os_x$ ($0 \leq x \leq 50$) alloys. As the composition of Os is added, the pseudogap moves towards the E_F which may imply that the system becomes electronically stable above 18.75 at. % Os. It is seen that at 50 at. % Os ($Ti_{50}Os_{50}$) the E_f coincides with the pseudogap. This is consistent with the fact that Os has fewer electrons compared to Pd. The stability trend according to the density of states agrees very well with the predicted heats of formation (ΔH_f) results, this Figure has been published [24].
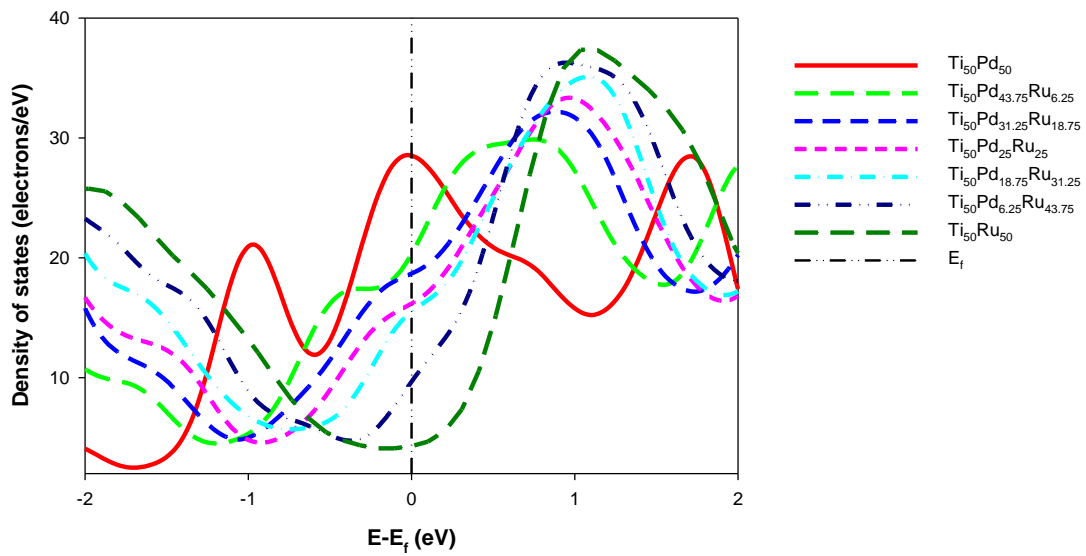
Figure 6-5 The total density of states of $Ti_{50}Pd_{50-x}Ru_x$ SMAs against energy ($0 \leq x \leq 50$). The Fermi level is taken as the energy zero ($E-E_f=0$) [35].
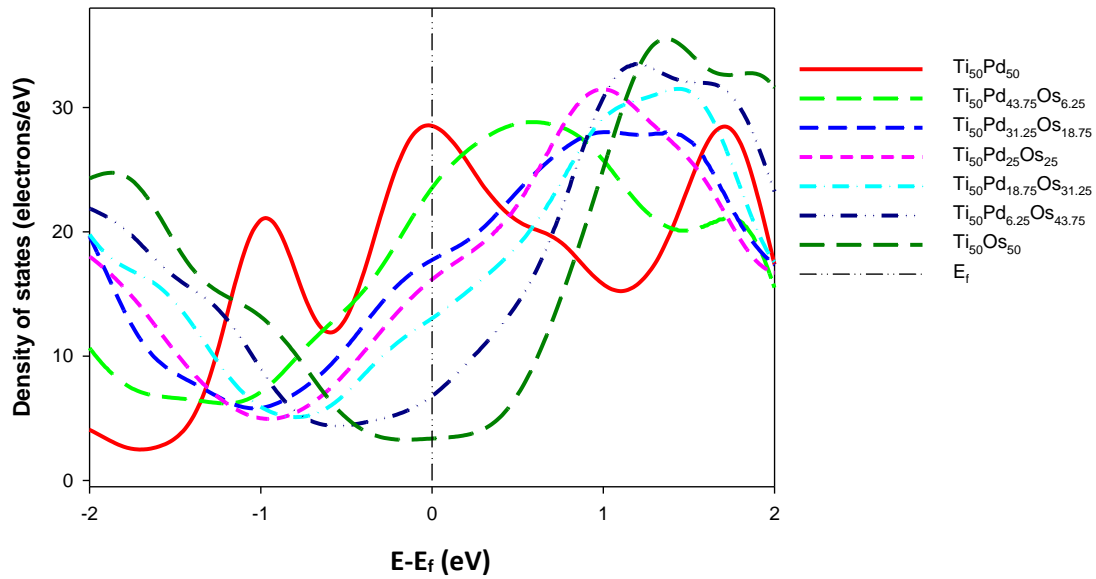
Figure 6-6 Comparison of the total density of state for Ti$_{50}$Pd$_{50-x}$Os$_x$ systems (0 ≤ x ≤ 50) against energy. The Fermi level is taken as the energy zero (E-E$_f$=0) [24].

6.3.2   B2 Ti$_{50}$Pd$_{50-x}$M$_x$ alloys: (M= Pt, Ir)

Figures 6-6 and 6-7 show the calculated total density of states at various compositions (0≤ x ≤ 50) for Ti$_{50}$Pd$_{50-x}$M$_x$ alloys. As the composition of Pt is added, the pseudogap moves towards the E$_f$ indicating that the electronic stability is enhanced. It is seen that Ti$_{50}$Pt$_{50}$ is more stable than other compositions since it has the lowest density of states near the E$_f$. Furthermore, Ti$_{50}$Pd$_{43.75}$Pt$_{6.25}$ has the highest density of states at E$_f$ as compared to the other structures which confirm the least stable. The predicted density of states analysis is consistent with the stability trend as predicted by the ΔH$_f$.

As Ir content is added, the DOS for Ti$_{50}$Pd$_{43.75}$Ir$_{6.25}$ hits the peak at the shoulder near the E$_f$ as shown in Figure 6-7. Furthermore, at 18.75 at. % Ir, the pseudogap moves toward the E$_f$ with the lower energy which may suggest that the system starts to stabilize. Similar behaviour was observed with other compositions such

as $Ti_{50}Pd_{25}Ir_{25}$, $Ti_{50}Pd_{18.75}Ir_{31.25}$, and $Ti_{50}Pd_{6.25}Ir_{43.75}$. It is noted that $Ti_{50}Ir_{50}$ has the lowest DOS at the E_f which suggests that it is the most stable while the $Ti_{50}Pd_{43.75}Ir_{6.25}$ is the least stable compared to other compositions. The result suggests that $Ti_{50}Pd_{50-x}M_x$ is electronically stable at higher content of Pt and Ir, consistent with the predicted ΔH_f.
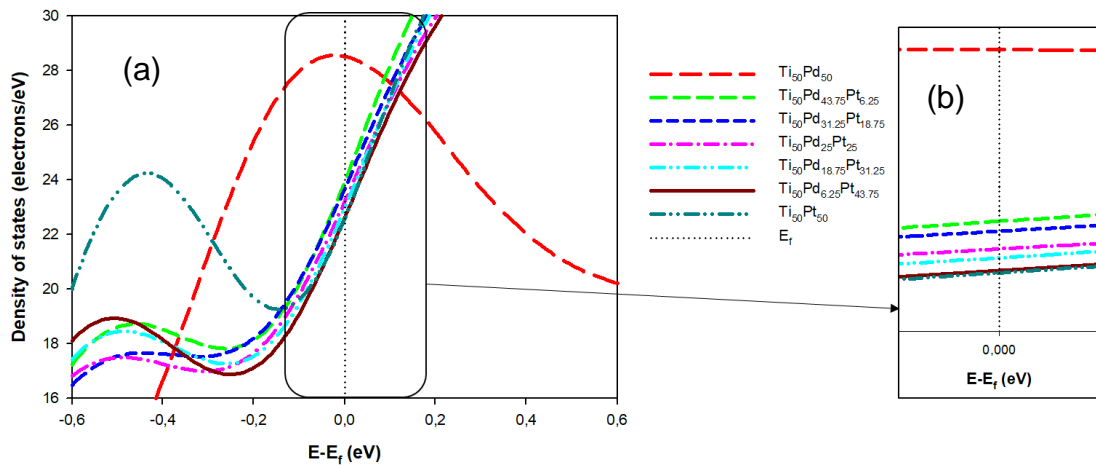
Figure 6-7 (a) Comparison of the total density of state for $Ti_{50}Pd_{50-x}Pt_x$ systems against energy and (b) is the enlargement of the DOS near the Fermi energies. The Fermi level is taken as the energy zero ($E-E_f=0$).
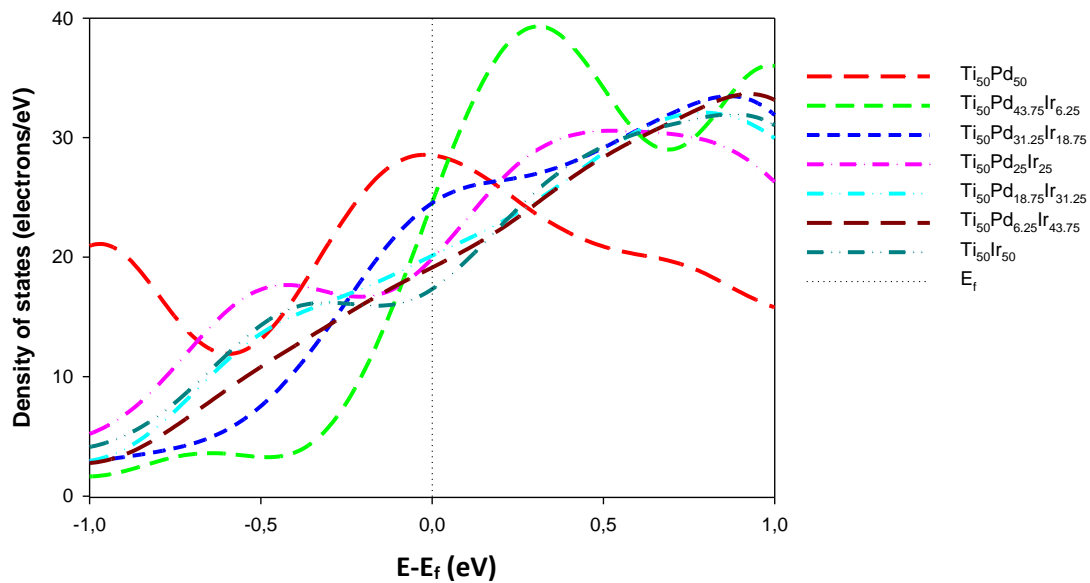
Figure 6-8 Comparison of the total density of state for $Ti_{50}Pd_{50-x}Ir_x$ systems against energy. The Fermi level is taken as the energy zero (E-E$_f$=0).

6.3.3 B2 $Ti_{50}Pd_{50-x}M_x$ alloys: (M= Ni, Co, Al)

The total density of states for $Ti_{50}Pd_{50-x}Ni_x$ ($0 \geq x \geq 50$) alloys are compared in Figure 6-9. The E$_f$ hits the top of the total DOS peak which suggests the instability at 6.25 at. % Ni. Similar behaviour was observed at 18.75 at. % Ni. Moreover, the $Ti_{50}Pd_{43.75}Ni_{6.25}$ was found to have the lowest DOS peak at E$_f$ compared to $Ti_{50}Pd_{31.25}Ni_{18.75}$. This behaviour suggests that the system is electronically unstable with the addition of Ni for all at. % compositions. The electronic stability trend is confirmed by the results of the ΔH_f discussed above (Figure 6-2).

Figure 6-10 show and compare the calculated tDOS for $Ti_{50}Pd_{50-x}Co_x$ alloys. It is noted that as the Co content is increased the DOS hit the shoulder of the peak at E$_f$. The highest DOS along the E$_f$ is observed at the high composition of Co (50 at %) while 6.25 at. % Co has the lowest DOS peak. This observation indicates

that Co is not preferable to enhancing the electronic stability of $Ti_{50}Pd_{50}$ in good agreement with the predicted ΔH_f. A similar trend is observed for Al additions as shown in Figure 6-11. This suggests that $Ti_{50}Pd_{50-x}Al_x$ is electronically unstable at the higher content of Al. The stability trend agrees very well with the predicted heats of formation (Figure 6-2).
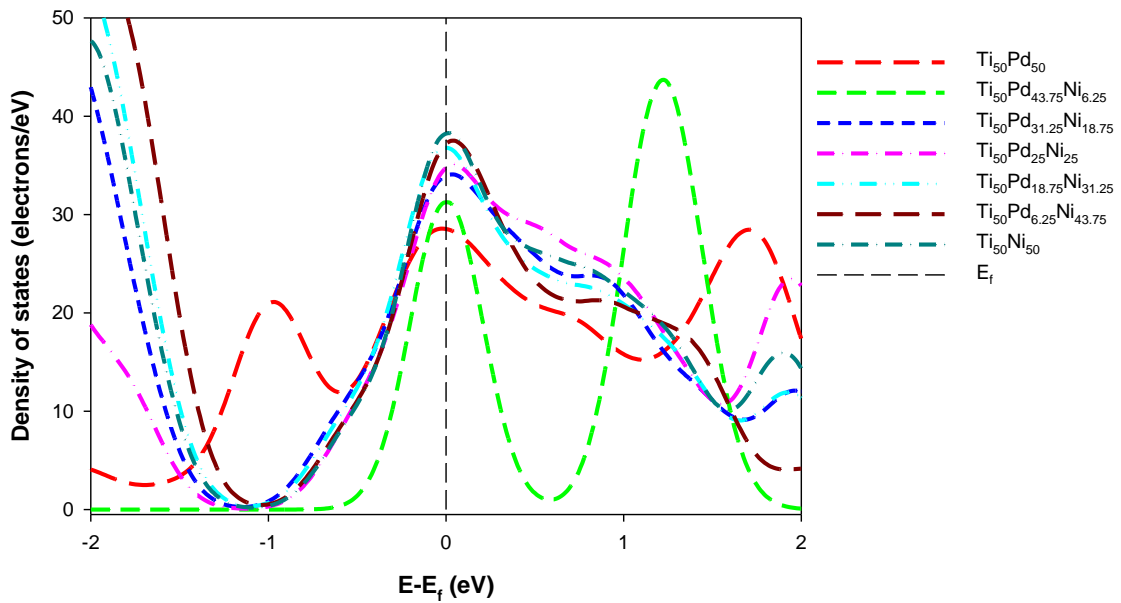
Figure 6-9 Comparison of the total density of state against energy for $Ti_{50}Pd_{50-x}Ni_x$ systems ($0 \leq x \leq 50$). The Fermi level is taken as the energy zero ($E-E_f=0$).
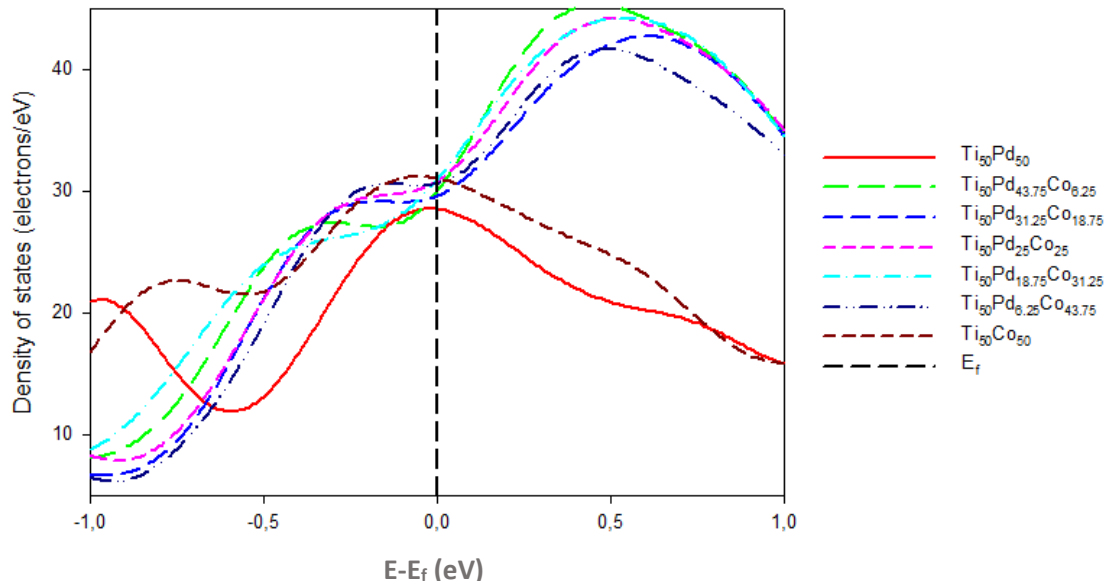
Figure 6-10 Comparison of the total density of state against energy for Ti$_{50}$Pd$_{50-x}$Co$_x$ systems (0 ≤ x ≤ 50). The Fermi level is taken as the energy zero (E-E$_f$=0).
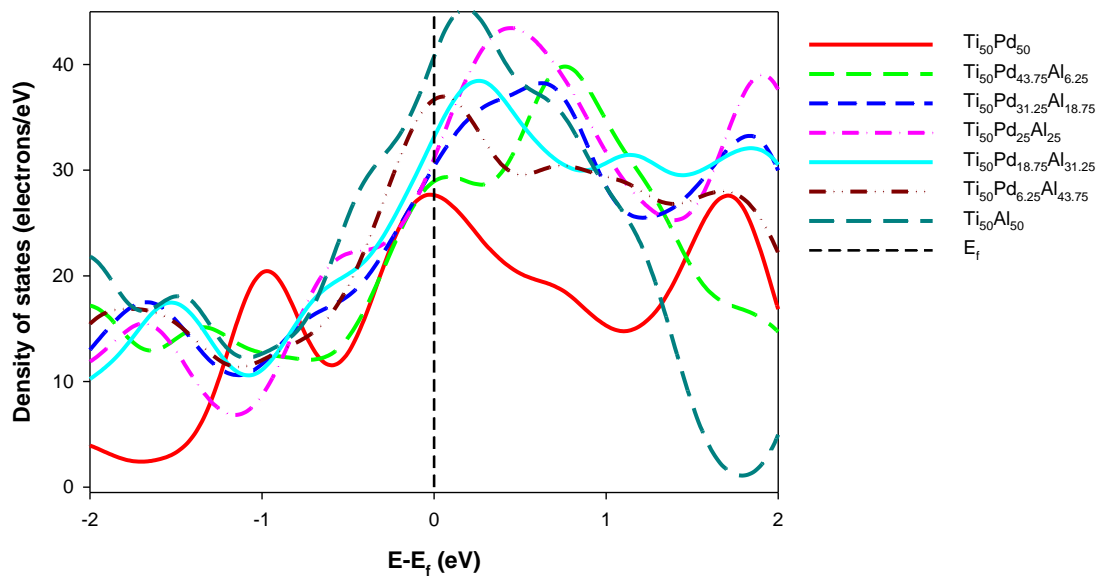
Figure 6-11 Comparison of the total density of state against energy for Ti$_{50}$Pd$_{50-x}$Al$_x$ systems (0 ≤ x ≤ 50). The Fermi level is taken as the energy zero (E-E$_f$=0).

Chapter 7

Mechanical properties for B2 Ti$_{50}$Pd$_{50-x}$M$_x$

In this chapter, we discuss the mechanical properties in particular the elastic constants, elastic moduli, ductile/brittle behaviour and elastic anisotropy of Ti$_{50}$Pd$_{50-x}$M$_x$ (M=Ru, Pt, Ir, Co, Ni, Al, and Os). Similar to the previous chapter, we used the supercell approach to explore their stability. The elastic properties were performed using the VASP code as discussed in detail in chapter 3. The elastic properties were calculated to check the elasticity and strength of the alloys.

The study of elasticity such as elastic constants, elastic moduli, ductile/brittle behaviour and elastic anisotropy is of critical importance in various industries such as medical and aerospace amongst others. So, the elastic properties are determined to check the elasticity as well as the strength of the material systems. The elastic stiffness constants are obtained from the linear finite strain–stress method within the VASP code [38]. The predicted independent elastic stiffness constants (C$_{ij}$) of the Ti$_{50}$Pd$_{50-X}$M$_X$ (M= Ru, Os, Co, Ni, Ir, Pt, and Al) alloys are shown in Figures 7-1 to 7-5.

7.1 Elastic constants of Ti$_{50}$Pd$_{50-x}$M$_x$

The elastic constants (C$_{ij}$) contain some of the more important information that can be obtained from ground-state total-energy calculations. In order for a

structure to exist in a stable phase, the elastic constants must obey certain relationships. The stability conditions for the cubic system is outlined in section 3.10.3.

7.1.1 $Ti_{50}Pd_{50-x}Ru_x$

In Figure 7-1, the calculated elastic constants of the $Ti_{50}Pd_{50-x}Ru_x$ alloys ($0 \leq x \leq 50$) are shown. Recall that in order for the structure to be stable, it must satisfy certain stability criteria as discussed in chapter 4. The positive C' ($(1/2(c_{11}-c_{12})>0)$) indicates the mechanical stability of the crystal, otherwise, it is unstable. As indicated in chapter 4, the binary B2 $Ti_{50}Pd_{50}$ alloy is mechanically unstable at 0 K due to negative elastic shear modulus ($C'= -5.37$ GPa). So, the addition of a third element has been suggested in order to stabilise the B2 $Ti_{50}Pd_{50}$ alloy. In this case, the addition of Ru shows that the elastic constants c_{11}, c_{12} and c_{44} are positive for the entire concentration range ($0 \leq x \leq 50$) (Figure 7-1). The c_{11} and c_{44} increase with the addition of Ru content while c_{12} decreases suggesting that the structure is becoming mechanically stable (satisfying the stability condition, $c_{11}>c_{12}$).

However, at small Ru content (6.25 and 18.75 at. % Ru), the C' is negative which renders the structures elastically unstable at these concentrations. Furthermore, the calculated C' value gives rise to negative anisotropy, thus indicating the instability of the B2 $Ti_{50}Pd_{50-x}Ru_x$ for 6.25 and 18.75 at. % Ru which is contributed by c_{11} being less than c_{12}. It is clearly seen that above 20 at. % Ru, the C' is enhanced leading to a mechanical stable system. As such Ru addition may decrease the martensitic transformation temperature of the B2 $Ti_{50}Pd_{50}$ alloy due

to an increase in C' above 20 at. % Ru. The coupling of c_{11} and c_{12} is found when x >20 at. % Ru corresponding to the observed stability trend. The coupling of c_{44} and C' can also be seen when x >37 at. % Ru, and a possible phase transformation occur as shown in Figure 7-1. This observation has also been discussed in the previous study [77] and Figure 7-1 has been published [35].
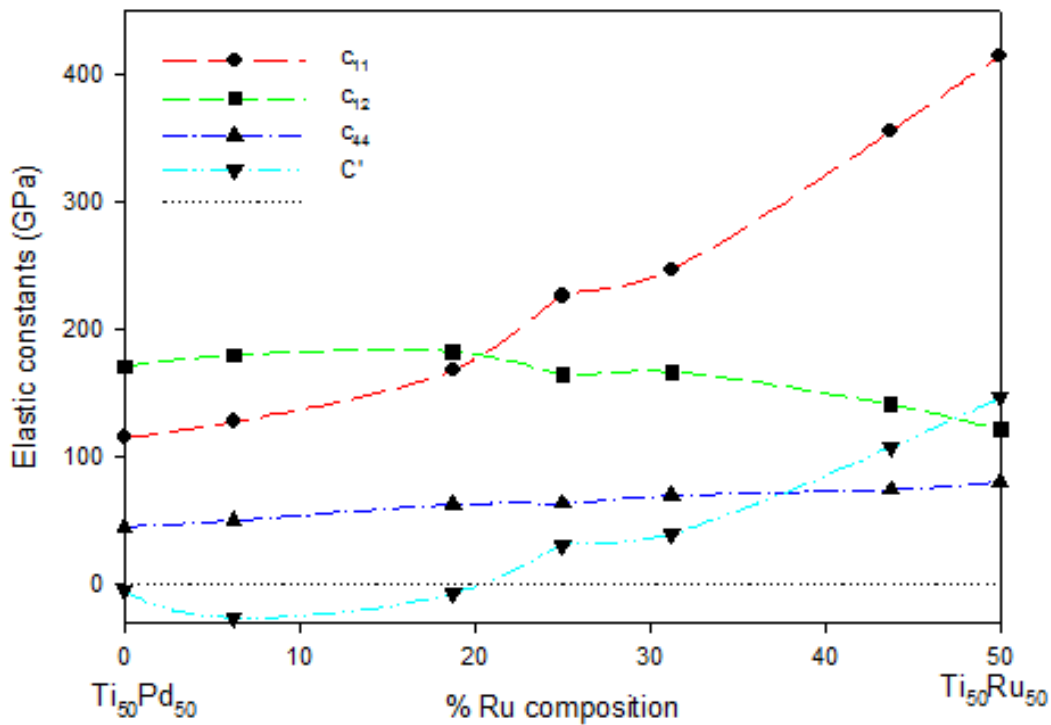
Figure 7-1 The elastic constants (GPa) as a function of the atomic % Ru composition of $Ti_{50}Pd_{50-x}Ru_x$ SMAs.

7.1.2 $Ti_{50}Pd_{50-x}Os_x$

The calculated elastic properties of the $Ti_{50}Pd_{50-x}Os_x$ alloys ($0 \leq x \leq 50$) is shown in Figure 7-2. It is noted that all the independent elastic constants c_{11}, c_{12} and c_{44} are positive in the entire range of $Ti_{50}Pd_{50-x}Os_x$ alloys ($0 \leq x \leq 50$). At small Os content (below 6.25 at. % Os), the C' is negative suggesting that the structure is elastically unstable at this concentration. Interestingly, the elastic shear modulus

(C') is positive above 18.75 at. % Os which indicates the structures are mechanically stable at high Os content. Note that Figure 7-2 has been published [24].
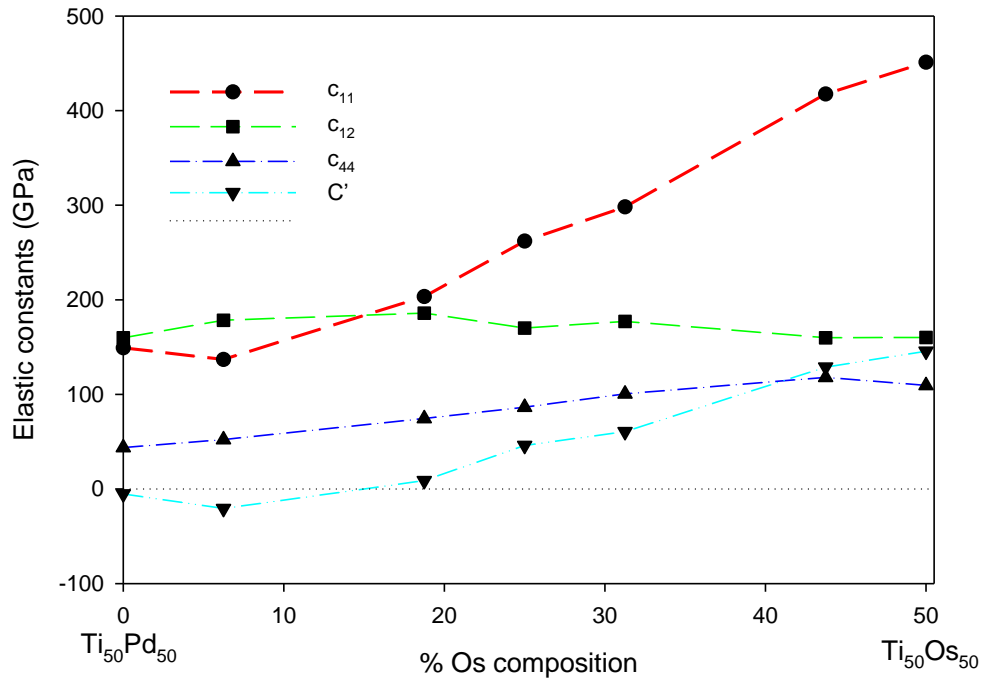
Figure 7-2 The elastic constants (GPa) as a function of the atomic % Os composition of Ti$_{50}$Pd$_{50-x}$Os$_x$ SMAs.

Figure 7-3 shows the comparison of the elastic constant c_{11} and c_{12} for Ti$_{50}$Pd$_{50-x}$M$_x$ (M= Ru, Os) alloys against concentrations. Below 20 at. % Ru, it is noted that $c_{11}<c_{12}$ suggests elastic instability. In the case of Os, it is found that $c_{11}<c_{12}$ below 18 at. % which indicates instability. Interestingly, it is noted that Os stabilise faster as compared to Ru since $c_{11}>c_{12}$ above 18.75 at. % which resulted in positive C'.
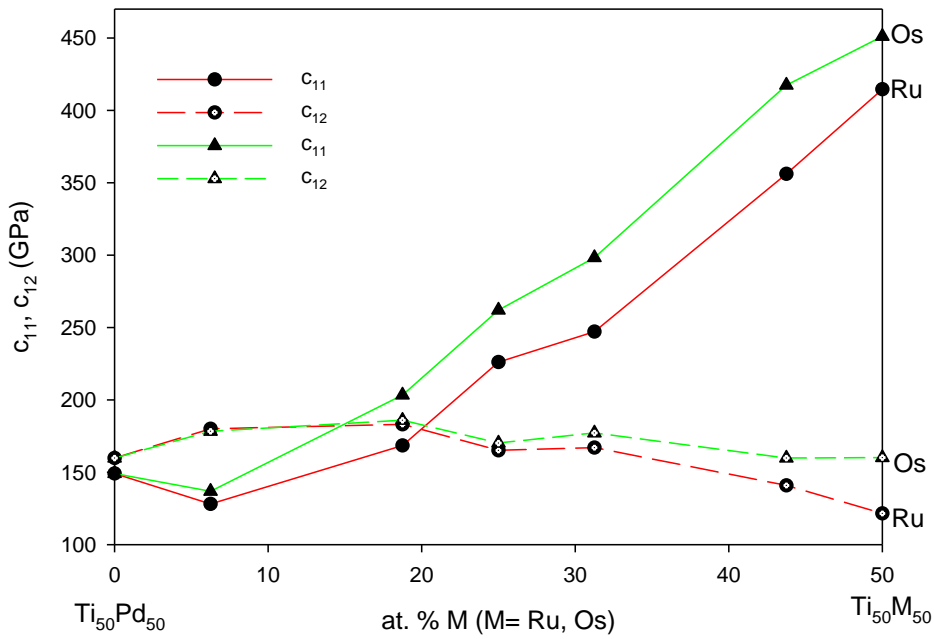
Figure 7-3 The elastic constants (c_{11} and c_{12}) against the composition of Ti$_{50}$Pd$_{50-x}$M$_x$ alloys.

7.1.3 Ti$_{50}$Pd$_{50-x}$M$_x$ (M= Ni, Co)

Figure 7-4 (a) shows the comparison of elastic constant c_{11} and the c_{12} for the Ti$_{50}$Pd$_{50-x}$M$_x$ (M= Co, Ni) at different concentrations. From the results, it is noted that the c_{11} is less than c_{12} below 25 at. % Co which suggests instability at those compositions. Furthermore, it was also found that the $c_{11}<c_{12}$ below 31.25 at. % Ni which implies that the system is unstable. This is confirmed in Figure 7-4 (b). It is clearly seen that the C' curve is below zero ($C'< 0$) at lower concentrations. However, the elastic constants satisfy the stability criterion above 43.75 at. % Ni and 31.25 at. % Co indicating elastic stability (since $C' > 0$) of Ti$_{50}$Pd$_{50-x}$M$_x$ alloys.
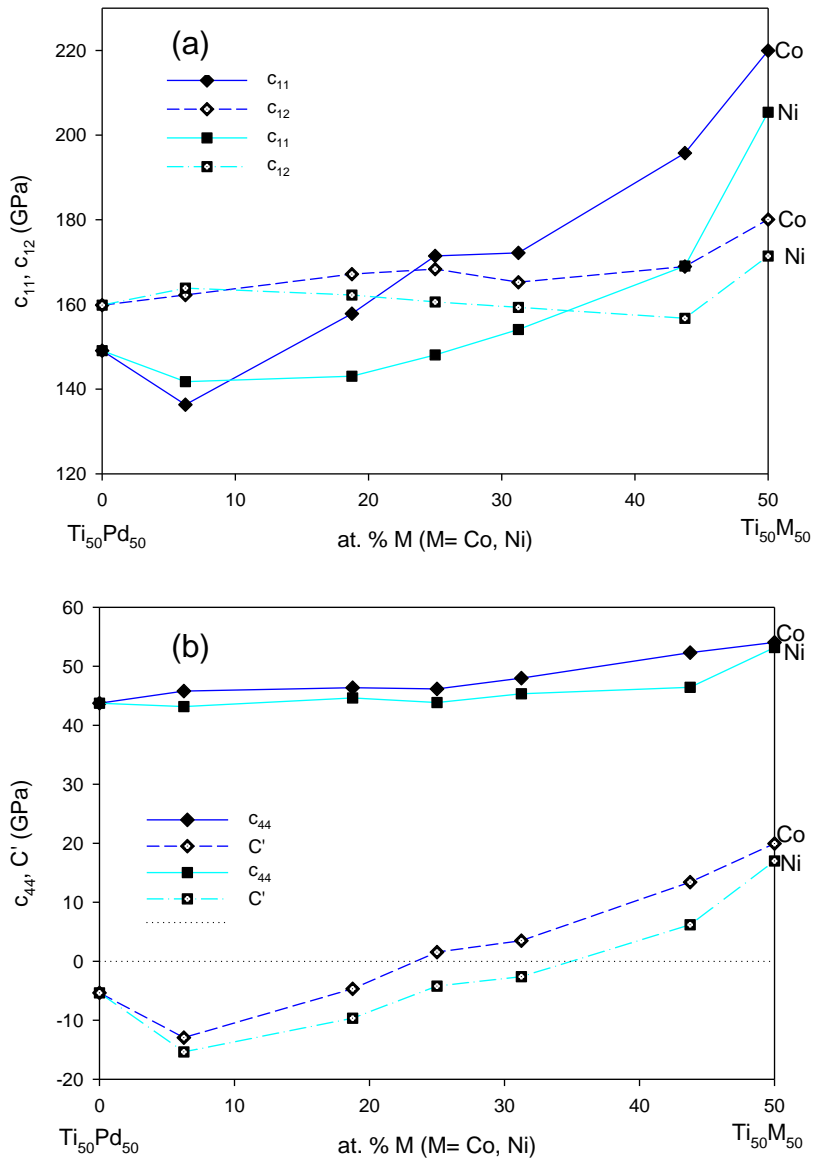
Figure 7-4 (a) the elastic constant and (b) elastic shear modulus against the composition of B2 $Ti_{50}Pd_{50-x}M_X$ (Co, Ni) alloys.

7.1.4 $Ti_{50}Pd_{50-x}M_x$ (M= Ir, Al, Pt)

In Figure 7-5 (a), all the predicted C_{ij} does not satisfy the stability criteria for $Ti_{50}Pd_{50-x}Al_x$ since c_{11} is less than c_{12} which resulted in negative elastic shear modulus ($C' < 0$). Similar behaviour was noted for Ir and Pt addition as the C' decrease with an increase in the concentration ($C' < 0$) for the entire concentration

141

range (Figure 7-5 (b)). Clearly, the C_{ij} for ternary addition is less than those for the binary $Ti_{50}Pd_{50}$ structure, which indicates that the doping element (Al, Ir, and Pt) have no potential to improve the C_{ij} of pure structure.
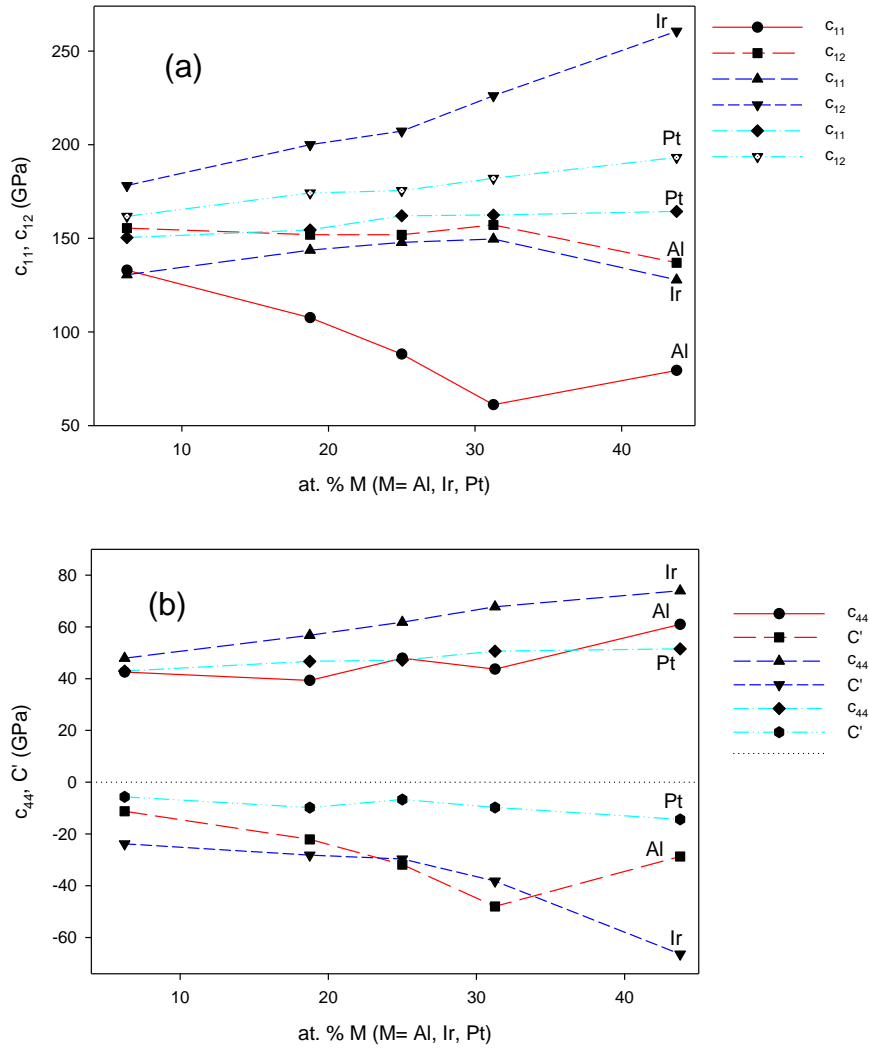
Figure 7-5 (a) the elastic constant and (b) elastic shear modulus as a function of compositions for B2 $Ti_{50}Pd_{50-x}M_x$ (M=Al, Ir, Pt) alloys.

7.2   Anisotropy ratio: $Ti_{50}Pd_{50-x}M_x$ (M= Ru, Os, Co, Ni)

This section focuses on the anisotropy ratio to describe isotropic behaviour and transformation of the $Ti_{50}Pd_{50-x}M_x$ systems. Note that the anisotropic ratio for Pt, Ir and Al are not shown because their $c_{11} < c_{12}$ resulted in a negative anisotropy value for the entire concentration range.

7.2.1   Isotropic and anisotropy behaviour

It is important to study the elastic anisotropy of the systems in order to understand material properties and improve their mechanical durability. The anisotropy can be calculated as:

$$A = \frac{c_{44}}{c'} \tag{7-1}$$

For an isotropic crystal, the factor (A) must be 1, while any value small or large than unity is a measure of the degree of elastic anisotropy.

The anisotropic plot depicts anisotropic behaviour below 25 at. % for Ru, Os, Co and Ni additions. However, A approaches unity ($A \approx 1$) for both Ru and Os between 25 and 50 at. % composition. These alloy systems have isotropic behaviour at this composition range. The Co and Ni additions are highly anisotropic in the entire composition ranges (Figure 7-6).
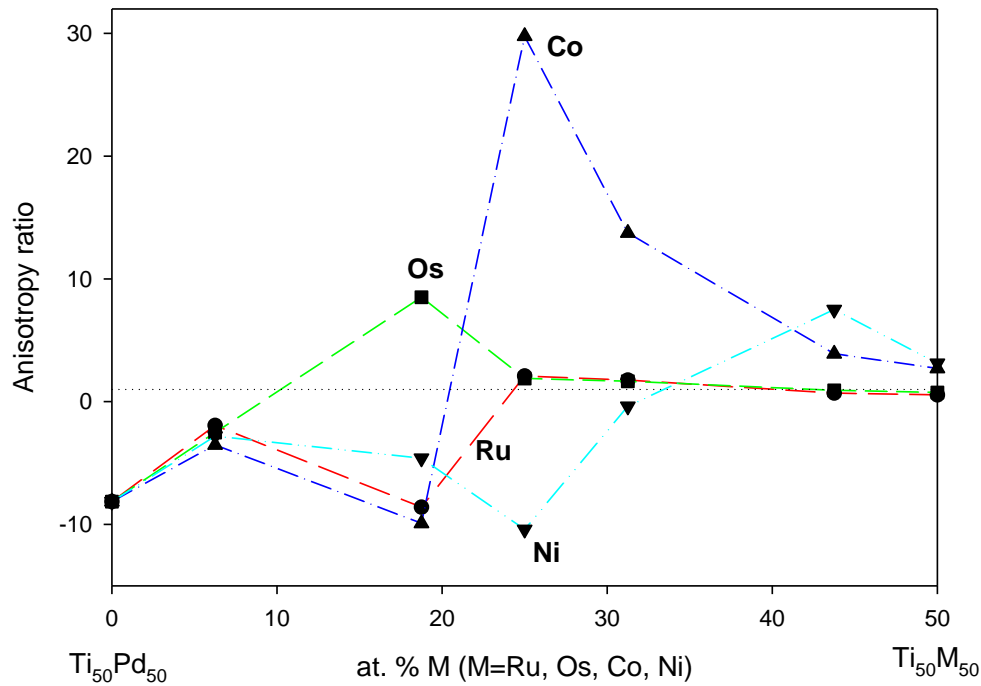
Figure 7-6 Predicted Anisotropy ratio against the composition of B2 Ti$_{50}$Pd$_{50-x}$M$_X$.

7.2.2 Anisotropy and martensite transformation

Previously, Yi et al. [157] indicated that the c$_{44}$ and C' can be used to predict the change of martensitic transformation (Ms) at the Zener anisotropy factor A<10. This factor measures the degree of anisotropy in solid and is calculated using equation (7-1). In a cubic crystal, C' is used to measure the basal-plane shear along the direction of {110} <1-10> while the c$_{44}$ is along direction {001} <100> shear (non-basal plane shear) which is equal to {001} <1-10> shear. Hence, the c$_{44}$ is playing an important role in controlling the transformation temperature of B2 to B19′ [158]. Recall that the formation of the B19′ phase is attributed to the coupling between c$_{44}$ and C' as proposed by Ren et al. [158]. Interestingly, as the Os is added the C' decreases and becomes negative below 6 at. % and positive

above which suggest stability (Figure 7-7). The results suggest that the transformation temperature increases below 6 at. % due to negative elastic shear modulus (C') and decreases above (since $C' > 0$). It is noted that the entire Zener anisotropy factors are less than 10 for Os and Ru at. % composition which indicates a possibility and reliability of prediction of Ms (see Figure 7-6). Furthermore, it was observed that the Zener anisotropy ratio is less than 10 for the addition of 6.25, 18.75, 43.75 and 50 at. % Co (except 25 and 31.25 at. % Co) as shown in Figure 7-8.
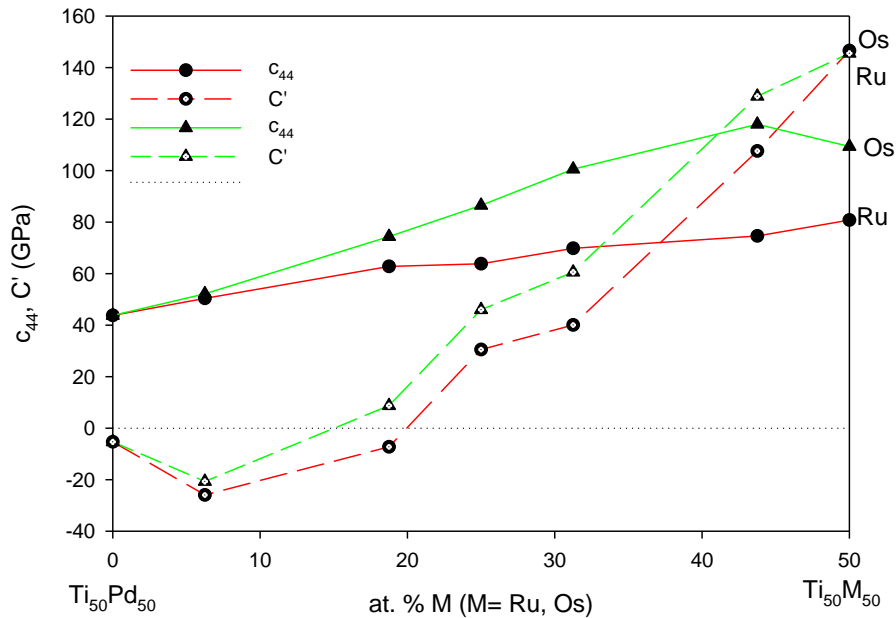
Figure 7-7 The elastic constants c_{44} and C' against the composition of Ti$_{50}$Pd$_{50-x}$M$_x$ alloys.
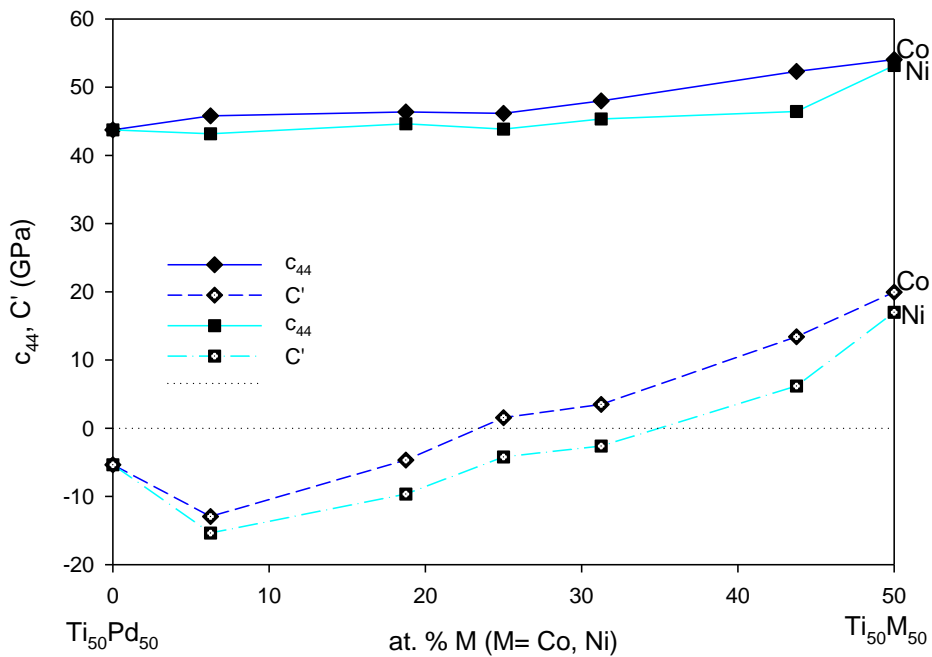
Figure 7-8 The elastic constants c_{44} and C′ against the composition of Ti$_{50}$Pd$_{50-x}$M$_x$ alloys

7.2.3 Martensite transformation

An anisotropy ratio (A) is also important for determining the martensitic transformation of the material. A higher value of A indicates martensitic transformation from B2 to B19 while a smaller A implies a good correlation between c_{44} and C' which leads to the transformation from B2 to B19′ [158].

Ru addition

In Figure 7-6, a higher value of A is observed at 25 at. % Ru which suggests transformation from B2 to the B19 martensite phase. There is a coupling of c_{44} and C' at high concentration above 37 at. % Ru which may suggest possible phase transformation from B19 to the B19′ martensite phase. Thus, their addition

results in a reversible martensitic transformation that is from B2 to B19, and B19 to B2.

Os addition

In the case of Os addition, A is higher for 18.75 at. % Os, which may suggest the transformation from B2 to B19 (Figure 7-6). There is a strong coupling observed between the c_{44} and C' at 43.75 at. % Os which leads to the transformation from B19 to B19′ (since A is small). It can be concluded that $Ti_{50}Pd_{50-x}Os_x$ alloys transform from B2 to B19 (18.75 at. % Os) and then B19 transform into B19′ (43.75 at. % Os) due to a coupling of the c_{44} and C' at 0 K. This is a similar observation with TiNi and TiNi-based alloys [158].

Co and Ni addition

In the case of Co addition, it was observed that A is negative below 18.75 at. % Co indicating that the martensite transformation is suppressed and the B2 phase is preserved (Figure 7-6). As the composition of Co is increased to 31.25 at. %, A is higher than other compositions showing the transformation from B2 to B19. It can be deduced that B2 $Ti_{50}Pd_{50-x}Co_x$ alloys transform to B19 phase above 31 at. % Co.

It is also noted that A is negative below 31.25 at. % Ni indicating that there is no transformation observed in those compositions. Interestingly, it is seen that A is higher for $Ti_{50}Pd_{6.25}Ni_{43.75}$ which suggests transformation from parent B2 to martensite B19.

7.2.4 Anisotropy and ductility

The calculated A can also be used to check the ductility in metals. Thus for a material to be considered ductile, the anisotropy ratio should be greater than 0.8 otherwise brittle [159]. The anisotropy values were found to be greater than 0.8 for 25 and 31.75 at. % Ru (Figure 7-6). The results imply that the alloy becomes ductile at this composition's ranges and brittle elsewhere. It was also found that the anisotropy ratio is greater than 0.8 above 18.75 at. % Os which reveals ductile behaviour. Furthermore, the Co and Ni additions are favourable above 25 at. % and 43.75 at. %, respectively (condition of ductility).

7.3 Modulus: Bulk, Shear, and Young

In order to determine the strength, compressibility, and stiffness of the $Ti_{50}Pd_{50-x}M_x$, we calculated the various moduli. The predicted Bulk, Shear, Young´s modulus, Pugh and Poisson ratios are shown in Figure 7-9.

7.3.1 Bulk modulus

Generally, the Bulk modulus (B) is a measure of the hardness or strength in materials. A high B value is associated with high strength otherwise less hardness. We note that the bulk modulus increase with an increase in Os, Ir and Ru concentrations which suggests that the hardness is enhanced. It appears that the Os addition gave the highest B followed by Ir and Ru, while the addition of Pt, Co and Ni showed a minimal increase in B. It can also be noted that there is a close comparison between Ir and Ru, particularly at about 25 at. %. On the

contrary, the calculated Bulk modulus decreases with an increase in Al content, indicating that the resistance to volume change by applied pressure is eventually lowered. Thus, Al addition gave the lowest Bulk modulus compare to other alloying elements. The predicted trend of hardness is Os< Ir< Ru< Pt < Co < Ni< Al.

7.3.2 Shear modulus

The Shear modulus (G) plays an important role in checking the compressibility of the material. It provides a measure or ability to resists shape change caused by shear stress. A lower value of Shear modulus demonstrates lower shear resistance and weaker covalent bond while a higher value possesses larger shear resistance corresponding to more notable directional bonds between atoms.

It is clearly seen that the shear modulus increase with an increase in Os and Ru content above 6.25 at. % which indicates higher shear resistance of the material at these compositions as shown in Figure 7-9 (b). In the case of Co and Ni, the shear modulus increase with an increase in composition above 18.75 at. %, suggesting an increase in the ability to resists shape change. This behaviour demonstrates that there are more notable directional bonds between neighbouring atoms. Similar behaviour has been observed previously [160]. Furthermore, at low concentration (6.25 at. %) the addition of Al and Pt resulted in the reduced shear modulus (Figure 7-9 (b)). Moreover, it is observed that as the concentration of Ir is increased above 31.25 at. % Ir, the G is enhanced. Similar analyses have been found by Wu et al. [160].

7.3.3 Young's modulus

Young's modulus (E) of the $Ti_{50}Pd_{50-x}M_x$ alloys are shown in Figure 7-9 (c). It is used to measures the physical stiffness of the material, a higher value of Young's modulus can be classified as rigid and it is less likely to get deformed.

It can be noted that the $Ti_{50}Pd_{43.75}O_{6.25}$ alloy has the lowest value (-16.07 GPa) of Young modulus which indicates the weakest stiffness and the alloy can be easily deformed. The results suggest that Os addition is the stiffest with the highest value of Young modulus (317.38 GPa), particularly at the high composition i.e. $Ti_{50}Pd_{6.25}Os_{43.75}$, followed by Ru addition. The stiffness decreases for the case of Al and Pt indicating weak stiffness and the structure is likely to deform easily. Furthermore, it is noted that Young's modulus increases minimally above 18.75 at. % Co and Ni possessing the strongest resistance to uniaxial tensions [161].
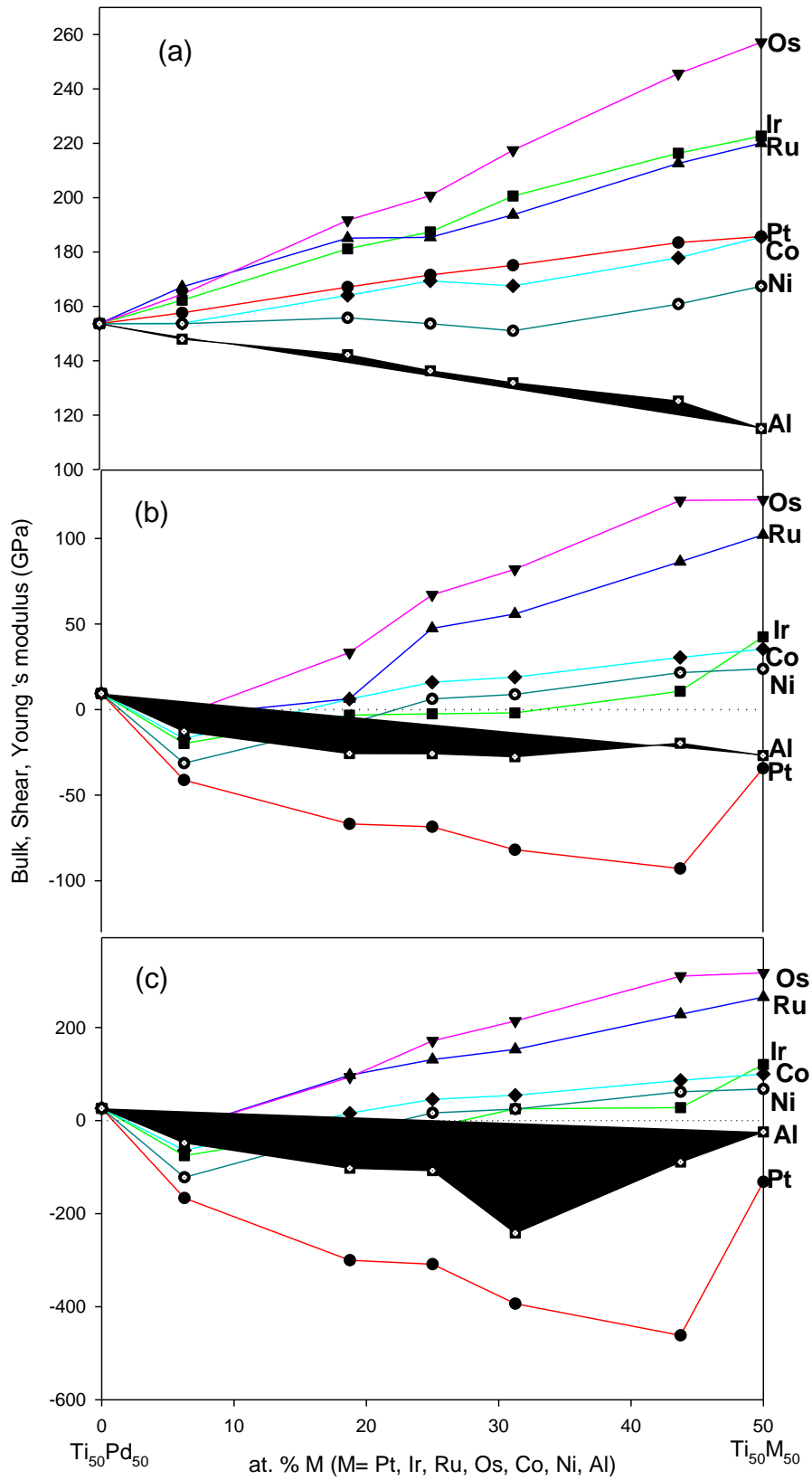
Figure 7-9 The calculated (a) Bulk (B), (b) Shear (G), and (c) Young's (E) modulus against various atomic percent M (at. % M) for (0 ≤ x ≤ 50) compositions range.

7.4 Ductility: B/G ratio, Poisson's ratio and the Cauchy pressure

Now, in order to relate the ductility and brittleness behaviour of the B2 $Ti_{50}Pd_{50-x}M_x$ alloys, we have calculated the B/G ratio, Poisson's ratios and the Cauchy pressure at different compositions. These are three major quantities that can also be used to describe the strength of the material.

7.4.1 The B/G ratio

We have calculated the ratio of bulk to shear modulus (B/G) to investigate the extent of fracture in the $Ti_{50}Pd_{50-x}M_x$ alloys and is shown in Figure 7-10. The material is considered to be ductile if B/G> 1.75, otherwise brittle [149]. This is a measure proposed by Pugh and is referred to as the ratio of brittle and ductility [149]. It is clear that above 18 at % Ru, Os and Co, the structures satisfy the ductile conditions since B/G values are greater than 1.75. However, below 18 at % Ru, Os and Co composition, the structures are regarded as less ductile with the B/G less than 1.75. In the case of Ni and Ir, the B/G is greater than the unit above 25.00 and 31.25 at. %, respectively which reveals ductile behaviour.

Furthermore, the values for $Ti_{50}Pd_{50-x}M_x$ with Al and Pt addition present brittle behaviour due to lower B/G ratios (<1.75) for the entire concentration range ($0 \leq x \leq 50$). This observation suggests that the addition of Al and Pt cannot transform the brittleness of $Ti_{50}Pd_{50}$ into ductility as indicated by the lower B/G ratio.
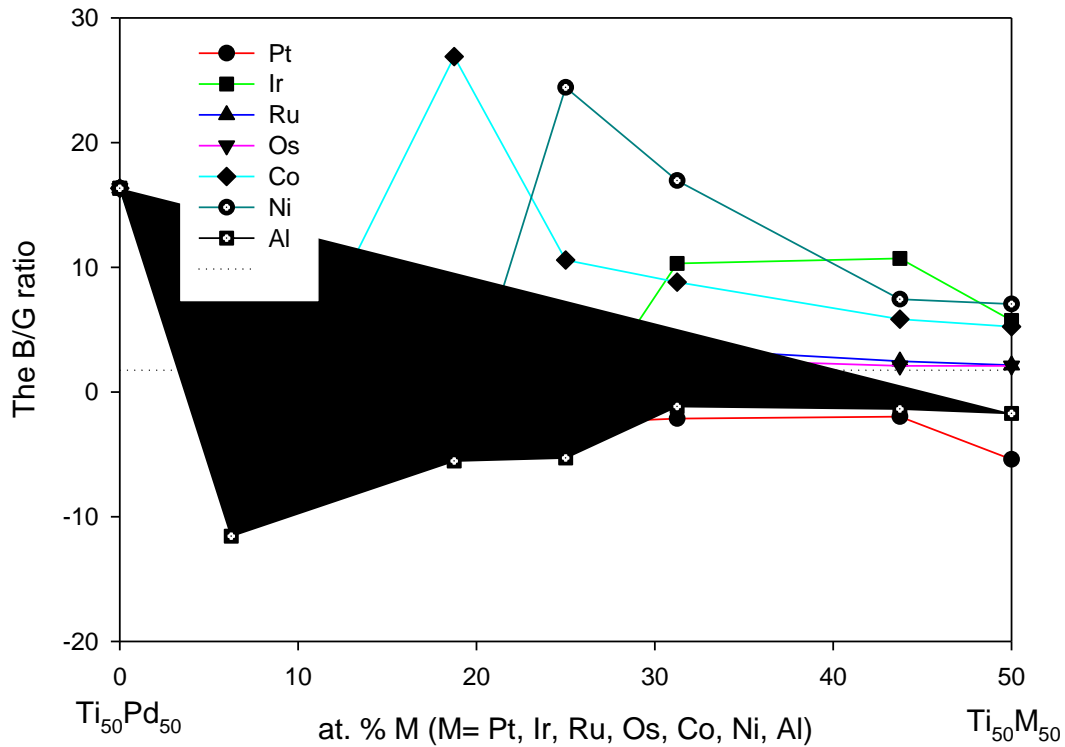
Figure 7-10 The B/G ratio against the composition of B2 $Ti_{50}Pd_{50-x}M_X$ alloys ($0 \leq x \leq 50$).

7.4.2 Poisson's ratio

The Poisson's ratio (σ) was also evaluated to check the ductility of the material. The structure is considered as ductile material when σ is greater than 0.26 otherwise brittle [140]. We see that as the composition of Ru, Os, Co, Ni, Al, Pt and Ir is increased, the σ values were found to be greater than 0.26 which suggests that the structures are ductile (see Figure 7-11).

Furthermore, Poisson's ratio is also used to analyse the bonding behaviour of $Ti_{50}Pd_{50-x}M_x$ alloys. Note that a covalently bonded structure has a small value of ~ 0.1, an ionic bonded structure has a value of 0.25 while for metallic materials is above 0.33 [162]. It is noted that the Poison's ratio (σ) is greater than 0.33

when Ru and Os concentration is increased up to 31 at. % Ru and Os, respectively (see Figure 7-11). This implies that the structures show metallic bonding behaviour below 31 at. % Ru and Os while above this concentration the structure show ionic bonding behaviour characteristics with a value of 0.31. In the case of Co, Ni, Al, Ir and Pt, the Poison's ratio (σ) is greater than 0.33 which implies that the structures have metallic bonding characteristics.
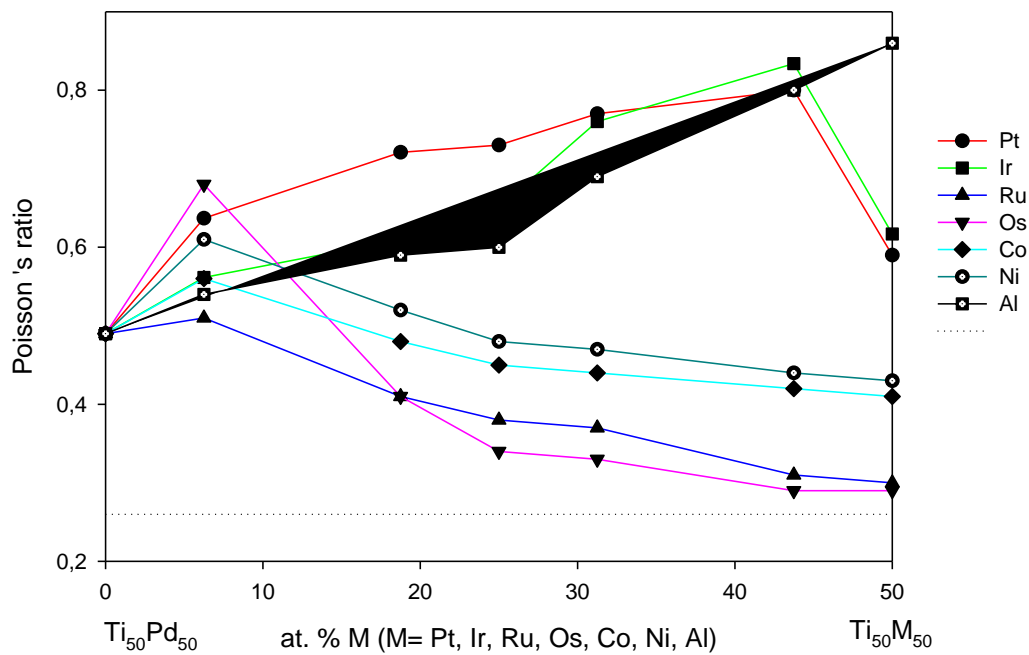
Figure 7-11 The Poisson's ratio against atomic percent M (at. % M) for ($0 \leq$ $x \leq 50$)

7.4.3 The Cauchy pressure: $Ti_{50}Pd_{50-x}M_x$

The Cauchy pressure was calculated to describe the angular and brittle/ductile characters of the $Ti_{50}Pd_{50-x}M_x$ alloys. Note that when Cauchy pressure has a positive value, the results reveal their ionic character and ductile behaviour, and the negative value reveals weak covalent and brittle behaviour [148].

As the composition of Ru is added to the system, the Cauchy pressure values are positive for the entire range ($0 \leq x \leq 50$) which confirms the ductility behaviour as shown in Figure 7-12. The results indicate that the structures are mechanically stable under normal pressure and room temperature conditions (as discussed in section 7-1). Similar behaviour was observed for Ni, Al, Co, Pt and Ir.

In Figure 7-12, the calculated Cauchy pressure is positive below 40 at. % Os which reveals the ionic character and ductile behaviour. At high concentration above 40 at. % Os, the Cauchy pressure is negative which suggests the brittle nature. The results agree very well with the conclusion drawn from Pugh's ratio above. The increasing ductility trend predicted from Cauchy pressure is Os< Ru< Al< Ni< Co < Pt < Ir.
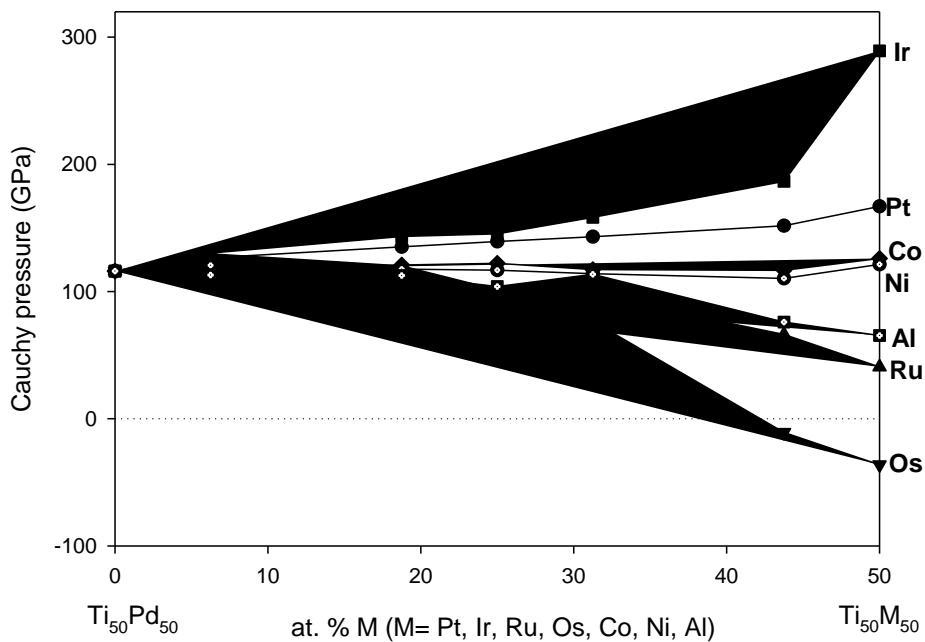
Figure 7-12 Cauchy pressure against the composition of B2 $Ti_{50}Pd_{50-x}M_x$ alloys.

7.5 Vickers hardness

Vickers hardness (Hv) is an important parameter of materials, which can be used to estimate the ability to resists localized deformation [163]. The Vickers hardness (H_V) can be calculated as follows:

$$H_V = \frac{E(1-2v)}{6(1+v)} \qquad (7\text{-}2)$$

where E is Young's modulus and v is Poisson's ratio. The H_V of $Ti_{50}Pd_{50-x}M_x$ has been calculated and is shown in Figure 7-13. It was found that the H_V increases as the concentration of Os and Ru are increased, particularly above 18.75 at. %. This suggests that the hardest material can be obtained at high content of Os and Ru for example, $Ti_{50}Pd_{6.25}Os_{43.75}$ and $Ti_{50}Pd_{6.25}Ru_{43.75}$ with the H_V of 12.49 and 8.51, respectively. In the case of Co and Ni, it is clearly seen that the H_V increase above 25 and 31 at. %, respectively.

Furthermore, we note that hardness increases minimally with an increase in Al and Ir concentration whereas Pt shows a decrease (Figure 7-13). The predicted results revealed that Os addition has the strongest ability to enhance the hardness of the binary $Ti_{50}Pd_{50}$ system as compared to other alloying elements (Ru, Co, Ni, Al, Pt, and Ir). Thus the predicted trend in the decreasing order is $Ti_{50}Pd_{50-x}Os_x > Ti_{50}Pd_{50-x}Ru_x > Ti_{50}Pd_{50-x}Al_x > Ti_{50}Pd_{50-x}Ir_x > Ti_{50}Pd_{50-x}Co_x > Ti_{50}Pd_{50-x}Ni_x > Ti_{50}Pd_{50-x}Pt_x$.
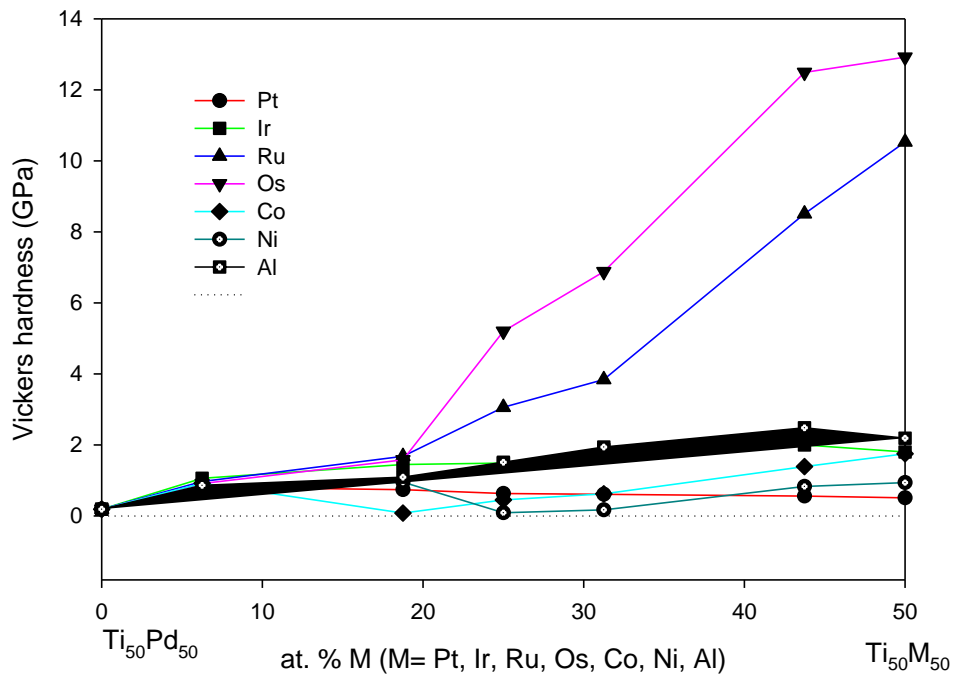
Figure 7-13 Vickers hardness against atomic percent M (at. % M) for (0 $\leq$ $x \leq$ 50).

Chapter 8

Vibrational and thermal properties for B2 $Ti_{50}Pd_{50-x}M_x$

In this section, we discuss the vibrational and thermal properties in particular the phonon dispersion curves, Debye temperature, heat capacity and thermal coefficient of linear expansion of $Ti_{50}Pd_{50-x}M_x$ (M=Ru, Pt, Ir, Co, Ni, Al, and Os). The phonon dispersion curves are presented and discussed to highlight vibrational stabilities. The thermal properties of $Ti_{50}Pd_{50-x}M_x$ alloys are calculated by the quasi-harmonic model with temperatures ranging from 0 to 3000 K to check the thermal conductivity and thermal expansion of the systems. The calculated results are compared with the available experimental and theoretical findings.

8.1 Phonon dispersion curves and phonon density of states for B2 $Ti_{50}Pd_{50-x}M_x$ alloys.

Phonon dispersion curves for the B2 $Ti_{50}Pd_{50-x}M_x$ system were calculated to determine the vibrational stability using a PHONON code [128]. The structure is considered stable if there are no soft modes along high symmetry directions in the Brillouin zone (Bz), otherwise, it is unstable (presence of soft modes). The Phonon dispersion curves are shown in Figures 8-1 to 8-7.

8.1.1 Ti$_{50}$Pd$_{50-x}$M$_x$ alloys: (M= Ru, Os)

Figures 8-1 and 8-2 show the phonon dispersion curves of B2 Ti$_{50}$Pd$_{50-x}$M$_x$ with Ru and Os addition, respectively. In Figure 8-1, the phonon curves display soft modes along all the high symmetry directions for Ti$_{50}$Pd$_{43.75}$Ru$_{6.25}$ and Ti$_{50}$Pd$_{31.25}$Ru$_{18.75}$. It is observed that the phonon soft modes at 18.75 at. % Ru is reduced showing improved vibrational stability. The presence of soft modes corresponds with the negative elastic shear moduli (C' < 0 in Figure 7-1). At 25 at % Ru the soft modes disappeared, only imaginary soft mode was observed along M which suggests that at this concentration the structure is vibrational stable. Interestingly, at 31.25, and 43.75 at. % Ru there are no soft modes observed which confirm vibrational stability in agreement with the predicted C$_{ij}$. Figure 8-1 was published [35].

In the case of Ti$_{50}$Pd$_{50-x}$Os$_x$ (Figure 8-2), the soft modes are observed at lower Os content of 6.25 at. % which suggests vibration instability. The stability is observed at higher Os content of 25 at % and above (25 ≤ x ≤ 50). It is noted that Os has the potential for enhancing stability compared to Ru. Our results are consistent with the predicted C$_{ij}$.
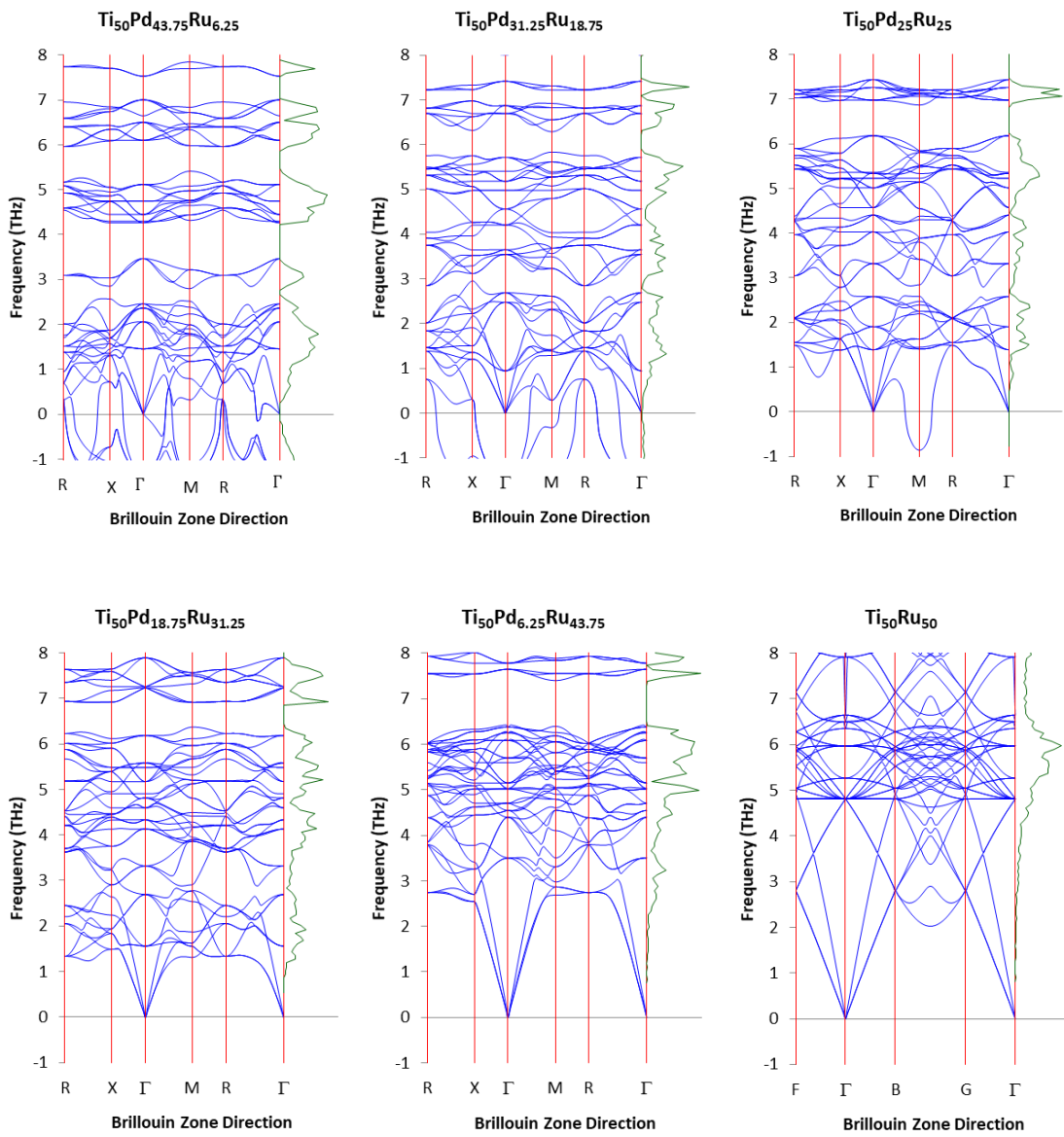
Figure 8-1 The phonon dispersion curves of the $Ti_{50}Pd_{50-x}Ru_x$ ($6.25 \leq x \leq 50$) ternary structures [35].
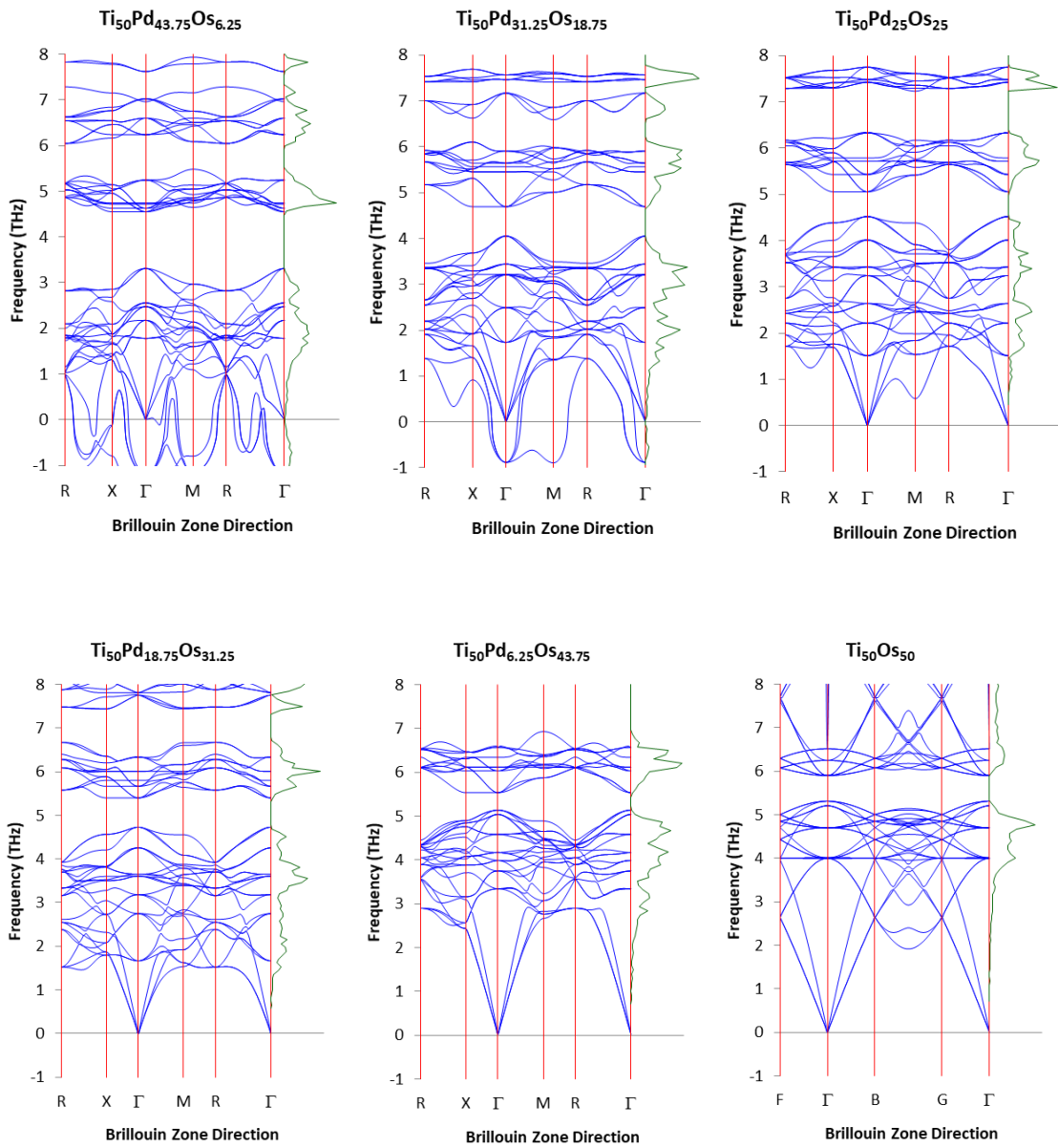
Figure 8-2 The phonon dispersion curves of the $Ti_{50}Pd_{50-x}Os_x$ (6.25 ≤ x ≤ 50) ternary structures.

8.1.2 Ti$_{50}$Pd$_{50-x}$M$_x$ (M= Ir, Pt) alloys

The phonon dispersion curves of B2 Ti$_{50}$Pd$_{50-x}$M$_x$ alloys are shown in Figures 8-3 and 8-4. It is clearly seen that the structure is vibrationally unstable since it displays soft modes along high symmetry direction in the Brillouin zone (Bz). Furthermore, vibrational instability is observed for all composition range (0 ≤ x ≤ 50). The presence of negative vibrations or soft modes suggests mechanical instability in agreement with the elastic shear modulus (as discussed in chapter 7, section 1.4).

Similar to the case of Ir addition, when the concentration of Pt is increased, the structure remains vibrationally unstable due to the presence of soft modes. The negative vibrations may be attributed to the negative elastic shear modulus (Figure 7-5 (b)) which confirms that the system is vibrationally unstable.

8.1.3 Ti$_{50}$Pd$_{50-x}$M$_x$ (M= Co, Ni, Al) alloys

The phonon dispersion curves for Ti$_{50}$Pd$_{50-x}$M$_x$ (M= Co, Ni, Al) alloys are shown in Figures 8-5 to 8-7. The Ti$_{50}$Pd$_{50-x}$Co$_x$ system is vibrationally unstable at a lower concentration of Co, due to the presence of soft modes (Figure 8-5). However, the increase in Co content has a significant effect since the soft mode becomes reduced. Possible stability could be attained at 31.25 at. % Co, since no soft mode was observed at Γ $(0,0,0)$. At 43.75 at. % Co, the structure is vibrational stable (Soft mode disappears). The Ti$_{50}$Co$_{50}$ system is vibrationally stable, consistent with the calculated C$_{ij}$ (Figure 7-8).
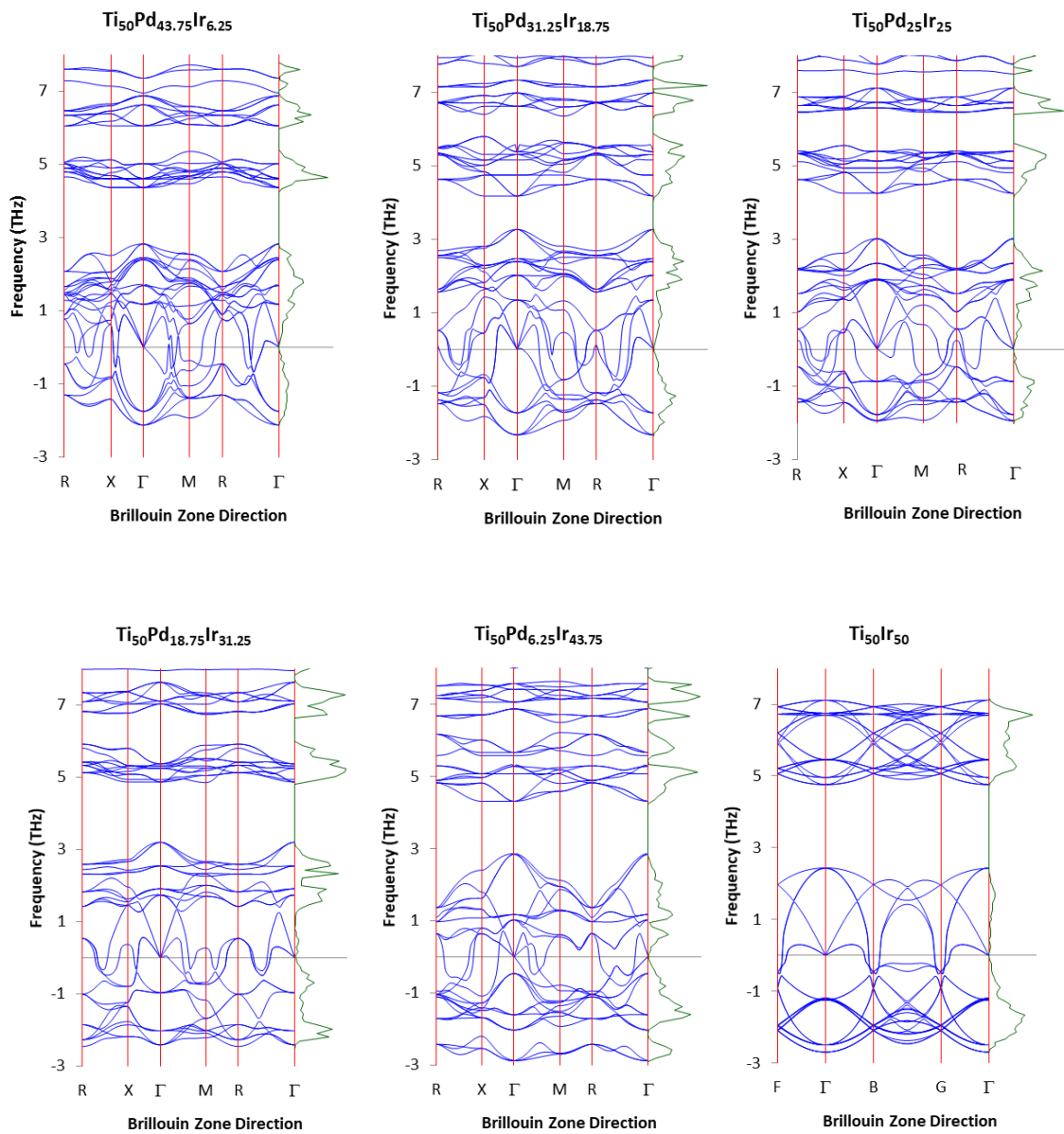
Figure 8-3 The phonon dispersion curves of the Ti$_{50}$Pd$_{50-x}$Ir$_x$ (6.25 ≤ x ≤ 50) ternary structures.
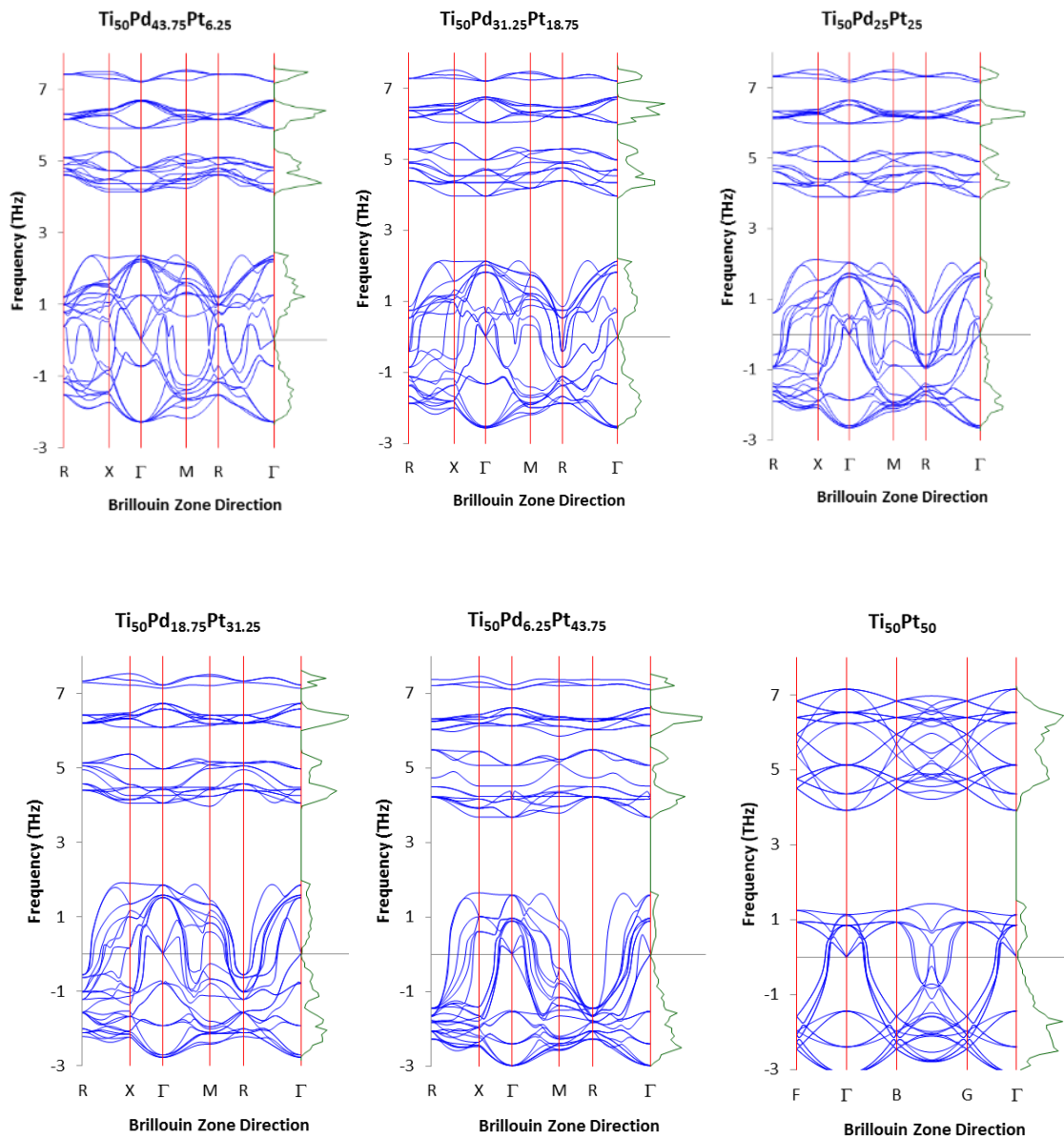
Figure 8-4 The phonon dispersion curves of the $Ti_{50}Pd_{50-x}Pt_x$ (6.25 ≤ x ≤ 50) ternary structures.

In the case of $Ti_{50}Pd_{50-x}Ni_x$ (Figure 8-6), the structure remains vibrationally unstable due to the presence of soft modes for all composition range (0 ≤ x ≤ 50). Interestingly, at 43.75 at. % Ni, the soft modes are reduced and are only observed along M and R-X directions. The negative vibrations are attributed to the negative

elastic shear modulus (Figure 7-8), which confirms that the system is mechanically unstable.

Similar to the case of Ni addition, $Ti_{50}Pd_{50-x}Al_x$ structures are vibrationally unstable due to the presence of soft modes along high symmetry direction in the Brillouin zone (Figure 8-7). The results are consistent with predicted C_{ij}.
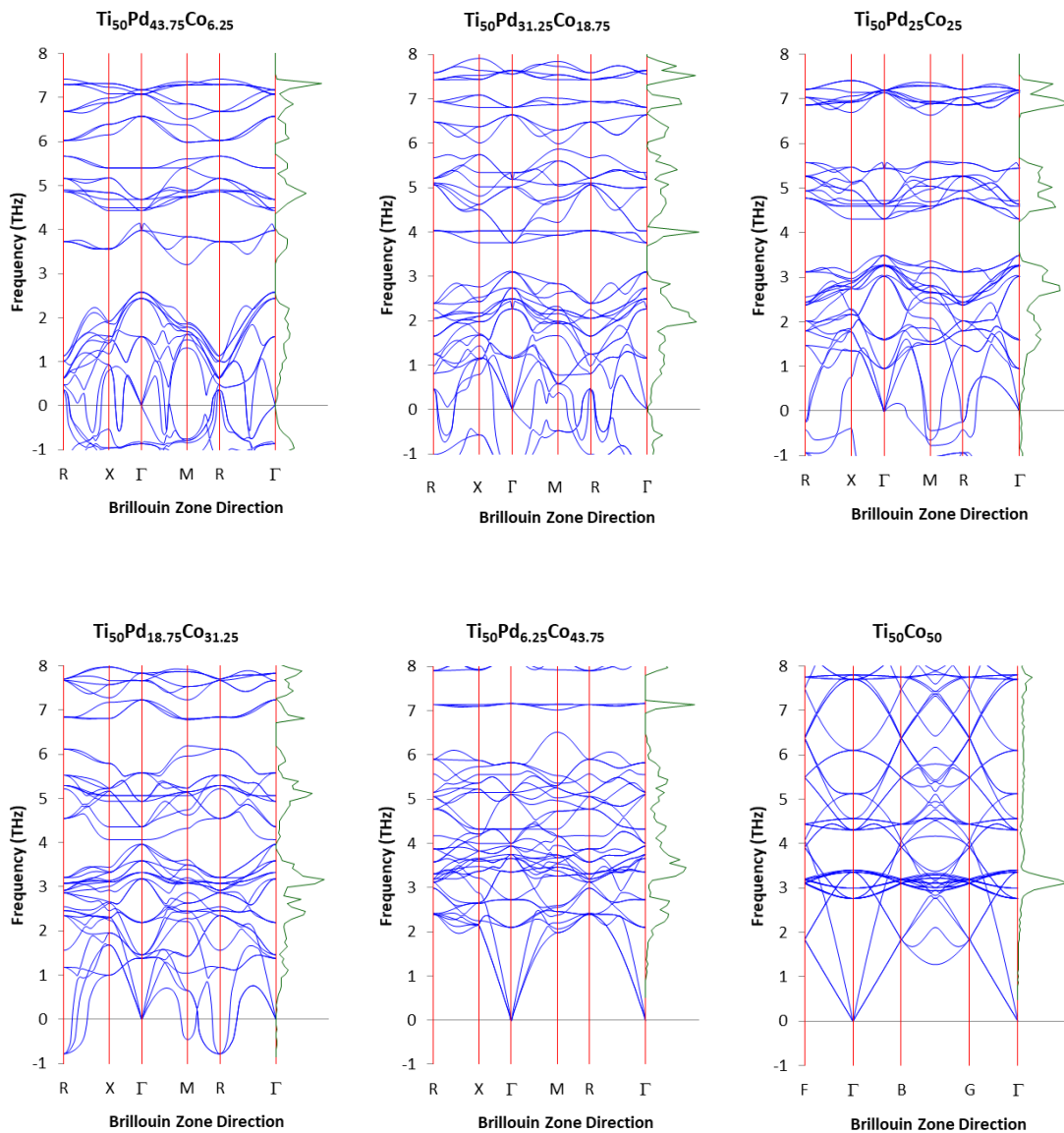
Figure 8-5 The phonon dispersion curves of the $Ti_{50}Pd_{50-x}Co_x$ (6.25 ≤ x ≤ 50) ternary structures.
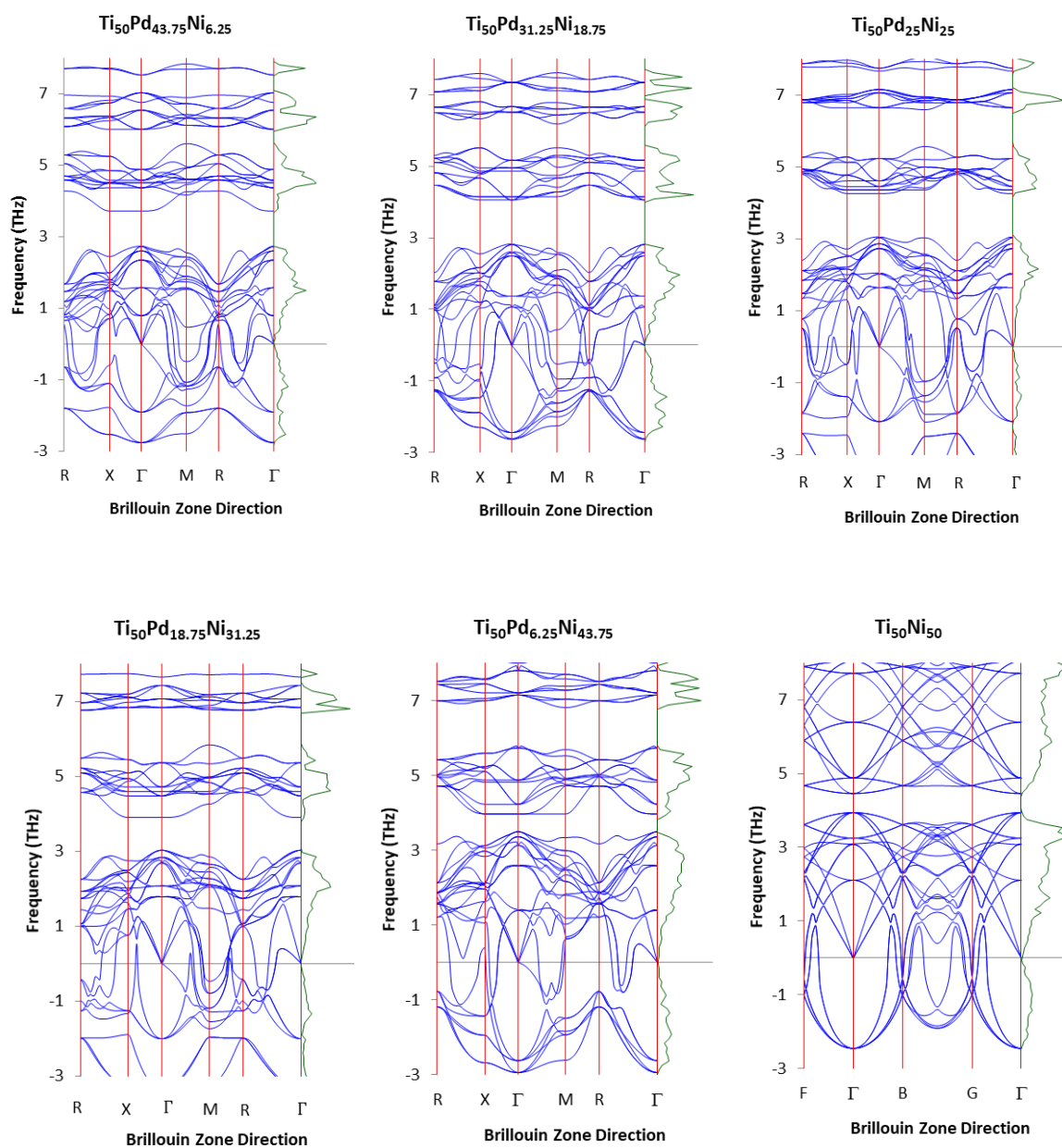
Figure 8-6 The phonon dispersion curves of the Ti$_{50}$Pd$_{50-x}$Ni$_x$ (6.25 ≤ x ≤ 50) ternary structures.
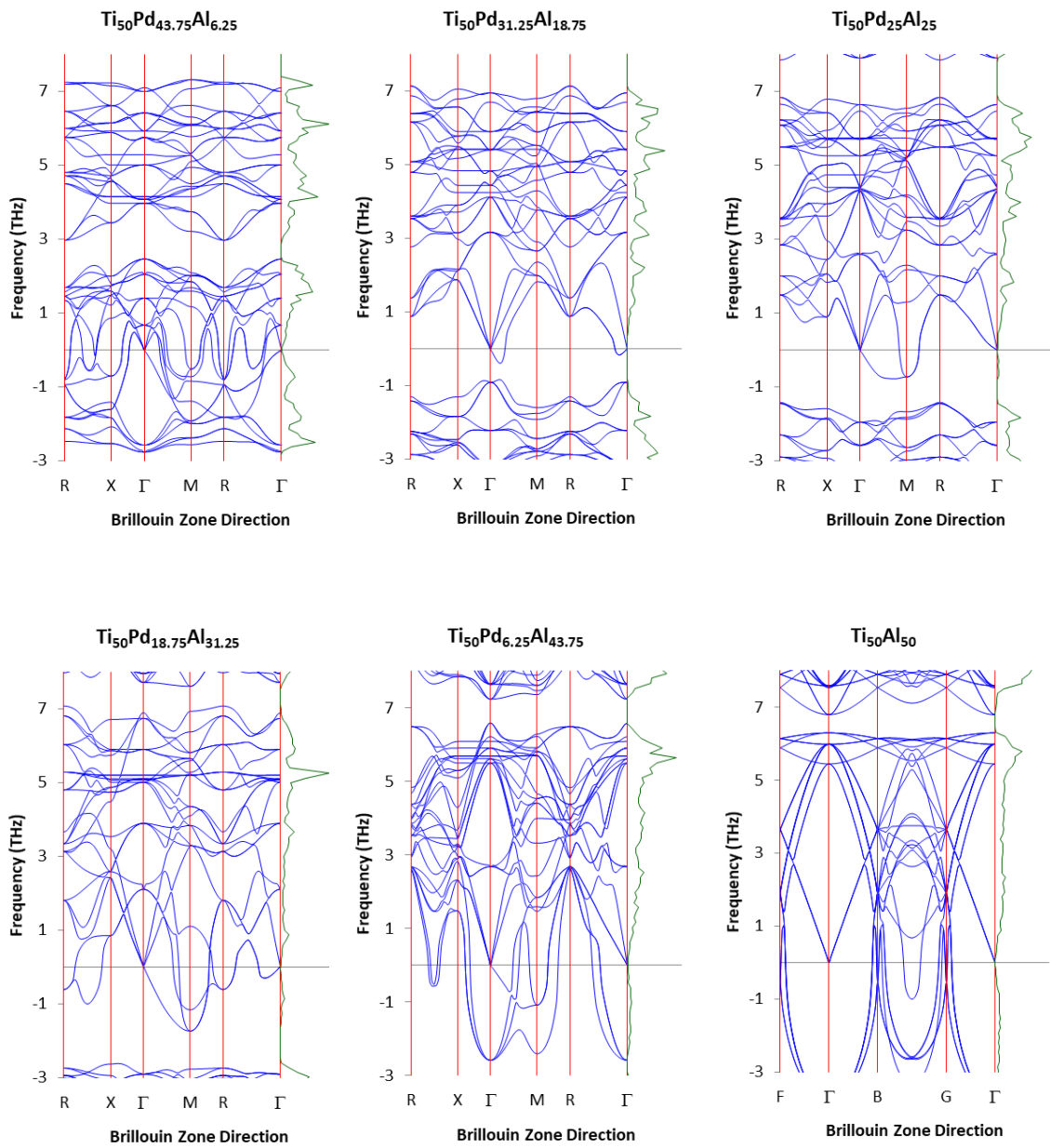
Figure 8-7 The phonon dispersion curves of the Ti$_{50}$Pd$_{50-x}$Al$_x$ (6.25 ≤ x ≤ 50) ternary structures.

8.2 Thermal properties: Debye temperature, heat capacity, thermal coefficient of linear expansion.

8.2.1 Debye temperature

Debye temperature is a very important fundamental parameter which is closely related to the thermodynamic properties of materials, such as entropy, thermal expansion and vibrational internal energy [150, 164, 165]. It can be estimated from the elastic constants using the average sound velocity v_m as follows:

$$\Theta_D = \frac{h}{k_B}\left(\frac{3n}{4\pi V_a}\right)^{1/3} v_m,$$ (8-1)

where h is Plank's constant, k_B is Boltzmann's constant, n is the number of atoms per unit cell and V_a is the atomic volume. The average sound velocity v_m is obtained from:

$$v_m = \left[\frac{1}{3}\left(\frac{2}{v_l^3} + \frac{1}{v_t^3}\right)\right]^{-1/3},$$ (8-2)

where v_l and v_t are the longitudinal and transverse sound velocities of an isotropic aggregate obtained by using the shear modulus (G) and the Bulk modulus (B) as follows:

$$v_l = \left(\frac{3B+4G}{3\rho}\right)^{1/2},$$ (8-3)

$$v_t = \left(\frac{G}{\rho}\right)^{1/2}. \tag{8-4}$$

The Θ_D for Ir, Pt, Ni and Al additions are not included, because one of the moduli is negative, and thus calculating the speed of sound is not possible [166].

Figure 8-8 shows the Θ_D against concentration for $Ti_{50}Pd_{50-x}M_x$ (M= Ru, Os, Co) alloys. A higher Θ_D implies a single normal vibration which results in a better thermal conductivity [164]. In general, the Θ_D is calculated from elastic moduli (Bulk and Shear modulus). It is noted from Figure 8-8 that Θ_D increases with an increase in Ru concentrations ($0 \leq x \leq 50$). It should be noted that the Θ_D for 6.25 at. % Ru cannot be attained due to negative elastic moduli.

In Figure 8-8, a sharp exponential increase in Θ_D is observed between 20 and 30 at. % Ru, and continue to increase slightly above this point. Thus a better thermal conductivity is reached at 25 at. % Ru corresponding to the sharp peak. This accord well with the increased ductility as confirmed by Poisson and Pugh's ratio. Above this concentration, the thermal conductivity increases slightly up to 50 at. % Ru. Therefore thermal conductivity of $Ti_{50}Pd_{50-x}Ru_x$ alloys may be favourable between 25 and 31.25 at. % Ru.

It is observed that Θ_D increases with an increase in Os contents ($0 \leq x \leq 50$) under normal pressure as shown in Figure 8-8. This behaviour suggests that the thermal conductivity of the structure is effectively improved with an increase in Os content. The Θ_D is mostly favourable between 18.75 and 25 at. % Os. There is a slight decrease in Θ_D as Os content is increased above 43.75 at. %, however

the thermal conductivity of the structure is still favourable as compared to other compositions.

Furthermore, it is noted from Figure 8-8 that Θ_D increases with an increase in Co concentrations ($0 \leq x \leq 50$). This may imply that the Θ_D is enhanced remarkably with an increase in Co concentration. It can be inferred that thermal conductivity could be effectively improved by the increase in Co concentration of 43.75 at. %. At 6.25 at. % Co, no Θ_D was recorded due to negative moduli which imply poor thermal conductivity at that composition.
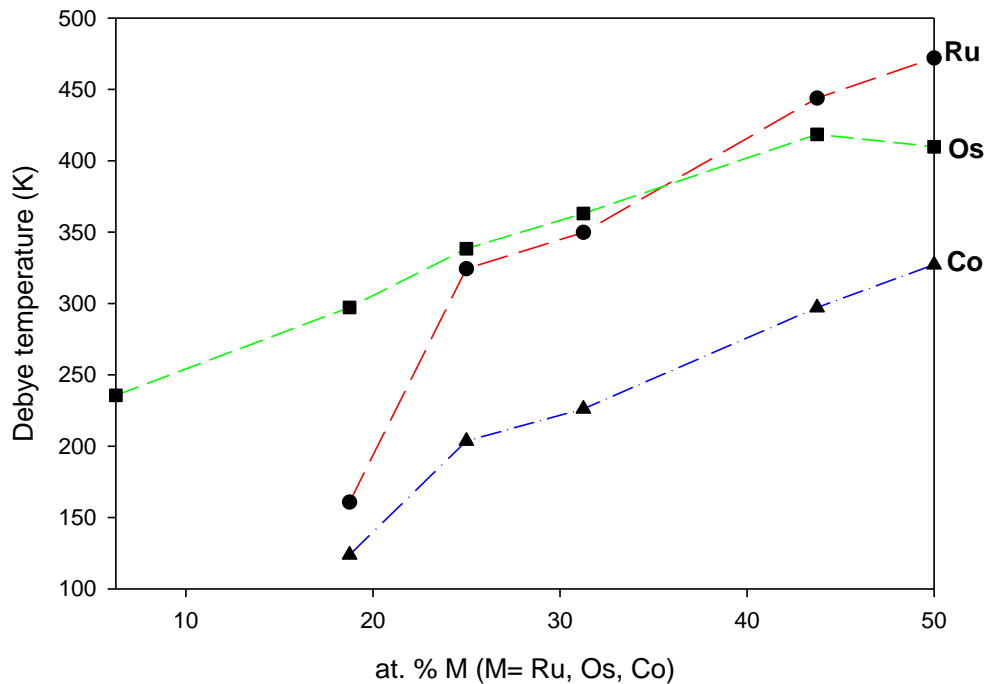
Figure 8-8 Debye temperature against the composition of Ti$_{50}$Pd$_{50-x}$M$_x$ (M= Ru, Os, Co) alloys (6.25 ≤ x ≤ 50).

8.2.2 Heat capacity

Heat capacity is an important physical parameter of materials, which provides essential information about vibration properties, heat transmission process and

reflects the inherent properties of the system, serving as a bridge between thermodynamics and microscopic structure [163].

The heat capacities at constant volume (C_V) of the $Ti_{50}Pd_{50-x}M_x$ (Ru, Os, and Co) alloys are shown in Figure 8-9. The calculations were done at various compositions for temperature ranging from 0 to 3000 K, and pressure at 0 GPa. It is observed that C_V rises sharply with the increase in Ru content at temperatures below 300 K and reaches a zero slope above this temperature, in agreement with the Dulong–Petit limit, which is common to all solids at high temperatures [166]. This limit is proposed by Dulong–Petit [167] and is observed at sufficiently low temperatures when C_V does not depend much on temperature and converges to a near-constant (C_V is proportional to T^3). This behaviour implies that the bond state is weaker and reaches bigger thermal vibrations of atoms above 300 K. Similar behaviour was obtained from nickel-based cast superalloys [168].

The current results indicate that the electron excitation occurs at a very low temperature below 300 K and the contributions from phonon excitations are significant at high temperatures for all compositions in $Ti_{50}Pd_{50-x}Ru_x$ alloys (Figure 8-9 (a)). The $Ti_{50}Pd_{31.25}Ru_{18.75}$ system, in particular, has the strongest heat capacity (high value) while the weakest heat capacity (low value) was observed for $Ti_{50}Ru_{50}$. The C_V tends to the Dulong-Petit limit (approaches of 398.5 Jmol^{-1}K^{-1}) at about 300 K. The Dulong-Petit limit is observed for all compositions ($6.25 \leq x \leq 50$) for the temperature above the Debye temperature.

A similar trend is observed when the amount of Os is added to the system (Figure 8-9 (b)). Moreover, the strongest heat capacity is observed for 6.25 at. % Os while the weakest heat capacity was observed for 50 at. % Os. At higher temperatures (>300 K) the C_V reaches the Dulong-Petit limit. The Dulong-Petit limit is observed for all compositions $(6.25 \leq x \leq 50)$ the temperature below the Debye temperature for the entire concentrations.

It is noted that the C_V in Figure 8-9 (c) increases with an increase in Co content when the temperature is below 300 K and reaches a zero slope above that temperature (>300 K). Similar bond state behaviour was observed for compositions (31.25, 43.75 and 50 at. % Co) except for 25 at. % Co. However, the strongest heat capacity was observed for 18.75 at. % while the weakest heat capacity was observed for 50 at. % Co.
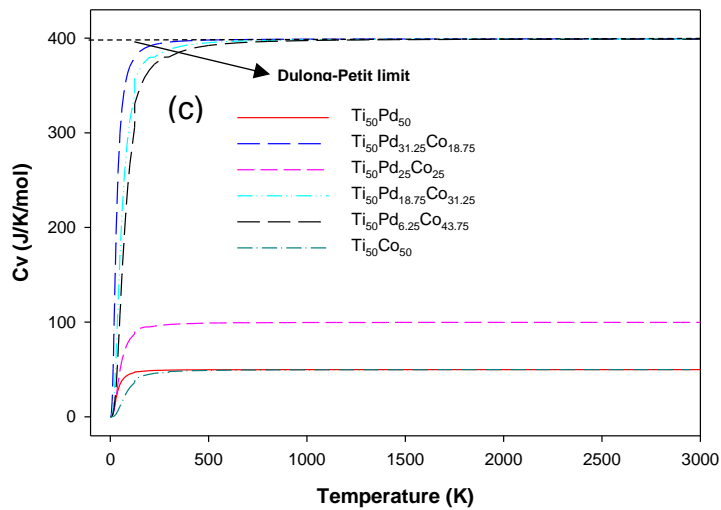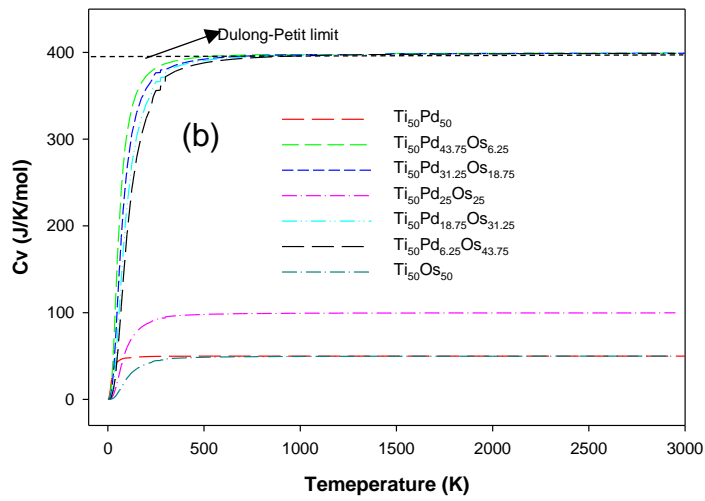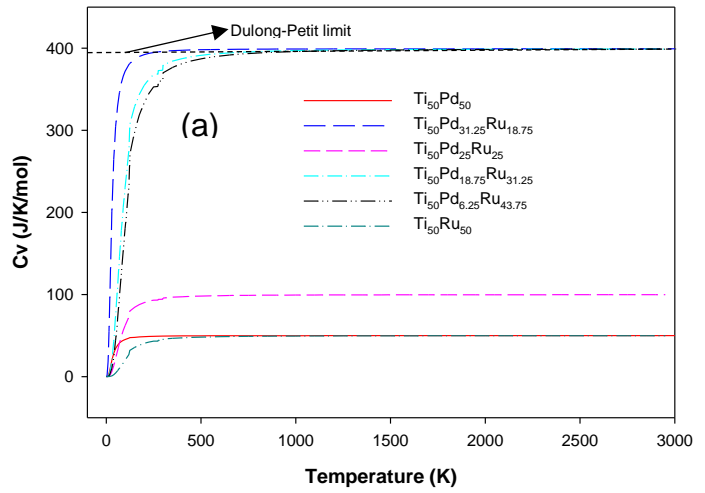
Figure 8-9 The heat capacity (C_V) against temperature for $Ti_{50}Pd_{50-x}M_x$ (Ru, Os and Co) alloys.

173

8.2.3 Thermal coefficient of linear expansion

The thermal coefficient of linear expansion expresses the tendency of a structure to change in volume due to a temperature change. A larger value of α implies that the material expands moreover a chosen temperature range. Thermal expansion generally decreases with increasing bond energy; hence materials with high melting temperatures are more likely to have lower thermal expansion. The thermal expansion (α) are expressed as [151]:

$$\alpha = \frac{\gamma C_V}{B_T V} \tag{8-6}$$

where B_T is the isothermal bulk modulus, V is volume and γ is the $Gr\ddot{u}neisen$ parameter which is defined as [151]:

$$\gamma = -\frac{dIn\Theta(V)}{dInV} \tag{8-7}$$

Figure 8-10 shows a thermal coefficient of linear expansion (α) with temperature for $Ti_{50}Pd_{50-x}M_x$ (Ru, Os, Co) alloys. The coefficient of linear expansion displays a similar trend for all alloying elements (Ru, Os, Co). The addition of dopants reduces the thermal coefficient of linear expansion. An increase in the concentration of the alloying element results in less expansion. This observation is necessary for the development of the alloys. However, the expansion rates are different.

For example, the thermal coefficient of linear expansion for the $Ti_{50}Pd_{31.25}Ru_{18.75}$ is higher than that of 43.75 at. % Ru below 500 K (Figure 8-10 (a)). Furthermore, we note that the material expands more at a low content of 18.75 at. % Ru than at higher content. It is also observed that as the Ru content is increased the

thermal expansion increases at a lower temperature (<300) and reaches a zero slope at a high temperature range. At this region, no further expansion is observed (Figure 8-10 (a)). In the case of Os, we observe a similar trend, however with a high expansion rate. It is clearly seen that 6 at. % Os is the highest. The highest thermal coefficient of linear expansion is observed for Co addition (Figure 8-10 (c)), compared to that of Ru and Os.
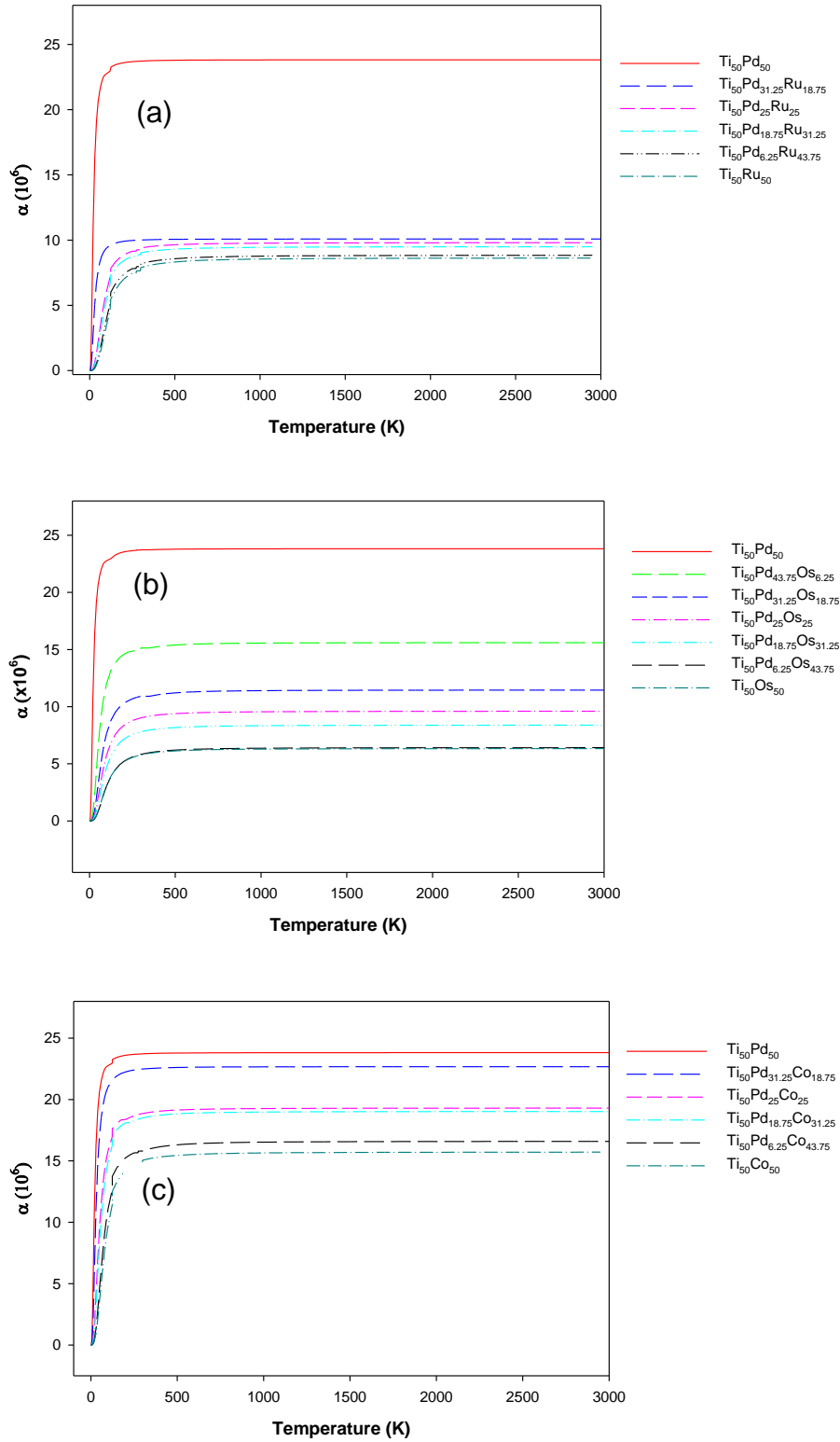
Figure 8-10 The linear thermal expansion coefficient (α) as a function of temperature for Ti₅₀Pd₅₀₋ₓMₓ (M= Ru, Os, Co) alloys.

Chapter 9

The temperature dependence of the $Ti_{50}Pd_{50-x}M_x$

In this chapter, the temperature dependence on the volume, density, lattice parameters and elastic properties of B19 $Ti_{50}Pd_{50-x}M_x$ (x = 6.25, 18.75 and 25) are presented. The alloying elements i.e. Co and Ni were chosen due to their promising thermodynamical and mechanical properties which were discussed in chapter 6. Pt and Al were not conducted since they display mechanical instability. LAMMPS code [103] which employs the embedded atom method (EAM) [104] was used, where the Zhou [139] interatomic potentials were invoked.

Previously, the LAMMPS code was successfully used to describe the temperature dependence of TiPt and TiPt- (Co, Ni) and the results were in agreement with experiments [4, 9, 13]. It was reported that Co addition decreases the transformation of TiPt in both computational and experimental findings.

In this chapter, a supercell containing 2048 atoms was constructed for the B19 $Ti_{50}Pd_{50-x}Co_x$ alloys and the systems were treated with NPT [124] ensemble, Nose Hoover thermostat [123] and barostat [169]. The temperature was varied between 273 and 1773 K to determine the transformation temperature of the systems, their lattice parameters and XRDs were determined. We will highlight an understanding of the transformation from the orthorhombic B19 (martensite phase) to the cubic B2 phase (austenite phase) using XRDs. In addition, the temperature dependence with the elastic properties is investigated to determine the elasticity strength of the material.

9.1 Temperature dependence of the volume and density of the $Ti_{50}Pd_{50-x}M_x$ (Co, and Ni).

Figure 9-1 shows volume against the temperature of the $Ti_{50}Pd_{50-x}Co_x$ ($0 \geq$ $x \geq 25$). The volume of the structures increases linearly with an increase in temperature as depicted by the plots in Figures 9-1 and 9-2; respectively. As Co content is added to the $Ti_{50}Pd_{50}$ system, the volume is lowered with 25 at. % Co having the lowest volume. Similar behaviour was observed with the addition of Ni for the concentration range of 6.25 to 25 at. % (see Figure 9-1 (b)). The obtained volume is lowered as Co and Ni content is added as compared to the pure $Ti_{50}Pd_{50}$ system which indicates that their lattice parameters expand more with an increase in temperature.
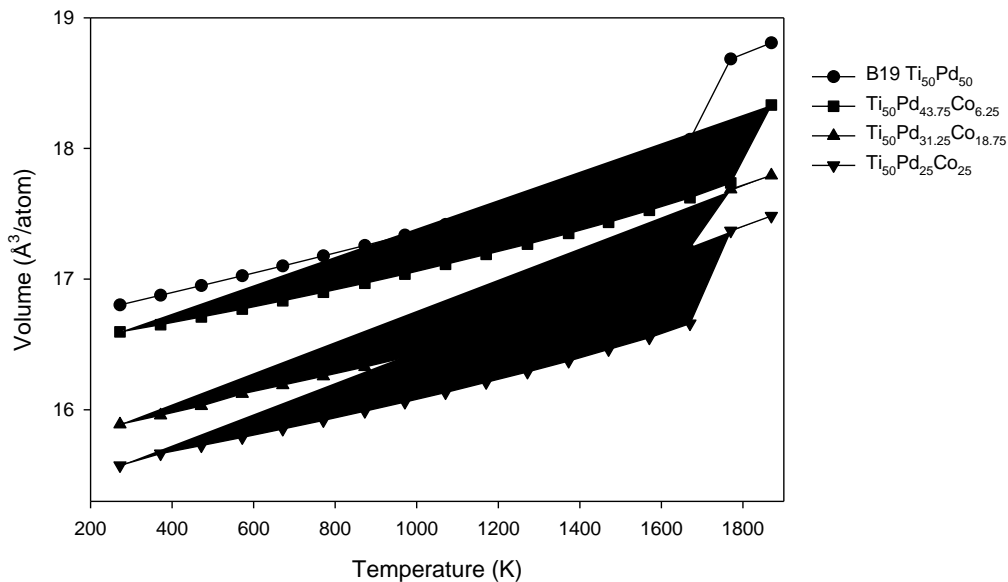
Figure 9-1 Volume against temperature for $Ti_{50}Pd_{50-x}Co_x$ alloys.
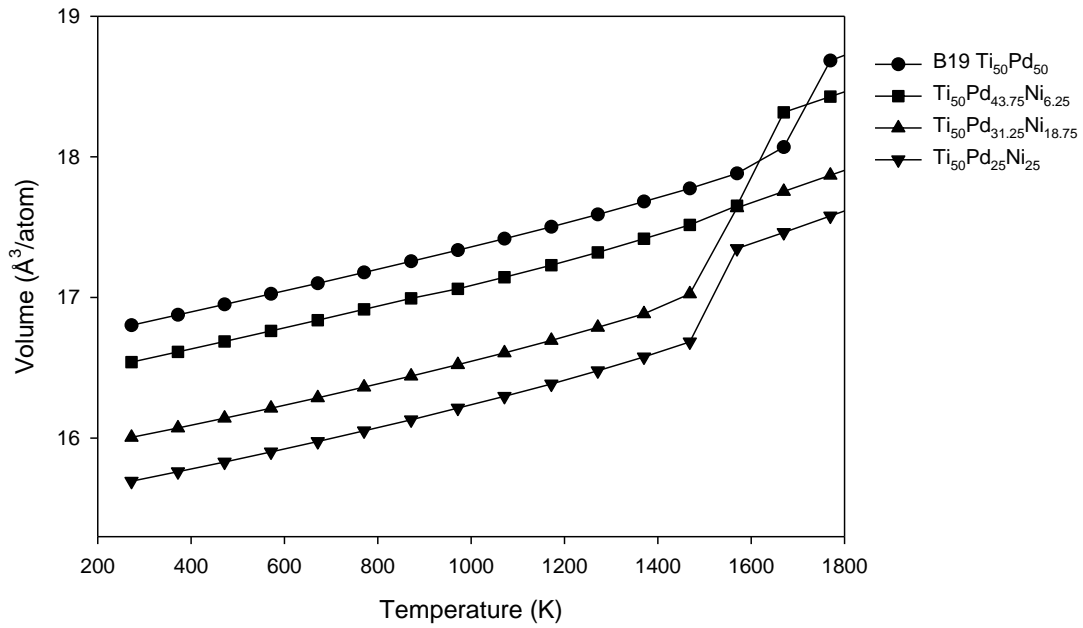
Figure 9-2 Volume against temperature for Ti$_{50}$Pd$_{50-x}$Ni$_x$ alloys.

The density of Ti$_{50}$Pd$_{50-x}$Co$_x$ alloys is shown and compared in Figure 9-3. As the amount of Co is added, the density decrease with an increase in temperature which may suggest that the system becomes less dense with temperature for the composition range ($0 \geq x \geq 25$). A similar trend was noted with the addition of Ni additions as shown in Figure 9-4. The finding suggests that the addition of Co resulted in less dense structures which agrees well with the fact that Co (8.86 g/cm^3) and Ni (8.90 g/cm^3) are less dense compared to Pd (12.02 g/cm^3).
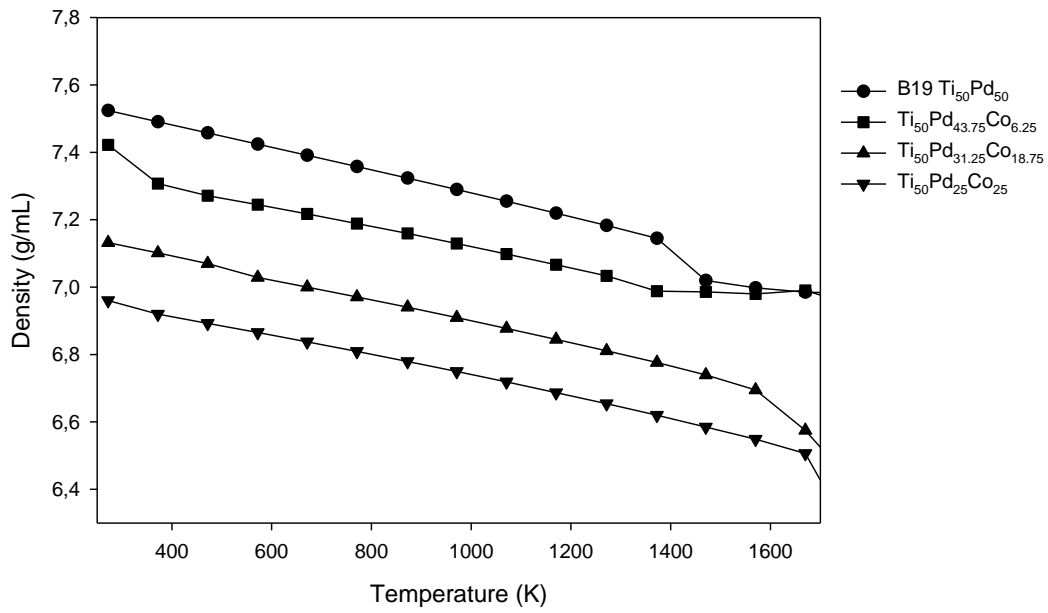
Figure 9-3 Density against temperature for Ti$_{50}$Pd$_{50-x}$Co$_x$ alloys.
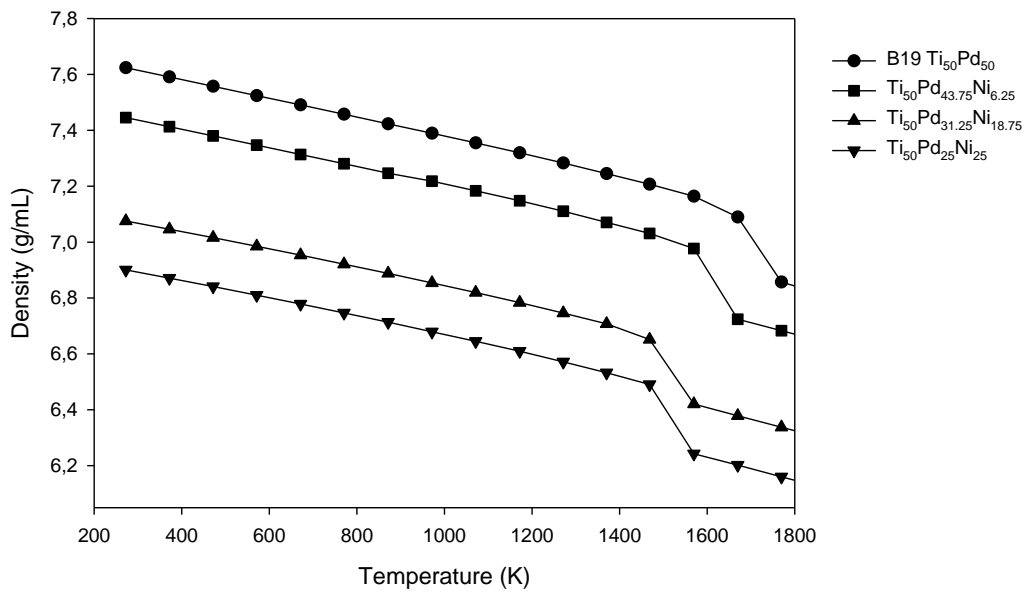
Figure 9-4 Density against temperature for Ti$_{50}$Pd$_{50-x}$Ni$_x$ alloys.

9.2 The lattice parameters and x-ray diffraction patterns of the B19 Ti$_{50}$Pd$_{50-x}$M$_x$ at high temperature

Lattice expansion is determined to check the transformation and melting temperature of B19 Ti$_{50}$Pd$_{50-x}$M$_x$ alloys varied from 273 to 1873 K. Figure 9-5

shows the effect of temperature on the lattice parameters of B19 $Ti_{50}Pd_{50-x}M_x$ alloys.

In this section, we evaluate X-ray diffraction patterns to determine the transformation temperature of B19 $Ti_{50}Pd_{50-x}M_x$ alloys with respect to the intensity of the peaks and temperature is varied from 273 to 1670 K. A supercell which consists of 2048 atoms was used for various composition ranges ($0 \leq x \leq 25$) of B19 $Ti_{50}Pd_{50-x}M_x$ alloys and is shown below.

9.2.1 Lattice expansion and XRD's for the B19 $Ti_{50}Pd_{50-x}Co_x$ alloys

Figure 9-5 shows the graph of lattice parameters with temperature for the B19 $Ti_{50}Pd_{50-x}Co_x$ ($0 \geq x \geq 25$). As discussed in chapter 5, the temperature transformation of the pure $Ti_{50}Pd_{50}$ from B19 to B2 was found to be at 1496 K as indicated by a ratio of 1.414. Mitarai et.al [13] reported on the temperature 1473 K and the same trend was observed on their lattice parameters. They also suggested that for a structure to transform the cubic B2 phase, the *a/c* and *c/b* ratio should be closer to 1.41. As 6.25 at. % Co is added to $Ti_{50}Pd_{50}$, the *a, c* and *b* lattice parameters increase linearly with temperature as shown in Figure 9-5 (a). Interestingly, a collapse is observed at temperatures around 971 K for both *a* and *c* and a sharp increase for *b* lattice parameters. At these temperatures, a transformation from B19 to B2 is predicted for the $Ti_{50}Pd_{43.75}Co_{6.25}$.

 In the case of $Ti_{50}Pd_{31.25}Co_{18.75}$, *a* collapse is observed at 572 K on the *a* and *c* lattice parameters. The *a/c* and *c/b* ratio become 1.31 at a temperature around

672 K suggesting that at this temperature, the structure has transformed to the B2 phase. Similarly with 25 at. % Co, the *a* and *c* lattice parameters increase with an increase in temperature and there is a drastic drop observed at 472 K. There is coupling observed between *a/b* and *c/b* ratio for 25 at. % Co at 472 K, suggesting transformation from B19 to B2 phase. Recently, Mitarai *et al* [4] investigated the martensitic and austenite transformation of $Ti_{50}Pd_{50-x}Co_x$ (x= 2, 4, and 8) experimentally and their results agree very well with our observations. It is noted that above 25 at. % Co, the transformation temperature occurs at a very low temperature which is shown in appendix A (Figure A-1). As Co is alloyed on the $Ti_{50}Pd_{50}$, the martensitic transformation of the system is reduced. The reported $Ti_{50}Co_{50}$ [170] transformation temperature is lower as compared to $Ti_{50}Pd_{50}$ which suggests that indeed Co reduces the transformation temperature.
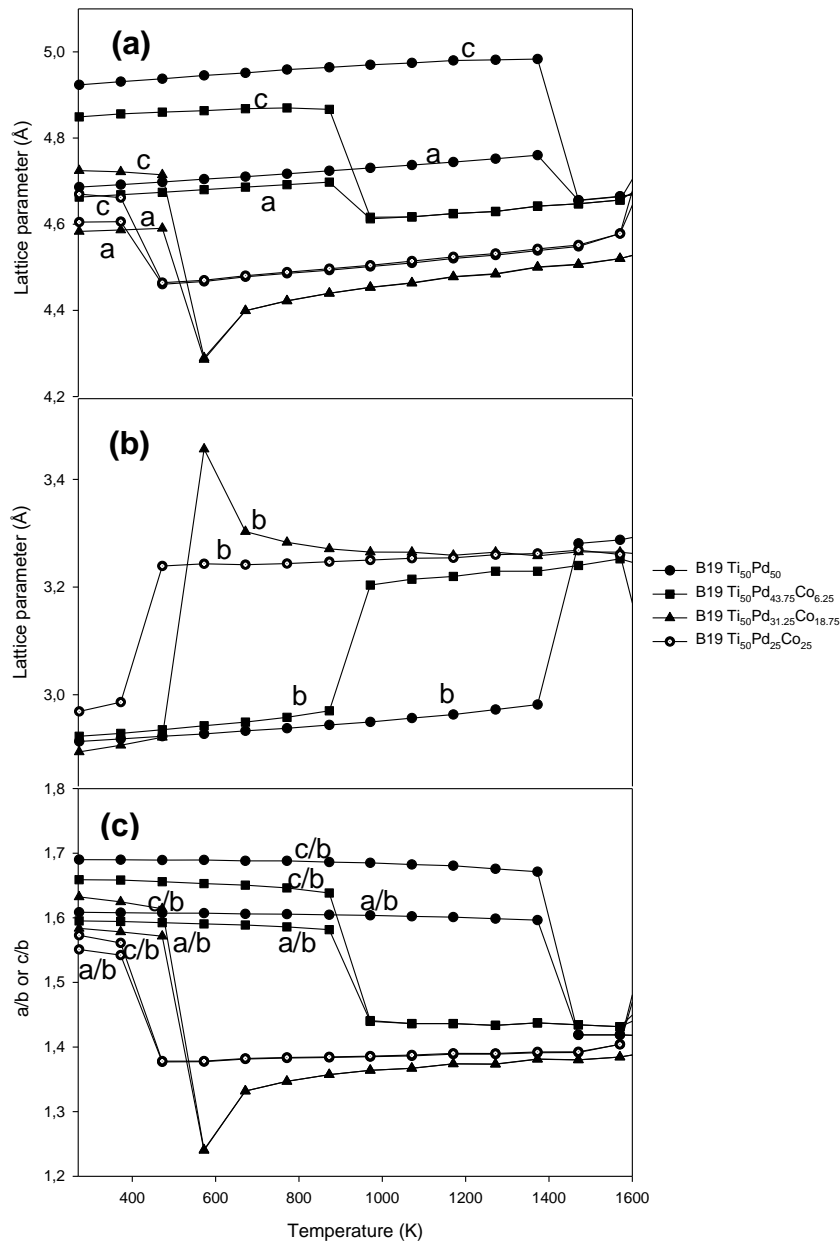
Figure 9-5 The effect of temperature on the (a) a and c (b) b (c) a/b and c/b lattice parameters of the B19 $Ti_{50}Pd_{50-x}Co_x$ (x = 0, 6.25, 18.75 and 25).

Figure 9-6 shows the XRD patterns of B19 $Ti_{50}Pd_{43.75}Co_{6.25}$ alloys from 273-1670 K. As indicated in chapter 5, the structure of $Ti_{50}Pd_{50}$ remains B19 phase up to 1298 K with the same set of peaks observed. At 1447 K, the new patterns of peaks were observed for B19 $Ti_{50}Pd_{50}$ which are assumed to be that of the cubic

B2 phase (as shown in Figure 5-7). As 6.25 at. % Co is added, we observe the same set of peaks of the B19 phase from the XRD patterns below 872 K. It is noted that when the temperature is increased to 972 K, the number of peaks reduces which may suggest a possible transformation from B19 to B2 phase. Furthermore, it is noted that the same set of peaks of the B19 phase is obtained from 972 to 1572 K with the same set of peaks of the B19 phase which indicates B2 phase patterns. As the temperature is increased above 1672 K, the peaks are broader and the structure becomes deformed which suggests that the melting temperature is reached.

Figure 9-6 shows the XRD patterns of B19 $Ti_{50}Pd_{31.25}Co_{18.75}$ alloy calculated at a temperature range from 273 to 1572 K. The same set of peaks of the B19 phase is observed from 273 to 472 K which implies that there is no transformation. A transformation is observed at 572 K as the number of peaks reduces. At 1572 K, the peak becomes broader and reaches the melting temperature. In the case of 25 at. % Co, it is observed that the number of peaks reduces at 472 K which implies transformation from B19 to B2 phase (see Figure 9-7). It is clearly seen that the transformation temperatures observed at 18.75 and 25 at. % Co were found very small and close to each other which suggests that those compositions do not enhance the transformation temperature of the pure system. The melting temperature is reached above 1572 K as the peak becomes broad and the intensity peaks are lost. It is interesting that the transformation temperature of the B19 $Ti_{50}Pd_{50-x}Co_x$ alloy correlates well with the *a/b* and *c/b* ratios change, as discussed above (see section 9.2.1).

9.2.2 Lattice expansion and XRD's for the B19 $Ti_{50}Pd_{50-x}Ni_x$ alloys

The effect of temperature on lattice parameters of B19 $Ti_{50}Pd_{50-x}Ni_x$ (x =6.25, 18.75 and 25) is shown in Figure 9-8. At temperature below 871 K, the a, *c* and *b* lattice parameters of $Ti_{50}Pd_{43.75}Ni_{6.25}$ increases linearly. A drastic decrease in *a* and *c* lattice parameters is observed from 871-971 K while the b lattice parameter increase sharply from 871- 971 K. It is observed that the *a/b* and *c/b* ratio for $Ti_{50}Pd_{43.75}Ni_{6.25}$ decreases with an increase in temperature with a sudden drop observed at approximately 971 K. There is coupling observed between *a/b* and *c/b* ratio and the ratio was found to be 1.43 at 971 K which is comparable to the expected value of 1.41. The results infer that there is a transformation from the B19 to B2 phase with an *a/b and c/b* ratio of 1.43 at 971 K.

It is clearly seen that the *a, c and b* lattice parameters of $Ti_{50}Pd_{31.25}Ni_{18.75}$ increase with an increase in temperature and there is a coupling observed between the *a and c* lattice parameters from 272-1572 K. The *a/b and c/b* ratio become 1.38 at a lower temperature (272 K), suggesting possible transformation from B19 to B2. A similar trend was observed for B19 $Ti_{50}Pd_{25}Ni_{25}$ as the transformation from B19 to B2 phase occurs at a very low temperature (see Figure 9-8 (c)). Note that above 25 at. % Ni the transformation temperature occurs at very low temperature which is highlighted in appendix A (Figure A-2).
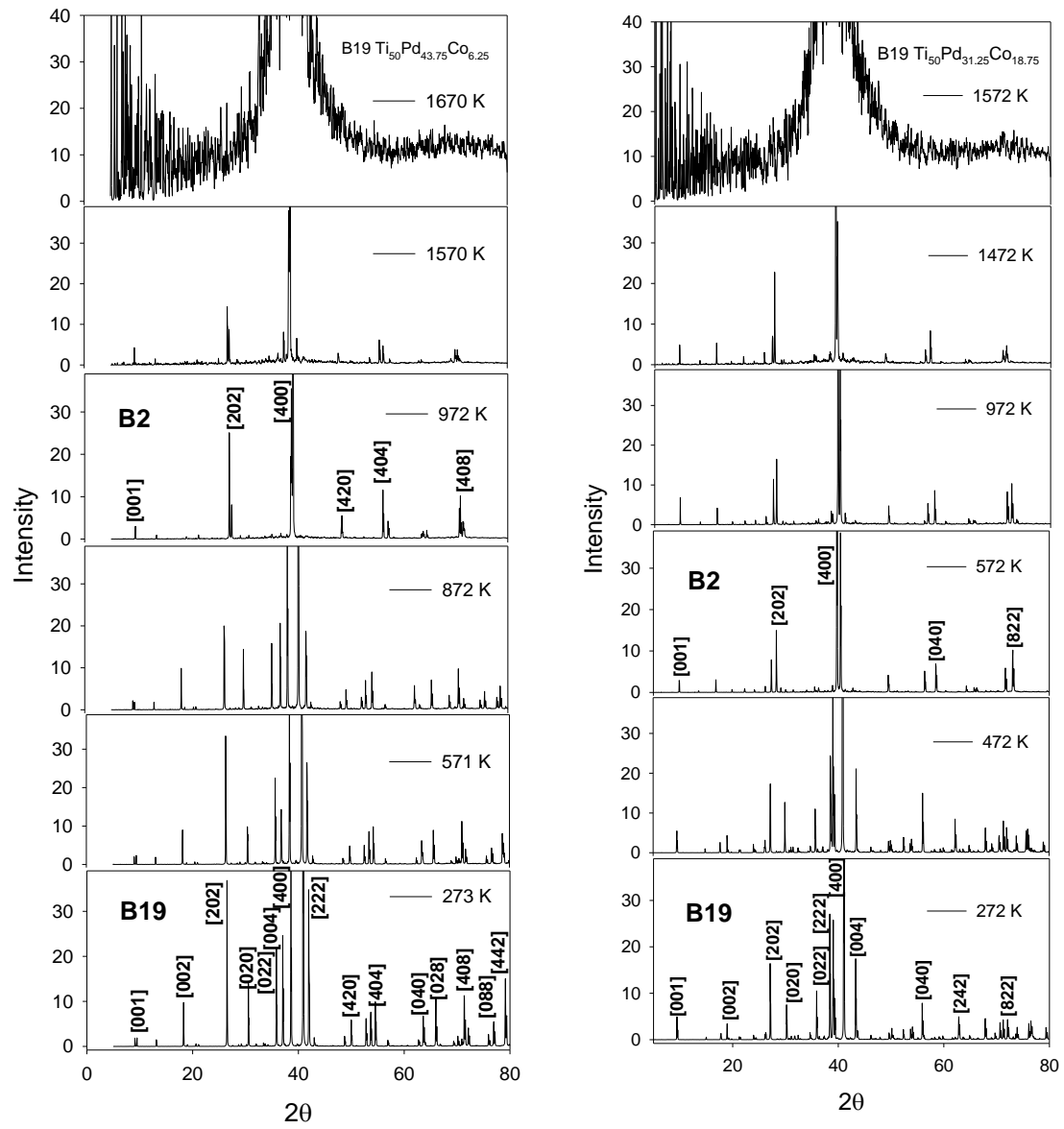
Figure 9-6 The simulated B19 Ti₅₀Pd₄₃.₇₅Co₆.₂₅ and Ti₅₀Pd₃₁.₂₅Co₁₈.₇₅ diffraction patterns from 273 to 1670 K.
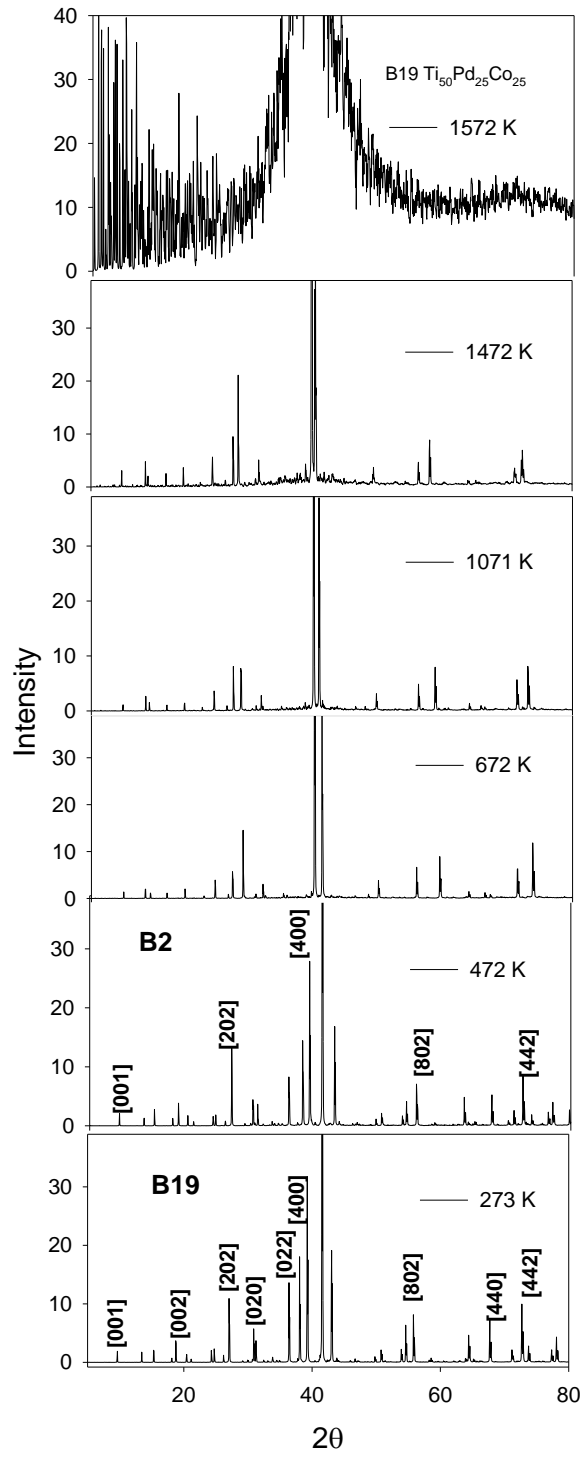
Figure 9-7 The simulated B19 Ti₅₀Pd₂₅Co₂₅ diffraction patterns from 273 to 1572 K
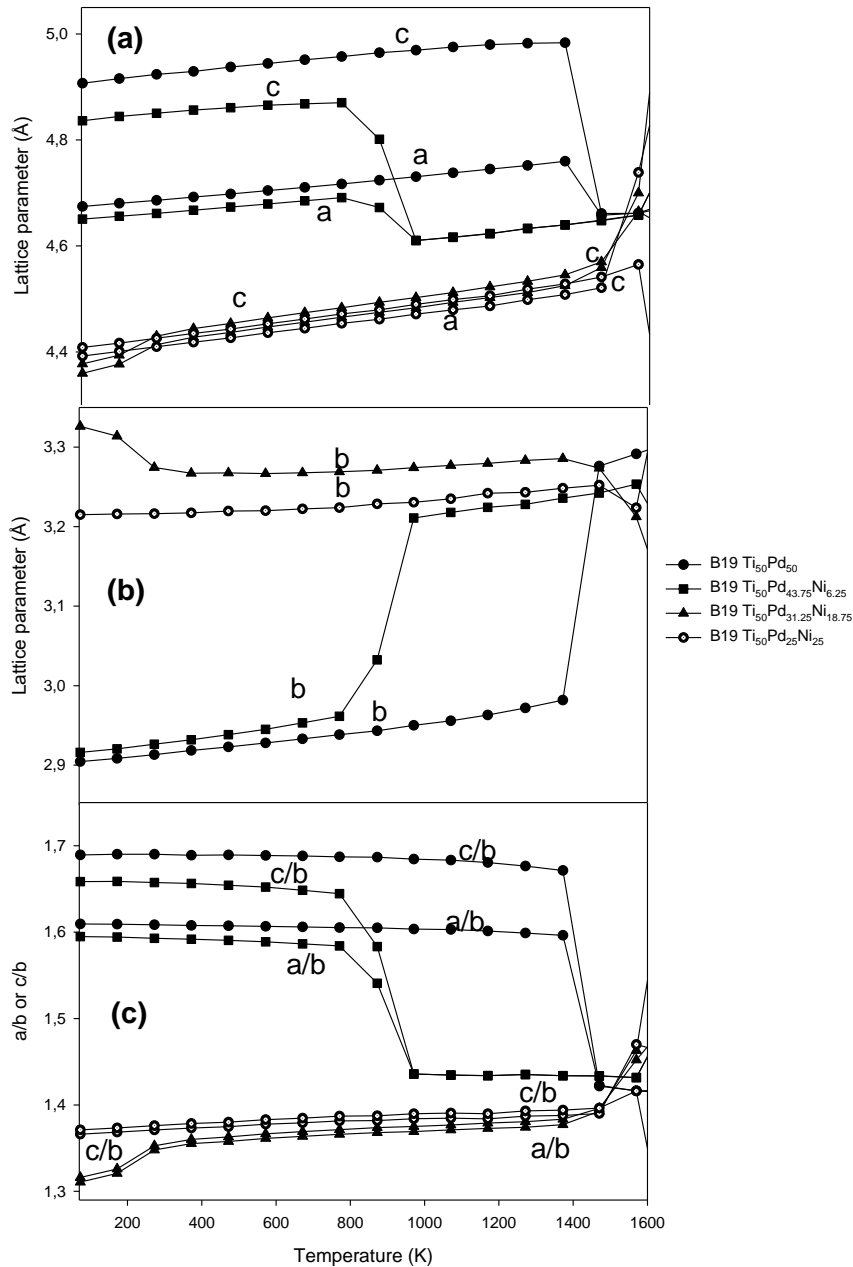
Figure 9-8 The effect of temperature on the (a) a and c (b) b (c) a/b and c/b lattice parameters of the B19 $Ti_{50}Pd_{50-x}Ni_x$ (x = 0, 6.25, 18.75 and 25).

Figure 9-9 shows the calculated XRD patterns of B19 $Ti_{50}Pd_{50-x}Ni_x$ alloys. The XRD patterns of B19 $Ti_{50}Pd_{50-x}Ni_x$ alloys are analyzed in order to determine the transformation temperature occurring at low and high temperature range. At 6.25 at. % Ni, it is observed that the number of peaks in the XRD pattern have the same sets of peaks from 73-871 K. This behaviour suggests that there is no

188

transformation at that temperature range. Furthermore, it is noted that the number of peaks reduces with an increase in temperature above 971 K which implies transformation from B19 to B2 phase. It is noted that the melting temperature is reached above 1669 K as the patterns become broad and deform. The result agrees very well with the predictions from lattice expansion as discussed in Figure 9-8. The simulated XRD patterns of B19 $Ti_{50}Pd_{31.75}Ni_{18.75}$ alloy at various temperature ranges (73-1572 K) are shown in Figure 9-9. As the temperature is increased from 73-472 K, it is observed that 18.75 at. % Ni maintains the same set of peaks of the B19 phase. It is clearly seen that above 572 K, the number of peaks for 18.75 at. % Ni is reduced and assumed to be the B2 phase patterns. The result suggests that there is a transformation from B19 to the B2 phase above 572 K and the structure becomes deformed at 1572 K.

In the case of B19 $Ti_{50}Pd_{25}Ni_{25}$ alloy, it is noted that the same set of peaks of the B19 phase are maintained below 172 K as shown in Figure 9-10. At 273 K, the number of peaks is reduced and are assumed to be B2 phase patterns. Furthermore, it is noted that when the temperature is increased to 1569 K, the peaks are broad which suggests that the melting temperature is reached. The transformation and the melting temperatures of B19 $Ti_{50}Pd_{50-x}Ni_x$ alloys obtained are lowered compared to the pure B19 $Ti_{50}Pd_{50}$.
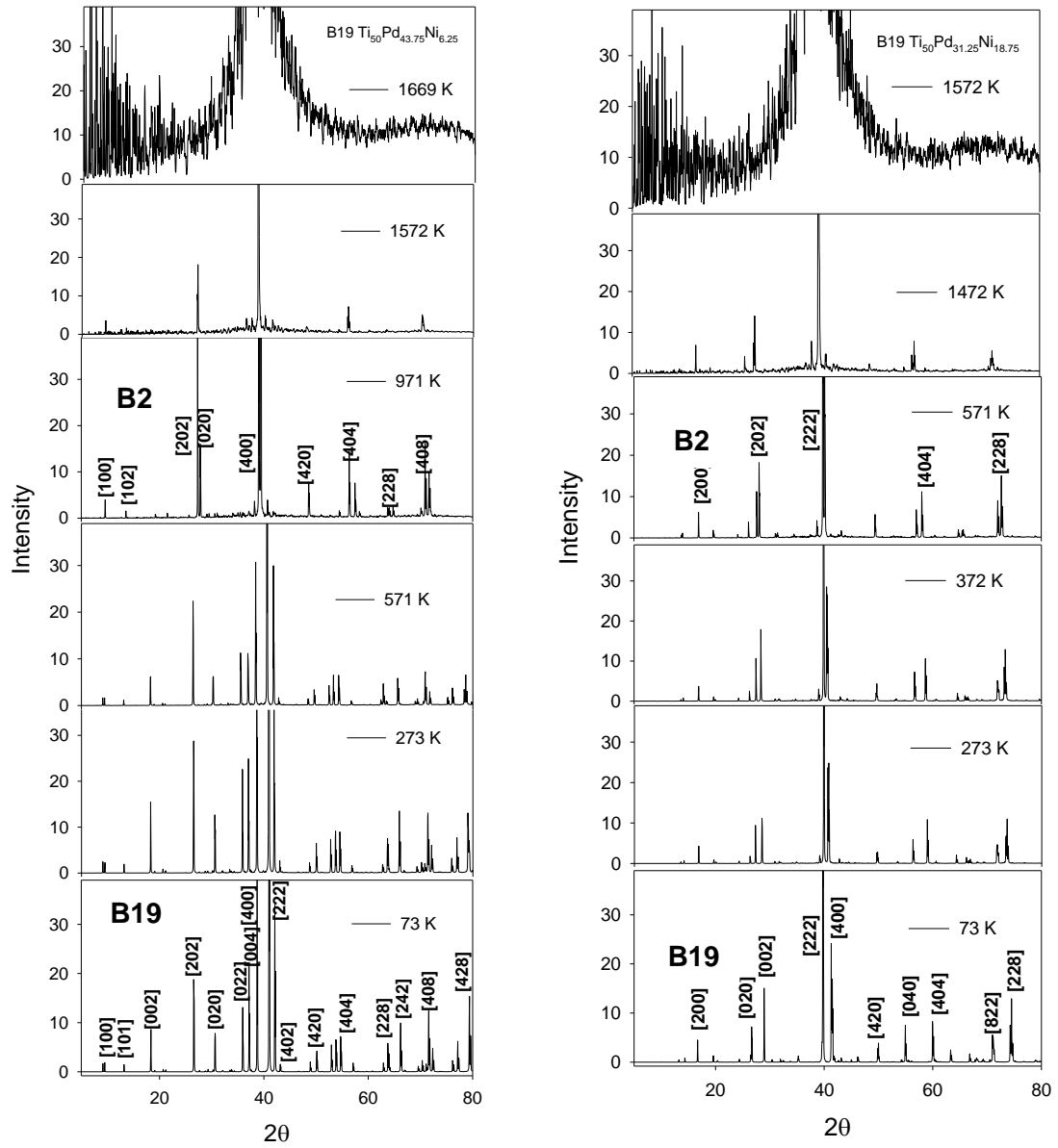
Figure 9-9 The simulated B19 Ti₅₀Pd₄₃.₇₅Ni₆.₂₅ and Ti₅₀Pd₃₁.₂₅Ni₁₈.₇₅ diffraction patterns from 73 to 1669 K.
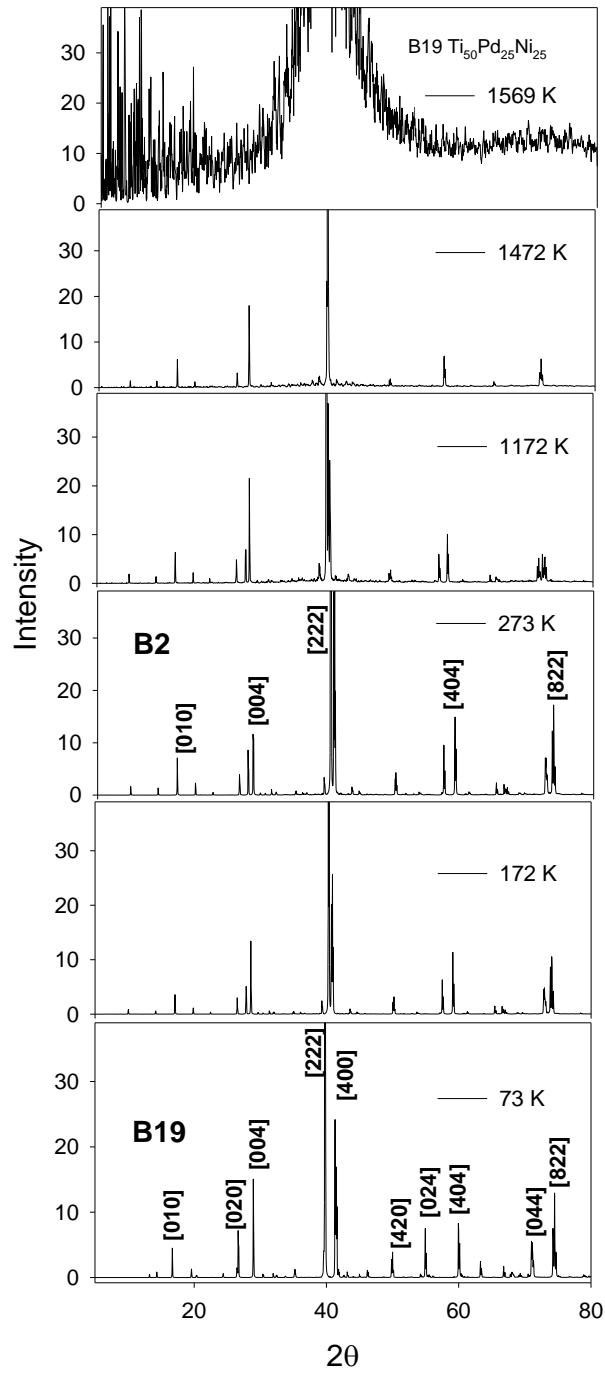
Figure 9-10 The simulated B19 Ti$_{50}$Pd$_{25}$Ni$_{25}$ diffraction patterns from 73 to 1569 K.

9.3 Elastic properties of B19 Ti$_{50}$Pd$_{50-x}$M$_x$ alloys with temperature.

The elastic properties are investigated to determine the strength of the material. The obtained nine independent elastic stiffness constants (C$_{ij}$) of the Ti$_{50}$Pd$_{50-x}$M$_x$ (M= Co and Ni) alloys are shown in Figures 9-11 to 9-14.

9.3.1 Elastic constants of B19 Ti$_{50}$Pd$_{50-x}$Co$_x$ with temperature

The temperature dependence of elastic constants for Ti$_{50}$Pd$_{50-x}$Co$_x$ (x= 6.25, 18.75 and 25) is calculated and shown in Figures 9-11. The elastic constants (c$_{11}$, c$_{12}$, c$_{13}$, c$_{22,}$ c$_{23}$, c$_{33}$, c$_{44}$, c$_{55}$ and c$_{66}$) decrease linearly with increase in temperature as 6.25 at. % Co is added to the system and all tend to converge to a common value at 1670 K. It is clearly seen that the values are very closer to each other between c$_{12}$ and c$_{13}$ for the entire temperature range. In the case of 18.75 at. % Co, the orthorhombic mechanical stability conditions are satisfied below 1572 K. It is noted that the elastic constants c$_{55}$ and c$_{66}$ are negative at 1670 K which implies instability of the structure at high temperature as the stability condition is not satisfied for 18.75 at. % Co.

At 18.75 at. %, almost similar values are observed between c$_{22}$ and c$_{33}$ at 273 K which may suggest possible transformation. The stability conditions of orthorhombic crystals are satisfied below 1572 K. A similar trend was observed with 25 at. % Co. We see a coupling between c$_{22}$ and c$_{33}$ at 273 K. Another coupling is observed between c$_{23}$ and c$_{33}$ above 1172 K indicating possible transformation. The last elastic constants (c$_{44}$, c$_{55}$ and c$_{66}$) reduces minimally with an increase in temperature. The instability is observed at 25 at. % Co as the c$_{55}$ and c$_{66}$ moduli become negative (-0.17 and -0.15 GPa) at temperature 1570 K.
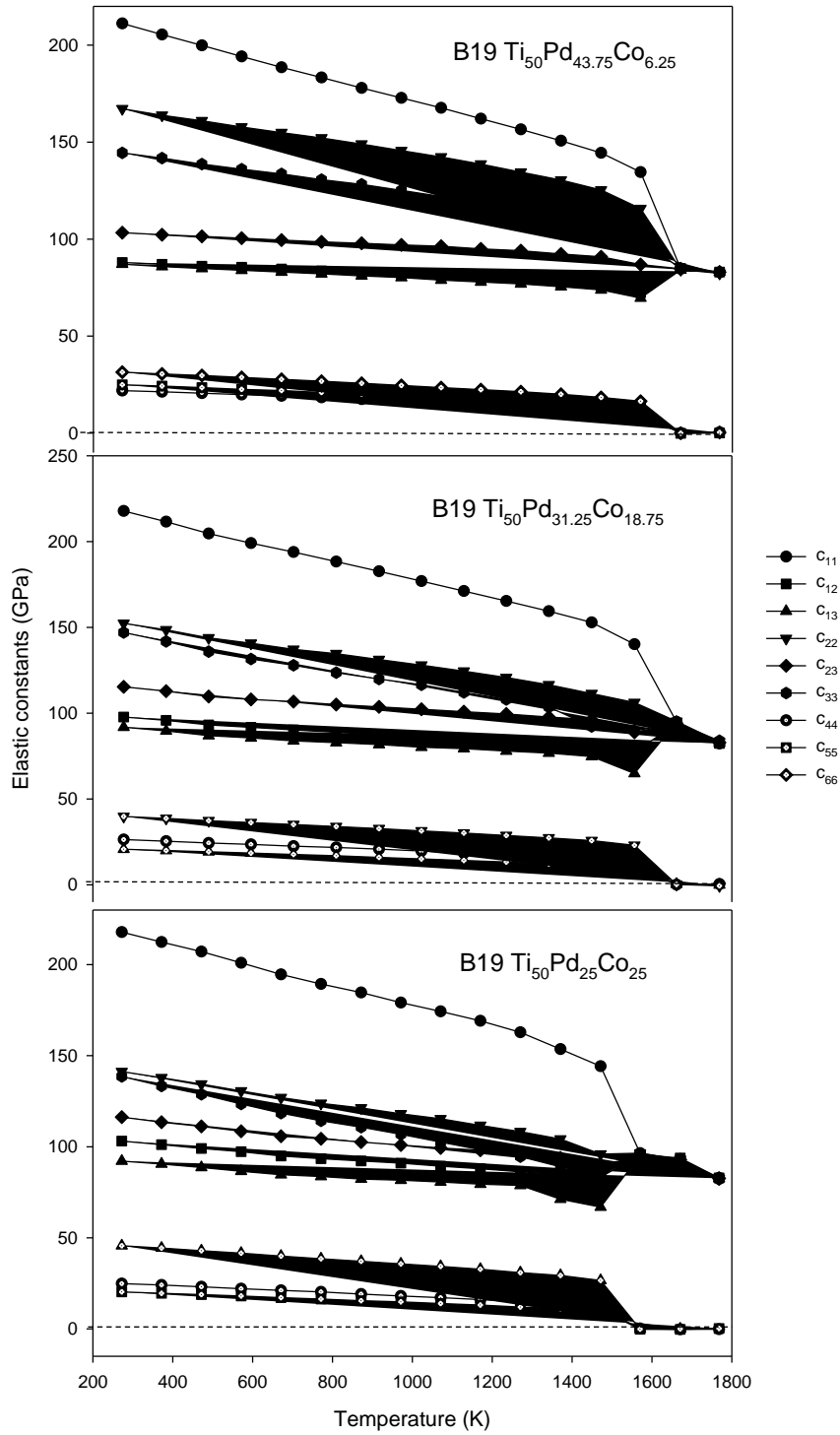
Figure 9-11 simulated elastic constants against temperature for Ti$_{50}$Pd$_{50-x}$Co$_x$ alloys (6.25 ≤ x ≤ 25). The dotted lines are used as a guide with respect to stability.

The elastic constant (c_{44}) becomes negative (-149.44 GPa) at 1370 K which suggests instability of structure at that temperature as shown in appendix A (Figure A-3). Again as shown in appendix A, the c_{44} and c_{55} moduli become negative (-0.35 and -0.06 GPa) at 1770 K for 50 at. % Co which suggests instability of the structure at a higher temperature.

The elastic shear moduli (C') are calculated and shown in Figure 9-12 at different temperature range (273-1800 K) for ternary B19 $Ti_{50}Pd_{50-x}Co_x$ alloys. There are three shear moduli ($c_{11} + c_{22} - 2c_{12}$), ($c_{11} + c_{33} - 2c_{13}$) and ($c_{22} + c_{33} - 2c_{23}$) for the orthorhombic system. At 6.25 at. % Co, it is noted that the shear moduli are positive below 1670 K and reduce as the temperature is increased to a negative value above. We observe a coupling between ($c_{11} + c_{22} - 2c_{12}$) and ($c_{22} + c_{33} - 2c_{23}$) at 18.75 at. % Co for the entire temperature range. We note sudden collapse from the three shear moduli from 1598 -1696 K which is due to the melting temperature being reached at 1680 K.

In the case of 25 at. % Co, it is noted that elastic shear modulus ($c_{11}+c_{22}-2c_{12}$) is negative at 1670 K which implies the mechanical instability of the structure. It is clearly seen that there is a coupling between ($c_{11} + c_{22} - 2c_{12}$) and ($c_{22} + c_{33} - 2c_{23}$) from 972 to 1273 K which suggest possible transformation from B19 to B2 phase. The mechanical stability of orthorhombic alloys is satisfied below 1670 K for 6.25 at. % Co and 1572 K for 18.75 and 25 at. % Co, respectively.
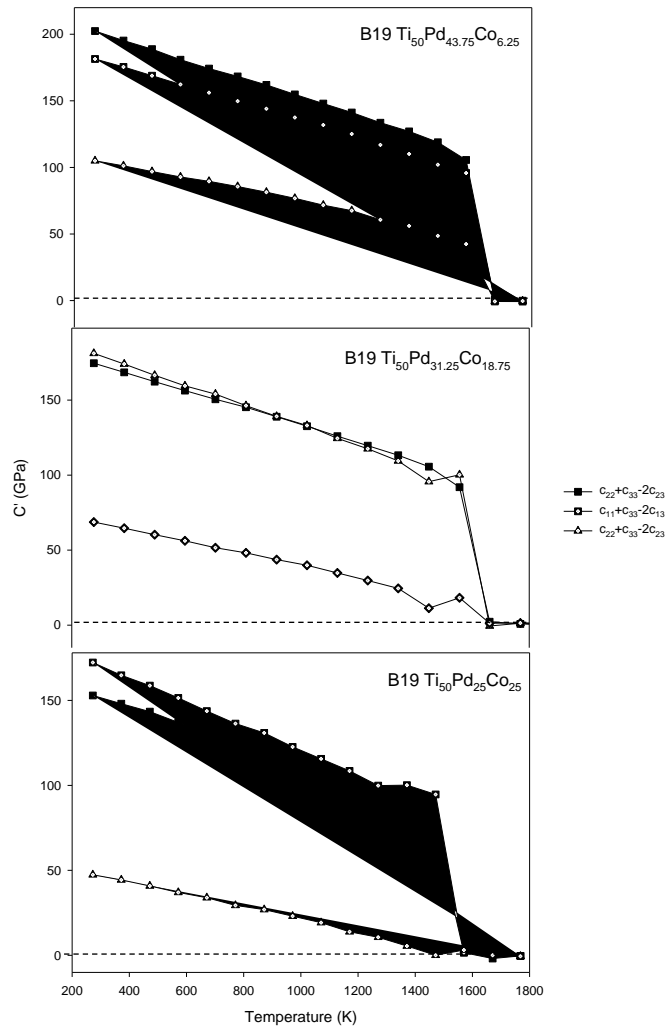
Figure 9-12 Calculated elastic shear modulus (C') against temperature for Ti$_{50}$Pd$_{50-x}$Co$_x$ alloys (6.25 ≤ x ≤ 25). The dotted lines are used as a guide with respect to stability.

9.3.2 B19 Ti$_{50}$Pd$_{50-x}$Ni$_x$ alloys elastic properties with temperature

Figure 9-13 shows the temperature dependence of the elastic constants for Ti$_{50}$Pd$_{50-x}$Ni$_x$ (x= 6.25, 18.75 and 25). At 6.25 at. % Ni, it is noted that the elastic constants decrease with an increase in temperature and converge to a common value at 1670 K. A coupling is observed between c_{12} and c_{13} (c_{12}= c_{13}) for the entire temperature range. A minimal decrease is found for c_{44}, c_{55} and c_{66} for the entire temperature range. In the case of 18.75 at. % Ni, It is clearly seen that c_{12}

and c_{13} have a common value for the entire temperature range while c_{23} and c_{33} are observed at 1472 K. On the other hand, the elastic constants (c_{44}, c_{55} and c_{66}) of 18.75 at. % Ni decreases minimally and tends to a common value above 1472 K.

In the case of 25 at. % Ni, the elastic constants decreases and tend to a common value at 1569 K. It is clearly seen that there is a coupling observed between c_{11} and c_{13} at 1372 K and between c_{23} and c_{33} at 1272 K. Furthermore, another coupling is found between c_{12} and c_{22} for the entire temperature range. This behaviour suggests possible transformation from the B19 B2 phase. The elastic constant (c_{44}) is negative above 1670 K while the elastic constant (c_{55}) becomes negative at 1769 K which indicates instability of the structure at high temperature as the stability condition is not satisfied.

Figure 9-14 shows the calculated shear moduli (C') of B19 $Ti_{50}Pd_{50-x}Ni_x$ alloys ($6.25 \leq x \leq 25$) at different temperature range (273-1800 K). It is noted that the shear moduli of $Ti_{50}Pd_{43.75}Ni_{6.25}$ are all positive below 1570 K and reduce to a common value as the temperature is increased above. The shear moduli ($c_{11} + c_{22} - 2c_{12}$), ($c_{11} + c_{33} - 2c_{13}$) became negative above 1670 K while ($c_{22} + c_{33} - 2c_{23}$) become negative above 1769 K, which indicate instability of 6.25 at. % Ni. The result indicates that $Ti_{50}Pd_{43.75}Ni_{6.25}$ is stable below 1570 K. In the case of $Ti_{50}Pd_{31.25}Ni_{18.75}$ and $Ti_{50}Pd_{25}Ni_{25}$ alloys, the result show stability below 1470 K and unstable above 1570 K. The orthorhombic mechanical stability conditions are satisfied below 1470, 1371 and 1569 K for $Ti_{50}Pd_{18.75}Ni_{31.25}$, $Ti_{50}Pd_{6.25}Ni_{43.75}$ and $Ti_{50}Ni_{50}$, respectively as shown in appendix A (Figure A-4).
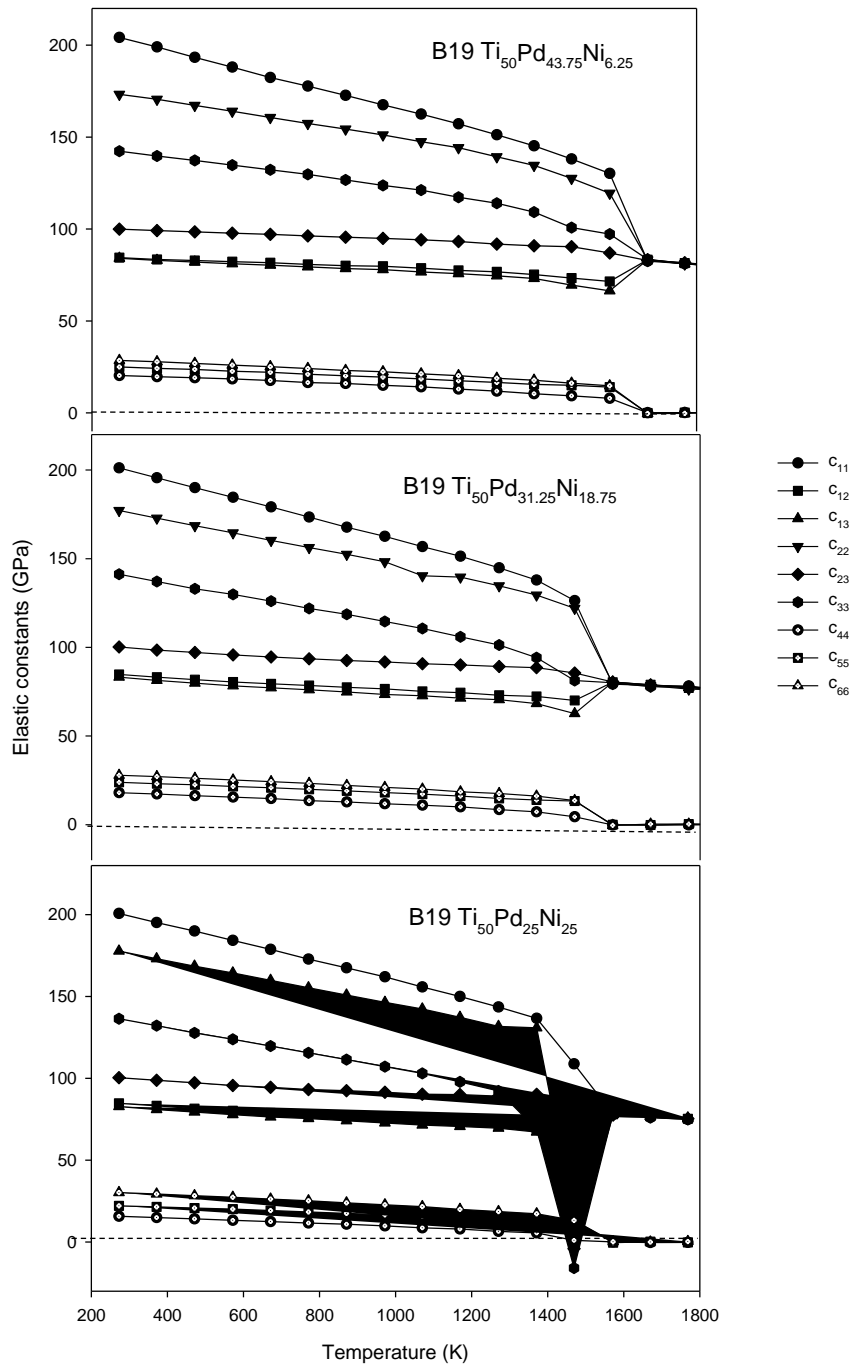
Figure 9-13 Simulated elastic constants against temperature for Ti₅₀Pd₅₀-ₓNiₓ alloys (6.25 ≤ x ≤ 25). The dotted lines are used as a guide with respect to stability.

197
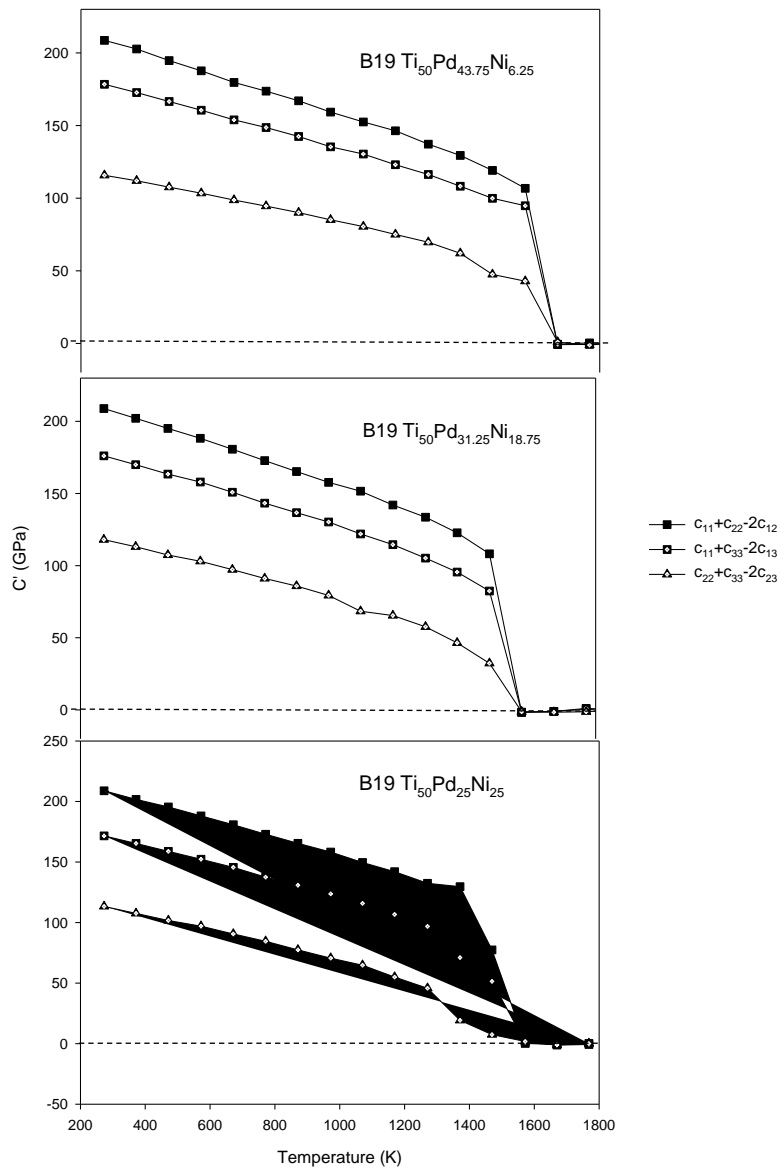
Figure 9-14 Calculated elastic shear modulus (C') against temperature for Ti$_{50}$Pd$_{50-x}$Ni$_x$ alloys (6.25 ≤ x ≤ 25). The dotted lines are used as a guide with respect to stability.

9.4   Elastic moduli and ductility of B19 Ti$_{50}$Pd$_{50-x}$M$_x$ alloys with temperature

Elastic moduli such as Bulk modulus (B), Young's modulus (E) and Shear modulus (G), play an important role in investigating their mechanical and the magnitude of the modulus which determines the ability to resist material

deformations such as resistances to bulk deformation, elastic deformation, and shear deformation.

9.4.1 Elastic moduli of B19 $Ti_{50}Pd_{50-x}M_x$ alloys with temperature

Figure 9-15 and Figure 9-16 show the calculated elastic modulus (Bulk, Young's and Shear modulus) with respect to temperature. It is found that as the temperature is increased, the values of Bulk modulus (B) decreases which suggests that high temperature does not enhance the ability to resist volume deformation for the entire concentrations of B19 $Ti_{50}Pd_{50-x}Co_x$ alloys. It is clearly seen that the B of 18.75 and 25 at. % Co is higher than 6.25 at. % Co below 600 K and lower above. A sudden drop is observed above 1600 K which suggests that the melting temperature is reached for 6.25 at. % Co. There is a fluctuation observed in B above1400 K for 18.75 at. % Co and above 1200 K for 25 at. % Co indicating that the material becomes soft before the melting temperature is reached. A similar trend was observed with the addition of Ni as shown in Figure 9-14. Interestingly, the B for the pure system, 6.25, 18.75 and 25 at. % Ni is similar and the same at 1572 K between the pure system and 6.25 at. % Ni. This behaviour suggests that the addition of Ni does not enhance hardness with temperature.

From the calculated results of Young's modulus (E) and Shear modulus (G), it can be seen that they all decrease with an increase in temperature which means that temperature can produce the weakest ability to resist elastic and shear deformations of B19 $Ti_{50}Pd_{50-x}Co_x$ alloys. The results indicate that the weakest

resistance to uniaxial tension and Shear deformation is observed above room temperature. It is clearly seen that G and E have the same values for the pure $Ti_{50}Pd_{50}$ system and $Ti_{50}Pd_{43.75}Co_{6.25}$ in the entire temperature range. A sudden drop is observed for both G and E at 1770 K for the pure system and 1670 K for the 6.25 at. % Co indicating that the melting temperature is reached. In the case of 18.75 and 25 at. % Co, a drop in G and E is observed at 1572 K. Similar trend is observed with Ni addition as indicated in Figure 9-14.
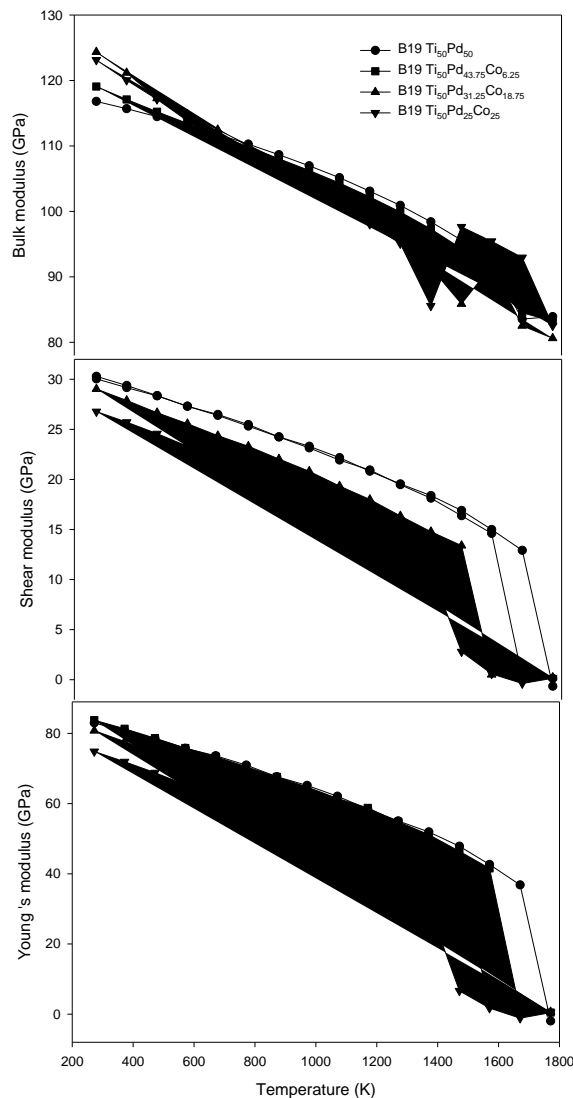
Figure 9-15 The predicted Bulk (B), Shear (G) and Young's (E) modulus against the temperature of $Ti_{50}Pd_{50-x}Co_x$ alloys (0 ≤ x ≤ 25).
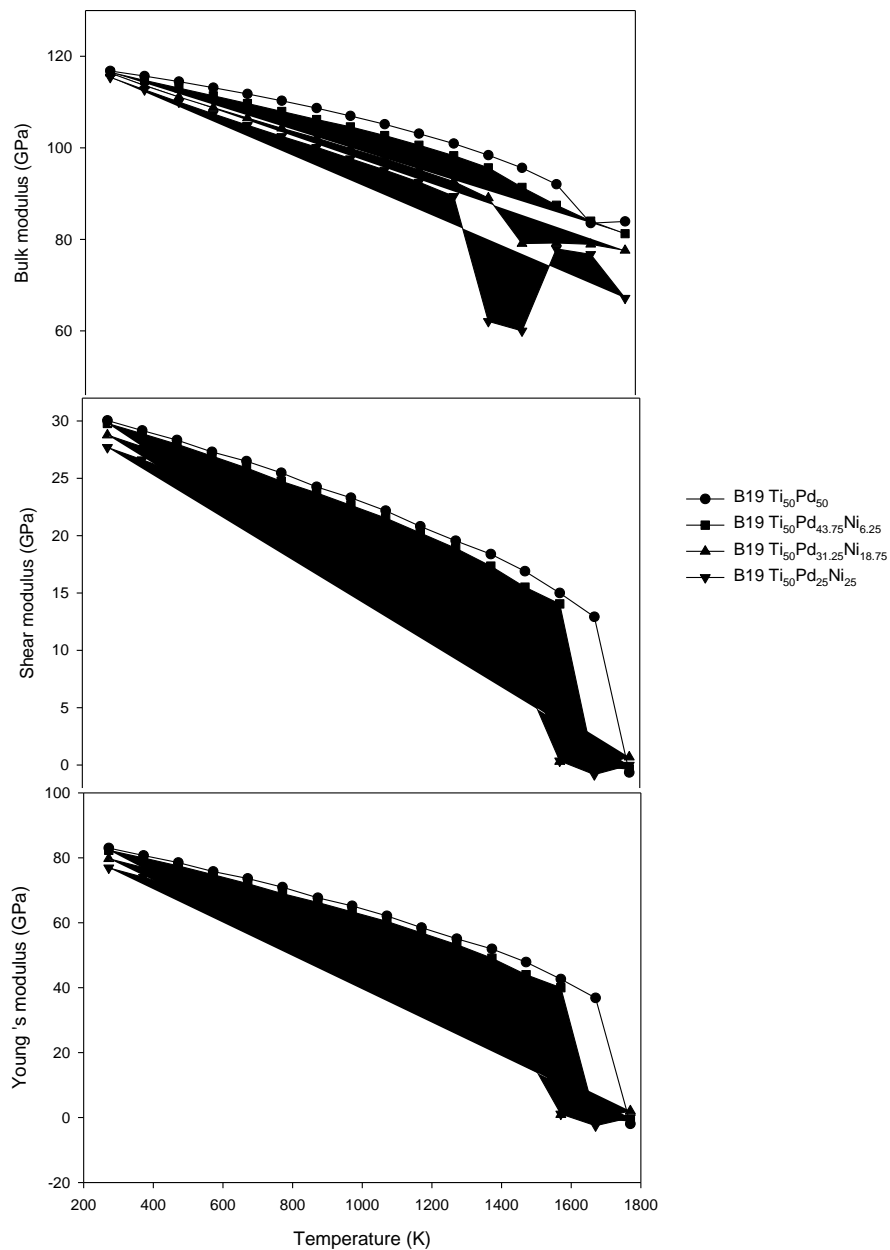
Figure 9-16 The calculated Bulk modulus, shear modulus G and Young's modulus E against temperature for $T_{i50}Pd_{50-x}Ni_x$ alloys (0 ≤ x ≤ 25).

9.4.2 Ductility of $Ti_{50}Pd_{50-x}M_x$ (M=Co, Ni) with temperature

Pugh (B/G) ratio was calculated to describe the ductility and brittleness of the material. As discussed in chapter 7, If the B/G>1.75 predicts the ductility otherwise the material has brittle behaviour (B/G<1.75). In Figure 9-17 (a), the

calculated B/G ratio for the entire concentrations is greater than 1.75 from 271-1771 K indicating that the ductility is improved with temperature. Poisson's ratio (σ) was evaluated to check the ductility of the material. If the σ exceeds 0.26 the structure is regarded as ductile otherwise, it is brittle. The calculated Poisson's ratio of $Ti_{50}Pd_{50-x}Co_x$ alloys is calculated and shown in Figure 9-17 (b). In Figure 9-17 (b), the calculated σ of $Ti_{50}Pd_{50-x}Co_x$ increases with an increase in temperature and the ratio is greater than 0.26. The results demonstrate that ductile behaviour with an increase in temperature. There is a good correlation between the B/G and Poisson's ratios as they show a similar trend.

The Poisson's ratio can be used to measure the compressibility of the material [171]. The materials will be considered incompressible if σ=0.5 and compressible when σ range from 0.2-0.49 [172]. The calculated σ of $Ti_{50}Pd_{43.75}Co_{6.25}$ alloy ranges from 0.38-0.42 as shown in Figure 9-17 (b). The result indicates that the material is compressible with an increase in temperature. It is noted that σ varies from 0.39-0.42 as the temperature is increased from 271-1470 and σ=0.5 above 1570 K. The finding implies that $Ti_{50}Pd_{31.25}Co_{18.75}$ is compressible below 1470 K and incompressible above 1570 K.

In Figure 9-17 (b), the σ of $Ti_{50}Pd_{25}Co_{25}$ range from 0.40-0.49 is compressible between 272-1470 K and incompressible as σ=0.5. The result suggests that the material is compressible below 1470 K and incompressible above 1570 K.
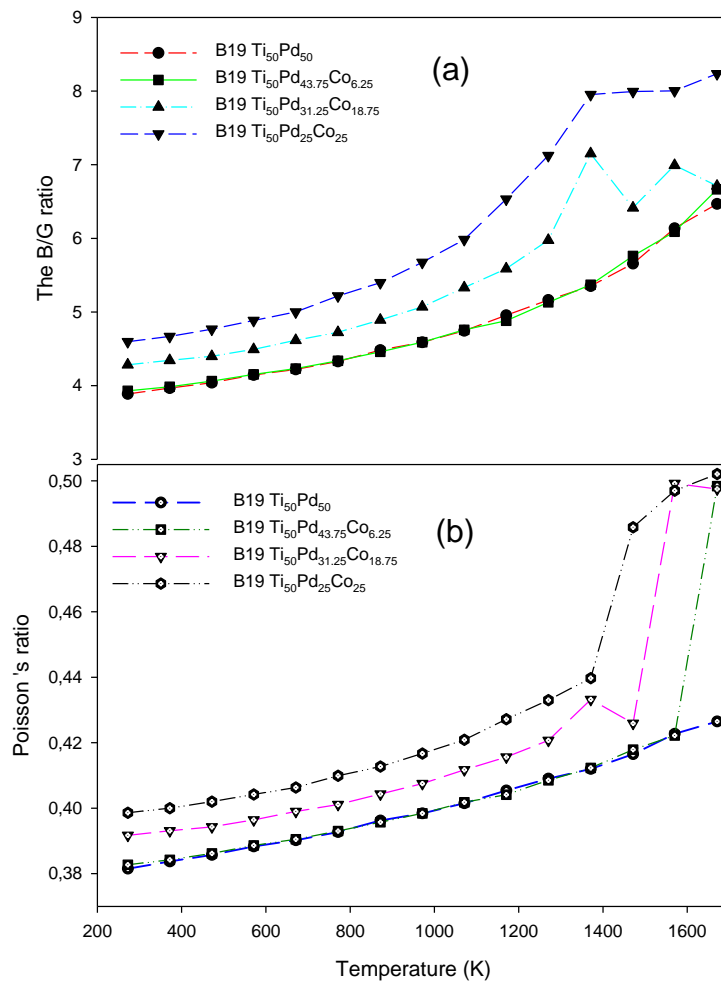
Figure 9-17 Simulated the (a) B/G and (b) Poisson's ratio against the temperature of Ti$_{50}$Pd$_{50-x}$Co$_x$ alloys.

As shown in Figure 9-18 (a), the calculated B/G ratio of Ti$_{50}$Pd$_{50-x}$Ni$_x$ alloys is greater than 1.75 which implies that the ductility is improved with temperature. Figure 9-18 (b) shows the calculated Poisson's ratio of Ti$_{50}$Pd$_{50-x}$Ni$_x$ alloys with temperature. As the amount of Ni is added, the calculated σ increase with an increase in temperature and the ratio is greater than 0.26. The result shows that Ti$_{50}$Pd$_{50-x}$Ni$_x$ alloys show ductile behaviour for the entire temperature range. Furthermore, Poisson's ratio (σ) can be used to check the compressibility of the material. The materials will be measured incompressible if σ= 0.5 and

compressible when σ range from 0.2-0.49 [172]. The measured σ of Ti$_{50}$Pd$_{43.75}$Ni$_{6.25}$ alloy vary from 0.38-0.42 below 1570 K which indicates that the material is compressible. It is observed that when the temperature is increased above 1670 K, the σ= 0.50 which implies that Ti$_{50}$Pd$_{43.75}$Ni$_{6.25}$ is incompressible. At 18.75 at. % Ni, the σ range from 0.38-0.42 with an increase in temperature from 271-1470 K which suggests that the material is compressible and incompressible above 1570 K as σ= 0.5.

In Figure 9-18 (b), the σ of Ti$_{50}$Pd$_{25}$Ni$_{25}$ vary from 0.39-0.43 from 272-1371 K revealing that the material is compressible while σ= 0.5 above 1470 K which indicates incompressible. The result of Ti$_{50}$Pd$_{50-x}$Ni$_{x}$ alloys suggests that the material is incompressible at a higher temperature depending on the compositions.
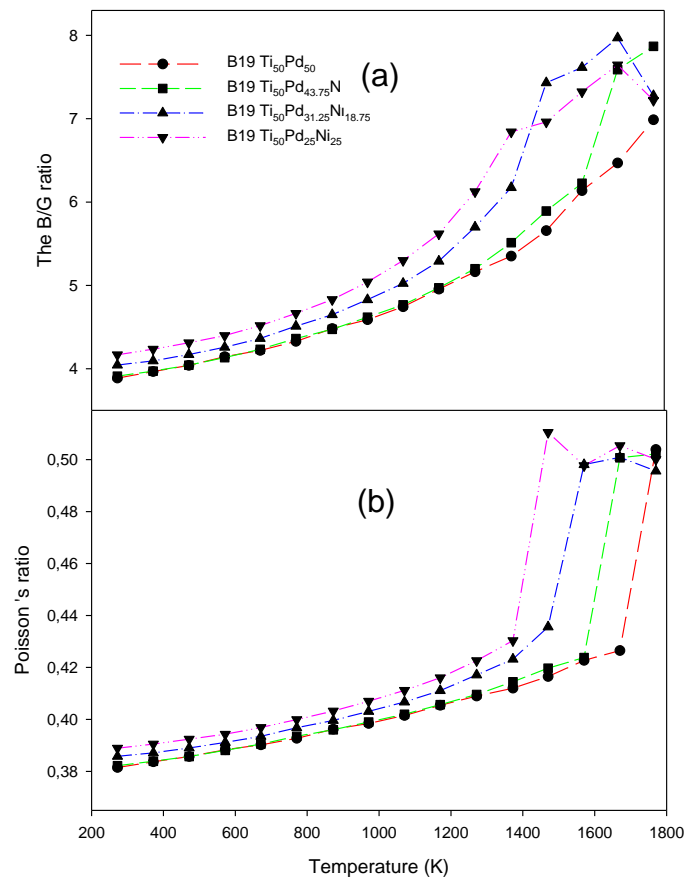
Figure 9-18 The predicted (a) B/G and (b) Poisson's ratio against temperature for Ti$_{50}$Pd$_{50-x}$Ni$_x$ alloys (0 ≤ x ≤ 25).

Chapter 10

Parameterization and transformation temperature of $Ti_{50}Pd_{50}$ and $Ti_{50}Pd_{50-x}Ru_x$ systems

In this chapter, we present and discuss the parameterization of the self-consistent-charge density functional tight-binding (SCC-DFTB) set of parameters for the binary $Ti_{50}Pd_{50}$ and ternary $Ti_{50}Pd_{50-x}Ru_x$. Ru was chosen due to its higher temperature capability as well as mechanical and thermal stability which was observed in chapters 7 and 8 as compared to other alloying elements. The parameterization technique is used to describe the suitable SCC sets of parameters necessary to describe the interactions within the systems. To describe the $Ti_{50}Pd_{50}$ structure, the Ti-Pd, Pd-Ti, Ti-Ti and Pd-Pd interactions are considered while for the $Ti_{50}Pd_{50-x}Ru_x$ system the Ti-Pd, Pd-Pd, Pd-Ti, Ti-Ru, Pd-Ru, Ru-Ti, Ru-Pd, Ru-Ru and Ti-Ti interactions are described. These parameters are then used to calculate the structural, electronic and elastic properties of $Ti_{50}Pd_{50}$ and $Ti_{50}Pd_{50-x}Ru_x$. The calculated bond distances and lattice parameters are compared with the available experimental and theoretical findings. Furthermore, the SCC sets of parameters were also used to determine the lattice expansions for both binary and ternary systems. Detailed illustration of the SCC-DFTB method has been described previously in chapter 3.

10.1 Development and validation of a SCC-DFTB set of parameters

Before any parameters can be deduced, parameterization of the systems is carried out. Firstly, parameterization is done in order to find the pairwise interaction set. Secondly, derived parameters are used to describe the interactions in the Ti-Pd and Ti-Pd-Ru systems. In particular the Ti-Pd, Pd-Pd, Pd-Ti, Ti-Ru, Pd-Ru, Ru-Ti, Ru-Pd, Ru-Ru and Ti-Ti interactions. The parameterization of the binary $Ti_{50}Pd_{50}$ and ternary $Ti_{50}Pd_{50-x}Ru_x$ structures was performed by adjusting the wave function confinement radius (Radii 1). This is done until the bond distance and lattice parameter are comparable with the theoretical (initial optimization of structure) and experimental results, to the allowed difference of < 10 %. These parameters are stored in a Slater-Koster library file of the program [173]. In addition, the Slater-Koster library file contains electronic parameters, short range potentials and the Hubbard terms for the element pairs of the structure.

Note, different exchange-correlation functionals were used to develop sets of the parameter that is the GGA-PBE and LDA-PWC. This was done to check which functional is suitable to describe the structural properties accurately. It is clearly seen that GGA overestimates the lattice parameters while LDA underestimates the value as expected [174], see Table 10-1. The GGA functional gave values close to the experimental as compared to LDA. Thus the GGA will be used in all calculations.

10.1.1 Binary Ti$_{50}$Pd$_{50}$ alloys

The SCC sets of parameters to describe the binary Ti$_{50}$Pd$_{50}$ systems were achieved when the wave function confinement radii were set to 1.500 Bohr for both Ti and Pd. The Hubbard terms for Ti was found to be (0.201 0.144 0.350) and (0.210 0.336 0.336) for Pd.

Table 10-1 shows the predicted structural properties for the Ti$_{50}$Pd$_{50}$ systems. In order to validate the developed sets of parameters, we have compared our results with the available experimental and theoretical results. The lattice parameters of B19 obtained using DFTB+ (GGA) are larger than those from VASP, DMol^3 and literature [54], but they are within the acceptable range of < 5-10 %. We note that the B19′, B2 and L1$_0$ gave lattice parameters that are in good agreement with those from VASP and DMol^3 code.

Table 10-2 shows the Ti-Pd, Ti-Ti and Pd-Pd bond distances. It was observed that the Ti-Pd bond distance is shorter (2.660 Å) for B19′ which leads to stronger interaction as compared to other phases (B19, L1$_0$ and B2). It was found that the bond distances are well reproduced to within 5 % with the values obtained from the literature. Interestingly, the bond distances obtained using DFTB+ gave similar values as compared to the DMol^3 findings. Furthermore, the calculated bond distance using the VASP code is in reasonable agreement with the literature to within 2 %. The obtained SCC parameters are reliable since the bond distances gave better comparison with the DMol^3, VASP and literature to within 2 % agreement.

Table 10-1 Comparison of the equilibrium lattice parameters (a, b, c) using LDA and GGA functional with available experimental values of the B19, B19′, B2 and L1$_0$ Ti$_{50}$Pd$_{50}$ alloy.

Structure	Method	a (Å)	b (Å)	c (Å)
B19	DMol^3 (GGA)	4.649	2.851	4.966
	DFTB+ (LDA)	4.587	2.545	4.687
	DFTB+ (GGA)	4.710	2.879	4.899
	VASP (GGA)	4.587	2.789	4.897
	Exp. [20]	4.550	2.780	4.860
B19′	DMol^3 (GGA)	2.848	4.983	4.638
	DFTB+ (LDA)	2.631	4.670	4.452
	DFTB+ (GGA)	2.815	4.831	4.684
	VASP (GGA)	2.792	4.912	4.582
B2	DMol^3 (GGA)	3.165	3.165	3.165
	DFTB+ (LDA)	3.127	3.127	3.127
	DFTB+ (GGA)	3.168	3.168	3.168
	VASP (GGA)	3.170	3.170	3.170
	Exp. [23]	3.180	3.180	3.180
L1$_0$	DMol^3 (GGA)	2.855	2.855	3.907
	DFTB+ (LDA)	2.579	2.579	3.671
	DFTB+ (GGA)	2.708	2.708	3.986
	VASP (GGA)	2.826	2.826	3.891

Table 10-2 Comparison of the bond distance of B2, L1$_0$, B19 and B19' Ti$_{50}$Pd$_{50}$ alloy using GGA functional.

Structure		Bond distance (Å)		
		Ti-Pd	Pd-Pd	Ti-Ti
B2	DFTB	2.744	3.168	3.168
	DMol^3	2.744	3.168	3.168
	VASP	2.754	3.180	3.180
	Exp. [23]	2.743	3.168	3.168
L1$_0$	DFTB	2.710	2.803	2.803
	DMol^3	2.710	2.803	2.803
	VASP	2.701	2.855	2.855
	Theo. [34]	2.701	2.855	2.855
B19	DFTB	2.719	2.796	3.031
	DMol^3	2.719	2.796	3.031
	VASP	2.717	2.810	3.023
	Exp. [20]	2.747	2.796	3.030
B19′	DFTB	2.600	3.413	3.460
	DMol^3	2.600	3.413	3.460
	VASP	2.661	3.391	3.469
	Theo. [34]	2.660	3.391	3.469

10.1.2 B2 and B19 Ternary Ti$_{50}$Pd$_{50-x}$Ru$_x$ alloys

In the case of B2 and B19 Ti$_{50}$Pd$_{50-x}$Ru$_x$ alloys, the SCC-DFTB approach has been used to accurately calculate their ground state properties. Firstly, parameterization was performed to establish the appropriate interaction parameters for the Ti$_{50}$Pd$_{50-x}$Ru$_x$ system. The developed SCC-DFTB set of

parameters for Ti-Pd, Pd-Pd, Pd-Ti, Ti-Ru, Pd-Ru, Ru-Ti, Ru-Pd, Ru-Ru and Ti-Ti pair of elements for describing $Ti_{50}Pd_{50-x}Ru_x$ system was validated by performing a geometry optimization using DFTB+ code. The validation was done using GGA-PBE exchange-correlation functionals. Smearing was varied from 0.003 to 0.008 to help improve the accuracy of the results. It is noted that smearing of 0.007 Ha gave better structural properties as compared to the literature [54] to about 3 % agreement.

The calculated lattice parameters are summarized in Table 10-3. It was found that DFTB results are in reasonable agreement with the $DMol^3$ results when the Radii 1 of Ti, Pd and Ru were set to be 1.900 Bohr. The resultant Hubbard terms were (0.201 0.144 0.351) for Ti, (0.210 0.336 0.336) for Pd and (0.212 0.118 0.329) for Ru.

It is noted that the lattice parameters decrease with the addition of Ru content and this may be attributed to the small atomic radius of Ru, compared to that of Pd (as shown in Table 10-3). The lattice parameters obtained using DFTB+ code are larger than those from VASP code, to within 5 % agreement.

In the case of B19 $Ti_{50}Pd_{50-x}Ru_x$ alloys, it is noted that a and c parameters decrease with an increase in Ru while the b increases as shown in Table 10-4. The lattice parameters from the derived potentials are in good agreement to within 3 % with those from standard DFT calculations.

Table 10-3 The equilibrium lattice parameters of the B2 $Ti_{50}Pd_{50-x}Ru_x$ alloys. The experimental value is shown in parenthesis.

Structure	a (Å)		
	DFTB+	DMol3	VASP
$Ti_{50}Pd_{43.75}Ru_{6.25}$	3.216	3.208	3.200
$Ti_{50}Pd_{31.25}Ru_{18.75}$	3.195	3.179	3.158
$Ti_{50}Pd_{25}Ru_{25}$	3.171	3.161	3.132
$Ti_{50}Pd_{18.75}Ru_{31.25}$	3.152	3.145	3.120
$Ti_{50}Pd_{6.25}Ru_{43.75}$	3.130	3.117	3.108
$Ti_{50}Ru_{50}$	3.113 (3.085) [54]	3.106	3.084

Table 10-4 The equilibrium lattice parameters of the B19 $Ti_{50}Pd_{50-x}Ru_x$ alloys

Structure	a (Å)		b (Å)		c (Å)	
	DFTB+	VASP	DFTB+	VASP	DFTB+	VASP
$Ti_{50}Pd_{43.75}Ru_{6.25}$	4.532	4.528	2.859	2.856	4.826	4.822
$Ti_{50}Pd_{31.25}Ru_{18.75}$	4.478	4.478	2.959	2.959	4.638	4.638
$Ti_{50}Pd_{25}Ru_{25}$	4.422	4.416	3.099	3.092	4.826	4.433
$Ti_{50}Pd_{18.75}Ru_{31.25}$	4.418	4.391	3.146	3.112	4.420	4.392
$Ti_{50}Pd_{6.25}Ru_{43.75}$	4.414	4.353	3.126	3.088	4.412	4.350
$Ti_{50}Ru_{50}$	4.398	4.338	3.110	3.071	4.399	4.348

10.2 Binding energy

The binding energy was calculated to validate our set parameters in order to determine the stability of $Ti_{50}Pd_{50}$ and $Ti_{50}Pd_{50-x}Ru_x$ alloys. It also plays an important role in understanding the properties of materials, such as diffusion kinetics and age-hardening response [175].

The binding energy is determined by the following expression:

$$E_b = E_{tot} - \sum_i E_{atom}^i, \qquad \text{(10-1)}$$

where E_{tot} is the calculated total energy of the system under consideration and $\sum_i E_{atom}^i$ is the sum of energies of the atoms constituting the system. Note that negative binding energy indicates an energetically favourable system otherwise unstable [175].

10.2.1 Binary Ti$_{50}$Pd$_{50}$ alloy

The binding energy of the binary systems is shown in Figure 10-1. All the structures displays negative binding energy which suggests that these structures (B2, L1$_0$, B19, B19') are stable and can be found experimentally. The results show that among all phases, the B19' display the lowest binding energy and B2 has the highest binding energy. This suggests that B19' binds strongly and is considered the most stable phase while B2 is the least stable. The order of stability is B19'> B19> L1$_0$> B2.
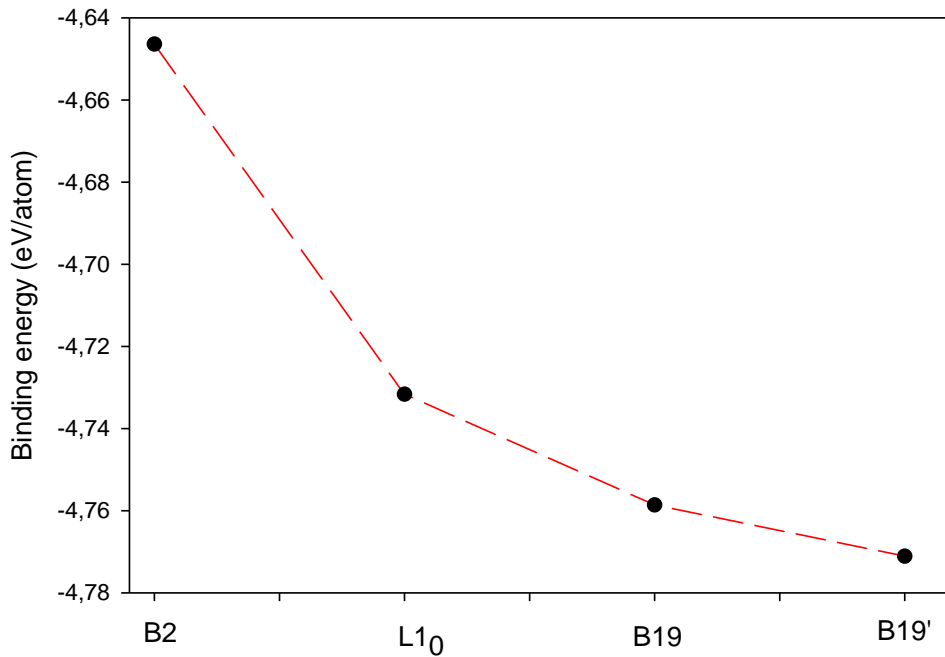
Figure 10-1 Calculated binding energy per atom for $Ti_{50}Pd_{50}$ systems: B2, $L1_0$, B19 and B19'.

10.2.2 Ternary B2 and B19 $Ti_{50}Pd_{50-x}Ru_x$ alloys

Figure 10-2 compares the binding energy for B2 and B19 $Ti_{50}Pd_{50-x}Ru_x$ systems ($0 \leq x \leq 50$). It is clearly seen that the binding energy decreases as the concentration of Ru are increased. At a small composition below 6.25 at. % Ru, the binding energy of B19 is more negative compared to B2. However, as the amount of Ru is increased above 18.75 at. %, the B2 phase becomes more stable at higher Ru compositions as compared to the B19 phase. This behaviour may suggest a possible transformation from B2 to the B19 phase. The results show that among all compositions, the B2 $Ti_{50}Pd_{6.25}Ru_{43.75}$ have the lowest binding energy and as compared to B19 $Ti_{50}Pd_{50-x}Ru_x$ alloys. The observations suggest that B2 $Ti_{50}Pd_{6.25}Ru_{43.75}$ binds strongly and is considered the most stable structure, while B2 $Ti_{50}Pd_{43.75}Ru_{6.25}$ is the least stable.

Similar behaviour was observed in B19 $Ti_{50}Pd_{50-x}Ru_x$ alloys since the binding energy curve decreases and becomes more negative with Ru additions. This shows that the additions of Ru stabilise the B2 phase, and are thus important for enhancing the properties of the system. Our results are consistent with the ΔH_f trend except for 6.25 and 18.75 at. % Ru as shown in Figure 6-4 (d). The energy difference between B2 and B19 at 25 at. % is -0.05 and -0.02 eV/atom for 43.75 at. % Ru which suggests that the values are very close to each other.
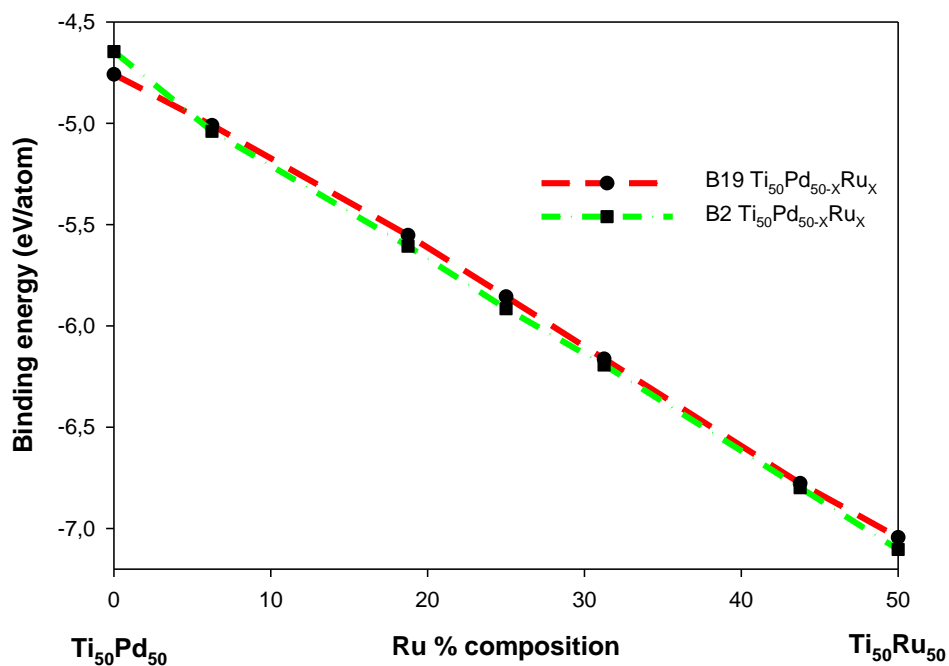
Figure 10-2 Trend of binding energy for B19 and B2 $Ti_{50}Pd_{50-x}Ru_x$ alloys ($0\leq x \leq 50$).

10.3 Density of states of $Ti_{50}Pd_{50}$ and $Ti_{50}Pd_{50-x}Ru_x$ alloys

The electronic density of states for the binary $Ti_{50}Pd_{50}$ and ternary $Ti_{50}Pd_{50-x}Ru_x$ has been calculated from derived sets of parameters using DFTB+ code. As highlighted in chapter 4, the tDOS can be used to predict the electronic stability

of the compound by observing the behaviour of states near the Fermi level ($E-E_f=0$) with respect to the pseudogap. The structure with the highest and lowest density of states at E_f is considered the least and most stable, respectively [26]. This will show how the tDOS calculated using standard DFT are comparable with those using the potential parameter in DFTB+.

10.3.1 Total DOS for binary $Ti_{50}Pd_{50}$ alloy

The electronic density of states calculations of B2, B19, B19′ and L1$_0$ $Ti_{50}Pd_{50}$ are compared in Figure 10-3 (a). It is noted that the total DOS peak of B19′, B19 and L1$_0$ structures shifted to the right of the Fermi level and a similar behaviour was observed for B19 and L1$_0$. As a result, the E_f hits the shoulder of the dropping total DOS peak which indicating less stability of the structure. Interestingly, amongst the three phases, the B19′ has the lowest states at the E_f followed by B19 then L1$_0$. In the case of the B2 structure, we see that the E_f hits the total DOS peak on the right shoulder near the E_f. The results suggest that B2 is less stable compared to other structures and this is consistent with the prediction of binding energy. The order of stability is predicted to be B19′> B19> L1$_0$> B2. The tDOS plot is similar to those predicted using standard DFT (as shown in Figure 10-3 (b)). However, DFTB+ does not distinguish clearly between B19 and B19', this may be due to similar potential parameters used. Furthermore, we obtained the improved tDOS behaviour which may be attributed to the effectiveness of the potential parameters. Particularly with regard to B2 tDOS which are lowered at Ef as compared to those in VASP. The derived potential parameters are able to reproduce the similar tDOS behaviour compared to the standard DFT.
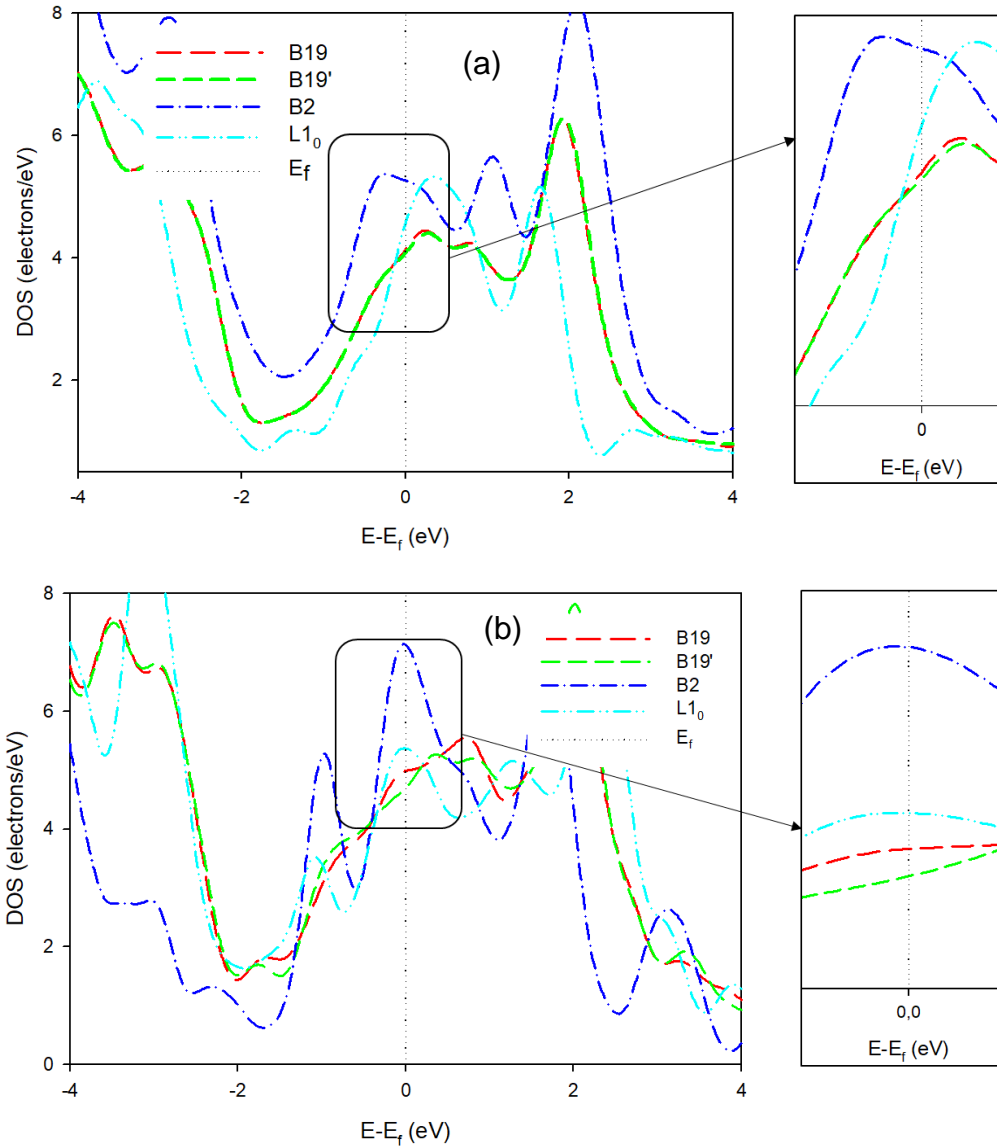
Figure 10-3 A comparison of the total density of states for B19, L1$_0$, B2 and B19' Ti$_{50}$Pd$_{50}$ system calculated from a) derived potentials using the DFTB+ code and b) first principle method with the VASP code. The Fermi level is taken as the zero energy (E-E$_f$=0).

10.3.2 Total DOS for B2 and B19 Ti$_{50}$Pd$_{50-x}$Ru$_x$ alloys

The B2 Ti$_{50}$Pd$_{50-x}$Ru$_x$ DOS are also presented in Figure 10-4 (a) to show precisely

the behaviour near E$_f$ as Ru is added to the system. It was observed that the DOS

peak shift towards the conduction band (CB) when Ru content is increased. Note

that the Ti$_{50}$Ru$_{50}$ tDOS are lowered at E$_f$, similar to the VASP results (Figure 6-5)

(showing the stability of the system). As the composition of Ru is added, the pseudogap moves toward the E_f showing that the $Ti_{50}Pd_{50}$ became electronically stable. It is clearly seen that the 43.75 at. % of Ru displays the lowest DOS at E_f which confirms that it is the most stable composition. This observation suggests that $Ti_{50}Pd_{50-x}Ru_x$ is electronically stable at high content of Ru. The stability trend according to the density of states agrees very well with binding energy results.

The tDOS of B19 $Ti_{50}Pd_{50-x}Ru_x$ alloys calculated using our derived potentials is also given in Figure 10-4 (b). Our derived potentials were able to produce the tDOS of B19 $Ti_{50}Pd_{50-x}Ru_x$ alloys. More importantly, the trend of the DOS peak is similar except that the intensities peak size is reduced as compared to the B2 $Ti_{50}Pd_{50-x}Ru_x$ alloys tDOS (Figure 10-4 (a)). These differences in the tDOS can be due to the SCC set parameters of the derived potentials.
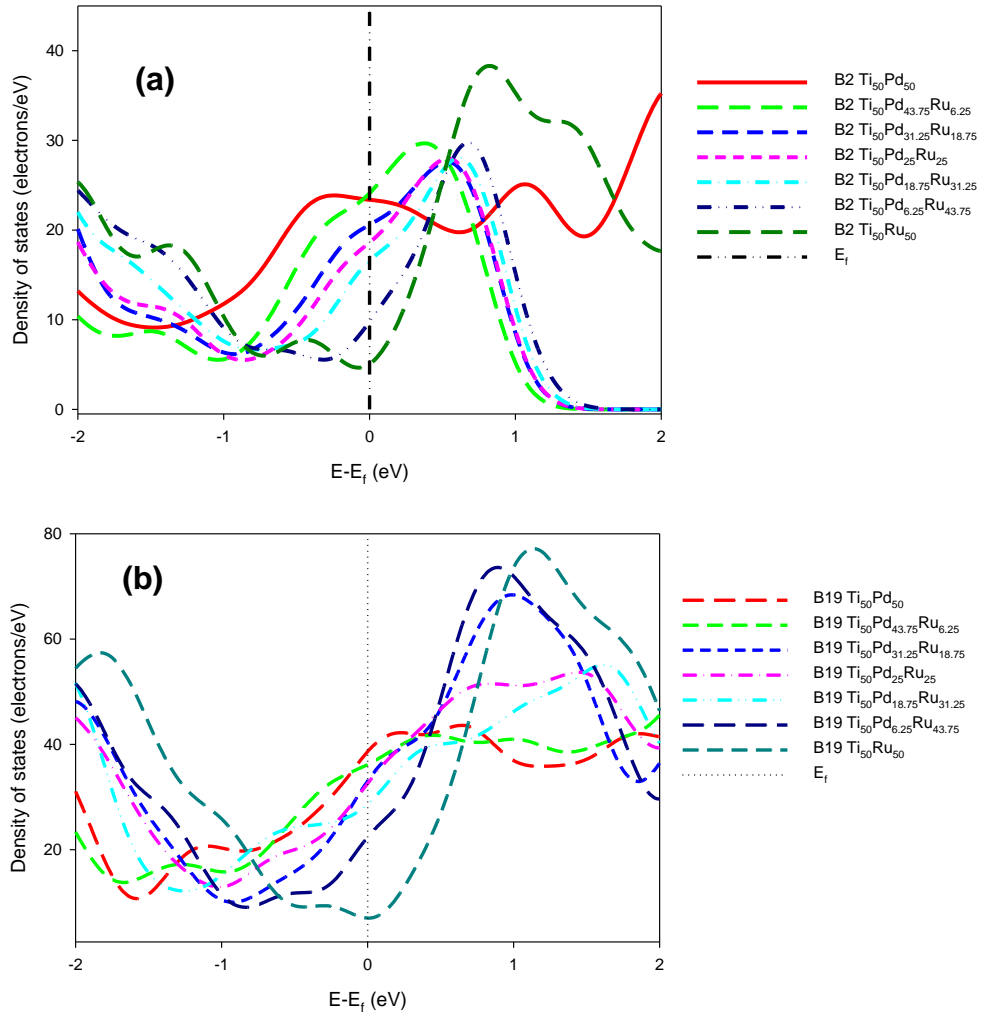
Figure 10-4 A comparison of the total densities of states (DOS) of (a) B2 and (b) B19 Ti$_{50}$Pd$_{50-x}$Ru$_x$ SMAs (0≤x≤50) calculated using a) DFTB+ code. The Fermi level is taken as the energy zero (E-E$_f$=0).

10.4 Elastic properties of Ti$_{50}$Pd$_{50}$ and ternary Ti$_{50}$Pd$_{50-x}$Ru$_x$ alloys

Now, we show the elastic properties of binary and ternary alloys, using DFTB code. These properties were obtained by using interatomic potential and are compared with other theoretical and those from standard DFT determined in the previous chapters 4 and 7.

10.4.1 Binary Ti$_{50}$Pd$_{50}$ alloy

Table 10-5 shows a comparison of the elastic properties of Ti$_{50}$Pd$_{50}$ for B19, L1$_0$, B2 and B19'. The DFTB elastic constants (determined using the interatomic potentials) are in good agreement with those calculated using DFT calculations to within 3 %. We pay attention specifically to the C'. The B2 showed negative elastic shear modulus (condition of instability) for both DFTB and VASP calculations. These values are comparable, with a slight improvement for the DFTB. The elastic constants of L1$_0$, B19 and B19′ satisfy the elastic stability criteria for tetragonal, orthorhombic and monoclinic crystals (as discussed in chapter 3).

Furthermore, we see that the DFTB Bulk modulus is in good agreement with the VASP values to within 3 %. It is clear that the L1$_0$ and B19 structures are ductile since the B/G is greater than 1.75 and less ductile for B19' (since B/G< 1.75) [149]. It can also be seen that the B2 structure shows a brittle manner as the B/G ratio is less than 1.75. This shows that the derived SCC sets of parameters are reasonably good since they are able to give comparable results.

Table 10-5 Elastic constants and Bulk modulus (B) for B2, L1$_0$, B19, B19'.

C_{ij} (GPa)	B2		L1$_0$		B19		B19′	
	DFTB+	VASP	DFTB+	VASP	DFTB+	VASP	DFTB+	VASP
c_{11}	145.30	149.10	230.56	228.83	245.82	240.82	311.16	300.88
c_{12}	160.67	159.83	108.23	105.48	128.60	125.19	84.32	80.10
c_{13}			129.68	128.31	125.71	124.42	86.55	85.18
c_{15}							-0.01	-0.05
c_{22}					274.05	262.65	268.50	265.43
c_{23}					80.17	90.00	140.46	136.46
c_{25}							-0.01	-0.06
c_{33}			261.45	251.16	242.80	250.62	249.56	244.70
c_{35}							-0.01	-0.06
c_{44}	45.03	43.74	95.02	91.81	28.45	30.52	43.00	41.57
c_{46}							33.00	32.33
c_{55}					38.65	39.17	54.76	53.82
c_{66}			19.32	17.42	50.44	48.52	115.12	112.04
C'	-7.69	-5.37	61.17	61.91	54.61	57.82	113.42	110.39
Bulk (GPa)	157.96	156.25	158.61	158.52	160.23	159.11	160.89	157.10
B/G	-20.54	-29.09	2.59	2.56	2.93	2.75	1.42	1.42

10.4.2 Ternary B2 and B19 Ti$_{50}$Pd$_{50-x}$Ru$_x$ alloys

Figure 10-5 shows the elastic properties of Ti$_{50}$Pd$_{50-x}$Ru$_x$ alloys. These were also calculated from our derived interatomic potentials employing the DFTB+ code. In a similar manner, the VASP results are used to benchmark. The SCC-DFTB elastic constants prediction is in good agreement with those from VASP calculations to within 3 %. In addition, the B2 Ti$_{50}$Pd$_{50-x}$Ru$_x$ values satisfy the generalized elastic stability criteria, particularly for cubic crystals. We observe that the alloy system is unstable below 20 at. % Ru (since $C' < 0$), and stable above

this composition ($C' > 0$). Similar behaviour was observed with VASP (as shown in Figure 7-1). The DFTB results gave a better trend due to the effectiveness of the derived potentials.
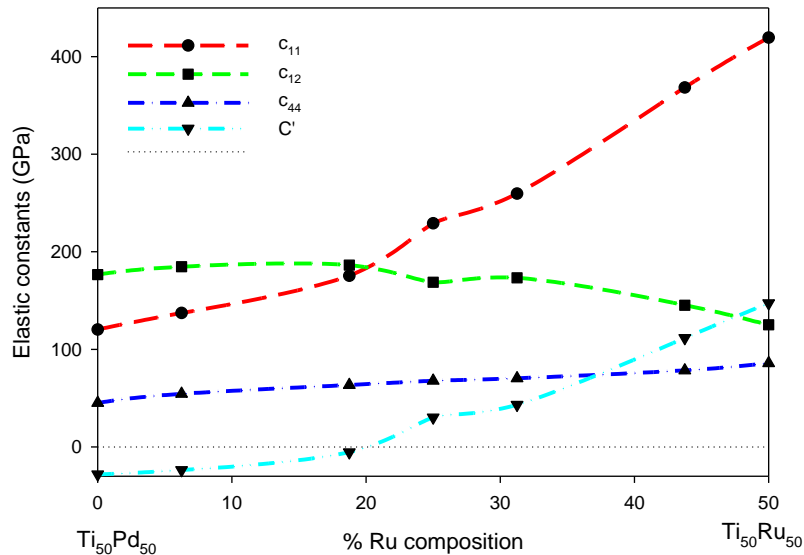
Figure 10-5 The elastic constants (GPa) and elastic shear modulus, *C'* (GPa) obtained from the derived interatomic potentials for B2 Ti$_{50}$Pd$_{50-x}$Ru$_x$ alloys.

The calculated Bulk modulus and the B/G ratio from derived potential are also compared in Figure 10-6 (a) and (b). It is noted that the Bulk modulus increases with an increase in Ru composition. This suggests that the hardest system can be obtained at higher composition i.e. Ti$_{50}$Pd$_{6.25}$Ru$_{43.75}$. More importantly, the DFTB and VASP plots show a similar trend. However, it can be noted that the DFTB gives larger values (harder system) than the VASP results. This implies that the derived potential overestimates the bulk modulus of the system.

Figure 10-6 (b) on the other hand reveals that the structures are ductile above 18 at. % Ru since B/G values are greater than 1.75 for both DFTB and VASP codes. The structure is brittle at 6.25 at. % Ru. Thus, it can be concluded that our derived

interatomic potential was able to reproduce the B/G ratio of B2 $Ti_{50}Pd_{50-x}Ru_x$ alloys, to within 2 % agreement as compared to the standard DFT results.
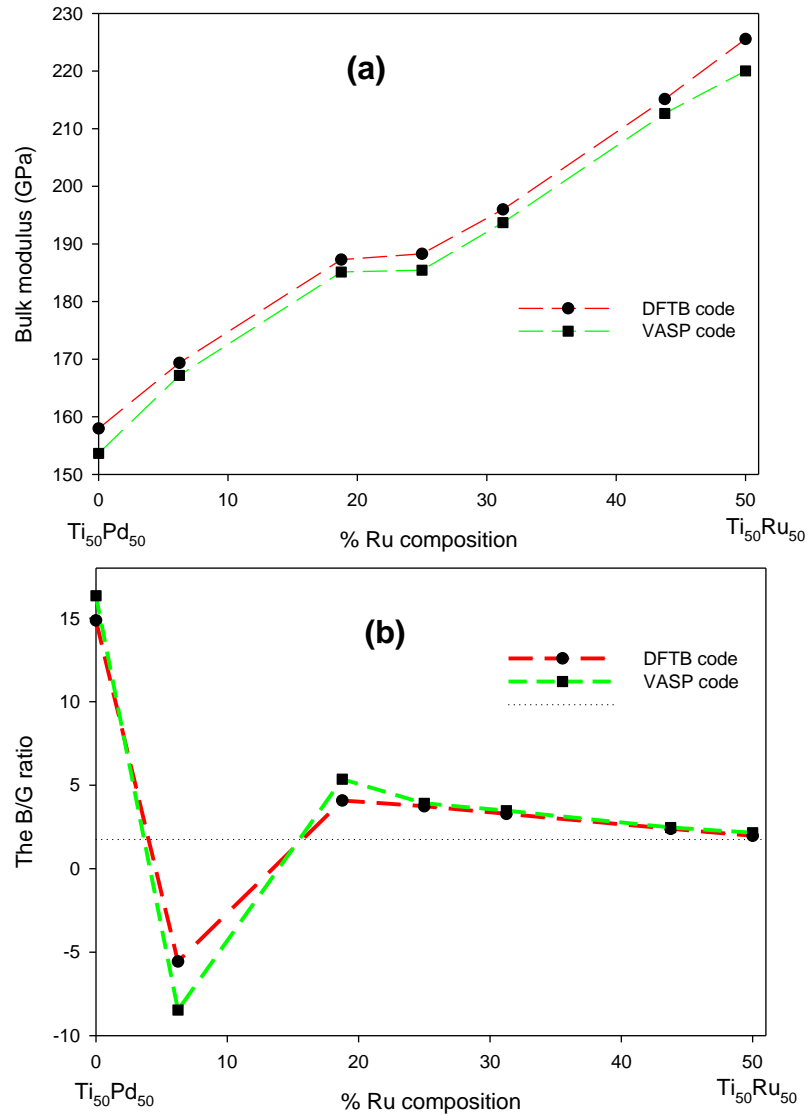
Figure 10-6 Comparison of the bulk modulus and the B/G ratio against the composition of B2 $Ti_{50}Pd_{50-x}Ru_x$, obtained from (a) the derived interatomic potentials, with the other calculated from (b) VASP code.

Figure 10-7 shows a comparison of the elastic properties of B19 $Ti_{50}Pd_{50-x}Ru_x$ alloys calculated using DFTB+ and VASP code. We see that the elastic constants satisfy the generalized elastic stability criteria for orthorhombic crystal as outlined in chapter 3. We found a good agreement of the results for both approaches.
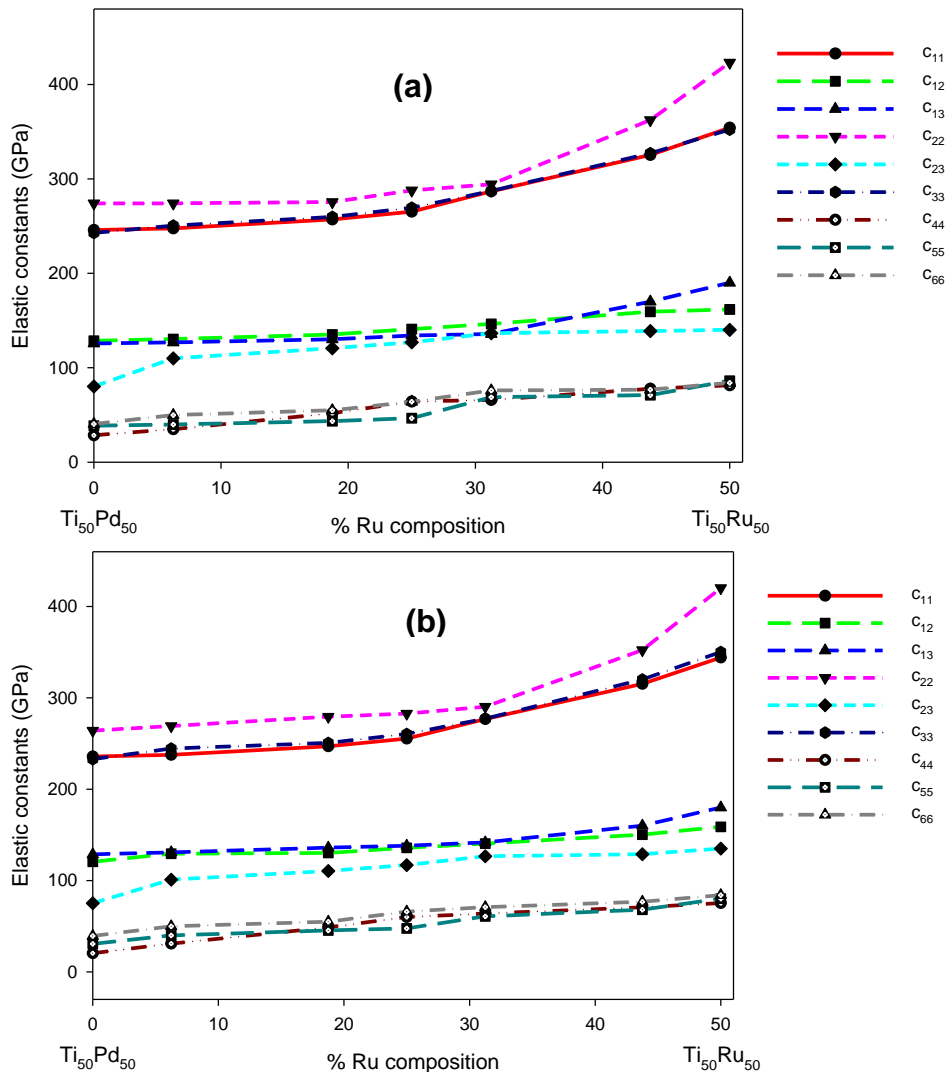
Figure 10-7 Comparison of elastic constants (GPa) obtained from (a) the derived interatomic potentials, with the other calculated (b) VASP code for B19 Ti$_{50}$Pd$_{50-x}$Ru$_x$ alloys.

Figure 10-8 shows a comparison of the elastic shear moduli (C'). Note that for the orthorhombic system, there are three types of elastic shear modulus as shown on the plot. The calculated shear moduli ($c_{11} + c_{22} -2c_{12}$), ($c_{11} + c_{33} -2c_{13}$) and ($c_{22} + c_{33} -2c_{23}$) compared very well to within 3 % with VASP results. It can be clearly seen that the structure is stable for the entire composition range ($C' >$

0). The predicted elastic shear moduli (C') correspond very well (displaying a similar trend) with the standard DFT results using the VASP code.
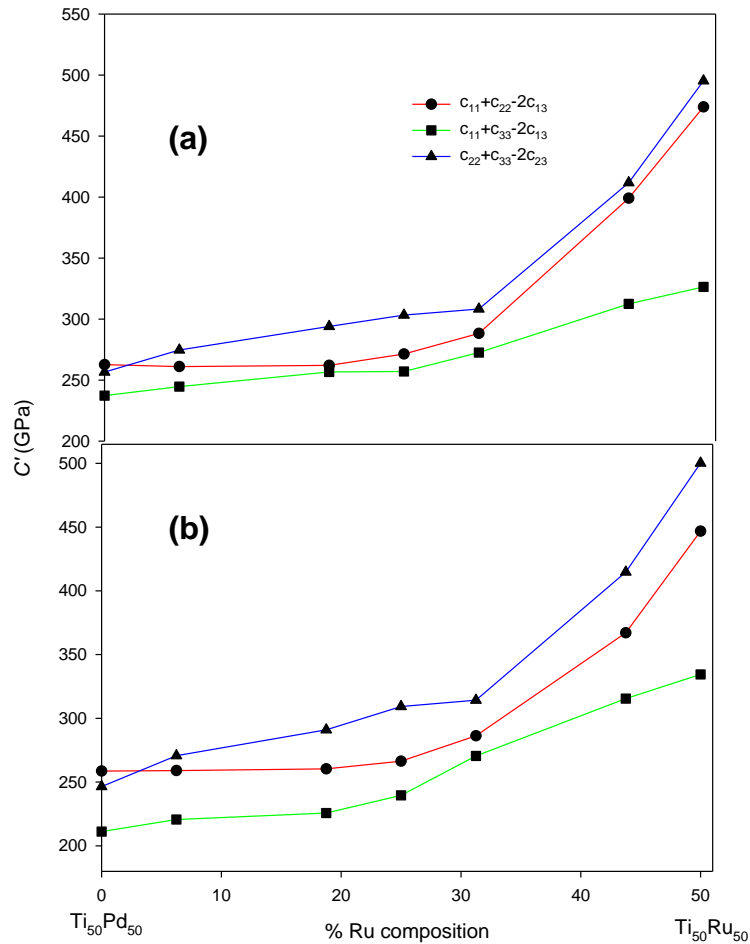
Figure 10-8 Comparison of the calculated elastic shear moduli (C') using (a) DFTB+ and (b) VASP data against composition.

In Figure 10-9 (a) and (b), we compare the Bulk modulus and the B/G ratio of B19 $Ti_{50}Pd_{50-x}Ru_x$. We see that our DFTB+ calculations predict the Bulk modulus to within 5 % agreement with the VASP code, which is an acceptable approximation. We also found that the predicted B/G ratio is greater than 1.75 for the entire concentration range ($0 \leq x \leq 50$), suggesting ductile behaviour.
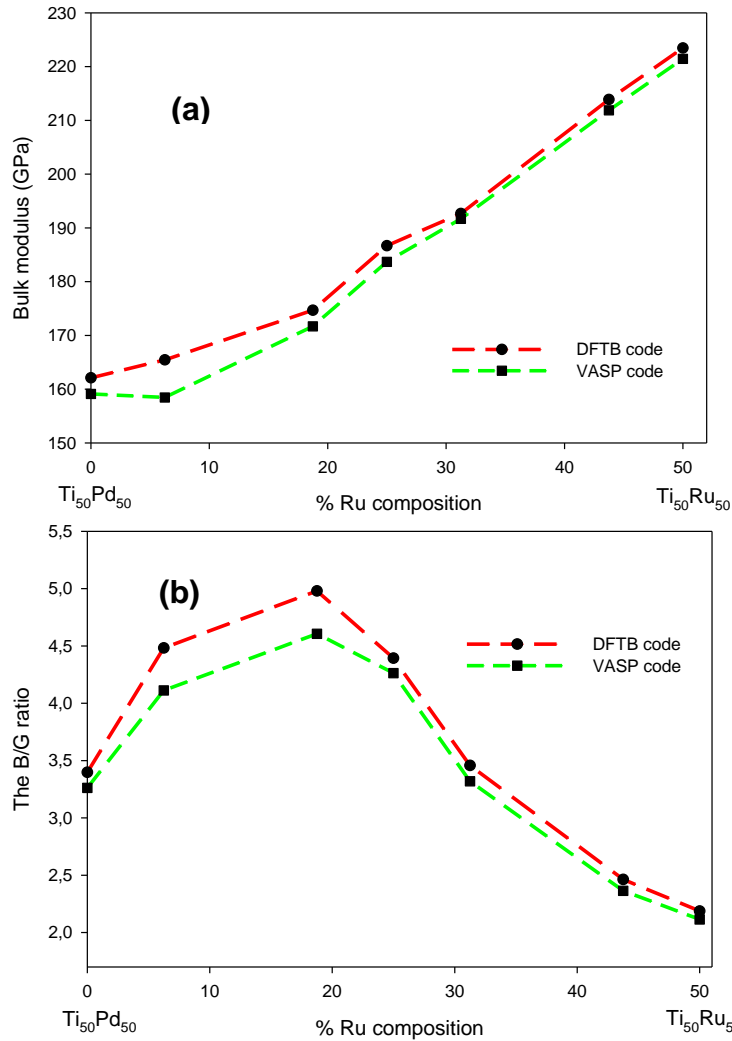
Figure 10-9 Comparison of the bulk modulus and the B/G ratio against the composition of B19 Ti$_{50}$Pd$_{50-x}$Ru$_x$, obtained from (a) DFTB+ code, with calculated from (b) VASP code.

10.5 DFTB: Temperature dependence

The molecular dynamics simulations have been performed using the SCC-DFTB approach. The Isothermal-isobaric (NPT) was chosen since the number of particles N, pressure P and temperature T are kept constant which enables us to see a change in volume or lattice parameters. We aim to gain knowledge on how the derived SCC set of parameters can influence the Ti-Pd and Ti-Pd-Ru

properties, particularly at increased temperatures. Before any calculations could be performed, it is important to establish the time step.

In order to determine the time step, the Newton equations of motion were integrated with the velocity Verlet algorithm, which varied from 0.5 to 12 fs. We see that the graph energy decreases as the time step is increased. At 8 fs, the plot is constant up to 12, suggesting that the energy does not change further (zero slopes). Thus the time step of 10 fs was found to be sufficient enough for this calculation (as shown in Figure 10-10 (a)). The Nosé-Hoover thermostat (time constant of 0.04 ps) and the system were allowed to evolve for 30 ps. The determined simulation time with respect to energy is shown in Figure 10-10 (b). In order to determine the appropriate simulation time of the $Ti_{50}Pd_{50}$ structure, dynamics calculations were performed for different simulation times at default temperature (100 K). The simulation time is necessary for determining the accuracy of the results at the ground state level. We see that at simulation time of 16 ps and above, the energy change is minimal (zero slopes), which suggests that the system has reached its equilibrium state (equilibration). Thus, the simulation time of 16 ps was chosen for all the MD calculations in this work.
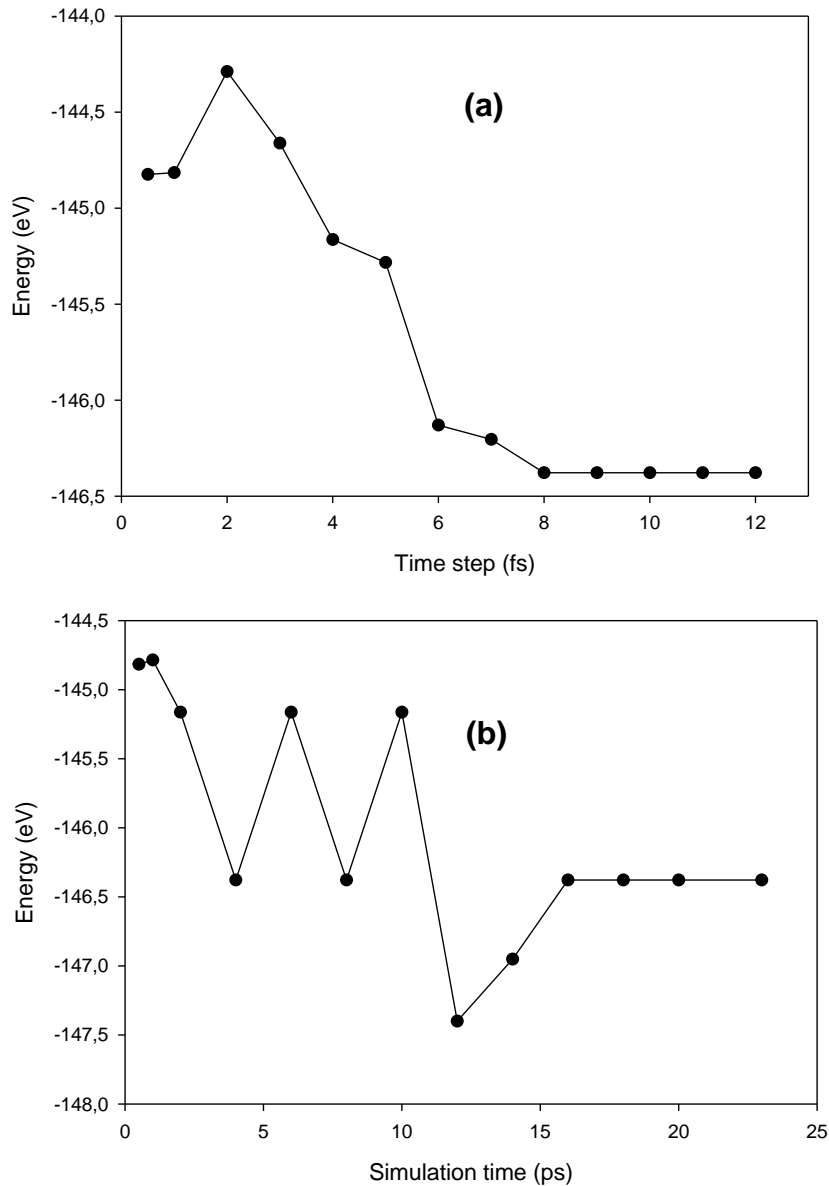
Figure 10-10 Total energy against (a) time step and (b) simulation time for B19 Ti$_{50}$Pd$_{50}$ alloy.

10.5.1 B19 Ti$_{50}$Pd$_{50}$ alloy

The effect of temperature on the lattice parameters of the B19 phase was investigated using the DFTB+ code and is shown in Figure 10-11. In this case, the lattice expansion is used to check the possible transformation behaviour at different temperatures. Structures were calibrated from 273-1773 K (above the

melting point, M_p= 1673 K) using velocity scale thermostats with a temperature difference of 10.0 K.

From the results, it can be noted that the lattice parameters increase minimally with an increase in temperature up to 1400 K. However, the a and c lattice parameters collapse to a common value (a=c= 4.555 Å) at about 1473 K which suggest a possible transformation. The lattice parameter b increases to 3.201 Å at this temperature. It can be noted that the a/b and c/b ratios decrease with an increase in temperature and the two ratios collapse to a common value of 1.423 at 1473 K. In order for transformation to occur from orthorhombic B19 to cubic B2, the ratios of a/b and c/b must be close to 1.414 [13]. The decrease in a/b and c/b is reasonable and significant to describe the structural change from B19 to cubic B2 above 1473 K. This implies that the B19 phase has transformed to the cubic B2 phase.

The result suggests that the DFTB derived potentials were able to predict phase transformation of B19 $Ti_{50}Pd_{50}$ alloy. This is in good agreement with the experimental phase diagram [81], where the B2 phase is stable at high temperatures. Similarly, the transformation behaviour is comparable with those predicted using a LAMMPS code, where the ratio a/b and c/b were predicted to be 1.426 at 1496 K (see Figure 5-6). The transformation temperatures are very close, suggesting that the derived interatomic potential managed to predict the transformation temperature.
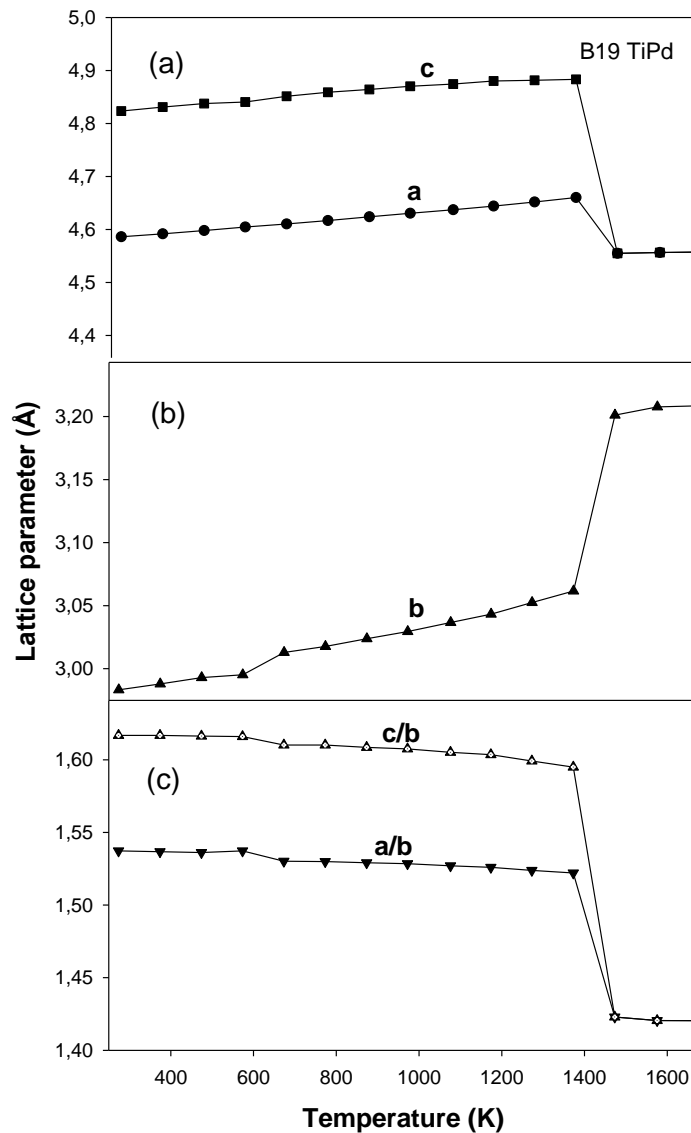
Figure 10-11 The effect of temperature on the (a) a and c (b) b (c) a/b and c/b lattice parameters of the B19 $Ti_{50}Pd_{50}$ alloy.

Furthermore, we show the density of B19 $Ti_{50}Pd_{50}$ alloy with temperature in Figure 10-12. It can be noted that the density decrease with an increase in temperature as expected. This behaviour may imply that the system becomes less dense with temperature. Similar behaviour was observed using the LAMMPS code (as shown in chapter 5, Figure 5-2). More importantly, the use of the SCC

potential parameter (DFTB) predicted structures to be less dense than the
LAMMPS code.
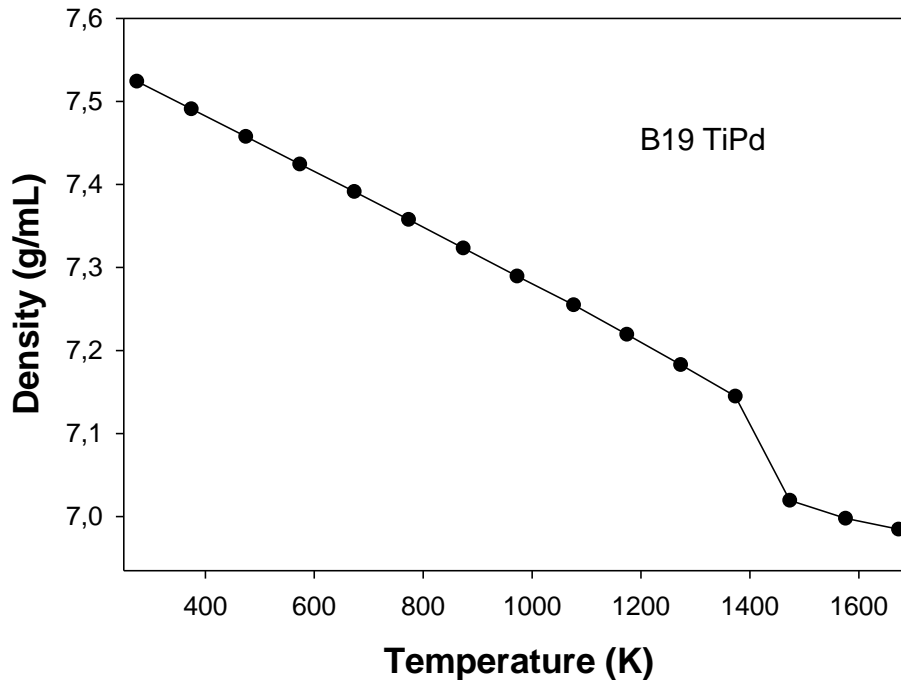
Figure 10-12 Density against temperature for B19 Ti$_{50}$Pd$_{50}$ alloy

10.5.2 B19 Ti$_{50}$Pd$_{50-x}$Ru$_x$ alloys

The temperature dependence on the lattice parameters of the B19 Ti$_{50}$Pd$_{50-x}$Ru$_x$
alloys is shown in Figures 10-13 and 10-14. This is used to investigate the effect
of Ru addition on the transformation temperature of Ti$_{50}$Pd$_{50}$ alloy. Similar to the
binary system above, the calculations were also calibrated at each temperature
from 273-1773 K using velocity scale thermostats. We observed that as the
temperature is increased, the lattice parameters increase minimally for 6.25, 18.
75 and 25 at. % Ru. Furthermore, a collapse is observed for both *a* and *c* lattice
parameters at approximately 1274, 1074 and 873 K for 6.25, 18. 75 and 25 at. %

Ru, respectively. This behaviour suggests a possible transformation in the system. Furthermore, there is a coupling observed between *a* and *c* lattice parameters above these temperatures which suggest that transformation from B19 to the B2 has taken place.

The ratio *a/b* and *c/b* of 6.25, 18.75, 25 at. % Ru is approximately 1.448 (at 1274 K), 1.446 (1074 K) and 1.430 (873 K), respectively. These values are comparable to the expected value of 1.414. The results suggest that the B19 phase has transformed to the B2 phase. Furthermore, it is clearly seen that the addition of Ru decreases the transformation temperature (Figure 10-13). As Ru concentration is increased to 31.25, 43.75 and 50 at. %, their transformation temperature is reduced to 774, 675 and 573 K, respectively. Our findings agree very well with previous work [93]. It can be deduced from the results that our derived potentials were able to predict phase transformation from B19 to B2 phase for B19 $Ti_{50}Pd_{50-x}Ru_x$ alloys. Unfortunately, the predicted transformation temperature cannot be compared with LAMMPS code results as there are no forcefields available for Ti-Pd-Ru currently.
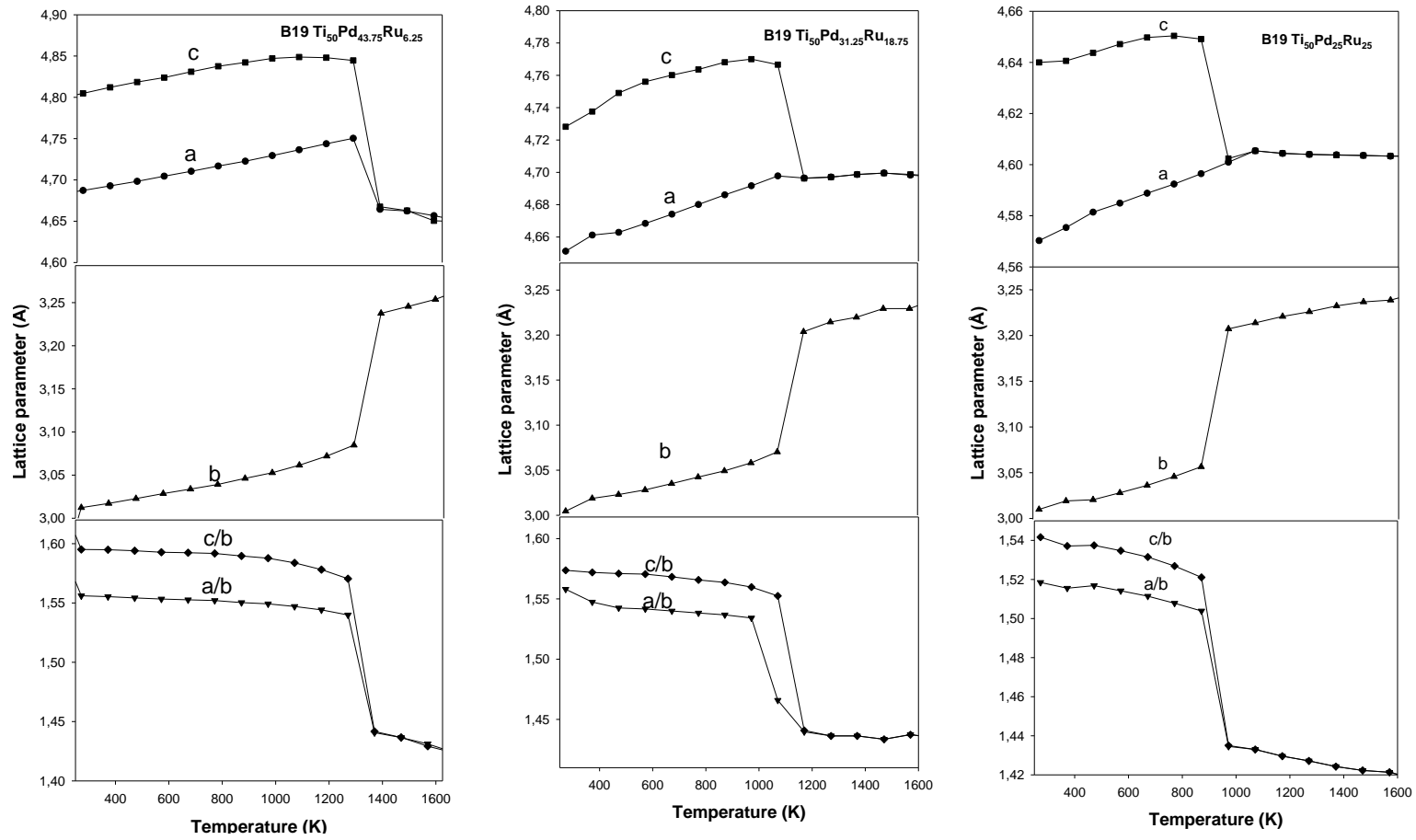
Figure 10-13 The effect of temperature on the a and c, b and, a/b and c/b lattice parameters of the B19 $Ti_{50}Pd_{43.75}Ru_{6.25}$ and $Ti_{50}Pd_{31.25}Ru_{18.75}$ and $Ti_{50}Pd_{25}Ru_{25}$ alloys.
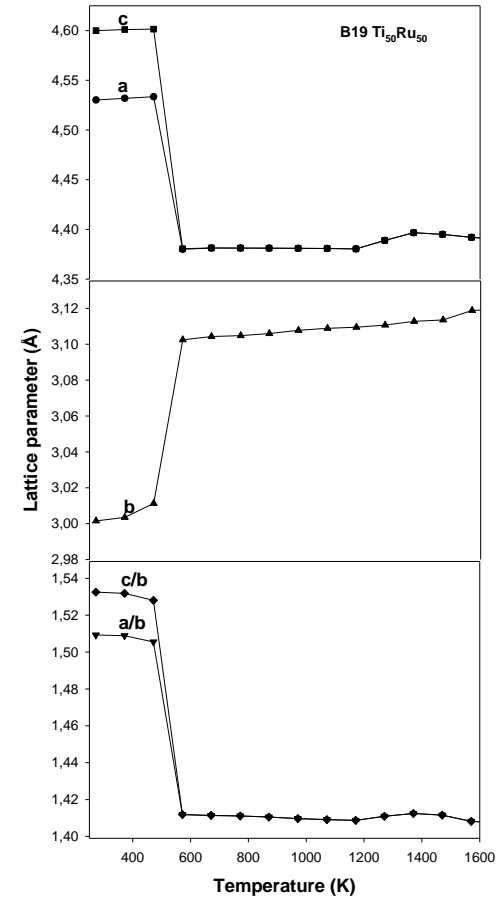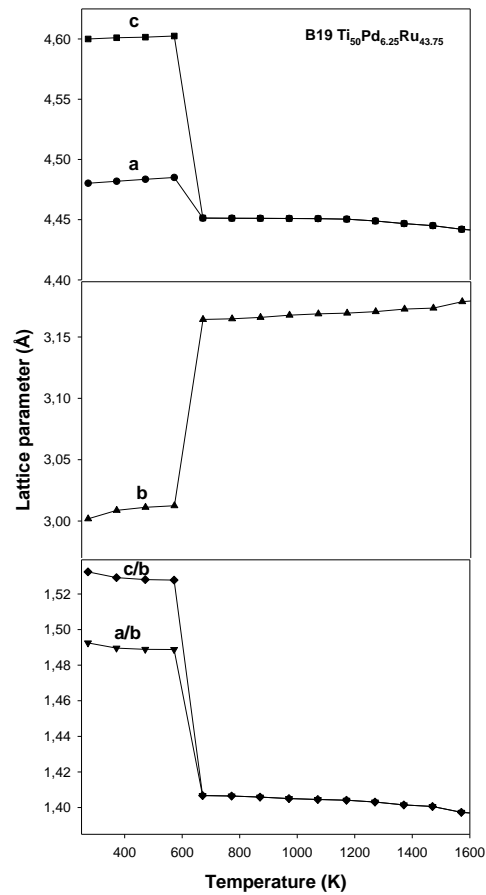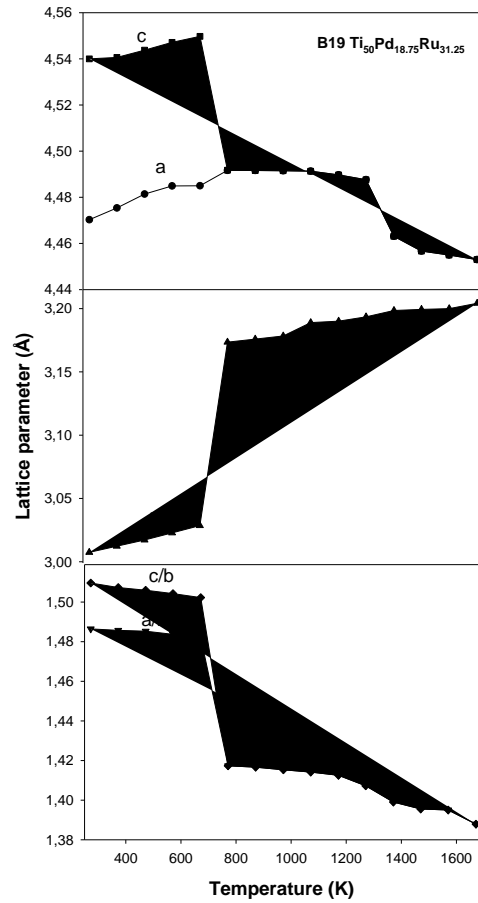
Figure 10-14 The effect of temperature on the (a) a and c (b) b (c) a/b and c/b lattice parameters of the B19 Ti$_{50}$Pd$_{18.75}$Ru$_{31.25}$, Ti$_{50}$Pd$_{6.25}$Ru$_{43.75}$ and Ti$_{50}$Ru$_{50}$ alloys.

Figure 10-15 shows the density against the temperature of $Ti_{50}Pd_{50-x}Ru_x$ alloys. Similar to the case of binary alloy, the density decreases minimally with temperature suggesting that the alloys become less dense at a higher temperature. This minimal decrease in the density is expected since the density of Ru (12.37 g/cm^3) is closer to that of Pd (12.03 g/cm^3). Unfortunately, there are no experimental and theoretical findings to compare our findings, and we consider this predictive data.
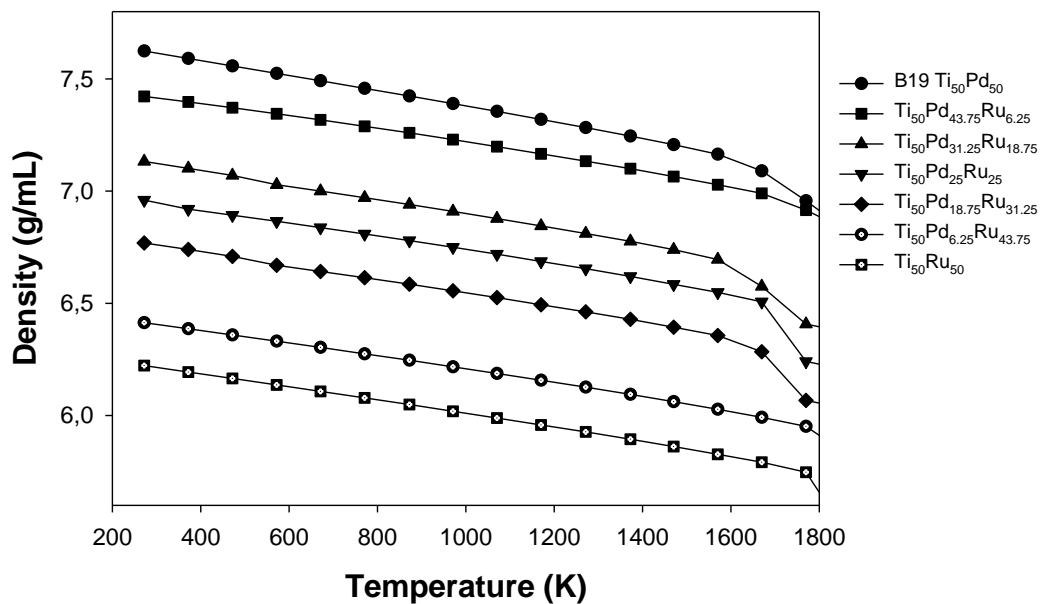
Figure 10-15 Density against temperature for B19 $Ti_{50}Pd_{50-x}Ru_x$ alloy.

Chapter 11

Cluster Expansions and Monte-Carlo Simulations for binary and ternary alloys

In this chapter, the Universal Cluster Expansion (UNCLE) [105] has been used to generate new ground state structures for both binary Ti-Pd and ternary Ti-Pd-Ru systems. Furthermore, we present lattice parameters and heats of formation from optimized ground state structures of ternary $TiPd_{1-x}Ru_x$ and $Ti_{1-x}PdRu_x$ alloys. We also discuss constructed phase diagrams and high temperature properties of the mixed $TiPd_{1-x}Ru_x$ and $Ti_{1-x}PdRu_x$ alloys for the entire range of Ru concentrations using Monte carlo simulation [125]. Detailed illustrations for this method can be found in chapter 3.

11.1 Cluster expansion

The UNCLE code as implemented in MedeA was used to search for the ground state structures of binary Ti-Pd and ternary Ti-Pd-Ru systems. Note that the code is able to perform a complete cluster expansion (CE) fit that contains up to two or more elements. During fitting the CE was allowed to run until the maximum number of iterations is reached while adding a maximum of four or more structures on each iteration and start from the initial training set of those four or more structures. So, this process continues until the energies of all structures are predicted by the CE at each concentration and the standard deviation of 96 % of

the structures is less than 5 meV of the cross validation score (CVS). The CVS is used to evaluate the predictive power of the cluster expansion. The smallest CVS (CVS<5 meV) value indicates that the predictive power of cluster expansion is excellent in the calculation [176].

In this study, accurate models were built for both binary Ti-Pd and Ti-Pd-Ru systems to predict the formation energy of atom site occupancy. More importantly, ground state curves were obtained in a self-consistent way by adding structures whose energy is predicted by cluster expansion to be lower than the energies of the structure already in the training set [177]. This is done iteratively until no new structures are predicted by cluster expansion to be more favourable than those already included in the training set. At this point, the cluster expansion has converged and all structures considered by the cluster expansion are thermodynamical. The most stable structures are the one which constitutes the convex hull (ground state line) of the composition dependent phase diagram. The output of CE generates ground state structures with different concentrations and symmetries.

11.2 Binary cluster expansion of Ti-Pd

Table 11-1 shows the predicted number of structures and cross validation score (CVS) on each alteration for Ti-Pd system. During full structural optimization in the minimisation stages, the DFT total energy values were calculated in the VASP flowchart with plane-wave basis cut-off of 500 eV in the GGA stage and k-spacing of 0.2 in the second minimisation stage. The cluster expansion generated 23 new structures of the Ti-Pd system. The CE truncated at iteration 6 since the proper

convergence was revealed. This is evident from the corresponding CVS. It is noted that CVS is 0.98 meV/pos., which is acceptable as prescribed above since CVS< 5 meV indication of a good cluster expansion.

Table 11-2 shows the predicted structures and their corresponding symmetries and formation energies (ΔE_f). Note that the predicted twenty one (21) structures exist and they are thermodynamically stable due to negative formation energies. The predicted structures are summarized in Figure 11-1.

Table 11-1 shows the number of structures and CVS determined in the cluster expansion for the binary Ti-Pd.

Iteration	No. of structures	No. of new structures	CVS (meV/pos.)
0	0	2	-
0	0	6	-
1	6	4	77.00
2	10	4	2.40
3	14	2	2.00
4	16	3	13.00
5	19	2	0.44
6	21	0	0.98

Table 11-2 Ground state formation energies (ΔE_f) as derived by CE for the binary Ti-Pd.

Compositions	Cell formula	Space group	ΔE_f (eV/atom)
0.00	Pd	I4/mmm	0.000
25.00	TiPd$_3$	I4/mmm	-0.538
25.00	TiPd$_3$	P4/mmm	-0.555
25.00	TiPd$_3$	Pmmm	-0.561
25.00	TiPd$_3$	Immm	-0.656
25.00	TiPd$_3$	Cmmm	-0.689
33.33	TiPd$_2$	Fmmm	-0.575
33.33	TiPd$_2$	C2/m	-0.584
33.33	TiPd$_2$	Immm	-0.685
50.00	Ti$_2$Pd$_2$	C2/m	-0.523
50.00	Ti$_2$Pd$_2$	Imma	-0.539
50.00	TiPd	P4/mmm	-0.554
50.00	TiPd	Cmmm	-0.594
66.67	Ti$_2$Pd	C2/m	-0.279
66.67	Ti$_2$Pd	Fmmm	-0.505
66.67	Ti$_2$Pd	Immm	-0.522
75.00	Ti$_3$Pd	I4/mmm	-0.268
75.00	Ti$_3$Pd	Immm	-0.378
75.00	Ti$_3$Pd	C2/m	-0.380
75.00	Ti$_3$Pd	Pmmm	-0.400
100.00	Ti	I4/mmm	0.000

The ground state structures and formation energy of the Ti-Pd system are shown in Table 11-3. As indicated in section 11.1, the CE indeed predicted stable structures with different compositions, space groups, lattice parameters, and different formation energies. The predicted ground state structures are TiPd$_3$, TiPd$_2$, Ti$_2$Pd and Ti$_3$Pd with different space groups. Thus, the results show that the TiPd$_3$ (Cmmm) is the most thermodynamically stable structure since it gave the lowest formation energy $(\Delta E_f = -0.690)$ compared to other compositions. However, it can be seen that there is a competing phase TiPd$_2$ (Immm). These results are reliable since a proper CE convergence was attained.

Table 11-3 list of the ground state stable structures contained in Ti-Pd system.

Composition	Structure	ΔE_f (eV/atom)	Space group
0.00	Pd	0.000	I4/mmm
25.00	TiPd$_3$	-0.690	Cmmm
33.33	TiPd$_2$	-0.685	Immm
66.66	Ti$_2$Pd	-0.524	Immm
75.00	Ti$_3$Pd	-0.398	Pmmm
100.00	Ti	0.000	I4/mmm

Figure 11-1 shows the ground state structure of Ti-Pd. Note that the ground state structures are those in the highlighted red line and are considered thermodynamically stable. The ground state line predicted four (4) stable structures relative to the predicted enthalpies of formation. The circles represent energies for a specific configuration as calculated by DFT and predicted by the CE. It can be noted that all the formation energies are negative for all ordered structures which indicates that the predicted structures are thermodynamically stable.
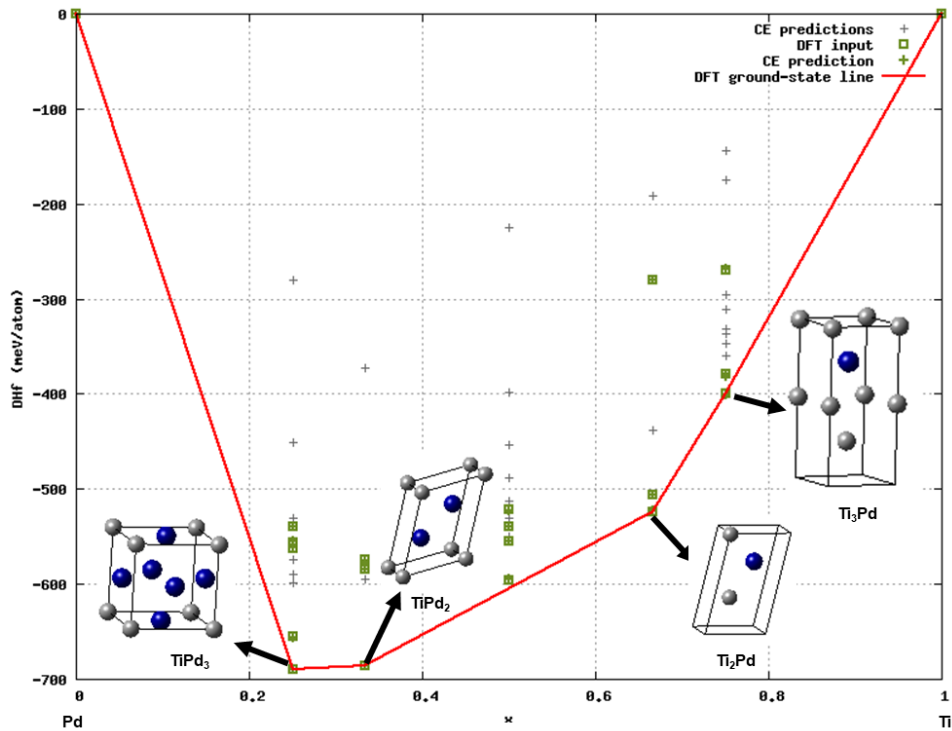
Figure 11-1 The convex hull plot of binary Ti-Pd (I4/mmm) obtained using cluster expansion. The grey and green crosses are predicted structures by CE and the red line is the ground-state line.

11.3 Ternary cluster expansion

The cluster expansion was used to determine the ground state structure for the ordered B2 Ti-Pd-Ru alloys. For the purpose of this study, the ternary cluster expansion is done on B2 $TiPd_{1-x}Ru_x$ and $Ti_{1-x}PdRu_x$ alloys. In this case, we explore the effect of Ru addition on the Pd and Ti sub-lattice.

11.3.1 Ternary B2 $TiPd_{1-x}Ru_x$ alloy

Table 11-4 shows the predicted number of structures and their CVS. The same plane-wave basis cut-off in the GGA stage and the k-spacing in the second

minimisation stage were used as in Figure 11-1. It is clearly seen that the fully

optimized ternary ground state diagram produced 27 new structures.

Unfortunately, there is no new ground state structures were produced by the DFT

ground-state line (red) found by CE. Note that a proper convergence is observed

at iteration 5 from CE as there was no new structure predicted by CE in the last

iteration. The cluster expansion of B2 TiPd$_{1-x}$Ru$_x$ was found to have CVS of 0.10

meV per atom suggesting good cluster expansion prediction (see Table 11-4).

Figure 11-4 shows the predicted formation energies (ΔE_f) which were used to fit

the cluster expansion Hamiltonians. It can be noted that the formation energies

of TiPd$_{1-x}$Ru$_x$ ordered structures are positive, which indicates the presence of a

miscibility gap system. This behaviour implies that the generated structures are

thermodynamically unstable (ΔE_f).

The predicted twenty seven (27) structures, compositions, space groups and

formation energies of ternary TiPd$_{1-x}$Ru$_x$ are shown in Table 11-5. The results

reveal that the predicted structures are thermodynamically unstable due to the

positive formation energies $(\Delta E_f > 0)$ at different symmetries.

Table 11-4 Show the number of structures and CVS determined in the cluster expansion for the ternary TiPd$_{1-x}$Ru$_x$.

Iteration	No. of structures	No. of new structures	CVS (meV/pos.)
0	0	2	-
0	0	7	-
1	7	5	0.13
2	12	5	0.09
3	17	5	0.00
4	22	5	0.03
5	27	0	0.10

Table 11-5 Ground state formation energies as derived by CE for the ternary TiPd$_{1-x}$Ru$_x$.

Compositions	Cell formula	Space group	ΔE_f (eV/atom)
0.00	TiRu	Pm-3m	0.000
25.00	Ti$_4$Ru$_3$Pd	R-3m	0.073
25.00	Ti$_4$Ru$_3$Pd	Pmmm	0.061
25.00	Ti$_4$Ru$_3$Pd	Cmmm	0.058
25.00	Ti$_4$Ru$_3$Pd	Im-3m	0.054
25.00	Ti$_4$Ru$_3$Pd	P4/mmm	0.053
25.00	Ti$_4$Ru$_3$Pd	P4/mmm	0.049
25.00	Ti$_4$Ru$_3$Pd	P4/mmm	0.044
33.33	Ti$_3$Ru$_2$Pd	P-3m1	0.089
33.33	Ti$_3$Ru$_2$Pd	Cmmm	0.075
50.00	Ti$_4$Ru$_2$Pd$_2$	Cmcm	0.088
50.00	Ti$_4$Ru$_2$Pd$_2$	I4/mmm	0.087
50.00	Ti$_2$RuPd	P4/mmm	0.071
50.00	Ti$_4$Ru$_2$Pd$_2$	Pmma	0.070
50.00	Ti$_4$Ru$_2$Pd$_2$	P4/mmm	0.053
66.67	Ti$_3$RuPd$_2$	P-3m1	0.076
66.67	Ti$_3$RuPd$_2$	Cmmm	0.058
75.00	Ti$_4$RuPd$_3$	R-3m	0.057
75.00	Ti$_4$RuPd$_3$	Cmmm	0.054
75.00	Ti$_4$RuPd$_3$	P4/mmm	0.051
75.00	Ti$_4$RuPd$_3$	Im-3m	0.050
75.00	Ti$_4$RuPd$_3$	P4/mmm	0.048
75.00	Ti$_4$RuPd$_3$	I4/mmm	0.047
75.00	Ti$_4$RuPd$_3$	Pmmm	0.046
75.00	Ti$_4$RuPd$_3$	Cmmm	0.045
75.00	Ti$_4$RuPd$_3$	P4/mmm	0.034
100.00	TiPd	Pm-3m	0.000

Figure 11-2 Ground state line of the ternary B2 TiPd$_{1-x}$Ru$_x$ systems enthalpy of formation against Ru concentration. The grey and green crosses predicted structures by CE and the red line is the DFT ground-state line.

11.3.2 Ternary B2 Ti$_{1-x}$PdRu$_x$ alloys

The number of new structures and cross validation score (CSV) are represented in Table 11-6. It can be observed that the CE converged at alteration 4 as there are no new ground state structures predicted. Cluster expansion predicted 17 new structures for B2 Ti$_{1-x}$PdRu$_x$ alloy at 0 K. A cross validation score is found to be 0.11 meV/pos., which is an indication of a good cluster expansion (since CVS< 5 meV).

Table 11-7 show the predicted seventeen (17) structure with their space group and formation energies of ternary Ti$_{1-x}$PdRu$_x$. The formation energies predicted by CE are negative revealing thermodynamically stability for any composition that

exists in Table 11-7. It is clearly seen that the lowest formation energy is observed

for 25 at. % Ru suggesting that the structure is the most stable as compared to

other compositions.

Table 11-6 Show the number of structures and CVS determined in the cluster expansion for the ternary Ti$_{1-x}$PdRu$_x$.

Iteration	No. of structures	No. of new structures	CVS (meV/pos.)
0	0	2	-
0	0	7	-
1	7	5	1.70
2	12	3	0.32
3	15	2	0.03
4	17	0	0.11

Table 11-7 Ground state formation energies derived by CE for the ternary Ti$_{1-x}$PdRu$_x$.

Compositions	Cell formula	Space group	ΔE_f (eV/atom)
0.00	RuPd	Pm-3m	0.000
25.00	TiRu$_3$Pd$_4$	P4/mmm	-0.102
25.00	TiRu$_3$Pd$_4$	Im-3m	-0.197
33.33	TiRu$_2$Pd$_3$	P4/mmm	-0.034
33.33	TiRu$_2$Pd$_3$	P-3m1	-0.151
50.00	TiRuPd$_2$	P4/mmm	-0.048
50.00	Ti$_2$Ru$_2$Pd$_4$	Cmcm	-0.171
50.00	TiRuPd$_2$	Fm-3m	-0.197
50.00	Ti$_2$Ru$_2$Pd$_4$	I4/mmm	-0.231
50.00	TiRuPd$_2$	P4/mmm	-0.255
66.67	Ti$_2$RuPd$_3$	P4/mmm	-0.011
66.67	Ti$_2$RuPd$_3$	P-3m1	-0.176
75.00	Ti$_3$RuPd$_4$	R-3m	-0.126
75.00	Ti$_3$RuPd$_4$	P4/mmm	-0.144
75.00	Ti$_3$RuPd$_4$	I4/mmm	-0.146
75.00	Ti$_3$RuPd$_4$	Im-3m	-0.185
100.00	TiPd	Pm-3m	0.000

The formation energies for each composition are shown in Table 11-8. It is clearly seen that the predicted ground state structures obtained from the ternary phase diagram have different space groups, different lattice parameters and different formation energies. The cluster expansion predicted three (3) ground state structures for the $Ti_{1-x}PdRu_x$ system i.e. Ti_3Pd_4Ru, $TiPd_2Ru$, and $TiPd_4Ru_3$ with negative formation energy showing thermodynamic stability. The most stable structure is found to be 25 at. % Ru ($TiPd_2Ru$) due to the lowest formation energy $(\Delta E_f < 0)$.

Table 11-8 The predicted structure constituting the DFT ground state line with their compositions and the formation energies of $Ti_{1-x}PdRu_x$.

Composition	Structure	ΔE_f (eV/atom)	Space group
0.00	TiPd	0.000	Pm-3m
25.00	Ti_3Pd_4Ru	-0.185	Im-3m
50.00	$TiPd_2Ru$	-0.255	P4/mmm
75.00	$TiPd_4Ru_3$	-0.197	Im-3m
100.00	PdRu	0.000	Pm-3m

Furthermore, the cluster expansion was also done on the Ti-site in order to check the site preference of Ru on TiPd alloy at 0 K which is highlighted in Figure 11-3. Once the ground states for a range of concentrations have been identified, the ones that are stable at T= 0 K are determined by the convexity condition, that is the given structure at concentration x is stable if it lies below any straight line connecting other compounds at concentrations [177]. From Figure 11-3, it can be noted that the $Ti_{1-x}PdRu_x$ structures display negative ΔE_f showing that the structures are stable, while those close to the convex hull contribute to miscible constituents [177].

Note that some CE enumerated structures (green crosses in Figure 11-3) are slightly below the convex hull. Stable compounds are those that form the vertices on the lower boundary of this convex hull. The predicted ground state structures as shown by the ground state line are RuPd, TiPd$_4$Ru$_3$, TiPd$_2$Ru, Ti$_3$PdRu, and TiPd. These results show that the TiPd$_2$Ru is the most thermodynamically stable structure due to the lowest ΔE_f compared to other compositions. It can be deduced from the findings that Ru prefers or perform better when substituted on the Ti-site. This may be due to the fact that the atomic ratios of Ru and Ti are close to each other.

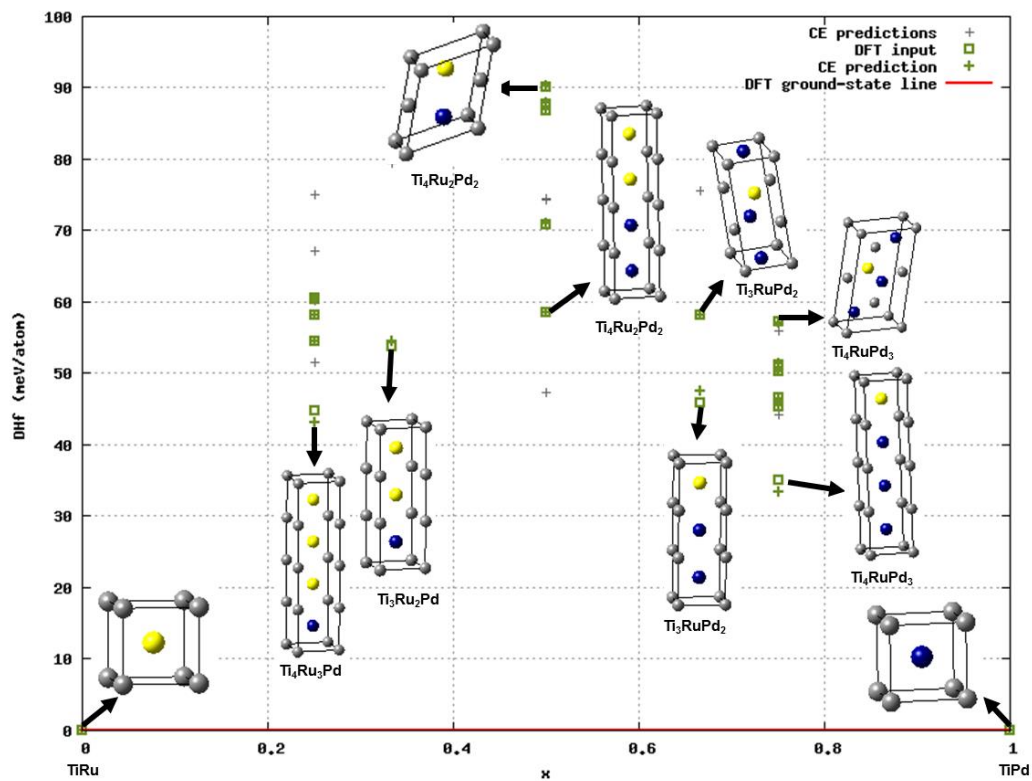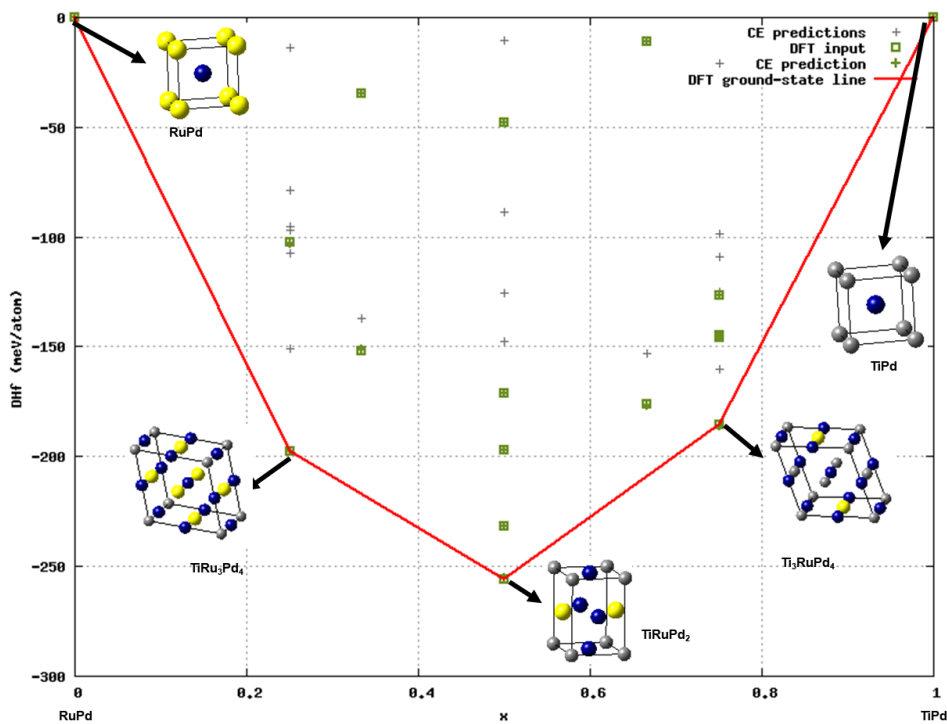**Figure 11-3 Ground state line of the ternary of B2 Ti$_{1-x}$PdRu$_X$ systems enthalpy of formation against Ru concentration. The grey and green crosses predicted structures by CE and the red line is the DFT ground-state line.**

11.4 Optimized ground-state Structures from Cluster Expansion

We evaluate the equilibrium lattice parameters and thermodynamic stability for $TiPd_{1-x}Ru_x$ and $Ti_{1-x}PdRu_x$ systems. This is to determine the effect of Ru addition on both Ti and Pd sub-lattices. The structures were subjected to full geometry optimization by alloying both the lattice constant and shape to change. Firstly, the equilibrium lattice parameters and heats of formation of B2 $TiPd_{1-x}Ru_x$ structures are discussed. We have calculated only the binary TiPd and TiRu systems since there was no stable structure obtained at the ground state line. The binary systems TiPd and TiRu gave equilibrium lattice parameters 3.169 Å (3.180 Å) [34] and 3.084 Å (3.085 Å) [54], respectively. It can be noted that the result obtained compared very well with the experimental values (in parenthesis) to within 3 %.

The heat of formation was determined to verify the existence of the two-parent or binary phases. Recall that for a structure to be stable, the heat of formation value must have the lowest negative value otherwise a positive value implies instability. The result of the heats of formation for TiPd and TiRu was found to be -0.453 eV/atom and -0.753 eV/atom, respectively. The result showed that TiPd and TiRu alloys exist as the heats of formation for both systems are negative which suggests thermodynamic stability of the two systems.

Now, considering $Ti_{1-x}PdRu_x$, where substitution was done on the Ti sublattice. Note that the results are for the substitution on the Ti sublattice, their equilibrium lattice parameter and heats of formation are presented in Table 11-4. The most stable structure is predicted to be the $TiPd_2Ru$ phase with the lowest heat of

formation of -0.404 eV/atom. Furthermore, the TiPd$_4$Ru$_3$ structure was found to be unstable with the heat of formation value of 0.505 eV/atom ($\Delta H_f > 0$). The results suggest that the TiPd$_4$Ru$_3$ cannot be found experimentally. Similar behaviour was observed for the binary PdRu, with $\Delta H_f > 0$ (condition of instability) the structure is unstable. Thus, the predicted stability trend according to the calculated ΔH_f deduced from the cluster expansions is as follows:

TiPd$_2$Ru > Ti$_3$Pd$_4$Ru > TiPd$_4$Ru$_3$.

Table 11-9 The predicted lattice parameters and heats of formation of B2 Ti$_{1-x}$PdRu$_x$ alloys.

Structure	Space group	a(A)	b(A)	c(A)	ΔH_f (eV/atom)
PdRu	Pm-3m	3.098	3.098	3.098	0.505
TiPd$_4$Ru$_3$	Im-3m	2.692	2.692	2.692	0.178
TiPd$_2$Ru	P4/mmm	4.005	3.843	3.843	-0.404
Ti$_3$Pd$_4$Ru	Im-3m	2.720	2.720	2.720	-0.302
TiPd	Pm-3m	3.169	3.169	3.169	-0.453

11.5 Monte carlo simulation

Monte Carlo (MC) simulation was performed on the TiPd$_{1-x}$Ru$_x$ and Ti$_{1-x}$PdRu$_x$ structures, using UNCLE code. It was used to check the mixing of the two structures (TiPd$_{1-x}$Ru$_x$ and Ti$_{1-x}$PdRu$_x$) as implemented. This code performs simulation with either the canonical or the grand canonical ensemble. In this simulation, a canonical ensemble was used to calculate the critical temperature since it is able to separate. It has been reported as the grand-canonical ensemble cannot separate the structures hence it was not conducted. A plot of these trajectories is used to reveal miscibility gaps, which are represented. In a Monte Carlo simulation, the energies of alloys were allowed to change in the calculation due to changes in the occupation (atom exchanges).

11.5.1 MC for B2 $TiPd_{1-x}Ru_x$ concentrations

The Monte Carlo profiles of $TiPd_{1-x}Ru_x$ alloys are computed and shown in Figures 11-4. Note that the plots are also shown in Appendix B. In Figure 11-4, we see that the energy difference between atoms increases with temperature for all compositions ($0 \leq x \leq 1$). At $x=0.1$ concentrations ($TiPd_{0.9}Ru_{0.1}$), the energy difference increases minimally above 800 K which indicates that the system mixes very well as shown in Figure 11-4 (a). As the amount of Ru concentration is increased to 0.3, the energy differences increase minimally with a temperature above 1300 K suggesting the mixing of the system has occurred.

As shown in Figure 11-4 (e), at low temperature, for example, at 200 K phase separation between TiPd and TiRu can be observed in $TiPd_{0.5}Ru_{0.5}$ alloy. This means that there are two phases within the $TiPd_{0.5}Ru_{0.5}$ alloy. As the temperature is increased above 1400 K, the $TiPd_{0.5}Ru_{0.5}$ alloy becomes more and more homogeneous. It means that the homogeneity of $TiPd_{0.5}Ru_{0.5}$ alloy increases with the increase in temperature above 1500 K. In Figure 11-4 (i), we also observe phase separation in $TiPd_{0.1}Ru_{0.9}$ alloy below 1600 K and the system become homogeneous above 1700 K.

Our result also shows that the $TiPd_{1-x}Ru_x$ alloys can exhibit phase separation at low temperatures below 200 K. The tendency of phase separation can cause alloy inhomogeneity to a certain extent [178]. The findings indicate that $TiPd_{1-x}Ru_x$ mix very well at temperatures above 1200 K, particularly for high Ru content.

As indicated in Figures 11-4, the miscibility gaps (bimodal curves) found in $TiPd_{1-x}Ru_x$ corresponds to the coexistence of two stable phases. Inside the miscibility

gaps, phase separation occurs at low temperatures. The $TiPd_{1-x}Ru_x$ forms a heterogeneous structure as Pd and Ru does not have similar properties at low temperature. This observation is similar to the analysis by Zhang F et al [178]. Unfortunately, there is no theoretical or experimental result to compare.

Figure 11-4 Energy difference against temperature of B2 Ti-Pd-Ru at different concentrations (a) Ti-Pd$_{0.9}$Ru$_{0.1}$, (b) Ti-Pd$_{0.8}$Ru$_{0.2}$, (c) Ti-Pd$_{0.7}$Ru$_{0.3}$, (d) Ti-Pd$_{0.6}$Ru$_{0.4}$ (e) Ti-Pd$_{0.5}$Ru$_{0.5}$, (f) Ti-Pd$_{0.4}$Ru$_{0.6}$, (g) Ti-Pd$_{0.3}$Ru$_{0.7}$, (h) Ti-Pd$_{0.2}$Ru$_{0.8}$ and (i) Ti-Pd$_{0.1}$Ru$_{0.9}$.

11.5.2 MC for B2 $Ti_{1-x}PdRu_x$ concentrations

Figures 11-5 show the energy difference of $Ti_{1-x}PdRu_x$ alloys with a temperature at various concentrations. It can be clearly seen that the energy difference between atoms increases with temperature for all compositions ($0 \leq x \leq 1$). At 0.1 concentrations ($Ti_{0.9}PdRu_{0.1}$), the energy difference increases minimally above 300 K which indicates that the system mixes very well as shown in Figure 11-5 (a) (see Figure B-4 in Appendix B).

A zero slope was observed at 0.3 and 0.5 concentrations and the energy difference increase minimally above 2000 and 2400 K, respectively. This indicates that the system mixes very well as shown in Figure 11-5 (c) and (e). Furthermore, at 0.9 concentrations the energy difference increases and reaches zero slopes at 1300 K as shown in Figure 11-5 (i). This observation indicates that the melting temperature is improved with Ru additions. This is due to the fact that Ti and Ru have similar properties and thus tend to mix very well [178]. The results suggest that Ru prefers Ti-site as compared to Pd-site in agreement with the predicted formation energies. The findings indicate that $Ti_{1-x}PdRu_x$ mix well very at low temperatures below 300 K.
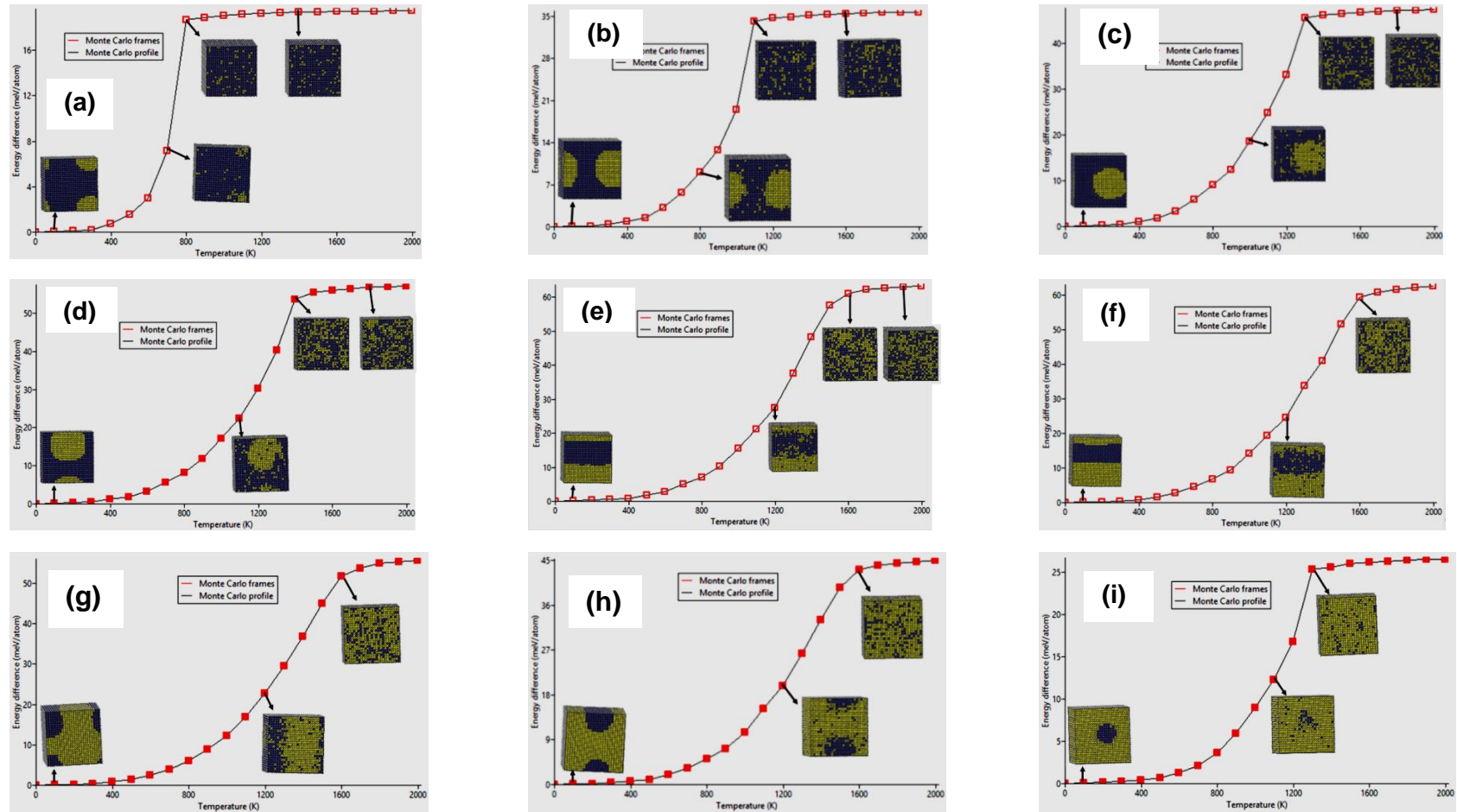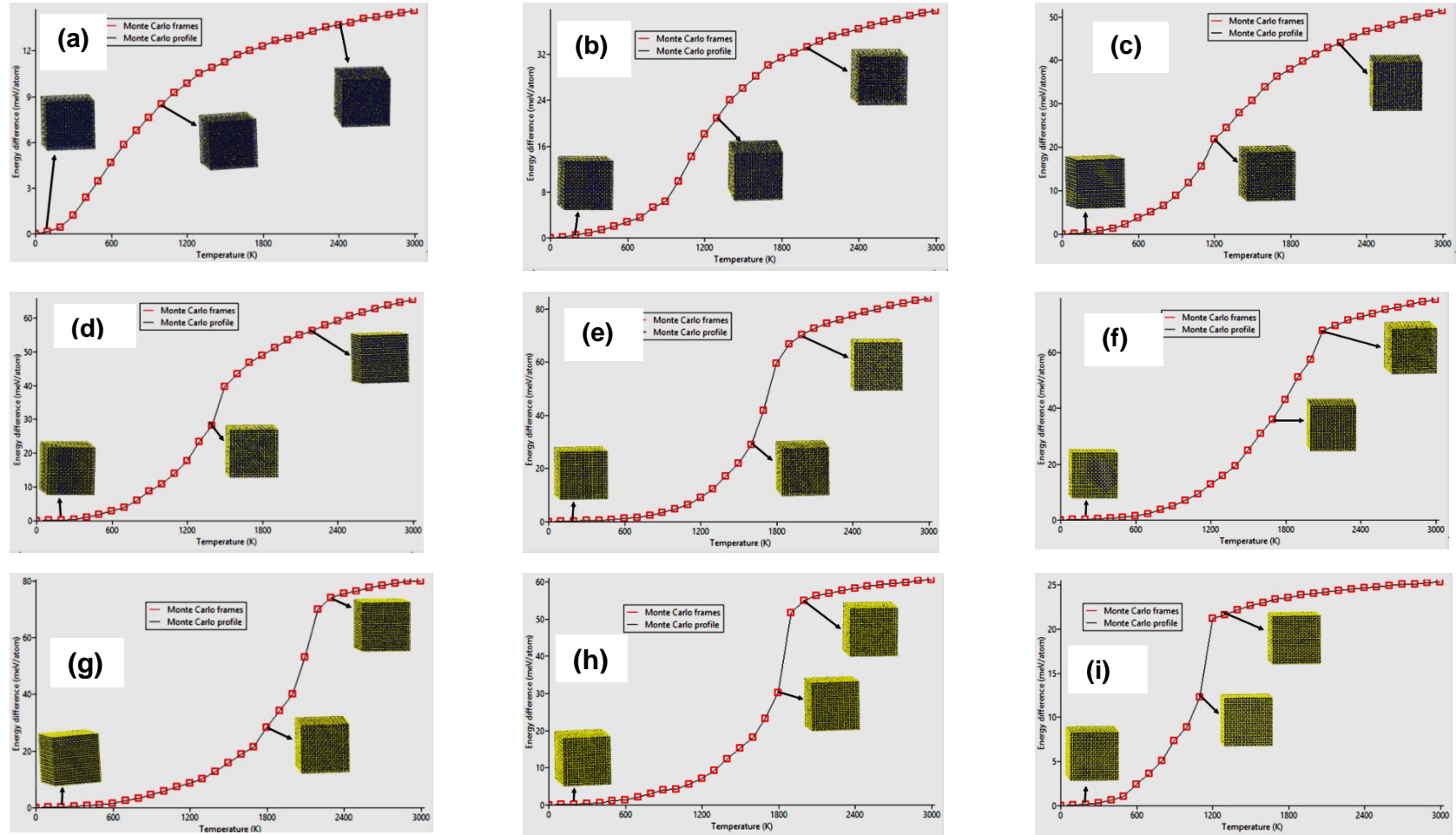
Figure 11-5 Energy difference against temperature of B2 Ti-Pd-Ru at various concentrations (a) Ti$_{0.9}$PdRu$_{0.1}$, (b) Ti$_{0.8}$PdRu$_{0.2}$, (c) Ti$_{0.7}$PdRu$_{0.3}$, (d) Ti$_{0.6}$PdRu$_{0.4}$, (e) Ti$_{0.5}$PdRu$_{0.5}$, (f) Ti$_{0.4}$PdRu$_{0.6}$, (g) Ti$_{0.3}$PdRu$_{0.7}$, (h) Ti$_{0.2}$PdRu$_{0.8}$ and (i) Ti$_{0.1}$PdRu$_{0.9}$.

11.6 Constructed phase diagram

Monte carlo simulation was used to construct the phase diagram from their critical temperature as implemented in the UNCLE code.

11.6.1 Phase diagram of TiPd$_{1-x}$Ru$_x$

The computed phase diagram of ternary TiPd$_{1-x}$Ru$_x$ alloys is shown in Figure 11-6. The critical temperatures determined in Figures 11-4 were used to construct a phase diagram concerning the compositions of Ru on Pd-site. Note that the critical temperature is observed when an increase in temperature resulted in the same energy difference of the system (Zero slope). The phase diagram consists of two regions, homogeneity (mixing) and heterogeneity (phase separation). The mixing region is observed below 50 at. % Ru while the phase separation is above this concentration. It is clearly seen that 50 at. % Ru mixes at a high temperature above 1600 K indicating that the diffusion might be too fast. Our result shows that the TiPd$_{1-x}$Ru$_x$ alloys exhibit phase separation at a temperature below 1700 K (see Figure 11-6). The TiPd$_{1-x}$Ru$_x$ forms a heterogeneous structure as Pd and Ru does not have similar properties.
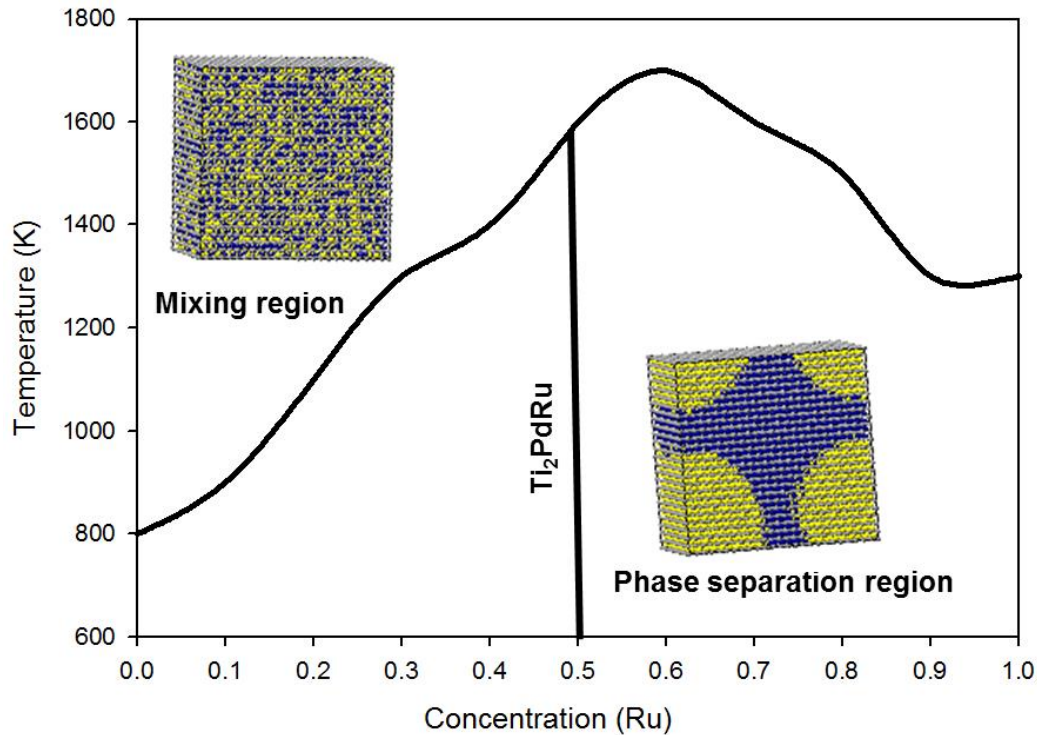
Figure 11-6 Constructed phase diagram of B2 TiPd$_{1-x}$Ru$_X$ using phase transition temperature at different concentrations.

11.6.2 Phase diagram of Ti$_{1-x}$PdRu$_x$

In Figure 11-7, the computed phase diagram of ternary Ti$_{1-x}$PdRu$_x$ alloys is shown where there are no miscibility gaps. The phase diagram is characterized by the mixing region only, contrary to the Pd sublattice TiPd$_{1-x}$Ru$_x$. The mixing occurs at high temperatures compared to Ti sublattice. There is no phase separation occurrence for Ti$_{1-x}$PdRu$_x$ and the system mixes very well at a temperature below 2000 K. This is due to the fact that Ti and Ru have similar properties and thus tend to mix very well. The results suggest that Ru prefers Ti-site compared to Pd-site in agreement with the predicted formation energies.
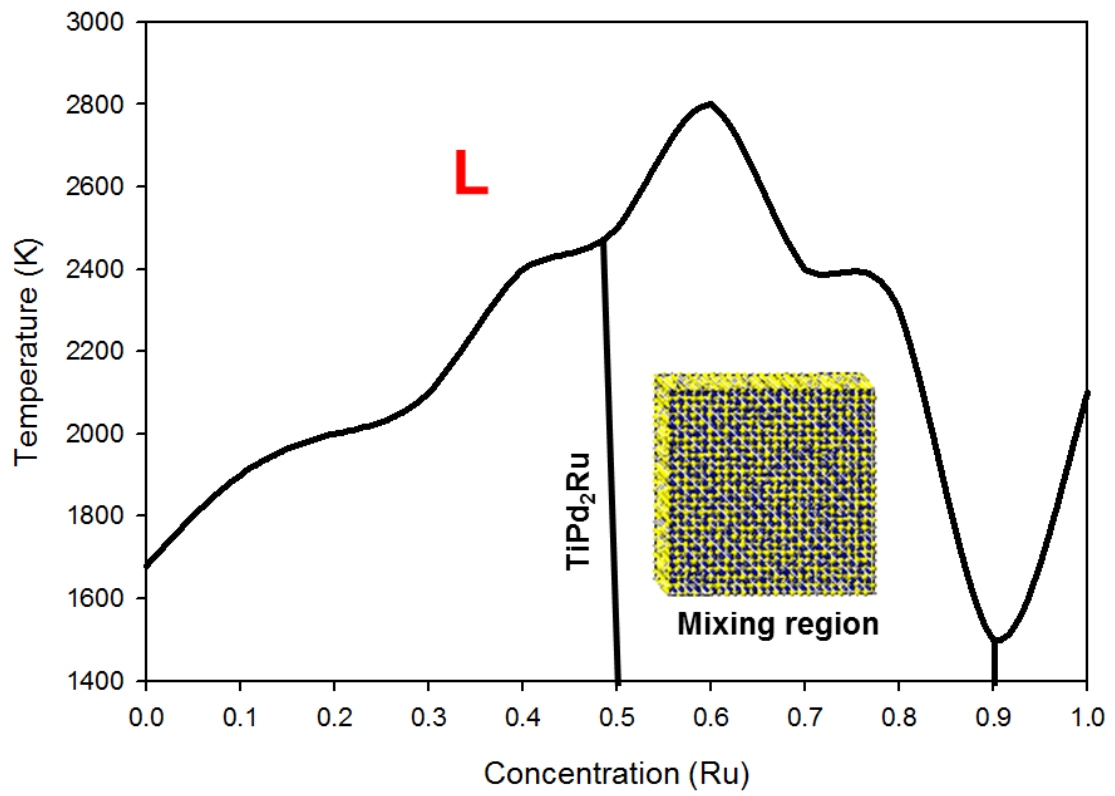
Figure 11-7 Constructed phase diagram of B2 $Ti_{1-x}PdRu_x$ using phase transition temperature at different concentrations.

Chapter 12

Summary and conclusion

In this chapter, we give the summary and conclusion of the study. Furthermore, recommendations and future work are presented.

Titanium-based shape memory alloys (SMAs) are being developed for high temperature applications in the automotive and aerospace industries due to their superior properties, such as shape memory effect and superelasticity [1, 2]. $Ti_{50}Pd_{50}$ is found as one of the promising alloy with excellent chemical and physical properties such as lightweight, resistance to oxidation and ductility at 823 K [21, 22].

The main aim of this study was to investigate stability and phase transformation of binary $Ti_{50}Pd_{50}$ and the ternary $Ti_{50}Pd_{50-x}M_x$ (M= Ru, Pt, Ir, Co, Ni, Os, Al) shape memory alloys using multi-scale computational methods. It was reported that the binary $Ti_{50}Pd_{50}$ alloy is mechanically unstable ($C' < 0$) at 0 K [24, 35], and displayed poor shape memory behaviour during a transformation from cubic to orthorhombic phase, which resulted in poor corrosion resistance [4, 14, 21, 23, 36].

We have employed the first-principles approach to study the stability of the $Ti_{50}Pd_{50}$ alloy using a VASP code [38]. Furthermore, the effect of Ru, Os, Ir, Pt, Co, Ni and Al additions on the stability of $Ti_{50}Pd_{50}$ was investigated using supercell approach at different compositions (6.25, 18.75, 25, 31.25 and 43.75) at 0 K. The LAMMPS code was used to determine the temperature dependence

on the lattice expansion, XRDs and elastic properties of binary $Ti_{50}Pd_{50}$ and ternary B19 $Ti_{50}Pd_{50-x}M_x$ (M= Co, Ni) alloy. The DFTB+ technique was used to derive interatomic potentials of both binary Ti-Pd and ternary Ti-Pd-Ru alloys. The Cluster expansion was used to generate new stable phases on both binary Ti-Pd and ternary Ti-Pd-Ru alloys. Monte carlo simulation was used to construct the ternary phase diagrams.

Ab initio DFT approach was used to study the equilibrium lattice parameters, heats of formation, elastic properties and phonon dispersion curves of B2, $L1_0$, B19 and B19' $Ti_{50}Pd_{50}$ as potential HTSMAs. Our results of lattice parameters were found to be in good agreement to within 5 % with the available experimental and theoretical values [20, 34]. Thus the ground state structures were well reproduced.

The thermodynamic stability was deduced from the heats of formation analysis. It was found that the results are in good agreement to within 5 % with available experimental and theoretical findings. At $Ti_{50}Pd_{50}$, we found that the monoclinic B19' is the most stable phase (lowest ΔH_f) while the cubic B2 is the least stable phase displaying the highest ΔH_f. Thus, the predicted stability trend is: B19'>B19>$L1_0$>B2.

We also evaluated the density of states for the four phases and compare their stability with respect to the trend of Fermi level and pseudogap [26]. The B2 phase was confirmed to be the least stable displaying the highest states at E_f. We also found B19' to be more stable with the lowest number of DOS at the Fermi

level which is consistent with the predicted heats of formation results. Thus a similar stability trend was obtained as: B19′>B19>L1$_0$>B2.

The mechanical properties were investigated to assess the strength of the four binary phases. The cubic B2 was found to have the highest value of c_{12} which is greater than c_{11}. This observation resulted in a negative elastic Shear modulus (C'<0) (condition of instability). The B19′, B19 and L1$_0$ phases were found to be stable since all the independent elastic constants (C_{ij}) and elastic Shear moduli (C'>0) were positive, satisfying the stability criteria of the system [141]. The B19′ showed to have the highest shear modulus compared to B19, L1$_0$ and B2 phases. Furthermore, B19 was found to be the hardest with the highest Bulk modulus while B19′ was found to have the highest value of Young and Shear suggesting that the structure is stiffer and ductile, respectively. Moreover, L1$_0$ was found to be ductile with the highest ratio of Bulk to Shear modulus value (B/G>1.75) and B2 as brittle (B/G<1.75), according to Pugh's ratio of ductility and brittleness [149].

The phonon dispersion curves were determined using the PHONON code [128]. The B2 structure showed the presence of soft modes along the high symmetry direction of Bz, which may be associated with the negative elastic Shear modulus (condition of vibrations instability). Furthermore, the B19' and L1$_0$ phases were found to be more vibrationally stable since there were no soft modes observed in the phonon dispersion curves and this can be attributed to the positive c_{44} and Shear modulus (condition of stability). The B19 structure displayed imaginary soft modes along the Z direction. However, the structure is considered stable as there

were no soft modes at the origin (gamma direction) in agreement with the predicted elastic Shear modulus ($C'>0$).

The temperature dependence calculations were used to evaluate the performance of the structure at high temperature, employing the LAMMPS code [103]. We observed that the volume of the B19, B19′, $L1_0$ and B2 structures increase with an increase in temperature while the densities decrease below the melting temperature (1695 K). The B19 phase has shown to transform to cubic B2 phase at approximately 1496 K and the c/b ratio was found to be 1.414 in agreement with previous work [13]. Interestingly, the $L1_0$ was found to transform to cubic B2 (with a c/b ratio of 1.00) at approximately 897 K. This prediction has never been reported before to our knowledge.

Furthermore, structural analyses were carried out using XRD patterns. It was observed that the XRD patterns of the B19 phase reveal a transformation from B19 to monoclinic B19′ at 1368 K, and transformation to cubic B2 phase at a higher temperature of 1496 K. The XRDs for the $L1_0$ $Ti_{50}Pd_{50}$ were also investigated and it was found that the cubic XRDs patterns appear at 897 K which is lower compared to B19 phase (1496 K). Finally, we found a good correlation between predicted lattice parameters and XRD results.

In addition, the effect of temperature on the elastic properties was investigated for the binary B2, B19′, $L1_0$ and B19 $Ti_{50}Pd_{50}$ structures. We observed that as the temperature is increased, the elastic Shear moduli of the orthorhombic B19 phase decrease (becoming negative). This suggests the instability of the phase at higher temperatures. Similar behaviour was observed for the B19′ structure. In the case

of L1$_0$ and B2, we note that as the temperature is increased, the elastic Shear moduli decrease. However, the elastic Shear modulus was positive throughout the entire temperature range which confirms the stability of L1$_0$ and B2 at higher temperatures. The predicted transformation temperatures from L1$_0$ to B2, B19 to B19′ and B19′ to B2 occurs at 897, 1368 and 1496 K, respectively. These predictions are in line with the experimental phase diagrams [19, 81], the B2 and B19 are stable at 1673 K and 783 K, respectively. The existence of L1$_0$ and B19′ has not been reflected in the current phase diagram, and this is considered as a new prediction that awaits experimental verification.

Ternary alloying with Pt, Ni, Co, Ru, Al, Ir and Os were investigated. The results suggested that the addition of Ru, Os, Pt and Ir stabilizes the Ti$_{50}$Pd$_{50}$ structure, since the heats of formation decrease with composition ($\Delta H_f < 0$). This was confirmed from DOS analysis. It was found that the states are shifted at E$_f$ as the concentration is increased. For example, as the composition of Ru is added, the pseudogap moved toward the E$_f$, indicating electronic stability especially above 20 at. % Ru. A similar trend was observed with Os addition.

The effect of ternary addition revealed that Ti$_{50}$Pd$_{50-x}$Os$_x$ alloys are mechanically stable above 18.75 at. % Os according to the criteria of mechanical stability [141]. Furthermore, the C' was found negative below 25 at. % Ru ($C'< 0$, condition of instability) and becomes positive above this composition ($C'> 0$, condition of stability). The c$_{11}$, c$_{44}$ and C' for Ti$_{50}$Pd$_{50-x}$Ru$_x$ increases with an increase in Ru concentrations, while c$_{12}$ decreases above 25 at. % Ru. It was found that the C' is negative below 31 at. % Co (instability characteristics) and becomes positive above this composition (condition of stability). This suggests that a possible

HTSMAs material could be achieved above 31 at. % Co. It was noted that the C' is negative for Ir, Al and Pt additions on $Ti_{50}Pd_{50-x}M_x$ indicating mechanical instability ($C' < 0$). This analysis has a direct impact on the transformation temperature. For example, a decrease in C' suggests that the Ms is likely to increase [158].

An elastic anisotropy ratio (A) was used to describe the isotropic and anisotropic behaviour of the $Ti_{50}Pd_{50-x}M_x$ systems. The analysis of A proves that the B2 $Ti_{50}Pd_{50-x}M_x$ (M= Co, Ni) alloys displayed elastic anisotropy behaviour (as A is less and greater than 1). It was found that A approaches unity ($A \approx 1$) for both Ru and Os between 25 and 50 at. % composition, suggesting isotropic behaviour.

The ductile nature of $Ti_{50}Pd_{50-x}M_x$ alloys was confirmed from the value of the B/G ratio [149], Poisson 's ratio [140], Cauchy pressure ($c_{12}–c_{44}$) [148] and anisotropy [159]. It was revealed that increasing Os and Ru above 6.25 at. % could effectively improve the ductility of the compound. At high Co content, the $Ti_{50}Pd_{6.25}Co_{43.75}$ is the hardest material (1.39 GPa) amongst other compositions. The Pugh (B/G) and Poisson 's ratio revealed that B2 $Ti_{50}Pd_{50-x}Co_x$ alloy is ductile above 18.75 at. % Co. It was found that the calculated anisotropy ratio is greater than 0.8 for 25 and 31.75 at. % Ru (condition of ductility). Furthermore, the anisotropy ratios were found greater than 0.8 above 18.75 at. % Os and Co which reveal ductility behaviour.

The Bulk modulus (B), Shear modulus (G), Young 's modulus (E), and Vickers hardness (H_V), for the $Ti_{50}Pd_{50-x}M_x$ (M= Os, Ru) alloys, showed an increasing tendency with an increase in Os and Ru content. This behaviour suggests that

Os and Ru are most preferred to enhance the strength of the $Ti_{50}Pd_{50}$. Our phonon dispersion calculations predicted vibrational instability below 18.75 and 25 at. % Os and Ru, respectively at room temperature. Os is favourable above 18.75 at. %, while Ru is preferred above 25 at %.

Furthermore, we have also evaluated how alloying can impact the transformation temperature. The results suggest that the addition of Ni, Co, Ru and Os on $Ti_{50}Pd_{50}$ alloy reduces the transformation temperature as indicated by positive C'. Similar observations were reported previously [92]. In addition, the findings revealed that Ru addition can promote transformation from B2 to B19 phase below 25 at. % Ru (as indicated by negative shear modulus C'). Interestingly, the addition of Ir and Pt was found to increase the martensitic transformation temperature of the TiPd since it gives the negative C'. This analysis is similar to the previous studies of $Ti_{50}Pt_{50}$, where it was indicated that the addition of Ir and Pd enhance the martensitic transformation temperature [92].

The Debye temperature was used to analyse the thermal conductivity of the systems. This quantity is responsible for strong ionic bonds and higher thermal conductivity [164]. A higher Debye temperature was observed for $Ti_{50}Pd_{6.25}Ru_{43.75}$ as compared to other compositions. An increase in Ru, Os and Co content increases the thermal conductivity only at a lower temperature (<300 K). It can be deduced that thermal conductivity could be effectively improved by the increase in Ru, Os and Co concentrations above 25 at. %.

The LAMMPS code which employs the embedded atom method was used to determine the temperature dependence on the lattice expansion, XRDs and

elastic constants for B19 $Ti_{50}Pd_{50-x}M_x$ ternary. Most notably, the volume increases with an increase in temperature while the densities decrease. At 6.25 at. % Co, it was found that the transformation from B19 to B2 occurs at 971 K as the *a/c* and *c/b* ratios are closer to 1.414. Similar behaviour was observed for 18.25 and 25 at. % Co as the transformation temperature decreases. It was observed that when 6.25 at. % Ni is added, the lattice parameters collapse at 970 K. This suggests the transformation temperature from B19 to B2 is lowered. The XRD patterns for B19 $Ti_{50}Pd_{50-x}M_x$ (Co, Ni) showed that the alloy transition occurs at a lower temperature. For example, at 6.25 at. % Co, it was found that the number of peaks reduces at 972 K which suggested a possible transformation from B19 to B2 phase. Furthermore, it was observed that at 6.25 at. % Ni the number of peaks reduces above 971 K which implies transformation from B19 to B2 phase. In addition, the temperature dependence of the elastic properties was investigated for the B19 $Ti_{50}Pd_{50-x}M_x$ ternary. It was observed that as the temperature is increased, the ($c_{11} + c_{22} - 2c_{12}$), ($c_{11} + c_{33} - 2c_{13}$) and ($c_{22} + c_{33} - 2c_{23}$) moduli for the orthorhombic B19 phase decrease for the entire concentration range and become negative. This suggests instability of the phase at higher temperatures.

The self-consistent-charge density functional tight-binding set of parameters for describing $Ti_{50}Pd_{50}$ and $Ti_{50}Pd_{50-x}Ru_x$ systems were developed using the DFTB+ code. It was noted that the calculated lattice parameters for binary $Ti_{50}Pd_{50}$ and ternary $Ti_{50}Pd_{50-x}Ru_x$ structures are in good agreement with available experimental and theoretical findings to within 5 %. The developed SCC-DFTB set of parameters were able to reproduce the structural and elastic properties in reasonable agreement with theoretical data [35]. The DFTB-based Molecular

dynamics calculations showed that the addition of 6.25, 18.75, 25 at. % Ru reduce the transformation temperature from B19 to B2 phase as the *a/b* and *c/b* ratio is approximately 1.448 (1274 K), 1.446 (1074 K) and 1.430 (873 K), respectively. This is consistent with the previous work where the transformation temperature of $Ti_{50}Pd_{50}$ decreased with the addition of 5 at. % Ru [93]. The DFTB+ code was able to predict the transformation temperature of $Ti_{50}Pd_{50-x}Ru_x$ alloy while a LAMMPS code was able to predict for $Ti_{50}Pd_{50-x}M_x$ (M= Co, Ni) alloys. Both codes were found robust in determining the transformation temperature.

We have also studied the phase stability of B2 $TiPd_{1-x}Ru_x$ and $Ti_{1-x}PdRu_x$ alloys using a multi-scale approach. A combination of DFT, Cluster expansion and Monte carlo simulation approaches were used. The cluster expansion method has generated about 27 new structures on B2 $TiPd_{1-x}Ru_x$ and 17 new structures for B2 $Ti_{1-x}PdRu_x$. Their heats of formation were found to be positive, indicating a phase separation tendency for $TiPd_{1-x}Ru_x$ alloys. The most thermodynamically stable structure of $Ti_{1-x}PdRu_x$ was found to be $TiPd_2Ru$ (P4/mmm) which displayed the lowest heats of formation (-0.404 eV/atom).

The phase diagrams of B2 $TiPd_{1-x}Ru_x$ and $Ti_{1-x}PdRu_x$ were constructed using Monte Carlo simulations. The findings revealed that Ru prefers Ti-site as compared to Pd-site, consistent with the predicted heats of formation. More importantly, the phase diagrams of ternary B2 $TiPd_{1-x}Ru_x$ and $Ti_{1-x}PdRu_x$ systems were constructed for the first time and then considered a prediction that awaits experimental investigation.

The stability and phase transformation of the binary $Ti_{50}Pd_{50}$ and ternary $Ti_{50}Pd_{50-x}M_x$ (M= Ru, Pt, Ir, Co, Ni, Os, Al) shape memory alloys were successfully studied using multi-scale methods. The findings indicate that a HTSMAs material could be achieved between 25 and 31.25 at. % Ru concentration. The current study will provide valuable insights which align guide experiments on stability, ductility and transformation temperature of binary $Ti_{50}Pd_{50}$ and ternary $Ti_{50}Pd_{50-x}M_x$. More importantly, to highlight where phase separation and mixing may occur in the B2 $TiPd_{1-x}Ru_x$ and $Ti_{1-x}PdRu_x$ systems which is important for alloy development.

Recommendations and future work

Several recommendations for future research are listed below:

I.   Use Monte carlo simulation to determine the strain and stress for binary Ti-Pd and ternary Ti-Pd-Ru systems.

II.   Use UNCLE Code to generate new ground state structures of Ti-Pd-Os. Monte Carlo simulations can be used to determine phase separation and the mixing of Ti-Pd-Os system.

III.   To derive sets of parameters of the B19 and B2 TiPd-Os alloys using DFTB+ code. The sets of parameters are important to determine structural, electronic and elastic properties and compare them with available experimental findings. Furthermore, the transformation temperature and stability will be investigated.

IV.   To determine the relative stability by investigating energies of different site-occupancy configurations using SOD code on binary Ti-Pd and ternary B2 TiPd-Ru alloys.

V.   To determine the temperature dependence on lattice parameters, XRDs and elastic properties of the ternary B19′, B2 and $L1_0$ $Ti_{50}Pd_{50-x}M_x$ (Co, Ni) using LAMMPS code.

References

[1]   J. M. Jani, M. Leary, A. Subic and M. A. Gibson, "A review of Shape Memory Alloy Research, Applications and Opportunities," *Mater. Des.,* vol. 56, pp. 1078-1113, 2014.

[2]   S. K. Yadav and R. S. Bobade, "Shape Memory Alloy Actuators: A Review," *IJRASET,* vol. 7, pp. 799 - 802, 2019.

[3]   G. S. Firstov, Y. N. Koval, J. V. Humbeeck and P. Ochin, "Martensitic transformation and shape memory effect in Ni3Ta: A novel high-temperature shape memory alloy," *Mater. Sci. Eng. A,* vol. 481, pp. 590-593, 2008.

[4]   Y. Yamabe-Mitarai , "TiPd- and TiPt-Based High-Temperature Shape Memory Alloys: A Review on Recent Advances," *Met.,* vol. 10, pp. 1531-1552, 2020.

[5]   K. Otsuka and C. M. Wayman, "Shape Memory Metals," *Cambridge University Press,* pp. 220-239, 1998.

[6]   J. Frenzel, A. Wieczorek, I. Opahle, B. Maaß, R. Drautz and G. Eggeler, "On the effect of alloy composition on martensite start temperatures and latent heats in Ni–Ti-based shape memory alloys," *Acta Mater.,* vol. 90, pp. 213-231, 2015.

[7]   R. Dasgupta , "A look into Cu-based shape memory alloys: Present scenario and future prospects," *J. Mater. Res.,* vol. 29, p. 1681, 2014.

[8]   J. Lee, Y. Ikeda and I. Tanaka, "First-principles screening of structural properties of intermetallic compounds on martensitic transformation," *Comput. Mater. Sci.,* vol. 3, p. 52, 2017.

[9]   A. Wadood and Y. Yamabe-Mitarai, "TiPt-Co and TiPt-Ru High Temperature Shape Memory Alloys," *Platin. Met. Rev.,* vol. 601, pp. 106-110, 2014.

[10]   K. C. Atli, I. Karaman, R. D. Noebe, A. Garg, Y. I. Chumlyakov and I. V. Kireeva, "Improvement in the Shape Memory Response of Ti50.5Ni24.5Pd25 High-Temperature Shape Memory Alloy with Scandium Microalloying," *Metall. Mater. Trans. A,* vol. 41, p. 2485, 2010.

[11]   S. O. Ponomaryova et. al., "Martensitic transformation and shape memory effect in Ni-Al based alloys," *MATEC Web Conf.,* vol. 33, p. 06004, 2015.

[12] T. Biggs, M. B. Cortie, M. J. Witcomb and L. A. Cornish, "Martensitic Transformations, Microstructure, and Mechanical Workability of TiPt," *Metall. Mater. Trans. A,* vol. 32, pp. 1881-1886, 2001.

[13] Y. Yamabe-Mitarai, T. Hara, S. Miura and H. Hosoda, "Shape memory effect and pseudoelasticity of TiPt," *Intermetallics,* vol. 18, pp. 2275-2280, 2010.

[14] K. Otsuka, K. Oda, Y. Ueno, M. Piao, T. Ueki and H. Horikawa, "The Shape Memory Effect in a Ti50Pd50 Alloy," *Scripta Metall Mater.,* vol. 29, pp. 1355-1358, 1993.

[15] V. C. Solomon and M. Nishida, "Martensitic Transformation in Ti-Rich Ti–Pd Shape Memory Alloys," *Mater. Trans,* vol. 43, pp. 908-915, 2002.

[16] S. Hisada, M. Matsuda and Y. Yamabe-Mitarai, "Shape Change and Crystal Orientation of B19 Martensite in Equiatomic TiPd Alloy by Isobaric Test," *Met.,* vol. 10, p. 3754, 2020.

[17] D. Golberg, Ya Xu, Y. Murakami, K. Otsuka, T. Ueki and H. Horikawa, "High-Temperature Shape Memory Effect in Ti50Pd50-xNix (x= 10, 15, 20) Alloys," *Intermetallics,* vol. 22, pp. 241-248, 1995.

[18] M. Nishida, T. Hara, Y. Morizono, A. Ikeya, H. Kijima and A. Chiba, "Transmission electron microscopy of twins in martensite in Ti-Pd shape memory alloy," *Acta mater.,* vol. 45, pp. 4847-4853, 1997.

[19] C. Guo, M. Li, C. Li and Z. Du, "A thermodynamic modeling of the Pd–Ti system," *CALPHAD,* vol. 23, pp. 512-517, 2011.

[20] A. E. Dwight, R. A. Conner Jr. and J. W. Downey, "Equiatomic compounds of the transition and lanthanide elements with Rh, Ir, Ni and Pt," *Acta Crystallogr.,* vol. 18, pp. 835-839, 1965.

[21] D. Golberg, Y. Xu, Y. Murakami, S. Morito and K. Otsuka, "Characteristics of Ti50Pd30Ni20 high-temperature shape memory alloy," *Intermetallics,* vol. 3, pp. 35-46, 1995.

[22] X. Huang, M. Karin and J. Ackland, "First-Principles Study of the Structural Energetics of PdTi and PtTi," *Phys. Rev. B,* vol. 67, pp. 024101-024107, 2003.

[23] H. C. Donkersloot and J. H. N. Van Vucht, "Martensitic Transformations in Gold–Titanium Palladium–Titanium, and Platinum–Titanium Alloys Near the Equiatomic Composition," *J. Less-Common Met.,* vol. 20, pp. 83-91, 1970.

[24] R. G. Diale, R. Modiba, P. E. Ngoepe and H. R. Chauke, "Density functional theory study of TiPd alloying with Os as potential high temperature shape memory alloys," *IOP Conf. Sr. Mater. Sci. Eng.,* vol. 655, p. 012042, 2019.

[25] G. Bozzolo, H. O. Mosca and R. D. Noebe, "Phase structure and site preference behavior of ternary alloying additions to PdTi and PtTi shape-memory alloys," *Intermetallics,* vol. 15, pp. 901-911, 2007.

[26] R. Mahlangu, M. J. Phasha, H. R. Chauke and P. E. Ngoepe, "Structural, elastic and electronic properties of equiatomic PtTi as potential high-temperature shape memory alloy," *Intermetallics,* vol. 33, pp. 27-32, 2013.

[27] K. Otsuka and X. Ren, "Recent developments in the research of shape memory alloys," *Intermetallics,* vol. 7, pp. 511-528, 1999.

[28] E. Baldwin, B. Thomas, J. W. Lee and A. Rabiei, "Processing TiPdNi base thin-filmshape memory alloys using ion beam assisted deposition," *Surf. Coat.Technol.,* vol. 200, pp. 2571-2579., 2005.

[29] P. K. Kumar, D. C. Lagoudas, J. Zanca, and M. Z. Lagouda , "Thermomechanical Characterization of High Temperature SMA Actuators," *Proc. of SPIE,* vol. 6170, pp. 306-312, 2006.

[30] D. Coutsouradis, A. Davin and M. Lamberigts, "Cobalt-based superalloys for applications in gas turbines," *Mater. Sci. Eng.,* vol. 88, pp. 11-19, 1987.

[31] C. R. Hamond, "The elements," *Boca Raton, FL: CRC,* 2005.

[32] M. Jahn´atek, O. Levy, G. L. W. Hart, L. J. Nelson, R. V. Chepulskii, J. Xue and S. Curtarolo,, "Ordered phases in ruthenium binary alloys from high-throughput first-principles calculations," *Phys. Rev. B,* vol. 84, pp. 214110-214118, 2011.

[33] Haynes, William M ed., "CRC Handbook of Chemistry and Physics (92nd ed.).," *CRC Press. ISBN 978-1439855119,* 2011.

[34] X. Q. Chen, C. L. Fu and J. R. Morris, "The electronic, elastic, and structural properties of Ti–Pd intermetallics and associated hydrides from first principles calculations," *Intermetallics,* vol. 18, pp. 998-1006, 2010.

[35] R. G. Diale, R. Modiba, P. E. Ngoepe and H. R. Chauke, "The effect of Ru on Ti50Pd50 high temperature shape memory alloy: a first-principles study," *MRS Adv.,* vol. 4, pp. 2419-2429, 2019.

[36] D. J. Frankel and G. B. Olson , "Design of Heusler Precipitation Strengthened NiTi- and PdTi-Base SMAs for Cyclic Performance," *Shap. Mem. Superelasticity,* vol. 1, pp. 162-179, 2015 .

[37] J. C. Phillips , "Energy-band interpolation scheme based on a pseudopotential.," *Phys. Rev.,* vol. 685., p. 112, 1958.

[38] G. Kresse and J. Furthmüller, "Efficient Iterative Schemes for Ab-initio Total-energy Calculations Using a Plane-wave Basis Set," *Phys. Rev. B,* vol. 54, pp. 11169-11186, 1996.

[39] J. P. Perdew, K. Burke and M. Ernzerhof, "Generalized Gradient Approximation Made Simple," *Phys. Rev. Lett.,* vol. 77, pp. 3865-3868, 1996.

[40] S. N. Prins, L. A. Cornish and P. S. Bouchera, "Derivation of the liquidus surface projection for the Al–Pt–Rusystem from as-cast samples," *J. Alloys Compd.,* vol. 403, pp. 245-257, 2005.

[41] P. K. Kumar and D. C. Lagoudas, "Introduction to Shape Memory Alloys," *In: Shape Memory Alloys. Springer, Boston, MA,* pp. 1-51, 2008.

[42] G. V. Kurjumov and L. G. Khandros, "First reports of the thermoelastic behaviour of the martensitic phase of Au-Cd alloys," *Dokl. Akad. Nauk SSSR,* vol. 66, pp. 211-213, 1949.

[43] A. Ölander, "An electrochemical investigation of solid cadmium-gold alloys," *Am. Chem. Soc.,* vol. 54, pp. 3819-3852, 1932.

[44] L. C. Chang and T. A. Read, "Plastic deformation and diffusionless phase changes in metals-the AuCd β-phase," *Trans. Met. Soc. AIME,* vol. 191, pp. 47-52, 1951.

[45] S. B. Kang, K. S. Yoon, T. H. Nam, J. S. Kim and V. E. Gjunter, "Smart materials-fundamentals and applications. Fracture treatment using TiNi shape memory alloy bone fixater (BRM-SH system)," *Mater. Trans.,* vol. 43, pp. 1049-1051, 2002.

[46] K. N. Melton , "General applications of shape memory alloys and smart materials. In: Otsuka K, Wayman CM, editors. Shape memory materials," *Cambridge University Press,* pp. 220-39, 1999.

[47] G. Kauffman and I. Mayo, "The Story of Nitinol: The Serendipitous Discovery of the Memory Metal and Its Applications," *J. Chem. Educ.,* vol. 2, pp. 1430-4171, 1997.

[48] C. T. Dotter, R. W. Buschmann, M. K. McKinney and J. Rösch, "Transluminal expandable nitinol coil stent grafting: preliminary report," *preliminary report Radiology,* vol. 147, pp. 259-260, 1983.

[49] G. F. Andreasen and T. B. Hilleman, "An evaluation of 55 cobalt substituted Nitinol wire for use in orthodontics," *J. Am. Assoc.,* vol. 82, pp. 1173-1375, 1971.

[50] D. Stoeckel, "Shape memory actuators for automotive applications," *Mater. Des.,* vol. 11, pp. 302-307, 1990.

[51] G. M. Chevrolet , "Chevrolet Debuts Lightweight 'Smart Material' on corvette," *General Motors News,* 2013.

[52] S. Zareie, A. S. Issa, R. J. Seethaler and A. Zabihollah, "Recent advances in the applications of shape memory alloys in civil infrastructures: A review," *J. Struct.,* vol. 27, pp. 1535-1550, 2020.

[53] E. Quandt et. al., "Sputter deposition of TiNi, TiNiPd and TiPd films displaying the two-way shape-memory effect," *Sens. Actuat. A,* vol. 53, pp. 434-439, 1996.

[54] W. Xing and X. Q. Chen, "First-principles studies of structural stabilities and enthalpies of formation of refractory intermetallics: TM and TM3 (T = Ti, Zr, Hf; M = Ru, Rh, Pd, Os, Ir, Pt)," *Intermetallics,* vol. 28, pp. 16-24, 2012.

[55] L. A. Bendersky, J. K. Stalick, R. Portier and R. M. Waterstrat, "Crystallographic structures and phase transformations in ZrPd," *J. Alloys Compd.,* vol. 236, pp. 19-25, 1996.

[56] F. H. M. Spit, J. W. Drijver and S. Radelaar, "Hydrogen sorption by the metallic glass Ni64Zr36 and by related crystalline compounds," *J. Scripta Metall.,* vol. 14, pp. 1071-1076, 1980.

[57] J. K. Stalicka and R. M. Waterstrat, "The zirconium–platinum phase diagram," *J. Alloys Compd.,* vol. 430, p. 123–131, 2007.

[58] E. Benko, E. Bielanska, V. M. Pereverteilo and O. B. Loginova, "Formation peculiarites of the interfacial structure during cBN wetting with Ag-Ti, Ag-Zr and Ag-Hf alloys," *Diam. Relat. Mater.,* vol. 6, pp. 931-934, 1997.

[59] M. L. Muolo, E. Ferrera, R. Novakovic and A. Passerone, "Wettability of zirconium diboride ceramics by Ag, Cu and their alloys with Zr," *Scripta Mater.,* vol. 48, pp. 191-196, 2003.

[60] H. M. Grandin, S. Berner and M. Dard, "A Review of Titanium Zirconium (TiZr) Alloys for Use in Endosseous Dental Implants," *J. Mater. Sci.,* vol. 5, pp. 1348-1360, 2012.

[61] K. P. Gupta , "The Fe-Ni-Ti System Update (Iron - Nickel - Titanium)," *J. Phase Equilib.,* vol. 22, pp. 171-175, 2001.

[62] J. K. Stalick and R. M. Waterstrat, "Crystal Structures and Phase Equilibria in the Hafnium-Palladium System," *J. Phase Equilib. Diff.,* vol. 37, pp. 416-422, 2016.

[63] S. Hisada, M. Matsuda, K. Takashima and Y. Yamabe-Mitarai, "Structural analysis and martensitic transformation in equiatomic HfPd alloy," *J. Solid State Chem.,* vol. 258, pp. 712-717, 2018.

[64] G. Ghosh , "First-principles calculations of structural energeticsof Cu–TM (TM = Ti, Zr, Hf) intermetallics," *Acta Mater.,* vol. 55, pp. 3347-3374, 2007.

[65] P. Villars, K. Cenzual, J. L. C. Daams, F. Hulliger, H. Okamoto,K. Osaki, A. Prince, M. Berndt, K. Brandenburg, H. Putz and S. Iwata, "The Pauling File, Binaries Edition," *J. Alloys Compd.,* vol. 367, pp. 293-297, 2004.

[66] H. Matsuno, A. Yokoyama, F. Watari, M. Uo and T. Kawasaki, "Biocompatibility and osteogenesis of refractory metal implants, titanium, hafnium, niobium, tantalum and rhenium," *Biomater.,* vol. 22, pp. 1253-1262, 2001.

[67] A. G. Imgram, D. N. Williams and H. R. Ogden, "Tensile Properties of Binary Titanium-Zirconium and Titanium-Hafnium Alloys," *J. Less-Common Met.,* vol. 4, pp. 217-225, 1962.

[68] Y. L. Zhou, M. Niinomi and T. Akahori, "Dynamic Young's Modulus and Mechanical Properties of Ti−Hf Alloys," *J. Mater. Trans.,* vol. 45, pp. 1549-1554, 2004.

[69] N. T. C. Oliveira, G. Aleixo, R. Caram and A. C. Guastaldi, "Development of Ti-Mo alloys for biomedical applications: Microstructure and electrochemical characterization," *Mater. Sci. Eng. A,* vol. 452, pp. 727-731, 2007.

[70] Y. Liu, W. F. Wei, K. C. Zhou, F. Chenl and H. P. Tang, "Microstructures and mechanical behavior of PM Ti-Mo alloy," *J. Central South Univ. Technol.,* vol. 2, pp. 81-86, 2003.

[71] L. C. Zhang, T. Zhou, M. Aindow, S. P. Alpay, M. J. Blackbur and M. H. Wu, "Nucleation of stress-induced martensites in a Ti/Mo-based alloy," *J. Mater. Sci.,* vol. 40, pp. 2833-2836, 2005.

[72] R. Davis, H. M. Flower and D. R. F. West, "Martensitic transformations in Ti-Mo alloys," *J. Mater. Sci.,* vol. 14, pp. 22-28, 1979.

[73] P. J. Bania, D. Eylon, R. R. Boyer, D. A. Koss (Eds.), "Beta titanium alloys and their role in the titanium industry — keynote lecture, Beta Titanium Alloys in the 1990's," *TMS, Paris, France,* pp. 3-14, 1993.

[74] M. Niinomi, D. Kuroda, K. Fukunaga, M. Morinaga, Y. Kato, T. Yashiro and A. Suzuki, "Corrosion wear fracture of new β type biomedical titanium alloys," *Mater. Sci. Eng. A,* vol. 263, pp. 193-199, 1999.

[75] T. G. Mazhuga, V. M. Danilenko, T. Y. A. Velikanova, and E. L. Semenov , "Thermodynamic calculation of phase equilibria in the Ti-Ru, Ti-Os, Ni-Ru binary systems," *CALPHAD,* vol. 22, pp. 59-67, 1998.

[76] V. A. Raman and K. S. Schubert, "Structural Investigations in some T 4-T 9 Homology and Quasihomology Alloy Systems," *Z. Metallkd.,* vol. 55, pp. 704-714, 1964.

[77] C. L. Tan, W. Cai and J. C. Zhu, "First-principles study on elastic properties and electronic structures of Ti-based binary and ternary shape memory alloys," *Chin. Phys. Lett.,* vol. 23, pp. 2863-2866, 2006.

[78] J. L. Murray , "Gold-Titanium Binary Alloy Phase Diagram," *J. ASM International,* vol. 1, pp. 442-445, 1990.

[79] G. S. Firstov, H. Van and Y. N. Koval, "High Temperature Shape Memory Alloys Problems and Prospects," *J. Intell. Material Syst. Struct.,* vol. 17, pp. 1041-1045, 2006.

[80] Y. Y. Ye, C. T. Chan and K. M. Ho, "Structural and electronic properties of the martensitic alloys TiNi, TiPd, and TiPt," *Phys. rev. B,* vol. 56, pp. 3678-3689, 1997.

[81] J. L. Murray, "The Pd-Ti (Palladium-titanium) system," *Bull. Alloy Phase Diagr.,* vol. 3 , pp. 321-329, 1982.

[82] A. F. Jankowski, "A15 structure formation in Ti-Pd," *J. Alloys Compd.,* vol. 182, pp. 35-42, 1992.

[83] T. Yamamuro, Y. Morizono, J. Honjyo and M. Nishida, "Phase equilibrium and martensitic transformation in near equiatomic Ti-Pd alloys," *Mater. Sci. Eng. A,* Vols. 438-440, pp. 327-331, 2006.

[84] E. Eckelmeyer , "The effect of alloying on the shape memory phenomenon in nitinol," *J. Scr. Metall.,* vol. 10, pp. 667-672, 1976.

[85] P. E. Thoma and J. J. Boehm, "Effect of composition on the amount of second phase and transformation temperatures of NixTi90−xHf10 shape memory alloys," *Mater Sci. Eng. A,* vol. 385, pp. 273-275, 1999.

[86] H. Y. Kim, T. Jinguu, T. H. Nam and S. Miyazaki, "Cold Workability and Shape Memory Properties of Novel Ti-Ni-Hf-Nb High-Temperature Shape Memory Alloys," *Scr. Mater.,* vol. 65, pp. 846-855, 2011.

[87] G. Bigelow, "Effects of palladium content, quaternary alloying, and thermomechanical processing on the behavior of Ni-Ti-Pd shape memory alloys for acuator applications," *MSc. Thesis Colorado School of Mines Golden CO.,* 2006.

[88] J. Ma, I. Karaman and R. D. Noebe, "High temperature shape memory alloys," *Int. Mater. Rev.,* vol. 55, pp. 257-315, 2010.

[89] A. Wadood and Y. Yamabe-Mitarai, "Recent research and developments related to near-equiatomic titanium-platinum alloys for high-temperature applications," *Platin. Met. Rev.,* vol. 58, pp. 61-67, 2014.

[90] A. Wadood, M. Takahashi, S. Takahashi, H. Hosoda and Y. Yamabe-Mitarai, "High-temperature mechanical and shape memory properties of TiPt–Zr and TiPt–Ru alloys," *Mater. Sci. Eng. A,* vol. 564, pp. 34-41, 2013.

[91] Y. Yamabe-Mitarai, R. Arockiakumar, A. Wadood, K. S. Suresh, T. Kitashima, T. Hara, M. Shimojo,W. Tasaki, M. Takahashi, S. Taahashi and H. Hosoda, "Ti(Pt, Pd, Au) based High Temperature Shape Memory Alloys," *Mater. Today Proc.,* vol. 2, pp. S517-S552, 2015.

[92] R. Mahlangu , "Computational modelling studies of Ti50Pt50-xMx (M: Co, Ni, Pd, Ir) shape memory alloys," *PhD thesis, University of Limpopo, South Africa,* 2015.

[93] Y. Yamabe-Mitarai, "Development of High-Temperature Shape Memory Alloys Above 673 K," *Mater. Sci.,* vol. 879, pp. 107-112, 2016.

[94] R. Arockiakumar, M. Takahashi, S.Takahashi and Y. Yamabe-Mitarai, "Microstructure, mechanical, and shape memory properties of Ti-55Pd-5x (x=Zr, Hf, V, Nb) alloys," *Mater. Sci. Eng. A,* vol. 585, pp. 86-93, 2013.

[95] Q. Tian and J. Wu, "Characterisation of phase transformation in Ti50+xPd30Ni20−x alloys," *Intermetallics,* vol. 10, pp. 675-682, 2002.

[96] H. Nakayama and M. Taya, "Characteristics of Ti50-Pd(50-x)-W(x) High Temperature Shape Memory Alloy," *Mater. Sci.,* Vols. 539-543, pp. 3190-3194, 2007.

[97] W. Cai, K. Otsuka and M. Asai, "Martensite Aging Effect in Ti–Pd and Ti–Pd–Ni High Temperature Shape Memory Alloys," *Mater. Trans. JIM,* vol. 40, pp. 895-898, 1999.

[98] P. Hohenberg and W. Kohn, "Inhomogeneous Electron Gas," *Phys. Rev. B,* vol. 136, pp. B864-B871, 1964.

[99] W. Kohn and L. J. Sham, "Self-Consistent Equations Including Exchange and Correlation Effects," *Phys. Rev. A,* vol. 140, pp. A1133-A1138, 1965.

[100] M. Elstner and G. Seifert, "Density Functional Tight Binding," *Philos. Trans. R. Soc. A,* vol. 372, pp. 483-494, 2012.

[101] B. J. Alder and T. E. Wainwright, "Phase Transition for a Hard Sphere System," *J. Chem. Phys. ,* vol. 27, p. 1208, 1957.

[102] B. J. Alder and T. E. Wainwright, "Studies in Molecular Dynamics. I. General Method," *J. Chem. Phys.,* vol. 31, p. 459, 1959.

[103] S. Plimpton , "Fast Parallel Algorithms for Short–Range Molecular Dynamics," *J. Comput. Phys.,* vol. 117, pp. 1-19, 1995.

[104] M. S. Daw and M. I. Baskes, "Embedded-Atom Method: Derivation and Application to Impurities, Surfaces and other Defects in Metals," *Phys. Rev. B,* vol. 29, pp. 6443-6453, 1984.

[105] D. Lerch, O. Wieckhorst, G. L. W. Hart, R. W. Forcade and S. Muller , "UNCLE: a code for constructing cluster expansions for arbitrary lattices with minimal user-input," *Modelling Simul. Mater. Sci. Eng.,* vol. 17, p. 330, 2009.

[106] A. E. Mattson, P. A. Schultz, M. P. Desjarlais, T. R. Mattsson and K. Leung, "Designing Meaningful Density Functional Theory Calculations in Materials Science—A Primer," *Mater. Sci. Eng.,* vol. 13, pp. R1-R32, 2005.

[107] L. Hedin and B. I. Lundqvist, "Explicit Local Exchange-Correlation Potentials," *J. Phys. C,* vol. 4, pp. 2064-2082, 1971.

[108] J. P. Perdew and Y. Wang, "Accurate and simple analytic representation of the electron-gas correlation energy," *Phys. Rev. B,* vol. 45, pp. 13244-13249, 1992.

[109] J. P. Perdew, A. Ruzsinszky, G. I. Csonka, O. A. Vy-drov, G. E. Scuseria, L. A. Constantin, X. Zhou and K. Burke, "Restoring the density-gradient expansion forexchange in solids and surfaces," *Phys. Rev. Lett.,* vol. 100, p. 136406, 2008.

[110] B. Hammer, L. B. Hansen and J. K. Nørskov, "Improved adsorption energetics within density-functionaltheory using revised Perdew-Burke-Ernzerhof functionals," *Phys. Rev. B,* vol. 59, p. 7413, 1999.

[111] Peter M. W. Gill, B. G. Johnson, J. A. Pople and M. J. Frisch, "The performance of the Becke-Lee-Yang-Parr (B-LYP) density functional theory with various ba-sis sets," *Chem. Phys. Lett.,* vol. 197, p. 499, 1992.

[112] R. Armiento and A. E. Mattsson, "Functional designed toinclude surface effects in self-consistent density functional theory," *Phys. Rev. B,* vol. 72, p. 085108, 2005.

[113] J. Tao, J. P. Perdew, V. N. Staroverov and G. E. Scuseria , "Climbing the density functional ladder: nonempirical meta-generalized gradient approximation designed for molecules and solids," *Phys. Rev. Lett.,* vol. 91 , p. 146401, 2003 .

[114] M. Eder, E. G. Moroni and J. Hafner, "Structural, electronic and magnetic properties of thin Mn films on Cu (100) substrates.," *Phys. Rev. B.,* vol. 61, p. 492, 2000.

[115] M. C. Payne, M. P. Teter, D. C. Allan, T. A. Arias and J. D. Joannopoulos, "Iterative Minimization Techniques for Ab ilitio Total-Energy Calculations: Molecular Dynamic and Conjugate Gradients," *Rev. Mod. Phys.,* vol. 64, p. 1045, 1992.

[116] N. W. Ashcroft and N. D. Mermin, "On Introductory Concepts,in Solid State Physics," *Philadelphia, Saunders College Publishing,* 1976.

[117] H. Hellmann , "A new approximation method in the problem of many electrons," *J.Chem. Phys.,* vol. 3, p. 61, 1935.

[118] M. L. Cohen and V. Heine, "The fitting of pseudo-potentiasl to experimental data and their subsequent applications, Advances in research and applications," *Solid State Phys.,* vol. 25, pp. 37-248, 1970.

[119] L. Kleinmann and D. M. Bylander, "Efficacious Form for Model Pseudopotentials," *Phys. Rev. Lett.,* vol. 48, p. 1425, 1982.

[120] H. J. Monkhorst and J. D. Pack,, "On Special Points for Brillouin Zone Integrations," *Phys. Rev. B,* vol. 13, pp. 5188-5192, 1976.

[121] P. E. Blöchl, "Projector augmented-wave method," *Physical Review B,* vol. 50, pp. 17953-17979, 1994.

[122] L. Verlet, "Computer 'experiments' on classical fluids. I. Thermodynamical properties of Lennard-Jones molecules," *Phys. Rev.,* vol. 159, p. 98, 1967.

[123] S. Nose, "A molecular dynamics method for simulations in the canonical ensemble," *J. Mol. Phys.,* vol. 52, pp. 255-268, 1984.

[124] W. B. Hoover, "Canonical dynamics: equilibrium phase-space distribution," *Phys. Rev. A,* vol. 31, p. 1695, 1985 .

[125] J. M. Sanchez, F. Ducastelle and D. Gratias , "Generalized cluster description of multicomponent systems," *Physica A,* vol. 128 , pp. 334-50, 1984 .

[126] A. van de Walle and G. Ceder, "Automating first-principles phase diagram calculations," *J. Phase Equilib.,* vol. 23, pp. 391-394, 2002.

[127] N. Metropolis, A. W. Rosenbluth, M. N. Rosenbluth, A. H. Teller and E. Teller, "Equation of state calculations by fast computing machines," *J. Chem. Phys.,* vol. 21, pp. 1087-1092, 1953.

[128] K. Parlinski, Z. Q. Li and Y. Kawazoe, "First-Principles Determination of the Soft Mode in Cubic ZrO2," *Phys. Rev. Lett.,* vol. 78, pp. 4063-4066, 1997.

[129] D. Vandebilt, "Soft self-consistent pseudopotentials in a generalized eigenvalue formalism," *Phys. Rev. B,* vol. 41, p. 7892 , 1990.

[130] B. Delley, "An all-electron numerical method for solving the local density functional for polyatomic molecules," *J. Chem. Phys.,* vol. 92, pp. 508-517, 1990.

[131] B. Delley , "Analytic energy derivatives in the numerical local-density-functional approach," *J. Chem. Phys.,* vol. 94, pp. 7245-7250, 1991.

[132] G. Seifert, H. Eschrig and W. Bieger , "An approximation variant of LCAO-X-ALPHA methods," *Z. Phys. Chem.,* vol. 267, pp. 529-539, 1986.

[133] T. Frauenheim, G. Seifert, M. Elstner, Z. Hajnal, G. Jungnickel, D. Porezag, S. Suhai and R. Scholz, "A Self-Consistent Charge Density-Functional Based Tight-Binding Method for Predictive Materials Simulations in Physics, Chemistry and Biology," *Phys. Status Solidi B,* vol. 217, p. 41, 2000.

[134] M. Elstner, D. Porezag, G. Jungnickel, J. Elsner, M. Haugk, Th. Frauenheim, S. Suhai and G. Seifert, "Self-consistent-charge density-functional tight-binding method for simulations of complex materials properties," *Phys. Rev. B,* vol. 58, pp. 7260-7268, 1998.

[135] G. Dolgonos, B. Aradi, N.H. Moreira and T. Frauenheim, "An inproved self-consistent-charge density functional tight binding (SCC-DFTB) set of parameters for simulation of bulk and molecular systems involving titanium," *J. Chem. Theory Comput.,* vol. 6, pp. 266-278, 2010.

[136] M. Elstner, T. Frauenheim and S. Suhai, "An approximate DFT method for QM/MM simulations of biological structures and processes," *J. Mol. Struct.,* vol. 632, pp. 29-41, 2003.

[137] P. Koskinen and V. Makinen, "Density-functional tight-binding for beginners," *Comput. Mater. Sci.,* vol. 47, pp. 237-253, 2009.

[138] M. S. Daw and M. I. Baskes, "Semiempirical, quantum mechanical calculation of hydrogen embrittlement in metals," *Phys. Rev. Lett.,* vol. 50, p. 1285, 1983.

[139] X. W. Zhou, R. A. Johnson and H. N. G. Wadley, "Misfit-Energy-Increasing Dislocations in Vapor-Deposited CoFe/NiFe Multilayers," *Phys. Rev. B,* vol. 69, pp. 144113-1-144113-10, 2004.

[140] I. N. Frantsevich and S. A. Voronov , "Elastic Constants and Elastic Moduli of Metals and Insulators," *Naukova Dumka, Kiev,* pp. 60-180, 1983.

[141] M. J. Mehl and B. M. Klein, "First-Principles Calculation of Elastic Properties," *in Intermetallic Compounds - Principles and Practice,* Vols. 1, J. W. a. R. Fleischer, Ed., J. Wiley and Sons Ltd, pp. 195-210, 1994.

[142] Z. J. Wu, E. J. Zhao, H. P. Xiang, X. F. Hao, X. J. Liu and J. Meng, "Crystal Structures and Elastic Properties of Superhard Ir N2 and Ir N3 from First Principles," *Phys. Rev. B,* vol. 76, p. 054115, 2007.

[143] G. Bao, D. Duan, D. Zhou, X. Jin, B. Liu and T. J. Cui, "A New High-Pressure Polar Phase of Crystalline Bromoform: A First-Principles Study," *J. Phys. Chem. B,* vol. 114, pp. 13933-13939, 2010.

[144] E. Raub and E. Röschel, "Phase relations and structures in titanium-palladium alloys," *Z. Metallk.,* vol. 59, pp. 112-116, 1968.

[145] Q. Chen and Q. Xie, "First-principles calculations on the electronic structure and optical properties of Mg2Si epitaxial on Si (111)," *Phys. Procedia,* vol. 11, pp. 134-137, 2011.

[146] V. Tvergaard and J. W. Hutchinson, "Microcracking in Ceramics Induced by Thermal Expansion or Elastic Anisotropy," *J. Am. Ceram. Soc.,* vol. 71, p. 157, 1988.

[147] H. Fu, D. Li, F. Peng, T. Gao and X. Cheng, "Ab initio calculations of elastic constants and thermodynamic properties of NiAl under high pressures," *Comput. Mater. Sci.,* vol. 44, pp. 774-778, 2008.

[148] D. G. Pettifor, "Theoretical predictions of structure and related properties of intermetallic," *Mater. Sci. Technol.,* vol. 8, pp. 345-349, 1992.

[149] S. Pugh , "Relations Between the Elastic Moduli and the Plastic Properties of Polycrystalline Pure Metals," *Philos. Mag.,* vol. 45, pp. 823-843, 1954.

[150] H. Li, Y. Chen, H. Wang, H. Wang, Y. Li, I. Harran, Y. Li and C. Guo, "First-principles study of mechanical and thermodynamic properties of Ti-Ga intermatallic compounds," *J. Alloys Compd.,* vol. 700, pp. 208-214, 2017.

[151] M. A. Blanco, E. Francisco and V. Luana, "GIBBS: Isothermal-Isobaric Thermodynamics of Solids From Energy Curves Using a Quasi-Harmonic Debye Model," *Comput. Phys. Commun.,* vol. 158, pp. 57-72, 2004.

[152] H. Hosoda, K. Enami, A. Kamio and K. Inoue, "Alloys Design of PdTi-Based Shape Memory Alloys Based on Defect Structures and Site Preference of Ternary Elements," *J. Intell. Mater. Syst. Struct.,* vol. 7, pp. 312-320, 1996.

[153] A. A. Bunaciu, E. G. Udriştioiu and H. Y. Aboul-Enein, "X-ray diffration: Instrumentation and appplications," *Crit. Rev. Anal. Chem.,* vol. 45, pp. 289-299, 2015.

[154] H. R. Chauke, D. Nguyen-Manh, P. E. Ngoepe, D. G. Pettifor and S. G. Fries, "Electronic structure and stability of the pentlandites Co 9 S 8 and (F e, N i) 9 S 8," *Phys. Rev. B,* vol. 66, p. 155105, 2002.

[155] Yu. N. Gornostyrev, O. Yu. Kontsevoi, A. F. Maksyutov, A. J. Freeman, M. I. Katsnelson, A. V. Trefilov and A. I. Lichtenshtein, "Negative yield stress temperature anomaly and structural instability of Pt3Al," *Phys. Rev. B,* vol. 70, p. 014102, 2004.

[156] D. A. Pankhurst, D. Nguyen-Manh and D. G. Pettifor, "Electronic origin of structural trends across early transition-metal disilicides: Anomalous behavior of CrSi2," *Phys. Rev. B,* vol. 69, p. 075113, 2004.

[157] C. Zener , "Contributions to the Theory of Beta-Phase Alloys," *Phys. Rev.,* vol. 71, pp. 846-851, 1947.

[158] X. Ren, N. Miura, L. Taniwaki, K. Otsuka, T. Suzuki, K. Tanaka, Y. I. Chumlyakov and M. Asai, "Understanding the Martensitic Transformations in TiNi-based Alloys by Elastic Constants Measurement," *Mater. Sci. Eng. A,* Vols. 273-275, pp. 190-194, 1999.

[159] K. Gschneidner et. al., "A family of Ductile Intermetallic Compounds," *Nat. Mater.,* vol. 2, pp. 587-591, 2003.

[160] J. Wu, B. Zhang and Y. Zhan, "Ab initio investigation into the structure and properties of Ir–Zr intermetallics for high-temperature structural applications," *Comput. Mater. Sci.,* vol. 131, pp. 146-159, 2017.

[161] Y. Pan, Y. Lin, X. Wang, S. Chen, L. Wang, C. Tong and Z. Cao, "Structural stability and mechanical properties of Pt–Zr alloys from first-principles," *J. Alloys Compd.,* vol. 643, pp. 49-55, 2015.

[162] G. Murtaza et al, "Structural, electronic, optical and thermodynamic properties of cubic REGa3 (RE = Sc or Lu) compounds: Ab initio study," *J. Alloys Compd.,* vol. 597, pp. 36-44, 2014.

[163] G. Yi, X. Zhang, J. Qin, J. Ning, S. Zhang, M. Ma and R. Liu, "Mechanical, electronic and thermal properties of Cu5Zr and Cu5Hf by first-principles calculations," *J. Alloys Compd.,* vol. 640, pp. 455-461, 2015.

[164] J. Yang, J. Huang, Z. Ye, D. Fan, S. Chen and Y. Zhao, "First-principles calculations on structural energetics of Cu-Ti binary system intermetallic compounds in Ag-Cu-Ti and Cu-Ni-Ti active filler metals," *Ceram. Int.,* vol. 43, pp. 7751-7761, 2017.

[165] T. Tohei, A. Kuwabara, F. Oba and I. Tanaka, "Debye Temperature and stiffness of carbon and boron nitride polymorphs from first principles calculations," *Phys. Rev. B,* vol. 73, p. 064304, 2006.

[166] P. Debye, "Zur Theorie der spezifischen Wärmen," *Ann. Phys.,* vol. 39, pp. 789-839, 1912.

[167] A. T. Petit and P. L. Dulong, "Recherches sur quelques points importants de la théorie de la chaleur," *Ann. Chim. Phys.,* vol. 10, pp. 395-413, 1819.

[168] R. Przeliorz and J. Piatkowski , "Thermophysical properties of nickel-based cast superalloys," *METALURGIJA,* vol. 54, pp. 543-546, 2015.

[169] G. J. Martyna,D. J. Tobias and M. L. Klein, "Constant pressure molecular dynamics algorithms," *J. Chern. Phys. ,* vol. 101 , pp. 4177-4189, 1994.

[170] D. Bandyopadhyay, R.C. Sharma and N. Chakraborti, "The Ti - Co - C system (Titanium - Cobalt - Carbon)," *Ph. Equilibria,* vol. 2, pp. 179-185, 2000.

[171] P. Ravindran, L. Fast, P. A. Korzhavyi, B. Johansson, J. Wills and O. Eriksson, "Density functional theory for calculation of elastic properties of orthorhombic crystals: application to TiSi2," *J. Appl. Phys.,* vol. 84, pp. 4891-4904, 1998.

[172] E. Deligoz and H. Ozisik, "Mechanical and dynamical stability of TiAsTe compound from ab initio calculations," *Philos. Mag. A,* vol. 95, pp. 2294-2305, 2015.

[173] J. C. Slater and G. F. Koster, "Simplified LCAO method for a periodic potential problem," *Phys. Rev.,* vol. 94, pp. 1498-1524, 1954.

[174] H. Bross, "LDA and GGA investigations of some ground state properties of aluminium with the all electron MAPW method," *Eur. Phys. J. B,* vol. 37, pp. 405-411, 2004.

[175] W. W. Xu, S. L. Shang, B. C. Zhou,Y. Wang, L. J. Chen, C. P. Wang, X. J. Liu and Z. K. Liu, "A first-principles study of the diffusion coefficients of alloying elements in dilute alpha-Ti alloys," *Phys. Chem. Chem. Phys.,* vol. 18, p. 1687, 2016.

[176] R. G. Diale, R. Modiba, P. E. Ngoepe and H. R. Chauke, "Phase stability of TiPd1-xRux and Ti1-xPdRux shape memory alloys," *Mater. Today: Proc.,* vol. 38, pp. 1071-1076, 2021.

[177] R. Salloom, D. Reith, R. Banerjee and S. G. Srinivasan, "First principles calculations on the effect of interstitial oxygen on phase stability and β–α″ martensitic transformation in Ti–Nb alloys," *J. Mater. Sci.,* vol. 53, pp. 11473-11487, 2018.

[178] F. Z. Zhang, H. T. Xue, F. L. Tang, X. K. Li, W. J. Lu and Y. D. Feng, "Phase equilibrium of Cd1–xZnxS alloys studied by first-principles calculations and Monte Carlo simulations," *Chin. Phys. B,* vol. 25, p. 013103, 2016.

APPENDIX A

Temperature dependence of the $Ti_{50}Pd_{50-x}M_x$ (M= Co, Ni)
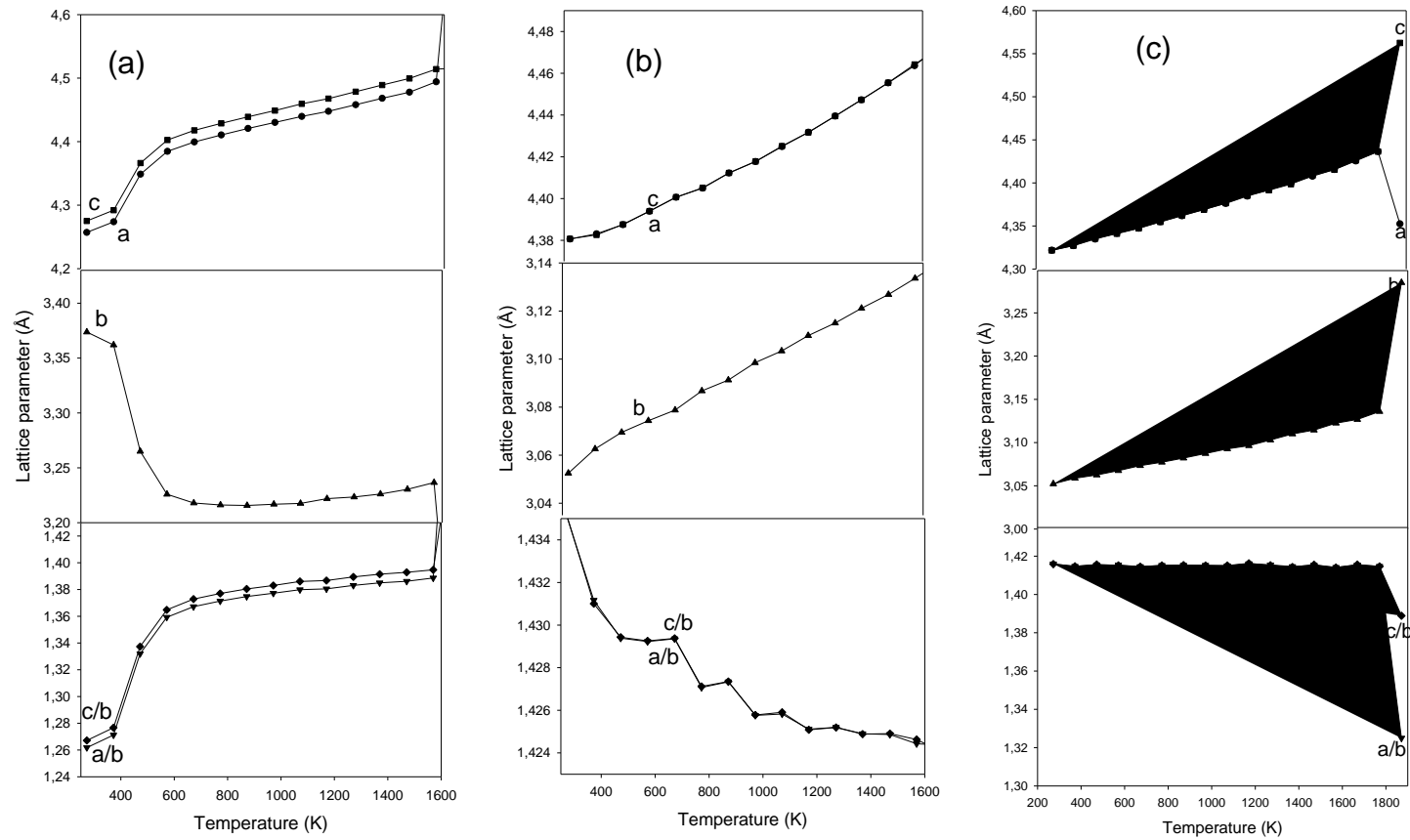
Figure A-1 Lattice expansions (a) 31.25 (b) 43.75 and (c) 50 at. % Co ($Ti_{50}Pd_{50-x}Co_X$ alloys) against temperature.
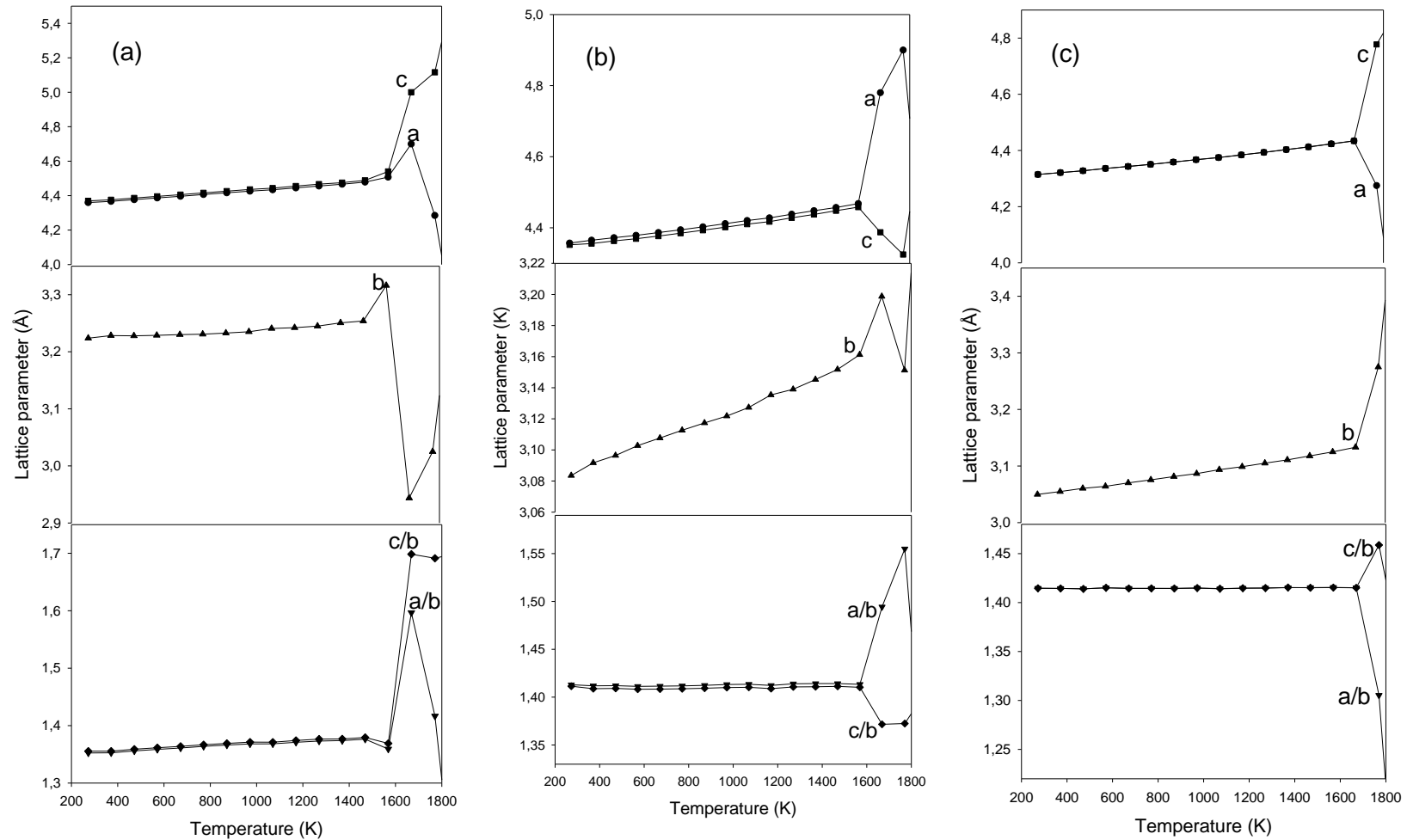
Figure A-2 Lattice expansions of (a) 31.25 (b) 43.75 and (c) 50 at. % Al (Ti$_{50}$Pd$_{50-X}$Al$_X$ alloys) against temperature.

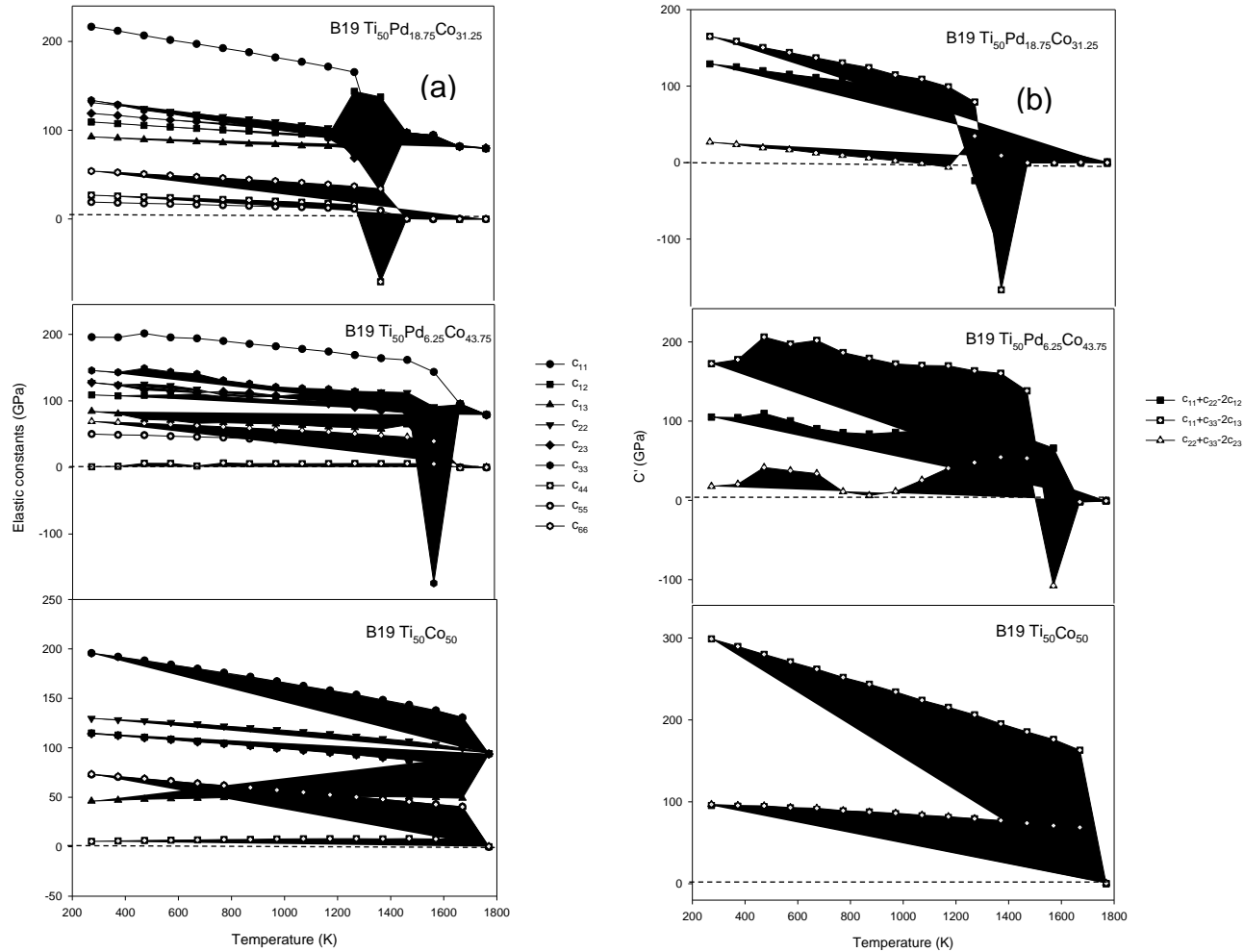**Elastic properties of B19 Ti₅₀Pd₅₀₋ₓMₓ (Co and Ni) alloys with temperature.**

Figure A-3 simulated (a) elastic constants and (b) elastic shear modulus (C') against temperature for Ti₅₀Pd₅₀₋ₓCoₓ alloys (31.25≤x≤50). The dotted lines are used as a guide with respect to stability.
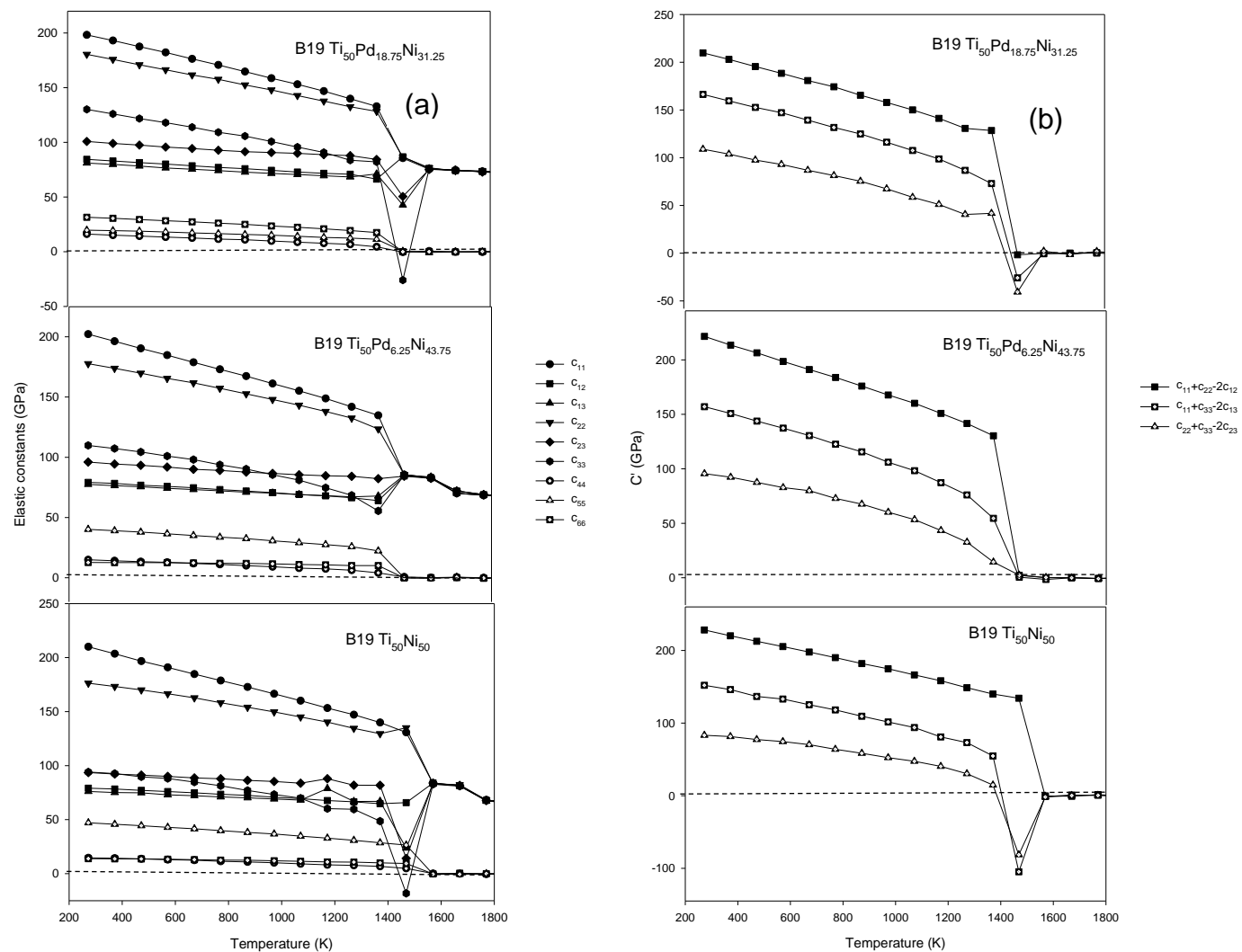
Figure A-4 Simulated (a) elastic constants and (b) elastic shear modulus (C') against temperature for Ti$_{50}$Pd$_{50-X}$Ni$_X$ alloys (31.25≤x≤50). The dotted lines are used as a guide with respect to stability.

APPENDIX B

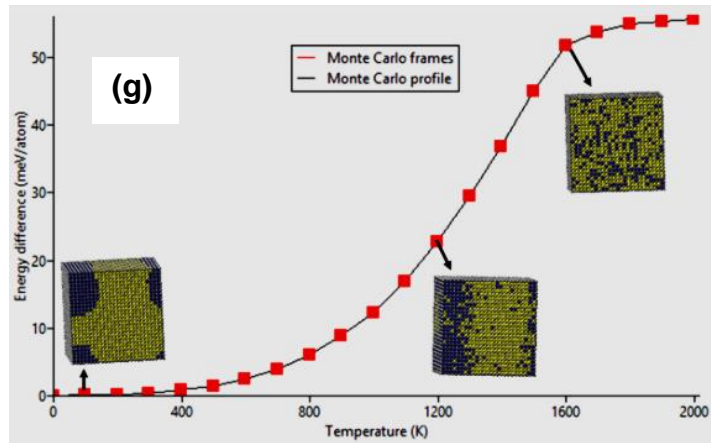## Temperatures Monte Carlo profiles of the B2 Ti-Pd-Ru
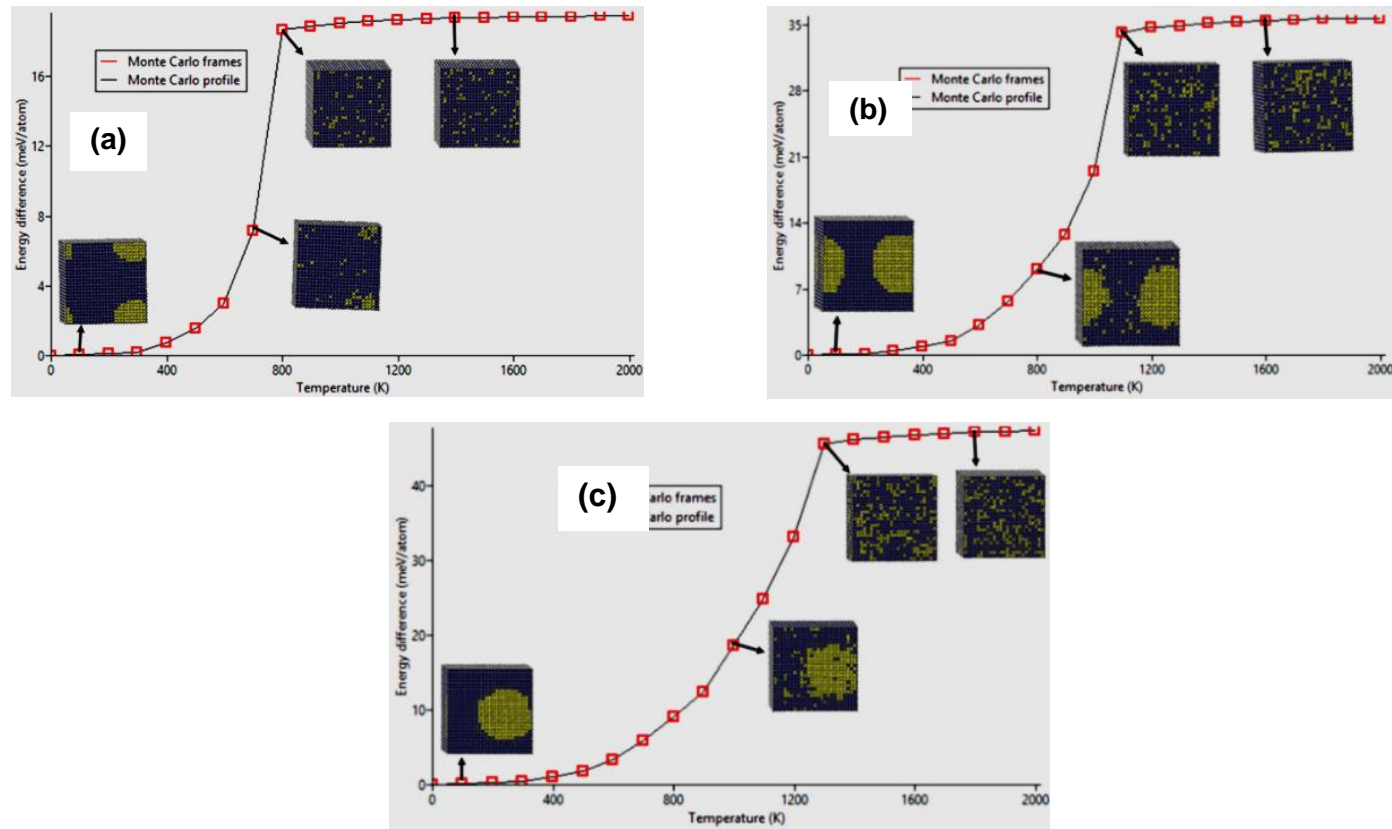
Figure B-1 Energy difference against temperature of B2 Ti-Pd-Ru at different concentrations (a) Ti-Pd$_{0.9}$Ru$_{0.1}$, (b) Ti-Pd$_{0.8}$Ru$_{0.2}$ and (c) Ti-Pd$_{0.7}$Ru$_{0.3}$.
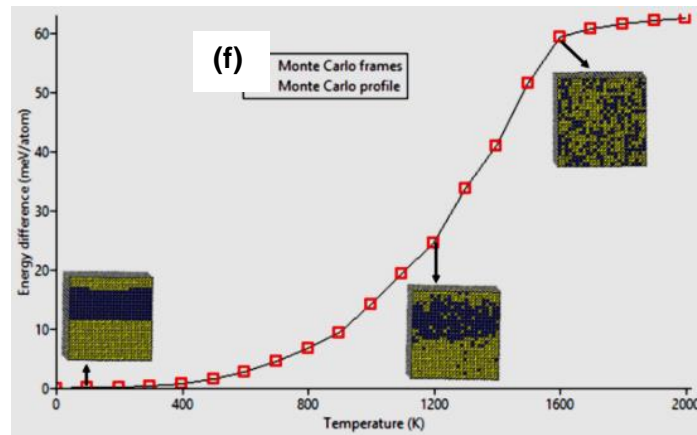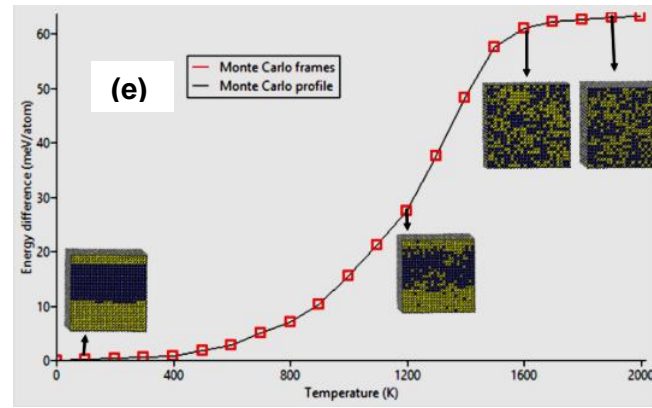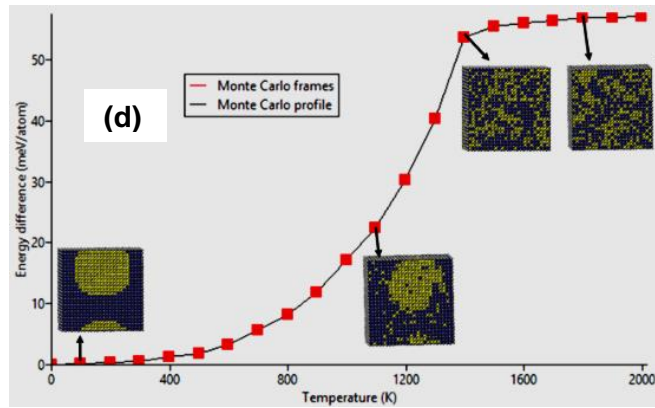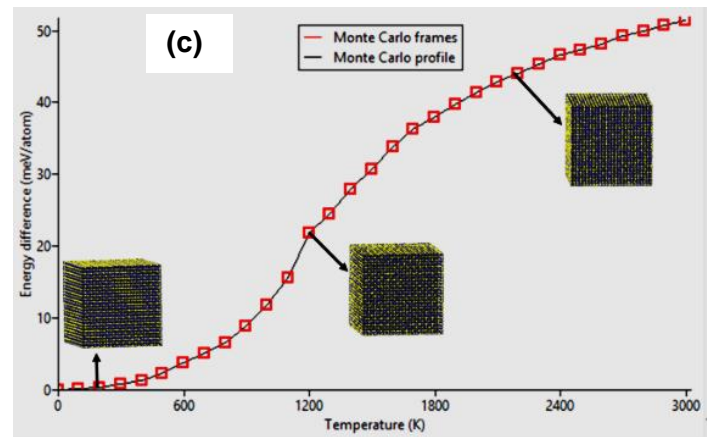
Figure B-2 Energy difference against temperature of B2 Ti-Pd-Ru at different concentrations (d) Ti-Pd$_{0.6}$Ru$_{0.4}$, (e) Ti-Pd$_{0.5}$Ru$_{0.5}$ and (f) Ti-Pd$_{0.4}$Ru$_{0.6}$.
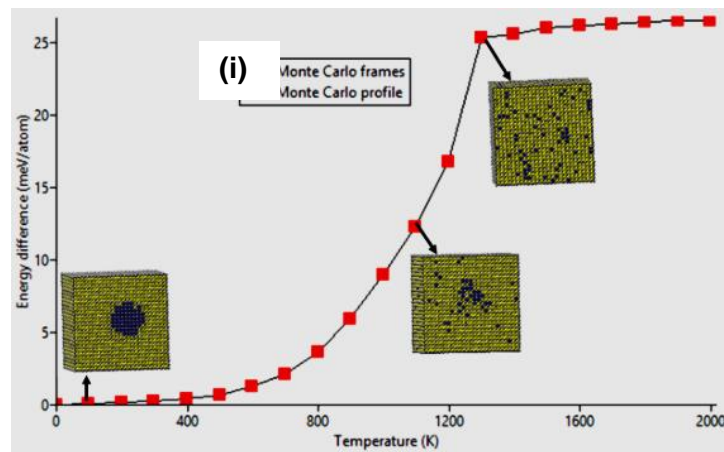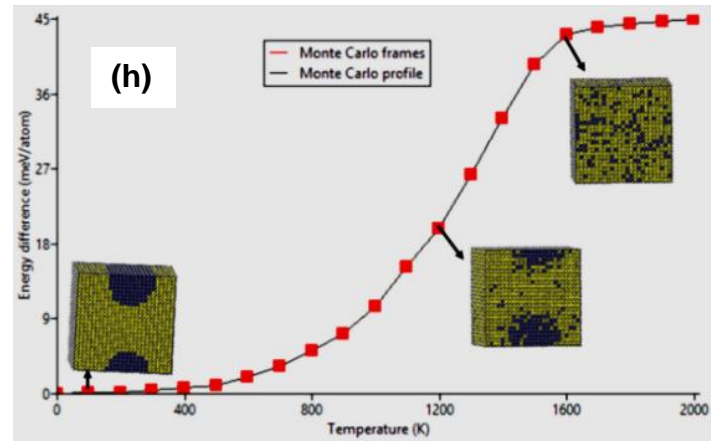
Figure B-3 Energy difference against temperature of B2 Ti-Pd-Ru at different concentrations (g) Ti-Pd$_{0.3}$Ru$_{0.7}$, (h) Ti-Pd$_{0.2}$Ru$_{0.8}$ and (i) Ti-Pd$_{0.1}$Ru$_{0.9}$.
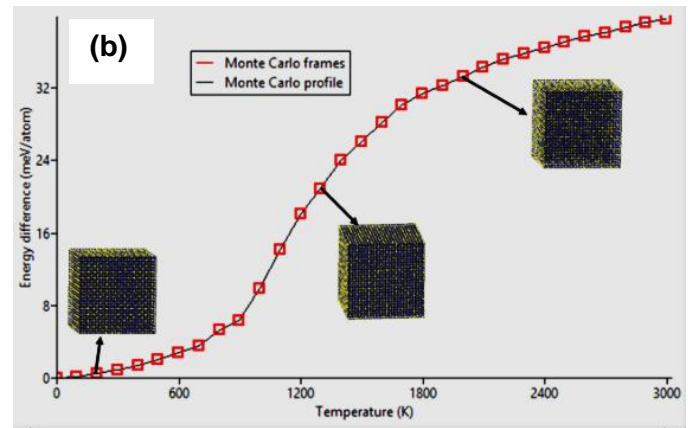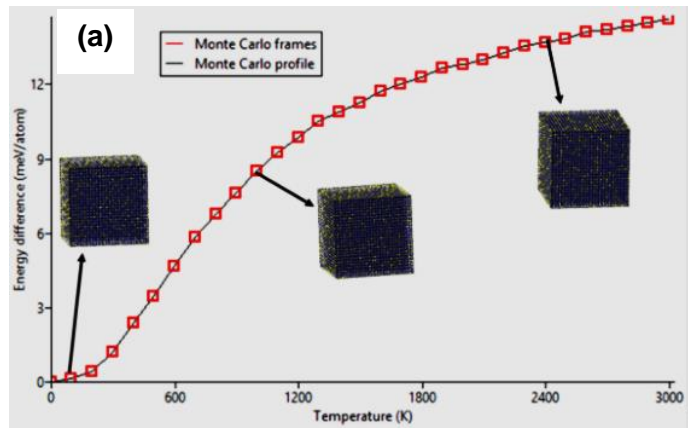
Figure B-4 Energy diffrence against temperature of B2 Ti-Pd-Ru at various concentrations (a) $Ti_{0.9}PdRu_{0.1}$, (b) $Ti_{0.8}PdRu_{0.2}$ and (c) $Ti_{0.7}PdRu_{0.3}$.
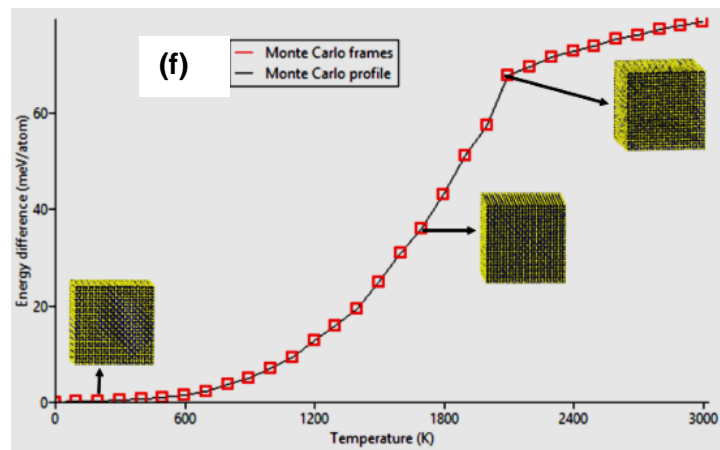
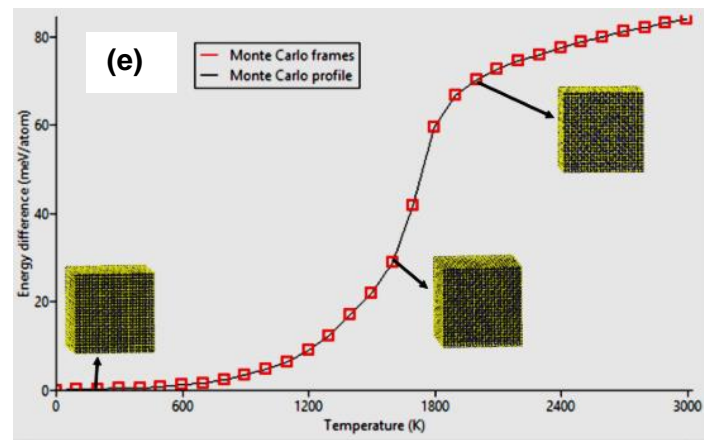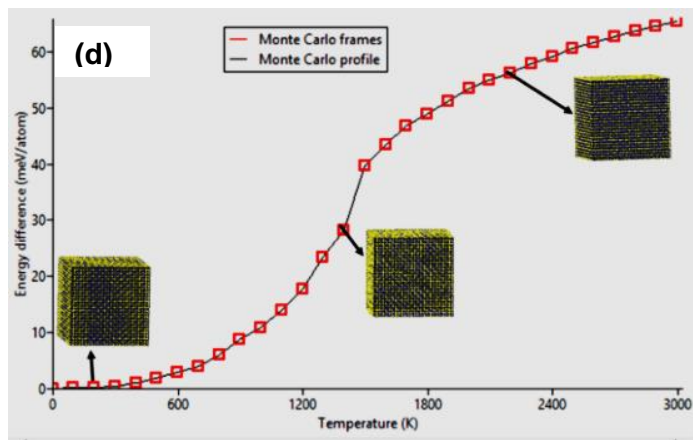**Figure B-5 Energy difference against temperature of B2 Ti-Pd-Ru at various concentrations (d) $Ti_{0.6}PdRu_{0.4}$, (e) $Ti_{0.5}PdRu_{0.5}$ and (f) $Ti_{0.4}PdRu_{0.6}$.**
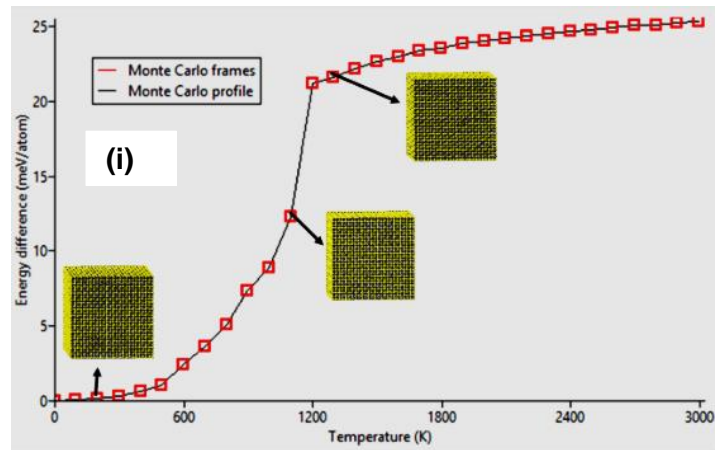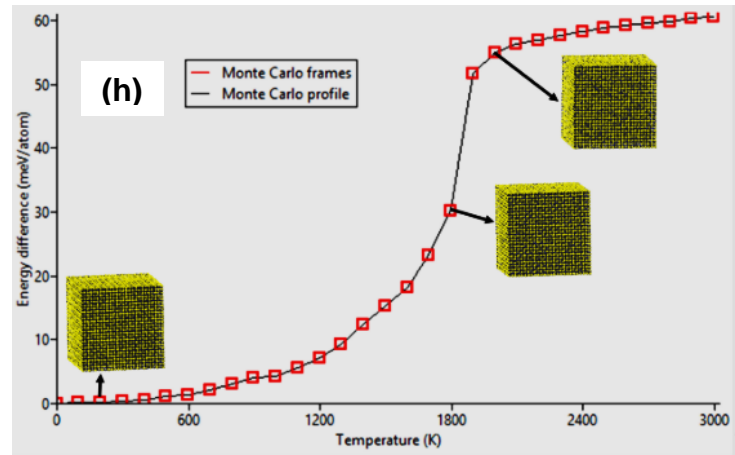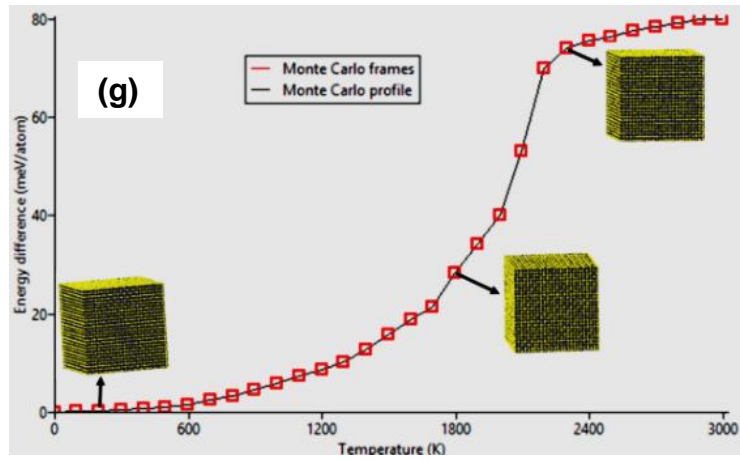
Figure B-6 Energy difference against temperature of B2 Ti-Pd-Ru at various concentrations (g) $Ti_{0.3}PdRu_{0.7}$, (h) $Ti_{0.2}PdRu_{0.8}$ and (i) $Ti_{0.1}PdRu_{0.9}$.

APPENDIX C

C. Presentations at Conferences

1. R.G. Diale, H.R. Chauke and P.E. Ngoepe, "First-principles study of phase stability, mechanical properties and electronic structure of Ti-Al-Ir alloys", AMI Precious Metals 2017, 17 -19 October 2017, Protea Hotel Ranch Resort Polokwane, South Africa.

2. R.G. Diale, R. Modiba, H.R. Chauke and P.E. Ngoepe "Computational Modelling studies of martensitic transformation behaviour in TiPd shape memory alloy " 8th Faculty of Science and Agriculture Research Day, 19-20 October 2017, Bolivia Lodge, Polokwane, South Africa.

3. R.G. Diale, R. Modiba, H.R. Chauke, and P.E. Ngoepe "Temperature dependence and martensitic transformation of B19 and $L1_0$ TiPd shape memory alloys" Centre for High Performance Computing National Meeting, 3-7 December 2017, Velmoré Hotel Estate, South Africa.

4. R.G. Diale, R. Modiba, H.R. Chauke and P.E. Ngoepe "computational Modelling studies of TiPd shape memory alloys" 9th International Conference of the African Materials Research Society 2017, 11-14 December 2017, Gaborone, Botswana.

5. R.G. Diale, R. Modiba, H.R. Chauke and P.E. Ngoepe "Martensitic transformation of TiPd-X as potential high temperature shape memory alloys (X=Ru, Ni, Au, OS)" 2nd International conference High Temperature Shape Memory Alloys, 15-18 May 2018, Kloster Irsee, Irsee (Germany).

6. R.G. Diale, R. Modiba, H.R. Chauke and P.E. Ngoepe "Computational Modelling of $Ti_{50}Pd_{50-x}Pt_{X}$ (1≤ x ≤50) shape memory alloys" 9th Faculty of Science and Agriculture Research Day, 20-21 September 2018, Fusion Boutique Hotel, Polokwane.

7. R.G. Diale, R. Modiba, H.R. Chauke and P.E. Ngoepe "First principles study of structural, thermodynamic, elastic, and electronic properties of TiPd-Ru shape memory alloys" Conference of the South African Advanced Materials Initiative (CoSAAMI-2018), 23-26 October 2018, Riverside Sun, Vanderbijlpark.

8. R.G. Diale, R. Modiba, H.R. Chauke and P.E. Ngoepe "Computational Modelling of TiPd-Ir high temperature shape memory alloys" Centre for High Performance Computing National Meeting, 2-6 December 2018, Century City Convention Centre, Cape Town.

9. R.G. Diale, R. Modiba, H.R. Chauke and P.E. Ngoepe "Investigating the effect of Co addition on the stability of B2 TiPd system using DFT approach" South African Institute of Physics (SAIP), 8-12 July 2019, Protea Hotel Ranch Resort Polokwane, South Africa.

10. R.G. Diale, R. Modiba, H.R. Chauke and P.E. Ngoepe "Theoretical Investigations of the stability and transformation temperature in TiPd-Co shape memory alloys" 10th Faculty of Science and Agriculture Research Day, 19-20 September 2019, Protea Hotel Ranch Resort Polokwane, South Africa.

11. R.G. Diale, R. Modiba, H.R. Chauke and P.E. Ngoepe "Density functional theory study of TiPd alloying with Os as potential high temperature shape memory alloys" Conference of the South African Advanced Materials Initiative (CoSAAMI-2019), 22-25 October 2019, Riverside Sun, Vanderbijlpark.

12. R.G. Diale, R. Modiba, H.R. Chauke and P.E. Ngoepe "A molecular dynamic simulation studies of structural and mechanical properties on B19 TiPd-Pt shape memory alloys" Centre for High Performance Computing National Meeting, 1-5 December 2019, Birchwood, Boksburg.

13. R.G. Diale, R. Modiba, H.R. Chauke and P.E. Ngoepe "Phase stability of $TiPd_{1-x}Ru_x$ and $Ti_{1-x}PdRu_x$ shape memory alloys" The 2020 International Symposium on Nanostructured, Nanoengineered, and Advanced Materials (ISNNAM 2020), 6-7 August 2020, Virtual Conference.

14. R.G. Diale, R. Modiba, H.R. Chauke and P.E. Ngoepe "Parameterization and transformation temperature of $Ti_{50}Pd_{50-x}Ru_x$ using SCC-DFTB approach" Materials Challenges for Memory, 11-13 April 2021, Virtual Conference.

APPENDIX D

D. Publications

1. R.G. Diale, H.R. Chauke and P.E. Ngoepe, "First-principles study of phase stability, mechanical properties and electronic structure of Ti-Al-Ir alloys", Symposium Series S94, proceedings of AMI Precious Metals 2017, 17 - 19 October 2017, held in Protea Hotel Ranch Resort, Polokwane, South Africa.

2. R.G. Diale, R. Modiba, P.E. Ngoepe and H.R. Chauke, "The effect of Ru on $Ti_{50}Pd_{50}$ high temperature shape memory alloy: a first-principles study" MRS Advances, vol. 4, pp. 2419-2429, 2019.

3. R.G. Diale, R. Modiba, P.E. Ngoepe and H.R. Chauke, "Density functional theory study of TiPd alloying with Os as potential high temperature shape memory alloys" IOP Conf. Sr. Mater. Sci. Eng., vol. 655, p. 012042, 2019.

4. A.F. Mazibuko, R.G. Diale, H.R. Chauke and P.E. Ngoepe, "First principle studies of palladium nanoparticles on titanium dioxide surfaces for catalytic application" Proceedings of the SA Institute of Physics (2018), pp. 37-43, 2019, ISBN: 978-0-620-85406-1.

5. R.G. Diale, R. Modiba, P.E. Ngoepe and H.R. Chauke, "Phase stability of $TiPd_{1-x}Ru_x$ and $Ti_{1-x}PdRu_x$ shape memory alloys" Materials Today: Proceedings, vol. 38, pp. 1071-1076, 2021.